IHEP-CEPC-DR-2018-XX

IHEP-EP-2018-XX

IHEP-TH-2018-XX

CEPC

Conceptual Design Report

Volume I - Physics & Detector

The CEPC Study Group

Spring 2018

ACKNOWLEDGMENTS

The CEPC-SPPC Conceptual Design Report (CDR) was prepared and written by the CEPC-SppC Study Group. The study was organised and led by scientists from the Institute of High Energy Physics (IHEP) of the Chinese Academy of Sciences (CAS), and from many universities and other institutes in China and abroad. The study was partially supported ...

...

CONTENTS

CHAPTER 1

INTRODUCTION

This [1] is only an example without plots, please edit ...

1.1 The CEPC-SPPC Study Group and the CDR

1.2 The Case for the CEPC-SppC in China

1.3 The Science in the CDR

1.4 The Accelerator and the Experiment

References

[1] CEPC project website. http://cepc.ihep.ac.cn.

CHAPTER 2

OVERVIEW OF THE PHYSICS CASE FOR CEPC-SPPC

Lorem ipsum dolor sit amet, consectetuer adipiscing elit. Ut purus elit, vestibulum ut, placerat ac, adipiscing vitae, felis. Curabitur dictum gravida mauris. Nam arcu libero, nonummy eget, consectetuer id, vulputate a, magna. Donec vehicula augue eu neque. Pellentesque habitant morbi tristique senectus et netus et malesuada fames ac turpis egestas. Mauris ut leo. Cras viverra metus rhoncus sem. Nulla et lectus vestibulum urna fringilla ultrices. Phasellus eu tellus sit amet tortor gravida placerat. Integer sapien est, iaculis in, pretium quis, viverra ac, nunc. Praesent eget sem vel leo ultrices bibendum. Aenean faucibus. Morbi dolor nulla, malesuada eu, pulvinar at, mollis ac, nulla. Curabitur auctor semper nulla. Donec varius orci eget risus. Duis nibh mi, congue eu, accumsan eleifend, sagittis quis, diam. Duis eget orci sit amet orci dignissim rutrum.

Nam dui ligula, fringilla a, euismod sodales, sollicitudin vel, wisi. Morbi auctor lorem non justo. Nam lacus libero, pretium at, lobortis vitae, ultricies et, tellus. Donec aliquet, tortor sed accumsan bibendum, erat ligula aliquet magna, vitae ornare odio metus a mi. Morbi ac orci et nisl hendrerit mollis. Suspendisse ut massa. Cras nec ante. Pellentesque a nulla. Cum sociis natoque penatibus et magnis dis parturient montes, nascetur ridiculus mus. Aliquam tincidunt urna. Nulla ullamcorper vestibulum turpis. Pellentesque cursus luctus mauris.

This [1] is an example with plots, please edit ...

2.1 First theory subsection

Lorem ipsum dolor sit amet, consectetuer adipiscing elit. Ut purus elit, vestibulum ut, placerat ac, adipiscing vitae, felis. Curabitur dictum gravida mauris. Nam arcu libero, nonummy eget, consectetuer id, vulputate a, magna. Donec vehicula augue eu neque.

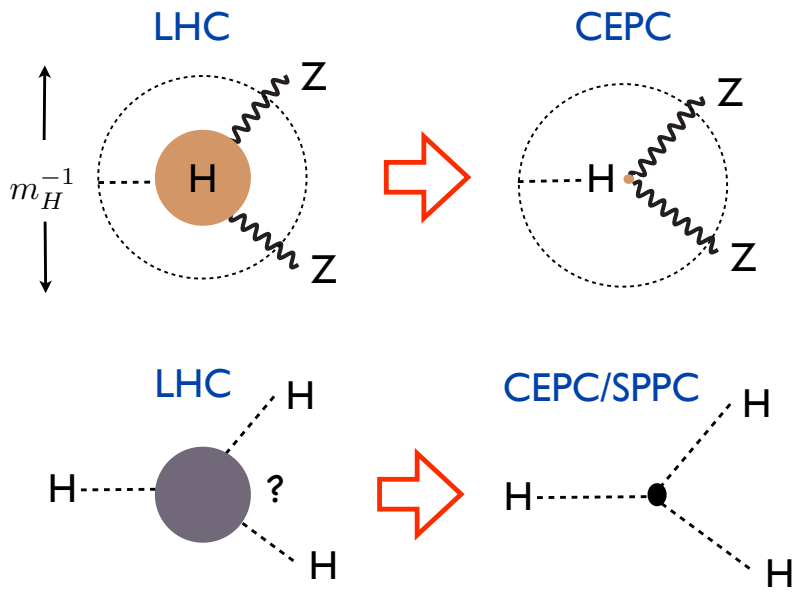

Figure 2.1: A sketch of two of the central goals of the CEPC and SPPC. The CEPC will probe whether the Higgs is truly “elementary", with a resolution up to a hundred times more powerful than the LHC. The SPPC will see, for the first time, a fundamentally new dynamical process — the self-interaction of an elementary particle — uniquely associated with the Higgs.

Pellentesque habitant morbi tristique senectus et netus et malesuada fames ac turpis egestas. Mauris ut leo. Cras viverra metus rhoncus sem. Nulla et lectus vestibulum urna fringilla ultrices. Phasellus eu tellus sit amet tortor gravida placerat. Integer sapien est, iaculis in, pretium quis, viverra ac, nunc. Praesent eget sem vel leo ultrices bibendum. Aenean faucibus. Morbi dolor nulla, malesuada eu, pulvinar at, mollis ac, nulla. Curabitur auctor semper nulla. Donec varius orci eget risus. Duis nibh mi, congue eu, accumsan eleifend, sagittis quis, diam. Duis eget orci sit amet orci dignissim rutrum.

Nam dui ligula, fringilla a, euismod sodales, sollicitudin vel, wisi. Morbi auctor lorem non justo. Nam lacus libero, pretium at, lobortis vitae, ultricies et, tellus. Donec aliquet, tortor sed accumsan bibendum, erat ligula aliquet magna, vitae ornare odio metus a mi. Morbi ac orci et nisl hendrerit mollis. Suspendisse ut massa. Cras nec ante. Pellentesque a nulla. Cum sociis natoque penatibus et magnis dis parturient montes, nascetur ridiculus mus. Aliquam tincidunt urna. Nulla ullamcorper vestibulum turpis. Pellentesque cursus luctus mauris.

References

[1] CEPC project website. http://cepc.ihep.ac.cn.

CHAPTER 3

EXPERIMENTAL CONDITIONS AND DETECTOR CONCEPTS

3.1 Experimental conditions

The machine is designed to collider electron and positron beams at the center-of-mass energy of $E_{\rm cm} = 240$ GeV ($e^+e^- \to ZH$ production) at a peak luminosity of 2×10^{34} cm$^{-2}\cdot$ s^{-1}. Machine operations at $E_{\rm cm} = 91$ GeV and $E_{\rm cm} = 160$ GeV for Z and W, respectively, are also possible. Two interactions points are available for exploring different detector design scenarios and technologies. Two common RF stations are deployed for the Higgs operation, which result in 286 bunches evenly distributed over a half ring. While for W and Z operations, independent RF cavities are used, and 5220 and 10900 bunches, respectively, are spreading in equal distance over the full ring. Therefore the bunch spacings are roughly 500 ns, 50 ns and 30 ns [1] for Higgs, W and Z, respectively.

Radiation backgrounds can impose significant constraints on the detector design and chosen technologies. They give rise to both primary and secondary particles to enter the detector. They can cause radiation damage, increase the detector and degrade the detector performance. Synchrotron radiation, as often considered one of the most critical backgrounds at circular machines, are being evaluated, preliminary results turns out promising though. Collimators and masks are being designed to reduce the radiation backgrounds to the acceptable level. Other important detector backgrounds originate from the pair production and the beam lost particles due to radiative Bhabha scattering. For the machine operation at Higgs, the maximum hit density at the first vertex detector layer is estimated to be ~ 2.5 hits/cm$^2\cdot$BX. The annual TID and NIEL at the inner most detector layer are

[1] It is estimated for the low luminosity configuration for Z operation. The bunch spacing can be significantly shorter if higher luminosity for Z operation is deployed.

around 2.5 MRad and 10^{12} $1\mathrm{MeV}$ $\mathrm{n_{eq}}/\mathrm{cm}^2$, respectively. Safety factors of 10 are always applied.

3.2 The CEPC detector requirements for e^+e^- physics

3.2.1 Track momentum resolution

3.2.2 Jet energy resolution

3.2.3 Impact parameter resolution and flavour tagging

3.2.4 Lepton Identification requirements

3.2.5 Summary

Lorem ipsum dolor sit amet, consectetuer adipiscing elit. Ut purus elit, vestibulum ut, placerat ac, adipiscing vitae, felis. Curabitur dictum gravida mauris. Nam arcu libero, nonummy eget, consectetuer id, vulputate a, magna. Donec vehicula augue eu neque. Pellentesque habitant morbi tristique senectus et netus et malesuada fames ac turpis egestas. Mauris ut leo. Cras viverra metus rhoncus sem. Nulla et lectus vestibulum urna fringilla ultrices. Phasellus eu tellus sit amet tortor gravida placerat. Integer sapien est, iaculis in, pretium quis, viverra ac, nunc. Praesent eget sem vel leo ultrices bibendum. Aenean faucibus. Morbi dolor nulla, malesuada eu, pulvinar at, mollis ac, nulla. Curabitur auctor semper nulla. Donec varius orci eget risus. Duis nibh mi, congue eu, accumsan eleifend, sagittis quis, diam. Duis eget orci sit amet orci dignissim rutrum.

3.3 Detector concepts

3.3.1 The baseline detector concept

3.3.1.1 Full silicon detector concept

3.3.2 An alternative low magnetic field detector concept

The baseline detector described in this CDR is a very straightforward evolution of the ILD detector originally conceived for the International Linear Collider (ILC) [1]. We propose here a new detector concept, IDEA, that is specifically designed for CepC and also attempts to significantly reduce the overall cost of the detector.

While most detector requirements needed for detectors at ILC are very similar to those for CepC [2], there are however some notable differences. First of all the typical luminosity expected both at the Z pole ($\sqrt{s} = 90\,GeV$) and above the ZH threshold ($\sqrt{s} = 240\,GeV$) is expected to be one or two orders of magnitude larger, with a much shorter bunch spacing and no large time gaps in the beam structure. This places severe constraints on the tracking system. In particular one would prefer an intrinsically fast main tracker to fully exploit the cleanliness of the e^+e^- environment, and a very low power vertex detector, since power pulsing is not allowed by the bunch spacing. Additional issues of emittance preservation, typical of circular machines, set limits on the maximum magnetic field usable for the tracker solenoid, especially when running at the lower energy. This could be a problem for a large volume TPC, due to the resolution degradation, and also for a silicon tracker, since it would require more layers at a large radius, thus significantly increasing the cost.

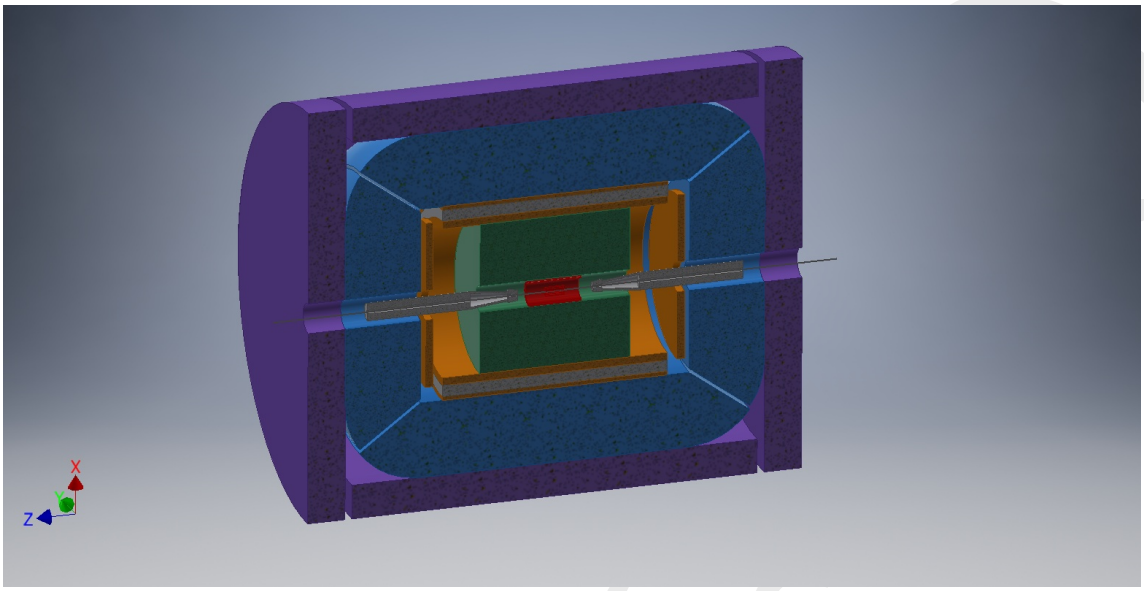

Figure 3.1: Schematic layout of the IDEA detector. Sub-detectors are outlined in different colors : vertex detector (red), drift chamber (green), pre-shower (orange), magnet (gray), calorimeter (blue), magnet yoke and muon system (violet).

Additional specific requirements on a detector for CepC come from precision physics at the Z pole, where the statistical accuracy on various electro-weak parameters is expected to be an order of magnitude better than at the ILC. This calls for a very tight control of the systematic error on the acceptance, with a definition of the acceptance boundaries at the level of a few μm, and a very good $e-\gamma-\pi_0$ discrimination to identify τ leptons efficiently and measure their polarization. A pre-shower, with the first measurement layer based on silicon micro-strip detectors, just outside the tracker, could be an effective solution, while at the same time improving the overall tracking system resolution.

The particle flow calorimeters currently proposed for both ILC and CLIC, are very expensive due to their extremely large number of readout channels and require significant data processing to obtain the optimal performance. A cheaper and more effective calorimeter can be made using the dual readout technique [3], which has been extensively studied and demonstrated in over ten years of R&D by the DREAM/RD52 collaboration [4, 5]. With this technology the electromagnetic and hadronic calorimeters come in a single package that plays both functions and allows an excellent discrimination between hadronic and electromagnetic showers [6].

Finally recent developments in multi-pattern gas detector technology, such as μRwell [7], can significantly reduce the cost of large area tracking chambers to be used for tracking muons outside the calorimeter volume.

3.3.2.1 The IDEA detector

The structure of the IDEA detector is outlined in figure 3.1.

A key element of IDEA is a thin, $\sim$30 cm, and low mass, $\sim 0.8\,X_0$, solenoid with a magnetic field of 2 Tesla. This field is optimal, according to studies done for FCC-ee, as it minimizes the impact on emittance growth and allows for manageable fields in the compensating solenoids [8], but is certainly too low to support a TPC or a silicon tracker of reasonable size.

The innermost detector, surrounding the 1.5 cm beam pipe, is a silicon pixel detector for the precise determination of the impact parameter of charged particle tracks. Recent test beam results on the detectors planned for the ALICE inner tracker upgrade (ITS), based on the ALPIDE readout chip [9], indicate an excellent resolution, $\sim$5 μm, and high efficiency at low power and dark noise rate [10]. This looks like a good starting point for the IDEA vertex detector and is a similar approach is proposed for the CepC baseline detector (see section 4.5). The two detector concepts could then share the same pixel technology as well as profit from the electronic and mechanical work of the ALICE ITS.

Outside the vertex detector we find a 4 m long cylindrical drift chamber starting from a radius of $\sim$30 cm and extending until 2 m. The chamber can be made extremely light, with low mass wires and operation on 90% helium gas; less than 1% X_0 is considered feasible for 90° tracks. Additional features of this chamber, which is described in detail in section 6.3, are a good spatial resolution, $<$100 μm, dE/dx resolution at the 2% level and a maximum drift time of only 150 nsec. Track momentum resolution of about 0.5% for 100 GeV tracks is expected when vertex detector and pre-shower information is included in the track fit. It is worth noting that the design of this chamber is the evolution of work done over many years on two existing chambers, that of the KLOE detector [11] and that of the recent MEG experiment upgrade [12]; major R&D work was done also for the 4th concept at ILC [13] and then for the Mu2E tracker [14].

A pre-shower is located between the drift chamber and the magnet in the barrel region and between the drift chamber and the end-cap calorimeter in the forward region. This detector consists of a $\sim$1 X_0 = 0.5 cm of lead followed by a layer of silicon micro-strip detectors. A second layer of MPGD chambers is located between the magnet and the calorimeter in the barrel region, while in the end-cap region an additional layer of lead is placed between the silicon and the chambers. This way about 75% of the π^0's can be tagged by having both γ's from their decay identified by the pre-shower. The silicon layer, besides increasing the tracking resolution, provides a very precise acceptance determination for both charged particles and γ's. The optimization of pre-shower thickness and calorimeter resolution is still in progress.

A solenoidal magnet surrounds the tracking system and the first pre-shower layer. Presently planned dimensions are 6 m of length and 4.2 m inner diameter. The relatively low two Tesla field and the small dimensions have important implications on the overall magnet package thickness, that can be kept at the 30-40 cm level, and on the size of the flux return yoke, which scales linearly with the field and the square of the coil diameter. With the given dimensions a yoke thickness of less than 100 cm of iron is sufficient to completely contain the magnetic flux and provide adequate shielding and support for the muon chambers.

A dual readout fiber calorimeter (see section 7) is located behind the second pre-shower layer. We assume a total calorimeter depth of 2 m, corresponding to approximately eight pion interaction lengths. The detector resolution is expected to be about $10.5\%/\sqrt{E}$ for electrons and $35\%/\sqrt{E}$ for isolated pions with negligible constant terms, as obtained from extrapolations from test beam data using GEANT4 without including the pre-shower. This detector has very good intrinsic discrimination between muons, electrons/photons and hadrons for isolated particles [6]. This discrimination power is further enhanced when the information of the pre-shower and the muon chambers is added, extending the separation power also into hadronic jets and making it suitable for the application of particle-flow-

like algorithms. The intrinsic high transverse granularity provides a good matching of showers to tracks and pre-shower signals.

The muon system consists of layers of muon chambers embedded in the magnet yoke. The area to be covered is substantial, several hundreds of square meters, requiring an inexpensive chamber technology. Recent developments in the industrialization of μRwell based large area chambers, as planned for the CMS Phase II upgrade, are very promising (see section 9).

3.3.2.2 Conclusions

A different concept for a detector at CepC has been proposed. This detector is designed specifically for CepC and its specific running conditions and physics goals. In particular it is safe with respect to interaction between the detector solenoid field and the beam. Although additional R&D to optimize performance, reduce costs and come to a detailed engineered design of the detector is still necessary, this detector is based on technologies which are established after many years of R&D and whose feasibility has by large been established. Furthermore several choices are made to simplify the detector structure and reduce the cost, which in the end should be significantly smaller than for an ILD-like detector.

References

[1] H. Abramowicz et al., *The International Linear Collider Technical Design Report - Volume 4: Detectors*, arXiv:1306.6329 [physics.ins-det].

[2] C.-S. S. Group, *CEPC-SPPC Preliminary Conceptual Design Report. 1. Physics and Detector*, .

[3] DREAM Collaboration, R. Wigmans, *The DREAM project: Towards the ultimate in calorimetry*, Nucl. Instrum. Meth. **A617** (2010) 129–133.

[4] N. Akchurin et al., *The electromagnetic performance of the RD52 fiber calorimeter*, Nucl. Instrum. Meth. **A735** (2014) 130–144.

[5] RD52 (DREAM) Collaboration, R. Wigmans, *New results from the RD52 project*, Nucl. Instrum. Meth. **A824** (2016) 721–725.

[6] N. Akchurin et al., *Particle identification in the longitudinally unsegmented RD52 calorimeter*, Nucl. Instrum. Meth. **A735** (2014) 120–129.

[7] M. Poli Lener, G. Bencivenni, R. de Olivera, G. Felici, S. Franchino, M. Gatta, M. Maggi, G. Morello, and A. Sharma, *The μ-RWELL: A compact, spark protected, single amplification-stage MPGD*, Nucl. Instrum. Meth. **A824** (2016) 565–568.

[8] M. Koratzinos et al., *Progress in the FCC-ee Interaction Region Magnet Design*, http://inspirehep.net/record/126211/files/wepik034.pdf (2017) , IPAC2017.

[9] ALICE Collaboration, M. Mager, *ALPIDE, the Monolithic Active Pixel Sensor for the ALICE ITS upgrade*, Nucl. Instrum. Meth. **A824** (2016) 434–438.

[10] ALICE Collaboration, G. Aglieri Rinella, *The ALPIDE pixel sensor chip for the upgrade of the ALICE Inner Tracking System*, Nucl. Instrum. Meth. **A845** (2017) 583–587.

[11] KLOE Collaboration, A. Calcaterra, *The KLOE drift chamber*, Nucl. Instrum. Meth. **A367** (1995) 104–107.

[12] MEG Collaboration, Y. Uchiyama, *Upgrade of MEG experiment*, PoS **EPS-HEP2013** (2013) 380.

[13] A. Mazzacane, *The 4th concept detector for the ILC*, Nucl. Instrum. Meth. **A617** (2010) 173–176.

[14] L. De Lorenzis, F. Grancagnolo, A. L'Erario, A. Maffezzoli, A. Miccoli, S. Rella, M. Spedicato, and G. Zavarise, *Analysis and Characterization of the Mechanical Structure for the I-Tracker of the Mu2e Experiment*, Nucl. Phys. Proc. Suppl. **248-250** (2014) 134–136.

CHAPTER 4

VERTEX

The identification of heavy-flavour (b- and c-) quarks τ leptons is essential for the CEPC physics program. It requires precise determination of the track parameters of charged particles in the vicinity of the interaction point (IP), permitting reconstruction of the displaced decay vertices of short-lived particles. This drives the need for a vertex detector with low material budget and high spatial resolution. The current design of the CEPC vertex detector adopts the same layout as the ILD vertex detector [1], but with special considerations for the sensors specifications.

4.1 Performance Requirements and Detector Challenges

As required for the precision physics program, the CEPC vertex detector is designed to achieve excellent impact parameter resolution, which in the $r\phi$ plane can be parameterized by:

$$\sigma_{r\phi} = a \oplus \frac{b}{p(GeV)sin^{3/2}\theta} \tag{4.1}$$

where $\sigma(r\phi)$ denotes the impact parameter resolution, p the track momentum, and θ the polar track angle. The first term describes the intrinsic resolution of the vertex detector in the absence of multiple scattering and is independent of the track parameters, while the second term reflects the effects of multiple scattering. a=5 and b=10 are taken as the design values for the CEPC vertex detector. The main performance goals should comply with the following specifications on the system:

- Spatial resolution near the IP better than 3 μm;
- Material budget below 0.15% X_0/layer;

- First layer located at as close to beam pipe as possible;
- Detector occupancy not exceeding 1%.

Unlike like the ILD vertex detector, which operates in power-pulsing mode, the CEPC detector will have to operate in continues mode. The power consumption of the sensors and readout electronics should be kept below $50mW/cm^2$, if air cooling is intended inside the sensitive volume of the vertex detector. The readout time of the pixel sensor needs to be shorter than 20μs, to minimize event accumulation from consecutive bunch crossings. The radiation tolerance requirements, which are critical for the innermost detector layer, are driven by the beam related backgrounds as described in Chapter 10. The annual values of Total Ionising Dose (TID) and Non-Ionising Energy Loss (NIEL) are estimated to be X00 kRad and $X \times 10^{10}$ 1 $MeV n_{eq}/cm^2$, respectively.

4.2 Baseline design

The baseline layout of the CEPC vertex detector is exactly the same as that of ILD detector. As shown in figure 4.1, it consists of three cylindrical and concentric double layers mounted on ladders, which are the basic mechanical structure, with high spatial resolution pixel sensors on both sides. The CEPC vertex detector is designed to deliver six precise space-points for each charged particle traveling the detector, between radii of 16 mm to 60 mm with respect to IP. The material budget of each detector layer amounts to $\sim$0.15% X_0. The main parameters of the CEPC vertex detector are summarized in table 4.1, based on extensive simulation and technical studies from ILD and CEPC. According to the simulation results (see Section 4.3), the impact parameter resolution can reach the requirements by using the single point resolutions provided in the table.

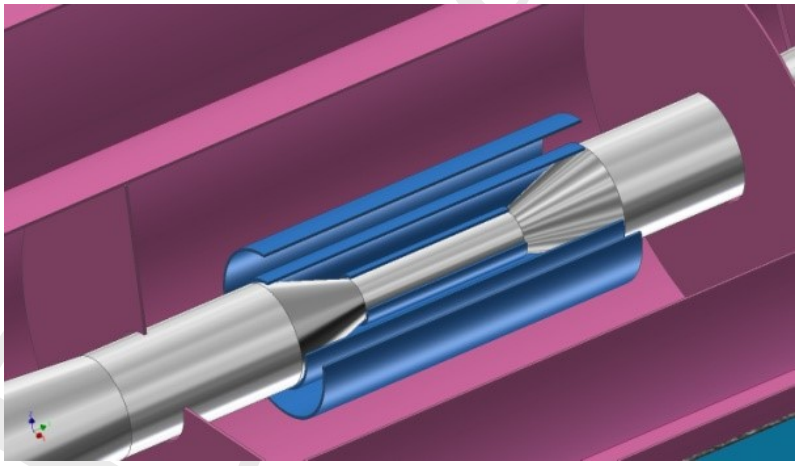

Figure 4.1: Schematic view of pixel detector (blue)

4.3 Detector performance studies

The identification of b/c-quark jets (called "flavor-tagging") plays an important role in physics analysis, where signal events with b/c-quark jets in the final state have to be separated requirements on the precise determination of impact parameter of the charged tracks

	$R(mm)$	$\|z\|(mm)$	$\|cos\theta\|$	$\sigma(\mu m)$	$Readout\ time(us)$
Layer 1	16	62.5	0.97	2.8	20
Layer 2	18	62.5	0.96	6	1-10
Layer 3	37	125.0	0.96	4	20
Layer 4	39	125.0	0.95	4	20
Layer 5	58	125.0	0.91	4	20
Layer 6	60	125.0	0.90	4	20

Table 4.1: Vertex detector parameters

embedded in the jets. For CEPC operation at the center-of mass energy of 240 GeV, those tracks are often of low momentum, for which the multiple scattering effect dominates the tracking performance as illustrated by Eq. 4.1

The CEPC vertex detector layout has been fully implemented in the GEANT4-based simulations framework MOKKA [2]. In addition, as inspired by the detailed studies for the CLIC detectors [3], fast simulation with the LiC Detector TOY simulation and reconstruction framework (LDT) [4] has been used for detector performance evaluation and layout optimisation. The preliminary studies for optimisation to evaluate the sensitivity of the results on the chosen parameters had been done, for the purpose of assessing the impact of the detector geometries and material budgets on required flavor-tagging performance. However, beam-induced background was not included at the moment.

4.3.1 Performance of the Baseline Configurations

The impact parameter resolution following from the single point resolutions provided in the table 4.1 is displayed in figure 4.2 as a function of the particle momentum, showing that the ambitious impact parameter resolution is achievable.

4.3.2 Material Budget

The baseline design includes very small material budget for the beam pipe as well as for the sensor layers and their support. To assess the sensitivity of the performance on the amount of material, the material budget for the detection layers of the vertex detector has been varied. The resulting transverse impact-parameter resolutions for low-momentum tracks are shown in Figure 4.3. When increasing the material of the detector layers by a factor of two, the resolution will be degraded by approximately 20%.

4.3.3 Dependence on Single-Point Resolution

The dependence of the transverse impact-parameter resolution on the pixel size was studied by varying the single-point resolution for the simulation of the vertex layers by worse of 50% w.r.t. the baseline values. The resulting resolutions for high and low track momenta as function of the polar angle θ are shown in Figure 4.4. The resolution for track momenta of 100GeV is found to change by approximately 50% in the barrel region. Here they exceed the target value for the high-momentum limit of a$\approx$5μm for both pixel sizes, as expected from the corresponding single-point resolutions. For 1GeV, where

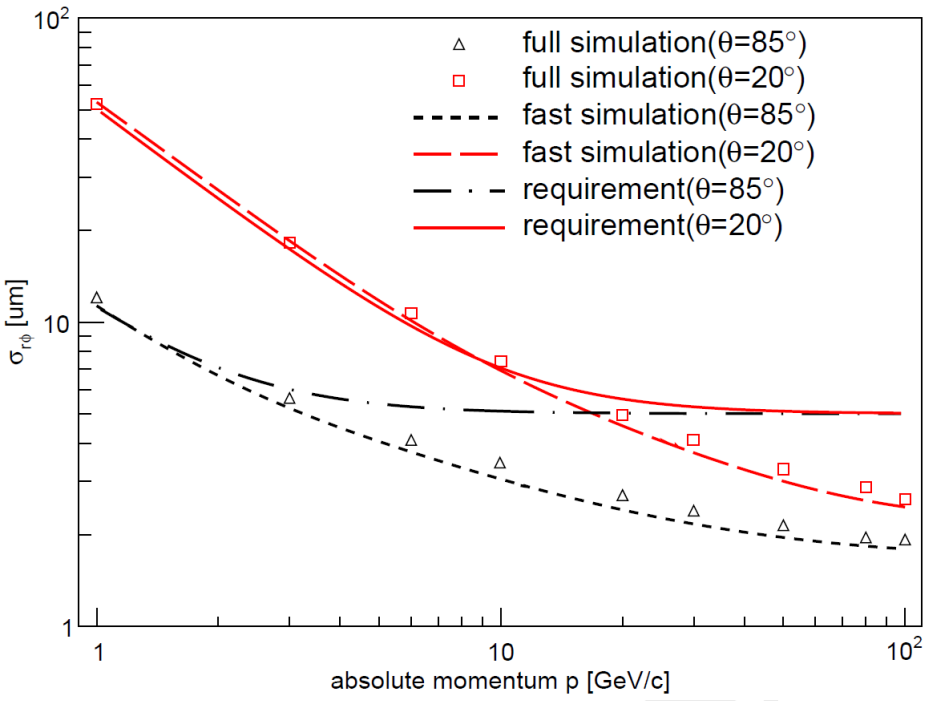

Figure 4.2: Transverse impact-parameter resolutions for single muon events as a function of the momentum for different polar angles.

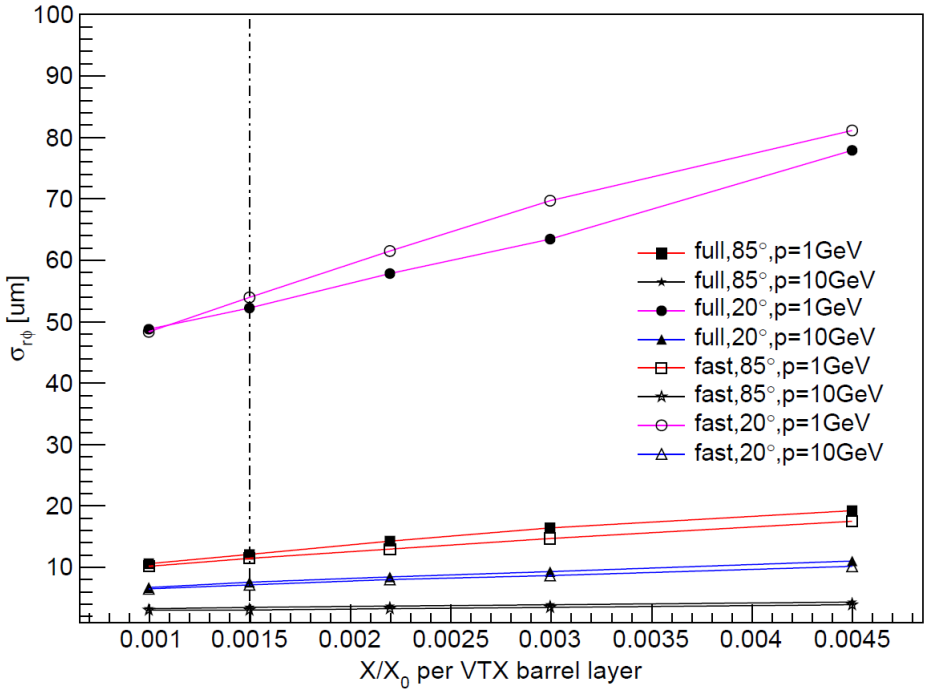

Figure 4.3: Transverse impact-parameter resolution as function of the amount of material inside the vertex barrel double layers, as obtained from the simulation. The results are shown for 1GeV and 10GeV tracks and for polar angles of θ=20 degrees and of θ=85 degrees. The material budget corresponding to the baseline configuration is indicated by dashed lines.

multiple-scattering effects dominate, the corresponding variation of the transverse impact-parameter resolution is only 10% larger. The target value for the multiple-scattering term of b≈10μm is approximately reached for both pixel sizes. It should be noted, however, that the pixel size is also constrained by the background occupancies (see Section 4.4) and the ability to separate adjacent tracks in very dense jets in the presence of such backgrounds.

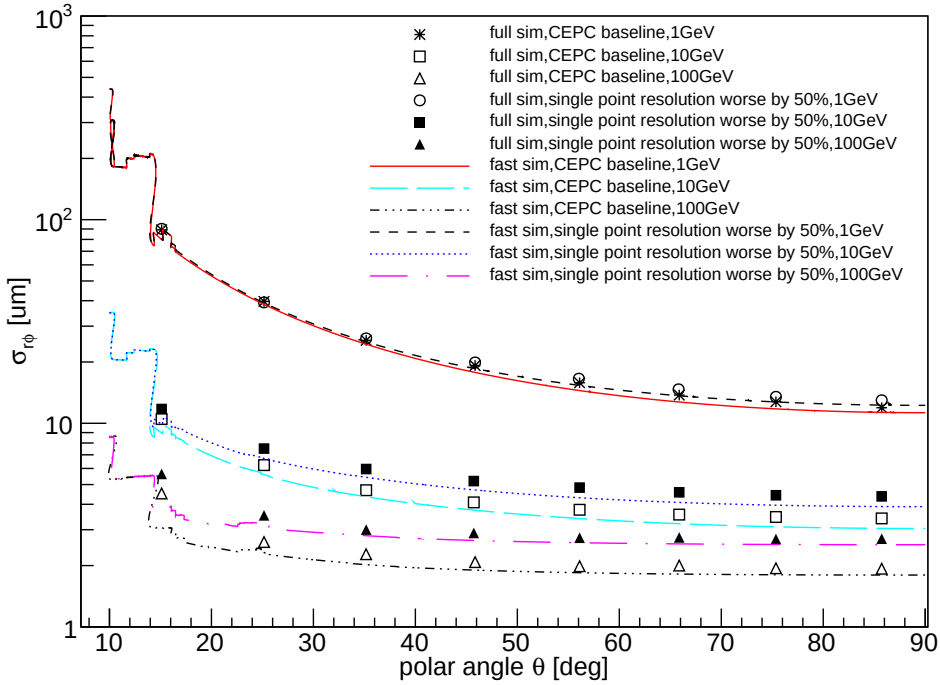

Figure 4.4: Transverse impact-parameter resolutions as function of the polar angle theta for different values of the single-point resolution of the CEPC barrel vertex detector. Shown are the resolutions for 1GeV, 10GeV and 100GeV tracks.

4.3.4 Distance to IP

The distance of the vertex layers 1 and 2 to the IP was varied by ±4mm relative to baseline geometry of the CEPC vertex detector. Figure 4.5 shows the resulting transverse impact-parameter resolutions at θ=85 degrees as function of the momentum with different radial distance of the innermost barrel vertex layer to the IP. For low momentum tracks, the transverse impact-parameter resolution is proportional to the inner radius, as expected from the parameter formula.

4.4 Beam-induced Background in the Vertex Detector

To be updated with radiation tolerance and detector layer occupancy (1% reachable by estimating tolerable hit density, even a safety factor of 10 included) according to the background studies, with B=3T

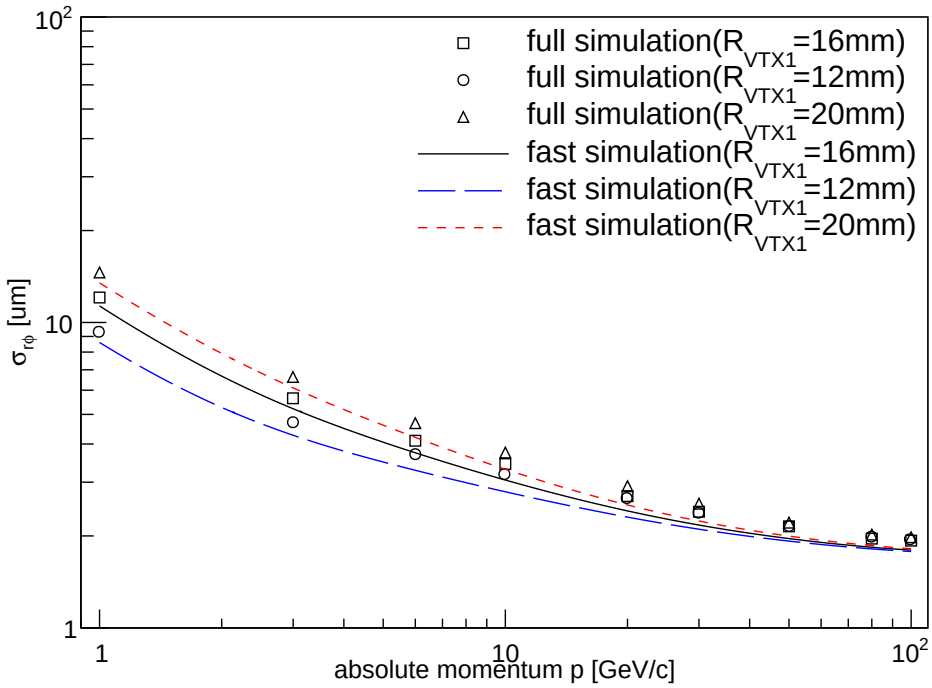

Figure 4.5: Transverse impact-parameter resolution at θ=85 degrees as function of the momentum for different values of inner most layer radius R_{min}. The black curve indicates the baseline configuration of R_{min}=20mm.

4.5 Sensor Technology Options

The history of silicon pixel vertex detector could be traced back to LEP era, when it was introduced in the DELPHI experiment [5], and significant progress has been made over the last 20 years [6]. There have been lots of R&D efforts towards pixel sensors for vertex tracking in the future particle physics experiments [7], driven by track density, single point resolution and radiation level.

As outlined in Section 4.1, the detector challenges include high IP resolution, low material budget, low occupancy and sufficient radiation tolerance (mild comparing to ILC but not necessarily easy to achieve). To fulfill these requirements of system level, the vertex must be based on sensor technologies which push for fine pitch, low power and fast readout. In the CEPC case it is a unique scenario that might be more requiring than previous applications. In the ILC[1] and CLIC[8], for example, the power consumption is expected to be significantly reduced by choosing operation of power pulsing, but it is not practical for CEPC. Some other experiments such as the STAR[9], BELLEII[10] and ALICE upgrade[11] do their readout continuously the same way the CEPC does. However, they require less in terms of IP resolution and material budget. A sensor technology that fits perfectly in needs of the CEPC does not exist. A few options are listed here for being either close to it or having outstanding potential.

The DEPFET has a unique feature that the main heat sources are located at the end of staves. As the thermal simulation of the BELLEII staves shown in figure 4.6, 1W for sensitive area and another 1W for switcher located within the acceptance can be cooled

by a gentle air flow, while the major heat of 16W in total for readout ASICs located out of acceptance can be removed by massive CO_2 cooling. The half stave for the BELLEII has achieved a low material budget of 0.21% and a fast readout of 20μs/frame. With a sensitive area of 64.4mm*12.5mm, it seems applicable as the inner most layers of the CEPC. A rough estimate results in 2.5W/ladder in sensitive area and 50μs/frame readout speed due to finer pixel pitch required by the CEPC. It needs further investigation as the largest possible size of a half stave is limited to be inside a 6-inch wafer, the length of outer layers gets out of reach for the DEPFET.

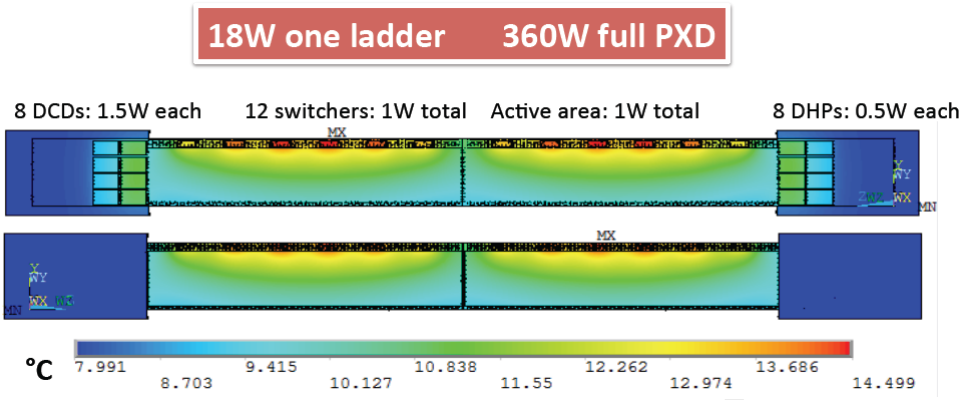

Figure 4.6: Thermal simulation of the BELLEII staves

The HR-CMOS is gaining momentum from R&Ds for the ALICE upgrade. Considering success of the MAPS (its predecessor) in the STAR and rapid progress achieved in the ALICE upgrade, HR-CMOS is possibly the most mature technology for an application like the CEPC. It has been approved to meet every single aspect of requirements of a CEPC-like detector. However, it is still challenging as to put all the specifications into a single chip. Intensive studies on circuit optimization (in-pixel discrimination) and innovative readout scheme (column sparsification) are underway. Pushing the power consumption down to $50mW/cm^2$ is a critical goal for application in the CEPC case.

The SOI is an option with great potential. The issue of coupling between sensor and circuit has been well understood and is addressed properly. There are a wide variety of applications in astrophysics[12], material science[13] and particle physics[14] which keep the MPW running steadily. This technology features fully depleted high resistive substrate, 0.2μm full CMOS process and being apt to 3D integration. The IHEP group has been developing both chips with fine pitch and chips with complicated function for over 3 years. Making best use of the high quality sensor and the SOI CMOS process could lead to good S/N ratio, which benefits an optimum solution of low power and fast readout. Similar to the HR-CMOS, the upper limit of power consumption is set to $50mW/cm^2$.

The criteria of being able to cope with continuous colliding and to still remain low power distinguished the 3 sensor options out of other technologies on market. Both the Chronopixel proposed for SiD/ILC and the CLICpix for the CLIC, for example, consume large amount of current in pixel level and rely on power pulsing heavily. HV-CMOS[15] is proposed more like a hybrid sensor and only minimum electronics on chip. The current R&D efforts are focusing on ATLAS-alike architectures and are definitely not suitable for precise measurement on an electron-positron collider.

4.6 Mechanics and Integration

The design of the vertex detector is conceived as a barrel structure, including six concentric layers. The preliminary layout of each layer is shown in table 4.2. The range of the radius covered by the detector is from 16mm to 60mm. The length of layers 3 to 6 is 125cm, which is twice as long as the first two layers.

No. of layer	radius (mm)	length (cm)
Layer 1	16	62.5
Layer 2	18	62.5
Layer 3	37	125.0
Layer 4	39	125.0
Layer 5	58	125.0
Layer 6	60	125.0

Table 4.2: Preliminary layout of each layer

The detector may be realized by 3 double-sided layers. Each double-sided layer is equipped with pixel chips on both sides, and has a common support frame. In the azimuthal direction, each layer is segmented in elements called ladders. The ladder, which extends over the whole length of the layer, is the basic building block of the detector. It contains all structural and functional components, such as chips, flex cable, support frame and cold plate if it is necessary. Pixel chips in a row are connected to flex cable by wire bonding or other bonding techniques, and then glued to the support frame, which is composed of low Z materials, such as carbon fiber and silicon carbide, providing stable mechanical support. The other side of the support frame is equipped with another pixel chips layer.

The design of the ladders should take into account the specifications of the vertex detector. In order to reduce a small multiple Coulomb scattering contribution to the charged-track vertex resolution and control deformations from gravity and cooling forces for the sensors position stability, the ladder mechanical support must fulfill stringent requirements in terms of minimum material budget and highest stiffness. The ladder design of other experiments can be as references, such as STAR pixel detector (PXL), the upgrade of ALICE inner tracking system (ITS) and BELLEII pixel detector (PXD), especially ILD vertex system, which takes double-sided ladder as an alternative ladder design.

The ladder mechanical support is inherently linked to the layout of the cooling system that will be adopted to remove the heat dissipated by the pixel sensors since the cooling system is integrated in the mechanical structure. The key point of the cooling system design of the vertex detector must balance the conflicting demands of efficient heat dissipation with a minimal material budget. So suitable cold plate, which is coupled with pixel sensors, with high thermal conductivity and low material budget should be taken into account in the ladder design. There are two main types of cooling methods in particle physics experiments, air cooling and active cooling. Table 4.3 gives a list of cooling methods and the corresponding material budget of each layer of the aforementioned experiments. The upgrade of ALICE ITS [11] adopts water cooling with respect to a chips power dissipation value of $300 mW/cm^2$. Polyimide cooling pipes fully filled with water

are embedded in the cold plate. STAR- PXL [16] uses air cooling according to its chips power consumption of $170mW/cm^2$. For ILD [1] vertex system, two different cooling options are considered, depending on the sensor technology. The sensors and SWITCHER chips of BELLE II PXD [17] require air cooling, while active cooling will be used for readout chips on each end of the detector, which is out of the sensitive region of the detector. So for CEPC vertex detector, the suitable cooling method will be determined according to the sensor option and the power consumption.

Vertex detector	Power dissipation	Cooling method	Material budget requirement/layer
Alice ITS	300 mW/cm^2	water	0.3%
STAR PXL	170 mW/cm^2	air	0.39%
ILD vertex	<120mW/cm^2 (CPS and DEPFEET)	air or N_2	0.15%
	35W inside cryostat (FPCCD)	two-phase CO_2	
BELLEII PXD	20W for sensor and SWITCHER	Air	0.2%
	180W on each end	CO_2	

Table 4.3: Cooling method of the vertex detector in each experiment

Simulation and module prototype studies should be carried out to find suitable designs that can meet requirements of stability, cooling and the performance of the vertex detector.

For the design of the whole mechanical structure of the vertex detector, some criteria must be taken into account. Firstly, minimum material has to be used in the sensitive region to reduce multiple Coulomb scattering. Secondly, to ensure high accuracy in the relative position of the detector sensors and provide an accurate position of the detector with respect to the central tracker of TPC and the beam pipe, a mechanical connector or locating pin at each end of the ladder should be considered to allow the fixation and alignment of the ladder itself on the end rings. Thirdly, cooling system should be arranged reasonably to ensure stable heat dissipation. At last, to reduce the dead region caused by the boundary of each ladder, neighboring ladders should be partially superimposed.

In addition, the main mechanical support structures of the vertex should also meet the requirements of the integration with the other detectors, such as time projection chamber (TPC) and forward tracking disks.

4.7 Critical R&D

The inner most layers have to fulfill the most demanding requirements imposed by the physics program. In addition, the system is bounded by stringent running constraints. The technology options in Section 4.5 are able to meet each individual requirement, including single point resolution, low material budget, fast readout, low power consumption and radiation tolerance, but a specific design is needed to meet the combination of all. Therefore R&D efforts have already been put into CMOS and SOI pixel sensor development to address the challenges concerning single point resolution and low power consumption. Further improvement of manufacturing process and design concepts are foreseen to follow in the future, including radiation hardness and 3D integration.

4.7.1 Current R&D activities

With the consideration of low material budget, two monolithic pixel technologies, CPS and SOI, are used for the sensor R&D. The TowerJazz 0.18μm quadruple-well process enables the full CMOS pixel circuit, while LAPIS 0.2μm double-SOI process has properly solved the crosstalk between sensor and digital part, and improved TID tolerance significantly.

In order to exploit the potential of these new developments, two design teams have started chip design using different technologies. Two designs have been submitted to the TowerJazz foundry. The first one uses simple 3T analog readout to carry out the optimization of sensing diode and evaluate the influence of radiation damage. The second one implements a well-proved rolling shutter readout as well as an innovative data-driven readout. When it comes to SOI R&D activities, two designs that adopt an aggressive strategy have been submitted. With the amplifier and discriminator integrated into each pixel, the pixel size has been shrunk to 16μm pitch. All the designs for current R&D are in line with the same principle of in-pixel discrimination even though each one has its own implementation. Compared to column discriminator, the in-pixel one can eliminate the large analog driven current which results in a largely reduced power consumption.

4.7.2 Future R&D

How to shrink the pixel size and achieve a single point resolution of 2.8μm is a question that may be solved by adding extra enhancement to the TowerJazz 0.18 μm process or Lapis 0.2μm process. A micro-bump 3D integration process is able to attach a second layer of pixel circuit on top of the existing layer of sensing diode and front-end circuit. The upper tier can be fully digital part that implements data-driven readout architecture, while the lower tier can be CPS or SOI pixel matrix. A promising result has been demonstrated by the successful formation of 2.5μm Au cone bump with NpD (Nano-particle deposition) technique. However, the throughput needs further improvement.

When it comes to the radiation tolerance, TowerJazz process is expected to be resistive to the TID. But in the low power design, the TID tolerance is degraded. It is believed that the transistors in the ultra-low-power design might be sensitive to the threshold shift induced by TID trapped charge due to sub-threshold operation. This issue is being studied by adjusting the trade-off between low power and radiation tolerance carefully. An N-type plain implant has recently been added to improve the charge collection efficiency, which therefore will benefit the non-ionization radiation damage. In terms of SOI process, the weak point is the BOX layer of SiO_2. By the introduction of Double-SOI and the optimization of transistor doping recipe (LDD, lightly doped drain), its TID tolerance has been improved dramatically. Similarly to the CPS process, SOI needs carefully study on the sub-threshold region in low power design.

Sensor thinning and ultra-low material construction of module are subject to the constraint of 0.15% X_0/layer. CPS wafer thinned to 50μm is routine in semiconductor industry nowadays. SOI wafers thinned to 75μm with backside implant have also been demonstrated. However, technical challenges are foreseen if the thin sensors have to be combined with micro-bump 3D integration. In addition, low material detector modules need to integrate mechanical support, power and signal connection, and sufficient stiffness to avoid vibration.

4.8 Summary

The basic concepts of the ILD Vertex detector, including the pixel sensors specifications required by the impact parameter resolution and radiation tolerance, the low-mass mechanical design, and the detector layout, are largely adapted to the baseline design of CEPC vertex detector. However, as power-pulsing will not be an option at the CEPC, it will be crucial to develop pixel sensors with lower power consumption and fast readout electronics. Detailed designs for mechanical supports and cooling, cabling, and power conversion are also necessary. Most of these issues have to be solved with future R&D work for the CEPC, exploring synergies with other experiments which have similar requirements.

References

[1] H. Abramowicz et al., *The International Linear Collider Technical Design Report - Volume 4: Detectors*, arXiv:1306.6329 [physics.ins-det].

[2] P. M. De Freitas and H. Videau, *Detector simulation with MOKKA/GEANT4: Present and future*, in *International Workshop on Linear Colliders (LCWS 2002), Jeju Island, Korea*, pp. 26–30. 2002.

[3] D. Dannheim and M. Vos, *Simulation studies for the layout of the vertex and tracking regions of the CLIC detectors*, , 2012.

[4] M. Regler, M. Valentan, and R. Frühwirth, *The LiC detector toy program*, Nuclear Instruments and Methods in Physics Research Section A:Accelerators,Spectrometers,Detectors and Associated Equipment **581** (2007) no. 1, 553–556.

[5] A. Andreazza, G. Barker, V. Chabaud, P. Collins, H. Dijkstra, Y. Dufour, M. Elsing, F. Ledroit, C. Eklund, R. Orava, et al., *The DELPHI Silicon Tracker at LEP2*, .

[6] F. Hartmann, *The DELPHI Microvertex Detector at LEP*, in *Evolution of Silicon Sensor Technology in Particle Physics*, pp. 1–20. Springer, 2009.

[7] M. Battaglia, C. Da Viá, D. Bortoletto, R. Brenner, M. Campbell, P. Collins, G. Dalla Betta, M. Demarteau, P. Denes, H. Graafsma, et al., *R&D paths of pixel detectors for vertex tracking and radiation imaging*, Nuclear Instruments and Methods in Physics Research Section A:Accelerators,Spectrometers,Detectors and Associated Equipment **716** (2013) 29–45.

[8] L. Linssen, A. Miyamoto, M. Stanitzki, and H. Weerts, *Physics and detectors at CLIC: CLIC conceptual design report*, arXiv preprint arXiv:1202.5940 (2012) .

[9] G. Contin, E. Anderssen, L. Greiner, J. Schambach, J. Silber, T. Stezelberger, X. Sun, M. Szelezniak, C. Vu, H. Wieman, et al., *The MAPS based PXL vertex detector for the STAR experiment*, Journal of Instrumentation **10** (2015) no. 03, C03026.

[10] C. Lacasta, *The DEPFET pixel detector for the Belle II experiment at SuperKEKB*, PoS (2014) 005.

[11] B. Abelev, J. Adam, D. Adamova, M. Aggarwal, G. A. Rinella, M. Agnello, A. Agostinelli, N. Agrawal, Z. Ahammed, N. Ahmad, et al., *Technical design report for the upgrade of the ALICE inner tracking system*, Journal of Physics G: Nuclear and Particle Physics **41** (2014) no. 8, .

[12] S. Nakashima, S. G. Ryu, T. Tanaka, T. G. Tsuru, A. Takeda, Y. Arai, T. Imamura, T. Ohmoto, and A. Iwata, *Development and characterization of the latest X-ray SOI pixel sensor for a future astronomical mission*, Nuclear Instruments and Methods in Physics Research Section A: Accelerators, Spectrometers, Detectors and Associated Equipment **731** (2013) 74–78.

[13] T. Hatsui, M. Omodani, T. Kudo, K. Kobayashi, T. Imamura, T. Ohmoto, A. Iwata, S. Ono, Y. Kirihara, T. Kameshima, et al., *A direct-detection X-ray CMOS image sensor with 500 μm thick high resistivity silicon*, in *Proc. Int. Image Sensor Workshop*, vol. 3. 2013.

[14] Y. Ono, A. Ishikawa, H. Yamamoto, Y. Arai, T. Tsuboyama, Y. Onuki, A. Iwata, T. Imamura, and T. Ohmoto, *Development of the Pixel OR SOI detector for high energy physics experiments*, Nuclear Instruments and Methods in Physics Research Section A: Accelerators, Spectrometers, Detectors and Associated Equipment **731** (2013) no. Supplement C, 266 – 269. http://www.sciencedirect.com/science/article/pii/S0168900213008772. PIXEL 2012.

[15] I. Peric, *Active pixel sensors in high-voltage CMOS technologies for ATLAS*, Journal of Instrumentation **7** (2012) no. 08, C08002.

[16] H. Wieman, E. Anderssen, L. Greiner, H. Matis, H. Ritter, X. Sun, and M. Szelezniak, *STAR PIXEL detector mechanical design*, Journal of Instrumentation **4** (2009) no. 05, P05015.

[17] Belle-II Collaboration, T. Abe et al., *Belle II Technical Design Report*, arXiv:1011.0352 [physics.ins-det].

CHAPTER 5

TRACKING SYSTEM

5.1 TPC tracker detector

The tracking system are expected to affect the flying of the tracks as less as possible, which require it to be as light as possible. The particle ID ability is one of the feasibility of the tracking system, however for such energetic tracks, the classic method, such as dE/dx, TOF are not reliable. In CEPC, the inner tracking system should be sensitive in momentum measurement to charged particles, which transverse momentum ranged from 0 to 80GeV, with an accuracy compatible to the beam energy uncertainty of the accelerator.

The TPC (Time Projection Chamber) could be used as a main central tracker, Time Projection Chambers (TPCs) have been extensively studied and used in many fields, especially in particle physics experiments, including STAR and ALICE. Their low material budget and excellent pattern recognition capability make them ideal for three dimensional tracking and identification of charged particles. They are also the only type of electronically read gaseous detector delivering direct three-dimensional track information. However, there has always been a critical problem with TPCs, especially in high background conditions, the space charge distortion due to the accumulation of positive ions in the drift volume.

TPC will be as a part of the detector concepts for the CEPC, it can measure the momentum of tracks of charged particles in the magnetic field. Micro Pattern Gas Detector (MPGD) such as Gas Electron Multiplier (GEM) and Micro-MEsh GAseous Structure (Micro MEGAS) or the Timepix chip are candidate for the readout technology. Used the MPGD as readout, the $r\phi$ position resolution could be reach to 100 μm, even it's better in the high magnetic field(3.0T). Also, the TPC can reconstruct and identify particle species using energy loss (dE/dx) measured by the readout pad rows. In the reaction event of the

electron-positron annhiliation in the CEPC experiment, it is required to identify charged particle species such as pion, kaon, electron, etc. and to reconstruct the events. For the CEPC-TPC, expected dE/dx resolution is less than 5% for clear identification.

Understanding the properties and achieving the best possible point resolution have been the object of $R\&D$ studies of Micro-Pattern Gas Detectors, GEM, MicroMEGAS, and pixel, and results from many years work in LC-TPC international collaboration group. To improve on the performance, to optimize readout module and to control effectively ion back flow in circular machine (CEPC), these studies will continue for the next few years in order to understand and solve many critical technology challenges.

5.1.1 Principle of a Time Projection Chamber

A TPC usually consists of a cylindrical drift volume with a central cathode and an anode at the two endplates. In the case of a colliding experiment, the TPC contains an inner radius in which the beam pipe and inner detectors are placed.

The anodes are at ground, while the cathode is at a potential high voltage to keep the rang of from 100V/cm to 1000V/cm in drift length. The walls of the volume are the field cage, which ensures a very homogeneous electrical field between the electrodes. The magnetic field is parallel to the electric field to suppress transverse diffusion. Without the magnetic field this diffusion would dominate, degrading the track and momentum reconstruction. The electrons are released after the ionization of the sensitive gas volume and drift along the electric field to the anodes, while the ions drift toward the cathode. An amplification device is placed in front of the anodes and creates an electron avalanche as the readout(GEM, MicroMEGAS or others).

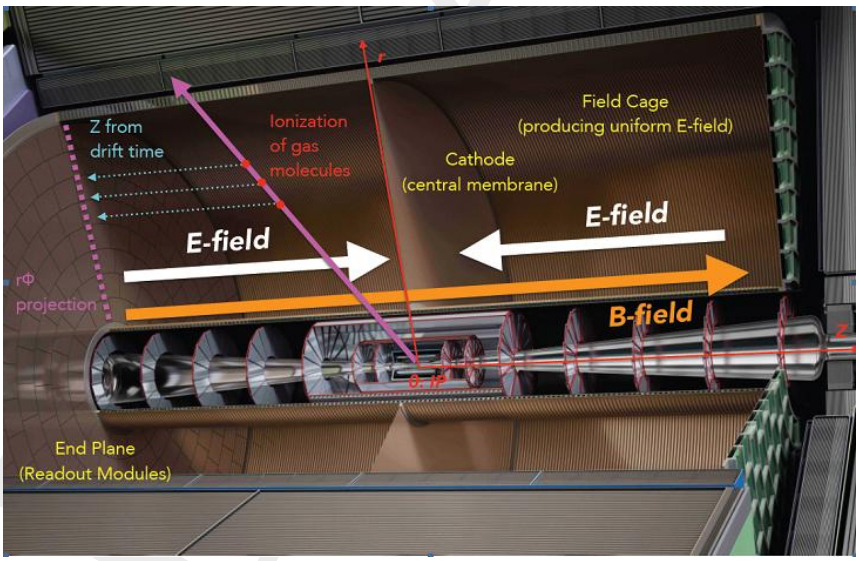

Figure 5.1: Sketch of the TPC structure.

All of TPC will be included some parts:

1. Chamber TPC chambers are typically cylindrical and operate under the atmospheric pressure with the working gas filled inside. Chambers in high magnetic field close to the centre of the magnet, usually have a higher occupancy due to the curling low-energy tracks. Hence the material budget of stations inside the magnet is kept as low

as possible. In the active area, the added the material due to the filled gas should be less than $1\%X_0$. The chambers are attached to the end-plate from the inside to minimise the dead area between neighbouring chambers. Special mounting technique is required to allow rotation and tilting of the chambers.

2. Field cage The cylindrical chamber's inner and outer composite walls hold field and forming strips, which are attached to a resistor divider chain network. The resistors must be no-magnetic. A central cathode will be held at approximately 50 kV when the drift field is 300 V/cm, with the end-plates and the other outer surfaces of the TPC at ground potential. Therefore the composite walls must self-stand the large potential of the central cathode. The mirror narrow strips will be arranged between the inner and outer walls to keep the electron field uniform in over the whole active TPC volume.

3. End-plate To obtain high position resolution, every end-plate is subdivided into many independent MPGD detector modules (GEM or Resistive/no Micromegas detector, so on), which can provide nearly full coverage of the end-plate. Power cables, electronic connectors, cooling pipes, PCB boards and support brackets wall are also mounted on the end-plate. In case the detector modules are damaged by the discharge or spark, they can be replaced and the end-plate should be kept stable during the replacement. In addition, the end-plate needs to built from lightweight material, not compromise the jet energy resolution in the forward region, but should be still sufficiently rigid to achieve stable positioning of the detector modules with a position accuracy better than 50 μm.The material budget of the mechanical structure accounts for $8\%X_0$. Additional materials for the readout planes, front-end electronics and cooling are estimated to be $7\%X_0$, and power cables and the connector up to $10\%X_0$.

The TPC could provide some physics information: First function is 3 dimensional track reconstruction, by getting the XY information from the anode segmented in pads and the Z coordinate delivered by the drift time. To obtain the Z coordinate from the drift time, the drift field has to be very homogeneous. Because this coordinate is obtained via the drift velocity of the electron, it should have a moderate dependence on the drift field for a given gas mixture. Seconde parameter is the total momentum of a charged particle, by measuring the radius, ρ, of the electron trajectory to get the transverse momentum, and adding this information to the knowledge of the trajectory in the Z plane. Final function is the particle identification, the energy loss can be extracted by measuring the charge deposited on the readout pads. The energy loss combined with the measurement of momentum in the magnetic field provides then the particle identification.

5.1.2 Baseline design and technology challenges

5.1.2.1 Main parameters of the detector geometry

In TPC parameters, the geometry will be limited with inner diameter, outer diameter, drift length, electric field, and the magnetic field. The transverse momentum resolution Δp_t of a tracking device - one of the basic figures of merit - is described by the Gluckstern formula

$$\frac{\Delta p_t}{p_t^2} \propto \frac{\sigma_{r\phi}}{BL^2}\sqrt{\frac{720}{n+4}} \tag{5.1}$$

where $\sigma r\phi$ denotes the spatial single-point resolution in the $r\phi$-plane, B is the magnetic field strength (which bends the particle trajectories depending on the momentum), L is the length over which the measuring points are distributed, and n is the number of single-point measurements that are used in the overall track fit.

From the formula, there is strong confidence that a TPC will be able to meet the performance goals of the CEPC tracker detector: with a single-point resolution of $r\phi$=100μm, with a magnetic field of 3T, with an inner radius of 0.3m and an outer radius of 1.5-1.8m, and with approximately 200 pad rows.

The resolution of the TPC is limited by the diffusion of the drifting electrons. An upper bound on the diffusion is calculated using the standard Gluckstern parameterization, assuming a large number of measurements along the length of the track

$$D < \frac{\sigma_p t}{p_t}\sqrt{\frac{n_T L}{720}}(L[m]^2)\frac{0.3B[T]}{p_t[GeV/c]}\frac{1}{\sqrt{L_{drift}}} = 100\frac{\mu m}{\sqrt{cm}} \tag{5.2}$$

where the diffusion component of the momentum resolution (σ_{pt}/p_t) is required to be less than 10^{-4} at p_t=1GeV/c, n_T=30 ionization electrons per cm of gas (mainly argon) for a track measured over L=1.8m and for a drift distance of L_{drift}=2.0m in the magnetic field of 3.0T.

A large volume TPC with about 200 points per track provides continuous tracking for a large volume (several meters level). The TPC is optimised for excellent three-dimensional point resolution and minimum material in the field cage and in the end plate. It also provides particle identification capabilities based on the energy loss of particles per unit of distance (dE/dx). The geometry baseline should be consider the following reasons: Sensitive to the track segment as long as possible, stronger enough magnetic field for track bending and as good as possible position resolution of the track measurement.

5.1.2.2 Modularization design

The figure5.2 shows that the diagram of large prototype module design in LC-TPC international collaboration group $R\&D$.

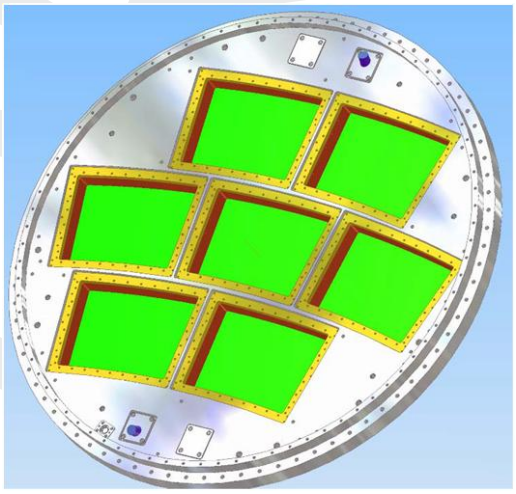

Figure 5.2: The diagram of large prototype module design.

In the large collider machine, the readout structure is designed to be modularised to easily change and maintain. Each module will consist of gas amplification system, readout

pad plane and following electronics. High density electronics make it possible to integrate the electronics directly on the back of the readout pad plane. The readout module will then have to provide all necessary high and low voltages and cooling for heat dissipation, however, especially because power-pulsing will not be available at the CEPC. To achieve the required performance, an MPGD-based gas amplification system will be developed. The charge from the amplification system will be collected on a pad board.

To meet the physics performance basing on the modularization design, tt has been demonstrated that any amplification technologies combined with pad readout can be built as modules which cover large areas with little dead space.

5.1.2.3 Gas amplification detector module

For the detector module, the electron gas amplification is obtained in very high fields generated by modest voltages (300-400V) across 50âĹŠ100μm structures suitable for large-area applications. Typically gains of 10^3âĹŠ10^4 are achieved with many gases under standard conditions. Gas Electron Multipliers and MICRO-Mesh GAseous structure are two example of MPGDs.

This gas amplification detector module for a pad-based TPC will be either GEM, MicroMEGAS or others structure, since they do not meet the ambitious performance goals. Two or three GEMs are stacked together to achieve sufficient charge amplification resistive MicroMEGAS have enough amplification in a single structure.

Micro-pattern devices for TPC provide:

1. Higher rate capability: MPGDs provide a rate capability over $10^5 Hz/mm^2$.
2. Intrinsic ion feedback suppression: The ions produced on these field lines do not go back to the drift volume and most of them will be neutralised on the mesh or GEM foil.
3. A direct electron signal, which gives a better time resolution.
4. A larger gain, by the specific operation high voltage.
5. Much smaller $E \times B$ effects than wires chamber for which the spacing of the wires is about a few mm.

5.1.2.4 Optimization readout pad size

Design of readout pad size is key parameter for the TPC detector module whether using GEM, MicroMEGAS or combination structure as the readout detector. Accurate position information require to process the adjacent pad's signal with the Center-of-Gravity Method(CGM).

The design of the two-dimensional readout strips has been developed with the triple GEMs of 100mm^2 in IHEP. The readout strips in X direction are 193μm wide at 752μm intervals. There are pads with a size of 356 $\mu m \times$356μm connected with each other in Y direction and their strip pitch is 457μm. The difference in strip widths is to improve signal sharing between X-axis and Y-axis strips, to ensure a homogeneous charge distribution between neighboring strips. The total number of strips in X and Y directions are 267 channels and 437 channels respectively. Each strip is connected with one electronic channel to process the signal.

In the figure5.3 of the typical profile of the electrons cluster in readout strips, the pink circle could be move to the blue circle and the profile is the Gaussian distribution. If

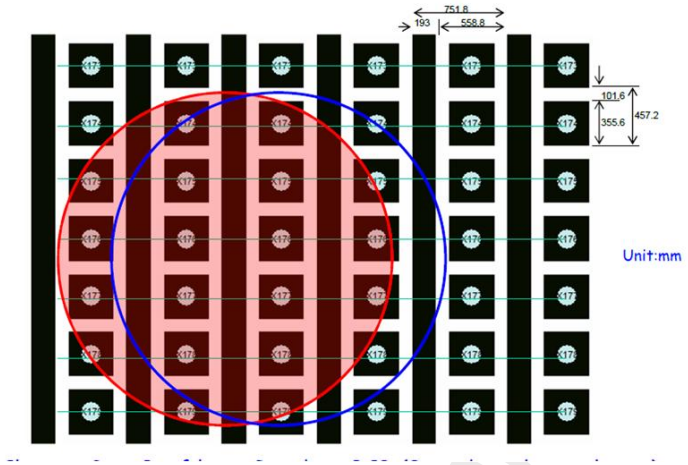

Figure 5.3: The profile of the electrons cluster in Triple GEMs.

there is a enough number pads to use Center-of-Gravity Method, the pad width should be designed to 1.0mm and the length of pad should be designed to 6.0mm to obtain the sufficient charge information when the amplifier gain is 10mV/fC.

5.1.2.5 Operation gas for the long drift

As with any gaseous detector, the choice of the chamber gas strongly affects the properties and eventually the performance of a TPC. Desirable characteristics are:

1. High drift velocity (to avoid accumulation of too many events inside the chamber)
2. A very low transverse and a low longitudinal diffu0sion coefficient (to prevent deterioration of the spatial resolution)
3. A sufficiently large specific energy loss $dE = dx$
4. A high enough stability against electrical breakthroughs (to allow reliable operation of the amplification device)
5. Nonhazardous chemical properties (to address safety concerns like in-flammability and damages to the hardware)

The gas mixture should be chosen to minimize the capture of electrons by the molecules of electronegative impurities. Due to the long drift distance of the several meters, and the fact that ions are heavier and much slower than electrons, ions can accumulate in the chamber. This effect can lead to electric field distortions and should therefore be avoided. To decrease this effect, the structure of the readout chambers is generally designed to avoid ions from escaping into the gas volume. A gas with a large drift velocity is also chosen in experiments with large interaction rate.

In given the working gas and the electric field, the drift velocity of electron could be determined with Eq. 5.3

$$\mu_e = f(\frac{E}{P}) \tag{5.3}$$

where E denotes the electric field vector, P the gas pressure and μ_e the electron drift velocity. After reaching saturation (nearly maximum), the electron drift velocity depends

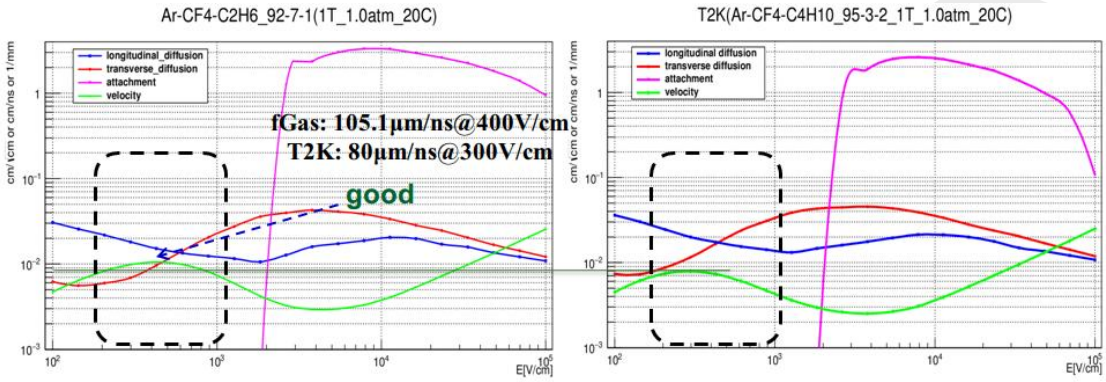

Figure 5.4: The drift velocity in different gas mixture.

slightly on the electric field. Fig. 5.4 shows that the drift velocity obtained in different mixture gases. For the CEPC TPC detector, it is required to be sensitive to as long as possible track segment. The working gas should be selected in such way to achieve high velocity in low drift field to lower the high voltage in all of the drift length, and small transverse diffusion in the magnetic field to decrease the electron cluster size on the readout pads.

The gas mixture of Ar/CF_4/iC_4H_{10} (95%/3%/2%) have been used for the Large Prototype of TPC Detector for the ILD TPC and the TPC chamber for the T2K experiment. The saturated drift velocity of the mixed gas reaches nearly 8 cm/μs in a drift field of 300 V/cm. In addition, the gas has a large parameter of $\omega\tau$ (same as the Eq. 5.3) and transverse diffusion coefficient of 30 μm/$\sqrt{\text{cm}}$ in the drift field of 300 V/cm. In the B-field, a reasonable transverse diffusion coefficient could be realised at 100 V/cm of the drift field. The bunch spacing at the CEPC is $\sim$ 3.6 μs. The working gas has an higher saturated drift velocity than the T2K mixed gas should be considered. In addition, the gas amplification needs to achieve approximately 6000 and the signal attenuation of the electron attachment should be kept below $1\%/m$.

5.1.2.6 Low power consumption electronics readout

Small readout pads of a few square millimeters (e.g. $1mm \times 6mm$)are needed to achieve high spatial and momentum resolution in TPC, demanding about 1 million channels of readout electronics per endcap.The total power consumption of the front-end electronics is limited by the cooling system to be several kilo-watts in practice and they have to work continuously in CEPC.Hence the technique of so-called power pulsing cannot be applied. There are no current existing electronics readout system can fulfill the requirements of such high density and low power consumption. The architecture of the TPC readout electronics is shown in Fig.1, selected from a broad range of survey on current electronics installed or under development during past decades, including ALTRO/S-ALTRO and more recently SAMPA for ALICE,AFTER/GET for T2K and Timepix for ILC. It consists of the front-end electronics on the detector panel and the data acquisition system several meters away from the detector.

The waveform sampling front end is preferable, including a preamplifier and a shaper as the analog front-end (AFE), a waveform sampling ADC in 10MSPS, a dedicated digital signal processing (DSP) and zero-suppression unit and an de-randomize event buffer for each channel. In order to meet the stringent requirements on the integration and the power

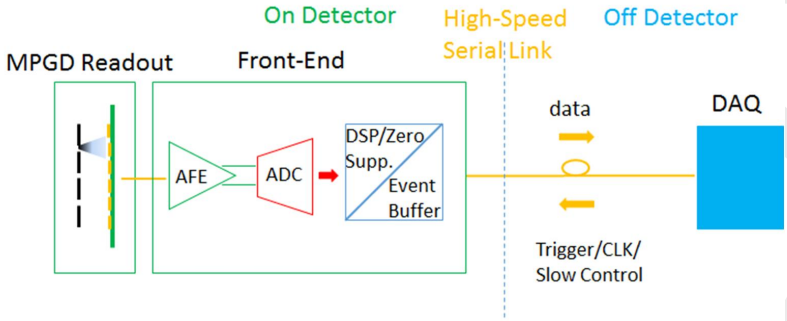

Figure 5.5: The architecture of the TPC readout electronics.

Total number of channels		1 million per endcap
APE	ENC	500e@10pF input cap
	Gain	$10mV/fC$
	Shaper	CR-RC
	Peaking time	100ns
ADC	Sampling rate	$\geq 20MSPS$
	Resolution	10 bit
Power consumption		$\leq 5mW$ per channel
Output data bandwidth		200 Mbps $\times$Occu. per channel*
Channel number		32
Process		TSMC 65nm LP
*Typical occupancy is less than 1% in CEPC-TPC		

Table 5.1: TPC readout electronics.

consumption, a front-end ASIC will be developed in advanced 65nm CMOS process. The key specifications of the front-end ASIC are summarized in Table 1.

CMOS scales down in favor of digital circuits in terms of power and density. The power consumption of the DSP circuits reported in $Ref.[3]$ was $4mW/ch$ in 130nm process and could be reduced by a factor at least of 2 by migrating the same design to 65nm. However this is not the same for the analog circuits. The design strategy for the front-end ASIC is to keep the analog part as simple as possible. The block diagram of the analog front-end and the successive approximation (SAR) ADCare shown in Fig.2 and Fig.3 respectively. The CR-RC shaper and the SAR ADC instead of pipeline ADC will be used for their simplicity in analog circuits and hence the higher power efficiency.

Dedicated digital filters will be applied to the continuously digitized input signals to suppress the pedestal perturbations caused by the non-ideal effects such as temperature variation and environment disturbance. Then the data will be compressed by only storing the data packets above a programmable threshold with a specified number of pre- and post-samples. A data head will be added to each packet with its time stamp and other information for reconstruction afterwards. The buffered data are readout through high

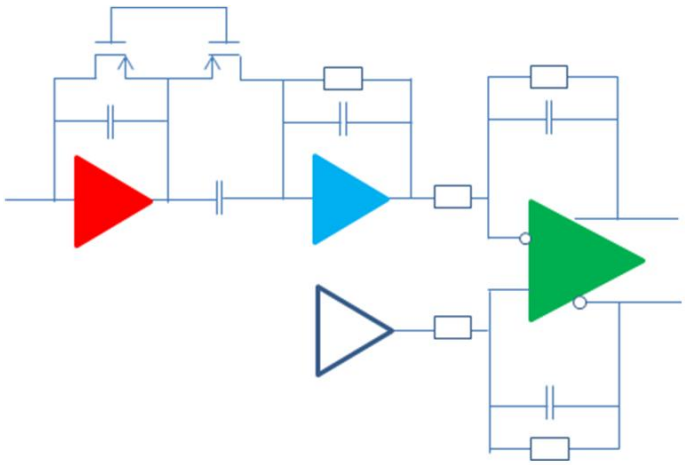

Figure 5.6: The block diagram of the analog front-end.

speed serial links to the DAQ system. The front-end electronics can support for both external trigger and self-trigger mode.

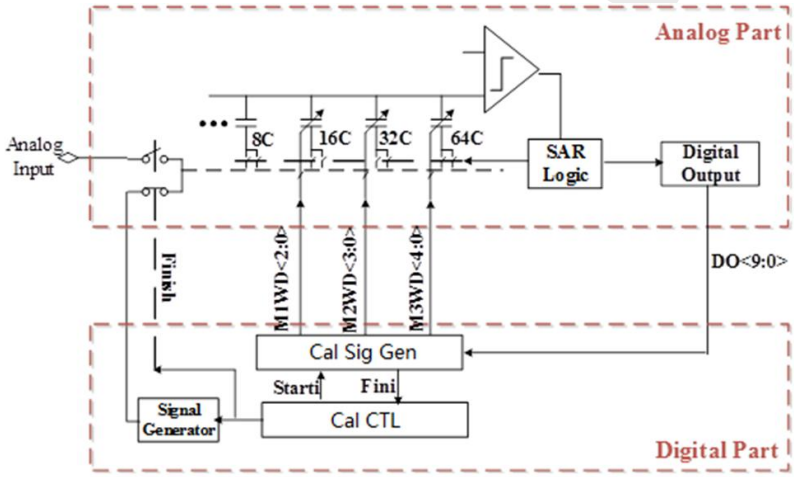

Figure 5.7: The block diagram of the SAR-ADC.

Even with the state of the art technology, the power density of TPC readout electronics for CEPC could still be several times higher than that for ILC-TPC. Two-phase CO_2 cooling[7] is a well-developed technology and can be used as a baseline solution to bring out the heat generated by the front-end electronics and to keep the temperature of the TPC chamber stable at 20°C. More efficient micro-channel CO_2 cooling may be studied further and can be an alternative technique to copper pipes [8].

The TPC readout electronics are meters away from the collision point and the radiation dose is rather low ($< 1krad$) at CEPC, which allows us to use standard, radiation soft technologies. On the other hand, energetic particles can always produce instantaneous failure (SEU or SEL) from time to time. Hence radiation tolerant design needs to be considered that the overall system performance will not be affected or even irreversibly damaged by the rare events.

5.1.2.7 Critical technology challenges in the circular machine

The mechanical structure of the TPC consists of a field cage, which is made with advanced composite materials, and two readout end-plates that are self-contained including the gas amplification, readout electronics, supply voltage, and cooling. It will be challenging to design and build the TPC support structure with relatively light material, and at the same time very rigid. It is required to maintain accuracy, robustness in all directions, and stability over long time periods. As the field cage is not strong enough due to the limited material budget, the end-plates become the only choice, where the support structure connects to. In current stage of design, how the TPC end-plate should be supported is not fixed yet. A promising solution is to suspend from the solenoid, in which a number of spokes run radically along the faces of the calorimeter to the TPC end-plates. Bearing is not the most challenging issue.

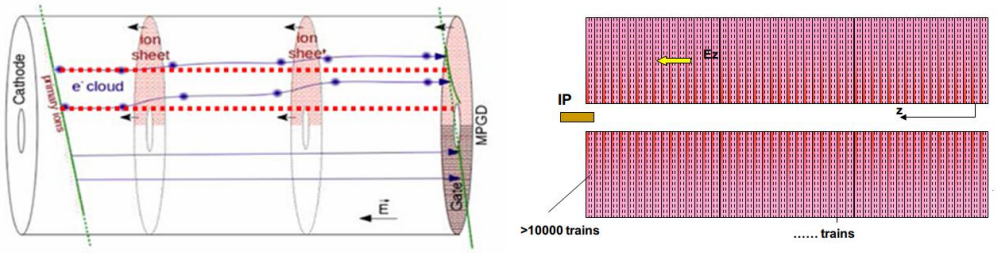

Figure 5.8: The diagram of distortion and ion disks in CEPC.

Any kind of amplification device creates not only secondary electrons, but also the same amount of ions. These ions move in the opposite direction away from the anode region into the main chamber volume - and furthermore have a much lower drift velocity, meaning that they could accumulate in the chamber gas and build up a significant space charge in the form of 'ion discs'. In CEPC, the majority of ions inside the drift volume are backflowing ions from the amplification region of the TPC readout devices. It is thus of great importance to limit ion backflow (IBF) from the amplification region. This might affect the drifting electron tracks through electrostatic attraction as well as inhomogeneities of the drift velocity (which depends on the electric field strength). In order to minimise this deteriorating influence on the spatial resolution of the chamber, the backflow of ions should be suppressed.

One possible mechanism of backflow suppression, often used together with wire mesh device, is a so-called gating grid. The critical problem with this relatively simple yet effective scheme is that it cannot be immediately applied to the timing structure of the CEPC: the bunch spacing of the machine is so small (μs or less, compared to the readout time) that tracks from many events are drifting through the chamber. It shows in the figure of the diagram of distortion and ion disks in CEPC. Another promising option is to exploit the 'built-in' ion backflow suppression of GEMs or MicroMEGAS. In next section, the $R\&D$ study of the hybrid detector module has been developed to control ions continuously and the update results will be described.

5.1.3 Simulation and estimation for the key issues

5.1.3.1 Occupancy requirement of Higgs and Z pole run

Using an sample of 9 thousand fully simulated $Z \rightarrow qq$ events at center of mass energy of 91.2 GeV, we studied the voxel occupancy and the local charge density of the CEPC TPC at Z pole operation for future circular electron positron colliders, with an instant luminosity of 2×10^{34} to 2×10^{36} cm^{-2} s^{-1}.

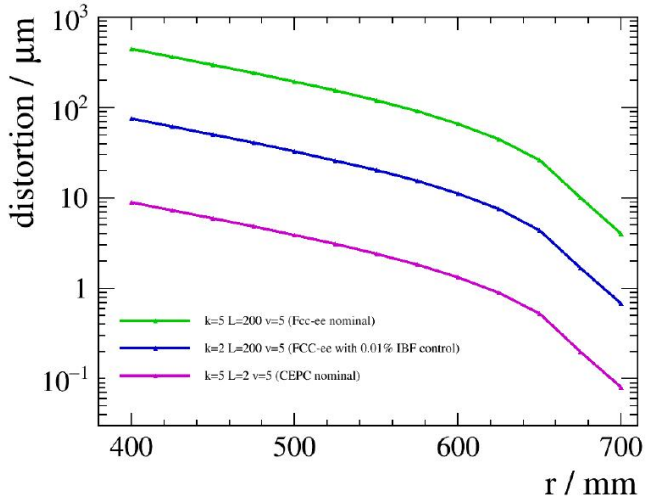

Figure 5.9: Distortion as a function of electron initial r position with different parameters.

Given the fact that the beam bunch is evenly distributed along the accelerator circumference, the voxel occupancy is extremely low ($1.4 \times 10^{-5}/1.4 \times 10^{-7}$ for the inner most layer and $3.4 \times 10^{-6}/3.4 \times 10^{-8}$ for average) and poses no pressure for the TPC usage. The distortion on TPC hit positions induced by the ion charges is estimated with dedicated program and calculation. At instant luminosity of 1×10^{36} and an ionback flow control of percent level, the distortion can be as large as 10 mm at the inner most TPC layer at the CEPC conceptual detector geometry, which is two orders of magnitude larger than the intrinsic TPC spatial resolution. A few approaches are proposed to reduce the effects caused by distortion:

1. Ion back flow control technology; the ion back flow should be controlled to per mille level, in other word, only $1-10$ back flow ions is allowed for each primary ionization.
2. Dedicated distortion correction algorithm, for the inner most layers, which should result in a mitigation of the hit position distortion by 1 order of magnitude.
3. Adequate track finding algorithm that could link the TPC track fragments to vertex tracks at high efficiency and purity.

Taking all of these approaches account, the distortion can be mitigated by approximately 2 orders of magnitude. To conclude, the pad occupancy and distortion stress no pressure to CEPC and if the above items can be achieved.

5.1.3.2 Distortion of Ions backflow in drift length

Early TPCs were equipped with multi-wire tional chambers (MWPCs) as gas amplification devices. The IBF ratio in a standard MWPC is $30-40\%$ so a gating grid is essential

to prevent ions from reaching the drift volume. In the presence of a trigger, the gating grid switches to the open state to allow ionization electrons to travel into the gas amplification region. After a maximum drift time of about 100 μs (depending on the drift length, electric field and gas mixture), the gating grid is closed to prevent positive ions from drifting back into the drift volume. Since it must remain closed until the ions have been collected on the grid wires, the ionization electrons are also blocked during this time and the dead time consequently increases.

Triggered operation of a gating grid will therefore lead to loss of data. Thus, the TPC at the proposed circular collider will have to be operated continuously and the backflow of ions must be minimized without the use of a gating grid.

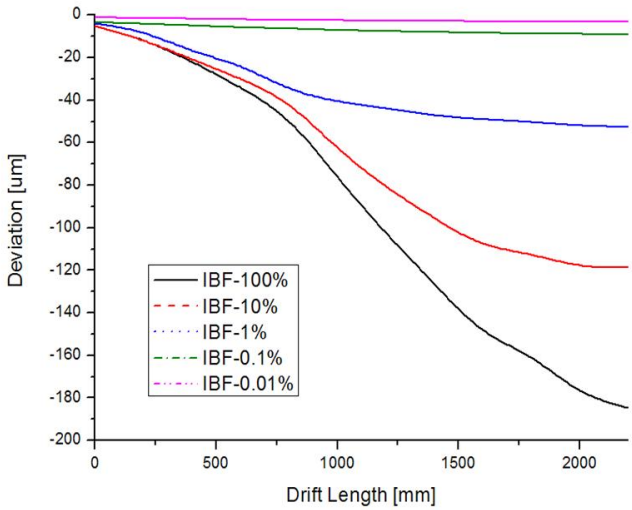

Figure 5.10: Evaluation of track distortions due to space charge effects of positive ions.

The ions generated from the ionisation in the drift volume or from the avalanche multiplication and have found their way into the drift region will not only introduce field distortion, but also deduce the TPC counting rate capability. This effect is called ion backflow, and should be fully suppressed in the TPC drift volume. With an averaged 300 eV required by per ion-electron ionisation and 2 keV energy loss per mili-meter, there will be roughly 12k primary electrons generated by a track with a typical length of 1.8 m in the TPC and there will be in total 240 k electrons in one event. With the electron drift velocity of 5 cm/μs, it takes $\sim$ 40 μs for all the electrons to drift 2 m to reach the end-plate. With the expected bunch spacing of 3.6 μs at the CEPC, there will be about 11 events overlapping in the TPC volume. Therefore there will be 240k$\times 11/2 = 1.32$ M electrons continuously drifting toward the end-plate. On the other hand, ions drift much slower than electrons, with a velocity of only 500 cm/s in an electric field of 500 V/cm. This leads to ions from 110,000 events overlapping in the TPC volume. If the 1% of the ions are trapped by the gate and with the gas amplification factor assumed to be 10000, there will be 240k$\times 10000 \times 1\% \times 110,000 = 2.64$T ions drifting back continuously. With the TPC volume to be $\sim$20M cm^3 in size, there will be on average 0.13M ions/cm^3.

5.1.4 Feasibility study of TPC detector module and future work

5.1.4.1 Continuous IBF detector module

TPC readout with micro-pattern gaseous detectors (MPGDs), especially Gas Electron Multipliers (GEM)and micro-mesh gaseous structures (Micromegas), is very attractive, because the IBF of those detectors is intrinsically low, usually around a few percent. GEM detectors have been extensively proved in the last decade to be the prime candidate, as they offer excellent results for spatial resolution and low IBF. Several GEM foils can be cascaded, allowing multilayer GEM detectors to be operated at an overall gas gain above 10^4 in the presence of highly ionized particles. Micromegas is another kind of MPGD that is likely to be used as endcap detectors for the TPC readout. It is a parallel plate device, composed of a very thin metallic micromesh which separates the detector region into drift and amplification volumes. The IBF of this detector is equal to the inverse of the field ratio between the amplification and the drift electric fields. Low IBF therefore favours high gain. However, high gain will make it particularly vulnerable to sparking. The idea of combining GEM with Micromegas was first proposed with the goal of reducing the spark rate of Micromegas detectors. Preamplification using GEMa also extends the maximum achievable gain, so there have also been studies on gaseous photomultipliers with this hybrid configuration.

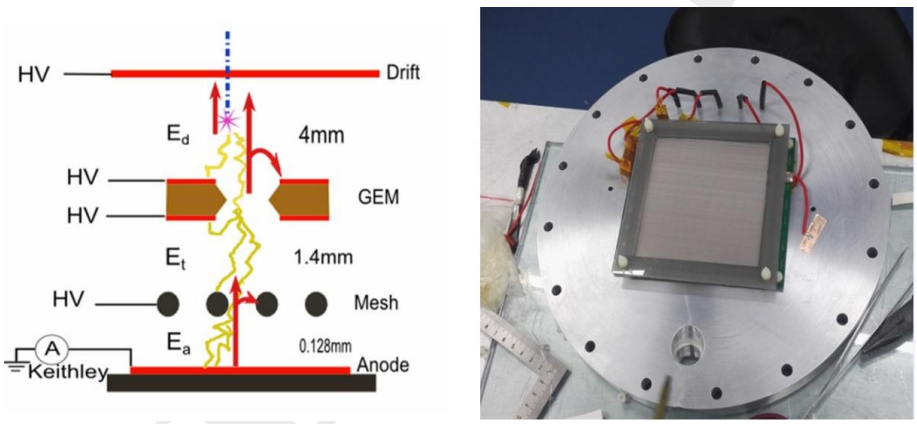

Figure 5.11: Schematic diagram of the detector module.

To fulfill the physics goals of the future circular collider, a TPC with excellent performance is required. MPGDs with outstanding single-point accuracy and excellent multi-track resolution are needed. We have proposed and investigated the performance of a novel configuration detector module: a combination of GEM and a Micromegas. The detector will be called GEM-MM for short throughout this paper. The aim of this study is to suppress IBF continually by eliminating the gating grid. The design concept and some preliminary results of the detector module are described as following.

A new concept of avalanche ion backflow reduction for a future MPGD readout based TPC, and a prototype has been developed. It is a hybrid structure with one GEM foil cascaded above the Micromegas detector. Tests of this detector have been carried out with an 55Fe X-ray source in $Ar/CO_2(90/10)$ gas mixture. The preamplification effect of GEM foil has been demonstrated in the energy spectrum measurement. With the novel hybrid structure, the effective gain of the GEM can be measured even when it is relatively low. The energy resolution of this hybrid structure gaseous detector is measured to

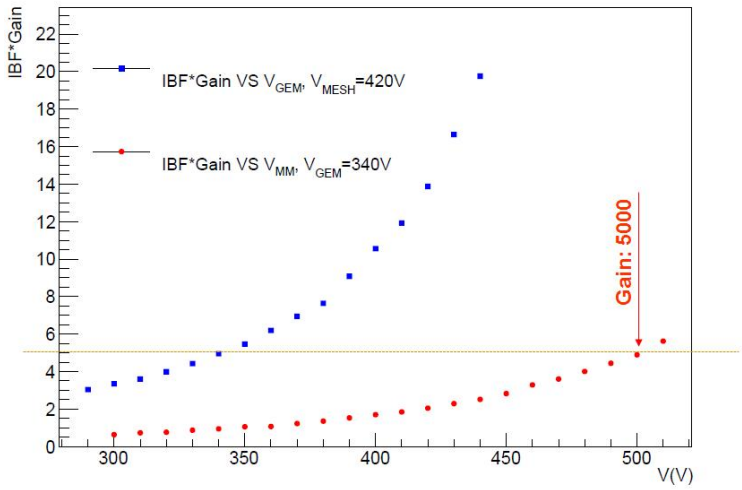

Figure 5.12: Result of the IBF TPC detector module.

be 27%(FWHM). The gain properties of this device were measured. A gain up to about 5000 can be achieved without any obvious discharge behaviour. The currents on the anode and drift cathode were measured precisely with an electro-meter. Out experimental measurements show that IBF can be reduced down to 0.19% at a gain of about 5000.

5.1.4.2 Laser calibration and alignment system

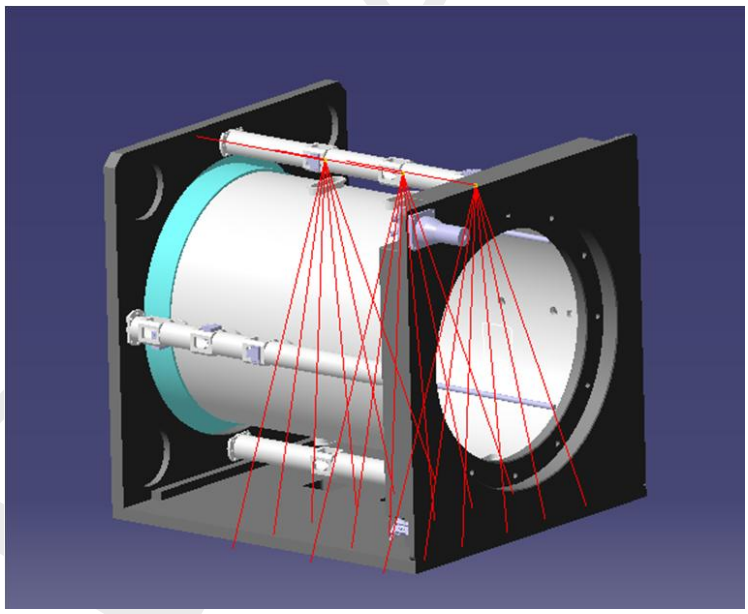

Figure 5.13: Schematic diagram of the detector module with the laser system.

The laser calibration system could be used for the TPC detector, the narrow laser beams inside the drift volume of the TPC simulate ionizing tracks at predefined locations. The goal is to obtain a uniformity of the TPC drift field within a relative error of 10^{-4} corresponding to a spacial resolution of $\sigma_{r\phi} = 100\mu m$. The system can be used for tests and calibration either outside or during normal data taking with the aim of understanding the

chamber performance. Of particular interest is the testing of electronics, alignment of the read-out chambers, and measurements of variations of the drift velocity due to mechanical imperfections and non-uniformities in the gas, temperature and the electric and magnetic fields.

The laser system would be used for calibration and for distortion measurement in the prototype with one module as readout or large, A Nd:YAG laser with a wavelength of 266nm shall be used to study the track distortions. An additional UV-lamp could generate additional ions. The complete optical path and the laser power will be split into $6-7$ laser tracks. The laser map coupling into the chamber and the planned laser tracks could be designed. The UV laser beam for calibration and alignment purposes to monitor the drift velocity, operation gas, gain uniformity and electric field. Nd:YAG laser device with 266nm wavelength could make the ionization in the gas volume along the laser path occurs via two photon absorption by organic impurities. The laser power should be reach $10J/mm^2$ to equal $10MIP$.

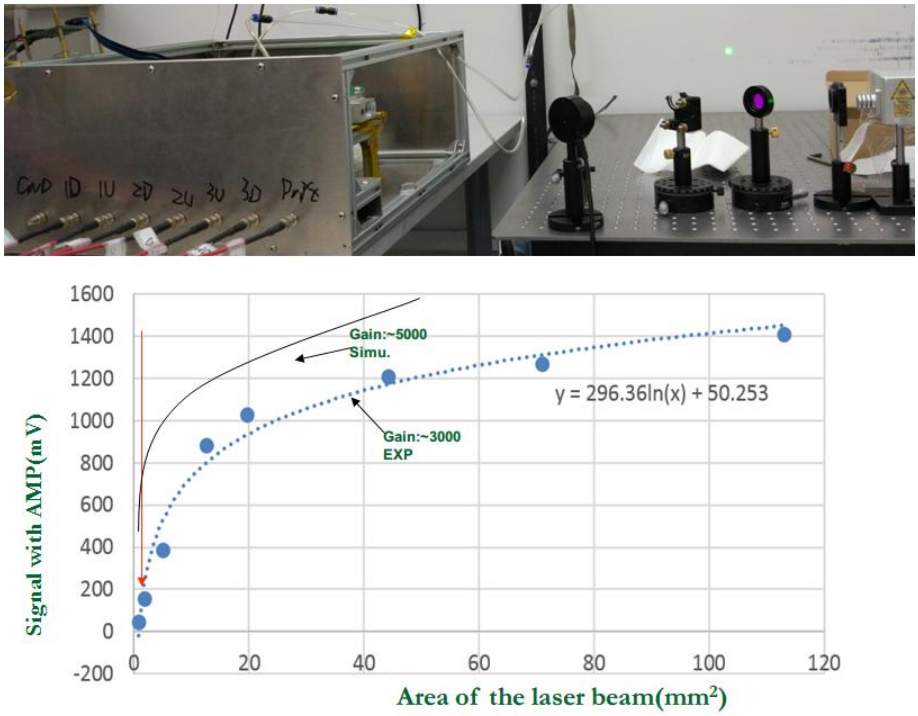

Figure 5.14: Signal with the different size of laser beam.

- Photoelectric laser source with UV light source: Enlights the cathode with UVs could produce photoelectrons to study and monitor distortions, the cathode with UVs to produce photoelectrons to study and monitor distortions, Deuterium lamp with $160nm-400nm$ of the wavelength as UV light source and smooth Aluminum film as cathode. To mimic the bunch structure and the ions distortion with UV light lamp by the specific time structure shine controller, UV could create more than about 10000 $electrons/s.mm^2$.
- Calibration laser beam size: The shine and entrance window could use the fused silica as of $99\%\ trans.@266nm$. Provides a UV laser beam for calibration and alignment purposes to monitor the drift velocity, operation gas, gain uniformity and electric field.

The ionization in the gas volume along the laser path occurs via two photon absorption by organic impurities. The study has been done using Nd:YAG laser device has the 266nm of wavelength(4.68eV). The optimization laser beam area of the laser device will be the range from $0.8mm^2$ to $1.0mm^2$ in the figure5.14.

To solve the critical technology problems in CEPC, the hybrid structure MPGD detector module has been developed and some preliminary results has been obtained and analyzed, the further study will be done from this combination detector module. Another small TPC prototype with 266nm laser calibration system and UV photoelectric function has been design and would be assembled, the calibration experiment would be further studied for CEPC.

5.1.5 Conclusion

The TPC designed following the LC-TPC concept provides a very good starting point for the CEPC TPC, but many modifications are foreseen due to the different performance requirements and experimental conditions. Several critical R&D issues have been identified in pre-studies. Possible solutions to those issues have been suggested and will have to be verified with a prototype TPC in future.

5.2 Silicon tracker detector

As described in the PreCDR [1], the silicon tracker, together with the vertex detector and the TPC, forms the complete tracking system of CEPC. With sufficiently low material budget to minimise the multi-scattering effect, the silicon tracker provides additional high-precision hit points along trajectories of charged particles, improving tracking efficiency and precision significantly. In addition to complementary tracking, it also provides the following functionalities:

- monitoring possible field distortion in the TPC,
- contributing detector alignment,
- separating events between bunch crossings with relative time-stamping,
- potentially dE/dx measurement.

The transverse momentum resolution can be parameterised as [2]

$$\sigma_{1/p_{\mathrm{T}}} = a \oplus \frac{b}{p \sin^{3/2}\theta} \quad [\mathrm{GeV}^{-1}] \tag{5.4}$$

with p and p_{T} in GeV, θ the polar angle, a and b dimensionless numbers characterising tracking resolution and multiple scattering effect separately. If a track is measured at N points equally distributed along the trajectory, we have

$$a = \frac{\sigma_{\mathrm{SP}}}{0.3BL'^2}\sqrt{\frac{720}{N+4}}$$

where B is in tesla, σ_{SP} in meter is the measurement resolution of each point and L' in meter is the projected length of the track onto the transverse plane. For multiple scattering

and for relativistic particles, namely $\beta = 1$, there is

$$b = 0.053 \frac{1}{BL'} \sqrt{\frac{L'}{X_0}}$$

where X_0 is radiation length in units of length. Assuming the CEPC baseline parameters and considering VTX as three layers, namely, $N = 6$, $B = 3.0\,\mathrm{T}$, $L = 1.795\,\mathrm{m}$, $\sigma_{\mathrm{SP}} = 7\,\mu\mathrm{m}$ and $L/X_0 = 2.85\%$, we have

$$a = 2.0 \times 10^{-5} \quad \text{and} \quad b = 1.7 \times 10^{-3}. \tag{5.5}$$

At low momenta, less than $50\,\mathrm{GeV}$ for perpendicular tracks, the resolution is dominant with the multiple scattering effect, and at high momenta, the resolution approaches to the tracking resolution, in turn determined by the single-point resolution. Hence, stringent constrain has to be put on material budget.

5.2.1 Baseline design

The main characteristic of the baseline design for the CEPC silicon tracker is a silicon envelope [3] around the TPC. It consists of four components: the Silicon Inner Tracker (SIT), the Silicon External Tracker (SET), the End-cap Tracking Detector (ETD) and the Forward Tracking Detector (FTD). The overall layout is shown in Figure 5.15, and the main parameters are summarized in Table 5.2.

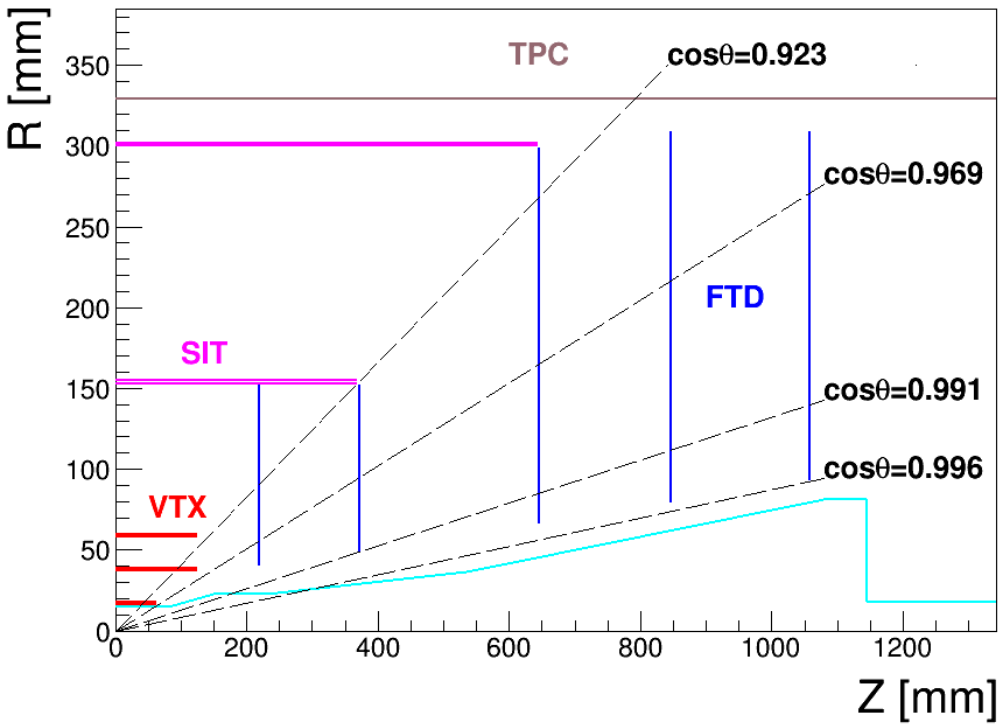

Figure 5.15: Preliminary layout of the CEPC silicon tracker. The red lines indicate the positions of the vertex detector layers and the blue lines the SIT and FTD for the silicon tracker. The SET and ETD, which sit outside the TPC, are not displayed.

Table 5.2: Main parameters of the CEPC silicon tracker.

Detector	Geometric dimensions			Material budget $[X/X_0]$
SIT	Layer 1:	$r = 153$ mm,	$z = 371.3$ mm	0.65%
	Layer 2:	$r = 300$ mm,	$z = 664.9$ mm	0.65%
SET	Layer 3:	$r = 1811$ mm,	$z = 2350$ mm	0.65%
FTD	Disk 1:	$r_{in} = 39$ mm, $r_{out} = 151.9$ mm,	$z = 220$ mm	0.50%
	Disk 2:	$r_{in} = 49.6$ mm, $r_{out} = 151.9$ mm,	$z = 371.3$ mm	0.50%
	Disk 3:	$r_{in} = 70.1$ mm, $r_{out} = 298.9$ mm,	$z = 644.9$ mm	0.65%
	Disk 4:	$r_{in} = 79.3$ mm, $r_{out} = 309$ mm,	$z = 846$ mm	0.65%
	Disk 5:	$r_{in} = 92.7$ mm, $r_{out} = 309$ mm,	$z = 1057.5$ mm	0.65%
ETD	Disk:	$r_{in} = 419.3$ mm, $r_{out} = 1822.7$ mm,	$z = 2420$ mm	0.65%

The barrel components SIT and SET provide precise hit points before and after the TPC, improving the overall tracking performance in the central region. The SIT helps the link between the vertex detector and the TPC, enhancing the reconstruction efficiency, particularly for low-momentum charged particles. The SET sits between the TPC and the calorimeter and helps in extrapolating from the TPC to the calorimeter. In addition, the good timing resolution of silicon sensors provides time-stamping for bunch separation.

The ETD is positioned in the gap between the endplate of the TPC and the end-cap calorimeter. It helps to reconstruct charged particles with a reduced path in the TPC. The SIT, SET and ETD covers the central tracking region. They form the complete silicon envelope and help in calibrating the tracking system.

The FTD is installed between the beam pipe and the inner cage of the TPC, covering the very forward region. It consists of five silicon disks on each side. The FTD is essential for precise and efficient tracking down to very small (or large) solid angles, where a number of challenges exist: the magnetic field approaching zero along the beam pipe, significantly larger occupancies due to forward going jets and high backgrounds from the interaction region. To achieve the best tracking performance, the FTD needs precise space points, a large lever arm, but low material budget. The baseline design would be a compromise among the constraints. Using highly granular pixel sensors for the first two disks can be forseen to lower the occupancy and improve the $r\phi$ resolution.

5.2.2 Sensor technologies

The basic sensor technology is silicon microstrips for all tracker components except the two innermost FTD disks where silicon pixels are forseen. Requirements of the single point resolution vary with positions of tracker components, but a general condition of $\sigma_{\text{SP}} < 7\,\mu\text{m}$ is required for high precision tracking. The microstrip sensors have proven to be capable of the resolution, taking into account material budget and power consumption. The baseline features of microstrip sensors will be a large detection area of $10 \times 10\ \text{cm}^2$, a fine pitch of $50\,\mu\text{m}$ and the thichness $< 200\,\mu\text{m}$ to minimise the multi-scattering effect.

The alternative is a fully, or at least for inner components, pixelated silicon tracker. Although the choice of pixel technologies is open, the CMOS pixel sensors (CPS) have

gained particular interest. The main advantages of the CPS comparing to the microstrip sensors are two folds:

- Granularity. The CPS provides better single-point spatial resolution and solves the problem of multiple hits.
- Material budget. The CPS can be thinned to less than $50\,\mu\mathrm{m}$, whereas the strip sensor is usually a few hundred microns.

As for the cost, because the CPS is based on the standard CMOS procedure in industry, production cost could be significantly reduced for fabricating large area sensors. In addition, the size of pixels used for the tracker can be comparatively large, hence it's possible to embed complicated circuits in the pixel to simplify the tracker readout circuitry. Initial R&D on large area CPS has been carried out.

5.2.3 Front-End electronics

The Front-End (FE) electronics will depend on the choice of sensor, namely microstrips or pixels.

For the microstrips, custom designed ASICs with deep sub-micron CMOS technology will be used. The chips will provide functions of the analogue to digital convertion (ADC), zero suppression, sparcification and possibly time stamping, together with necessary control circuitry. The high degree digitisation is for relaxing the data processing pressure on downstream electronics.

As for the pixels, all FE functions can be realised in a pixel chip, even with some functions, e.g., ADC on pixels themselves. Particular concerns are readout time and electronic channels.

Commonly, the FE chip will be developed in mind with low noise, low power consumption and high radiation tolerance. New developments, such as in the SiLC collaboration and the LHC experiment upgrades, will be good references.

5.2.4 Powering and cooling

Powering and cooling are a challenge for the CEPC silicon tracker. It is important to investigate the novel powering scheme based on DC-DC converters, which has been already actively pursued by the ATLAS and CMS experiments for silicon detector upgrades [4–6]. It allows significant reduction in material budget for the low-voltage power cables and gives less power dissipation in the delivery system. Cooling is another critical issue. Although cooling based on forced cooled gas flow might be still feasible to efficiently conduct away the heat generated by the sensors, ASICs and other electronics, it is important to look into other cooling techniques, such as silicon micro-channel cooling [7], which are being investigated by several other experiments. The technique chosen will have to provide sufficient cooling without compromising the detector performance.

5.2.5 Mechanics and integration

There will always be additional challenging aspects of the mechanical design for a large area silicon tracker. A lightweight but stiff support structure can be built based on Carbon-fibre Reinforced Plastic material [8]. The support structure, cable routing and electronics

common to other sub-detectors need to be carefully designed to minimise the overall quantity of material and make easy construction and integration possible. Precise and quick system alignment might be achieved with dedicated laser monitoring systems, while the final alignment will be accomplished using tracks from well-understood physics events [9].

5.2.6 Tracking performance

While the tracking performance in the central region, which features the same layout as the ILD detector, has been extensively studied [10, 11], the performance in the forward region, which has been re-designed to cope with the rather short L^*, requires additional careful evaluation. Figure 5.16 shows the estimated transverse momentum resolution for single muon tracks for two polar angles $\theta = 20°$ and $85°$, and the analytical results from Eq. (5.4) and Eq. (5.5). Due the reduced lever arm of the tracks and fewer FTD disks in the forward region ($\theta = 20°$), the resolution is worse than the required performance.

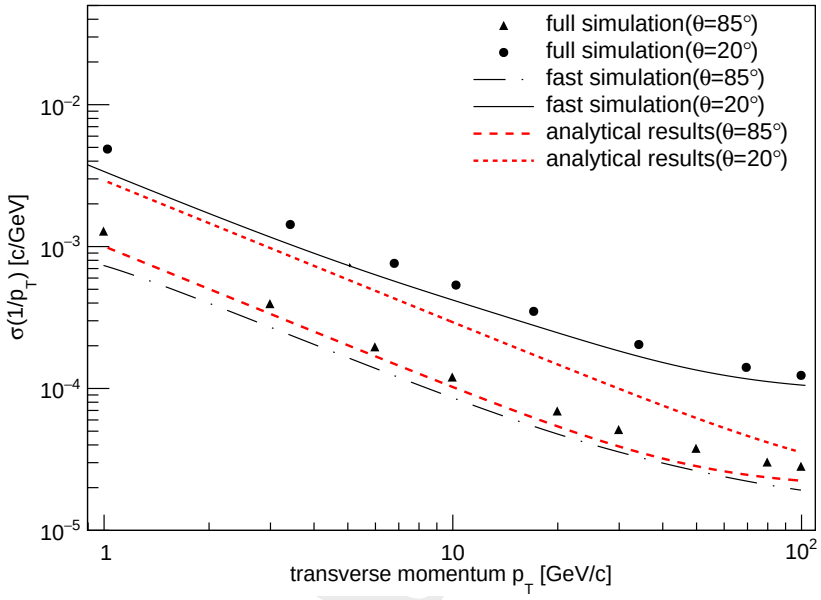

Figure 5.16: Transverse momentum resolution for single muon tracks as a function of the track momentum estimated for the CEPC baseline design with full simulation (dots) and fast simulation (black lines) compared to the analytical results obtained with Eq. 5.4 (red lines).

Tracking performance of the alternative pixleated silicon tracker has been studied with fast simulation, in which the microstrips are replaced with double-sided pixels with certain single point resolution and material budget reduced to $0.3\%X_0$, the same as VTX. Figure 5.17 shows the transverse momentum resolution for single muons with fixed momentum as a function of polar angle, comparing the pixelated tracker with various single point resolutions to the baseline microstrip tracker. Significant improvement can be observed when the polar angle is below about $20°$, in the tracking region of FTD. There is no, however, obvious difference for chosen pixel resolutions, all less than $10\,\mu\mathrm{m}$.

Given the importance for heavy-flavour tagging, the impact parameter resolution, both transverse and longitudinal, is assessed, as shown in Figure 5.18 with muon momentum

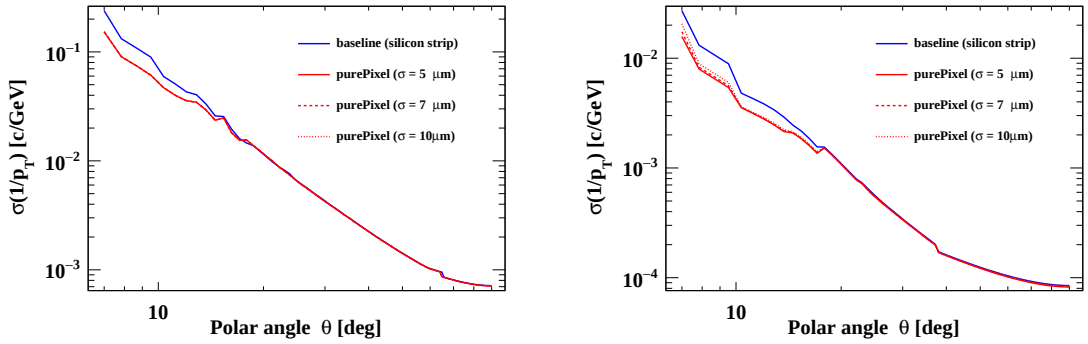

(a) $p = 1\,\mathrm{GeV}$ (b) $p = 10\,\mathrm{GeV}$

Figure 5.17: Transverse momentum resolution for single muons with momentum of $p = 1\,\mathrm{GeV}$ (a) and $p = 10\,\mathrm{GeV}$ (b) as a function of polar angle, obtained for the baseline CEPC silicon tracker with microstrips (in blue) and for pixelated tracker with various single point resolutions (in red).

of $10\,\mathrm{GeV}$. Similar improvements can be observed, even in the high momentum range for the longitudinal impact parameter.

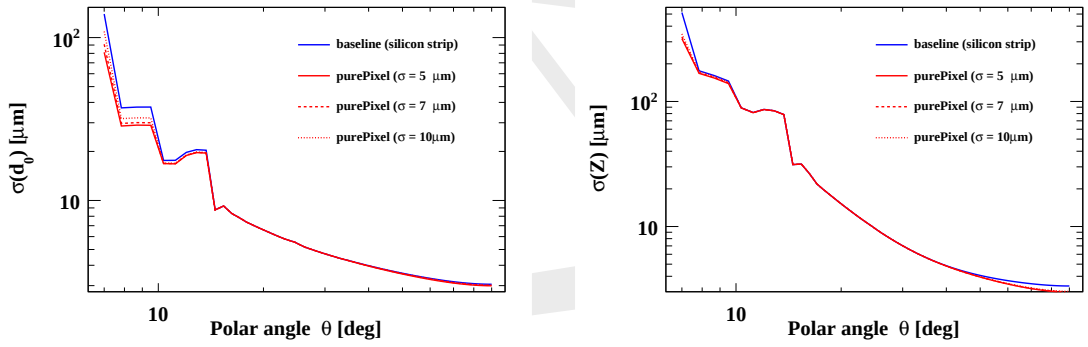

(a) σ_{d_0} (b) σ_z

Figure 5.18: Transverse (a) and longitudinal (b) impact-parameter resolution for single muons with momentum of $p = 10\,\mathrm{GeV}$ as a function of polar angle, obtained for the baseline CEPC silicon tracker with microstrips (in blue) and for pixelated tracker with various single point resolutions (in red).

Further comparison is made for tracks at a fixed forward polar angle, $10°$, which pass all five FTD disks, as shown in Figure 5.19. Significant improvements can be observed in the whole momentum range for resolutions of transverse momentum and transverse impact parameter. As for longitudinal impact parameter, there is only slight improvement for high momenta, that is understandable because the z-resolution mainly depends on disk positions.

The studies are quite preliminary. There are spaces to optimise the performance of the pixelated tracker, particularly the pixel layout of FTD disks. Some other preliminary studies on the resolution of transverse impact parameter can be found in PreCDR [1].

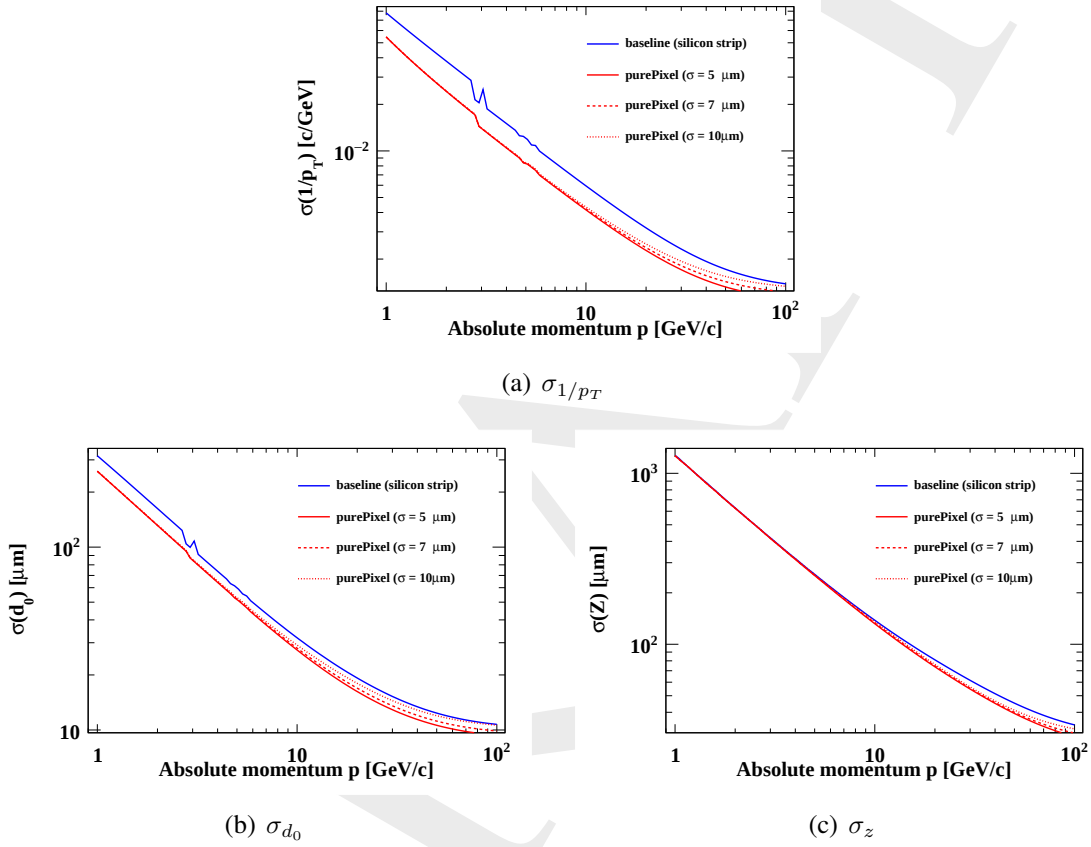

(a) σ_{1/p_T}

(b) σ_{d_0} (c) σ_z

Figure 5.19: Transverse momentum (a) and transverse (b) and longitudinal (c) impact-parameter resolution for single muons with the polar angle of 10° as a function of the track momentum, obtained for the baseline CEPC silicon tracker with microstrips (in blue) and for pixelated tracker with various single point resolutions (in red).

5.2.7 Critical R&D

Silicon technology for large-area tracking detectors will continue to evolve over the next few years [12]. There are ongoing R&D activities conducted by the ATLAS and CMS experiments to develop advanced silicon detectors for the High Luminosity LHC as well as several pioneering R&D projects by the SiLC (Silicon tracking for the Linear Collider) collaboration. Despite the rather different operation conditions and requirements, it is always important to exploit synergies with existing R&D from other experiments to share expertise. During the preliminary studies, several critical R&D items have been identified for the CEPC silicon tracker. All of them, as listed below, will be pursued in the R&D phase of the CEPC project and made available for engineering construction.

- Alternative pixelated strip sensors with CMOS technologies;
- p^+-on-n silicon microstrip sensors with slim-edge structure;
- Front-end electronics with low power consumption and low noise, fabricated with CMOS technologies of small feature size;
- Efficient powering with low material budget and CO_2 cooling techniques;
- Lightweight but robust support structure and related mechanics;
- Detector layout optimisation, in particular in the forward region.

It will be vital to develop necessary instrumentation for the module assembly and to verify the detector module performance with beam tests. Prototypes of support structures, including cooling solutions, shall be also built for mechanical and thermal tests.

5.3 Full-silicon tracker detector

The design concepts for the tracking system at CEPC are similar to the ones studied for ILC [11, 13], which are required to provide excellent tracking efficiency and precision over a wide range of momenta for charged particles from the interaction point as well as from the decay of secondary particles. The tracking system must be built with minimal material to preserve the momentum resolution and being covered hermetically down to the dip angle of $|cos\theta| < 0.992$ from the beam pipe. There are two design options for ILC detectors, the large TPC+Silicon detector (ILD) and the compact full-silicon detector (SID), with very different approaches to achieve the same performances. The full-silicon tracker offers a well known technology that provides excellent space point resolution and granularity to cope track separation in dense jets and hits from the high luminosity beam related background. The drawbacks include the relative high materia density within the tracking system, less redundancy, and limited dE/dx measurements. Nevertheless, the purpose of this study is to demonstrate that the full-silicon tracking concept is a viable option for CEPC.

For designing a full-silicon tracker, we use the same detector boundary conditions considered in the CEPC v_4 detector, which are summarized in the following,

- the solenoid B field is set to 3 Tesla,
- the tracking envolope consists of a cylinder with a radius of 1.83 m and a length of 4.6 m,

- the tracker covers down to 7.25 degree from the beam pipe,
- the Be beam pipe has a radius of 1.45 cm and 14 cm long.

5.3.1 Full silicon tracker layout

The ILD-like detector relies on a mixture of Time Projection Chamber (TPC) and silicon tracking system. However, the tracker could be converted using full silicon if the TPC is replaced with additional silicon stereo-strip layers (SIT) in the central region with disks of silicon stereo-strip detectors (FTD) on each side. In this design, the outer tracking system consists of a full-silicon tracker arranged as a set of six nested SIT layers in the central region with five FTD strip endcap disks on each side as shown in Fig. 5.20. Details for design of SIT and FTD detectors can be found in the discussion of CEPC-ILD design [**?**] and we will use the same module design to build a full silicon detector as CEPC-SID. The pixel vertex detector (VTX) is kept the same as in CEPC v_4.

This new proposed tracking system provides at least 11 precisely measured points for all tracks down to a polar angle of about 15 degree and at least 7 measured points down to a polar angle of about 7.25 degree, as shown in Fig. 5.21. With three double pixel layers and forward disks covering a wide of polar angle, they are capable of providing excellent tracking on their own. The outer tracker adds additional track-finding constrains at large radii where hit density is low while improving the momentum measurement over a large level arm with excellent hit resolution in the transverse plane.

Alternatively, we could optimize the design of ILC-SID detector for CEPC by enlarging the outer silicon strip layers to fulfil the space up to a radius of 1.83 m and z at $\pm$ 2.3 m in order to achieve comparable momentum resolution using a lower solenoid B filed of 3 Tesla as shown in Fig 5.20. The pixel detectors again are kept the same as in the ILC-SID design. We will label this option as "SIDB", which provides an independent cross check on the tracking performance using a full-silicon tracker. The number of expected hits on the track from SIDB is also shown in Fig. 5.21.

Table **??** summarizes the geometry parameters of the proposed outer strip silicon trackers for CEPC between two full silicon options.

5.3.2 Toy simulation

For each layout, we use a toy simulation (Idres) to calculate the expected tracking resolution as function of track momentum for a given incident angle θ, in which the effect of multiple scattering due to the materia are taken into account correctly. Idres was developed by the ATLAS experiment [14]. The results are also cross checked using LDT program [15], which gives a consistent result.

The coverage of the full-silicon tracking system is shown in Fig. 5.21 as function of track pesudo-rapidity. At least 7 hits are measured for all tracks with a polar angle down to about 7.25 degree. The total radiation length for all-silicon tracking systems, including dead material such as readout, cables and supports, is about 5-7% for CEPC-SID and 7-10% for SIDB, respectively.

The expected momentum (p_T) and impact parameters (d0, and z0) resolutions are compared as function of track p_T in GeV/c for tracks with $\theta = 85$ and 20 degree, respectively, as shown in Fig. 5.22. The z0 resolution is better for CEPC-SID than for SIDB due to extra stereo-strip layers while the p_T and d0 resolutions are similar.

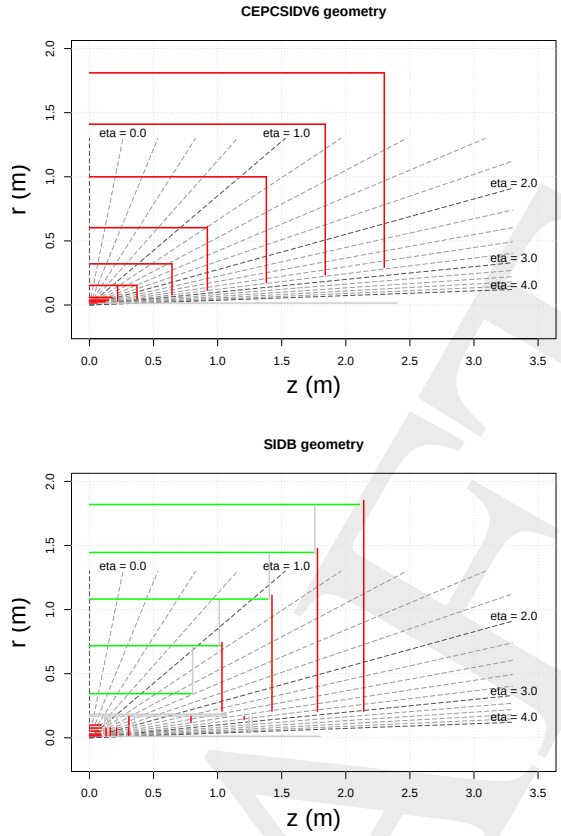

Figure 5.20: The R-Z view of the full silicon tracker proposed for CEPC (left) and the enlarged version of SID design (right).

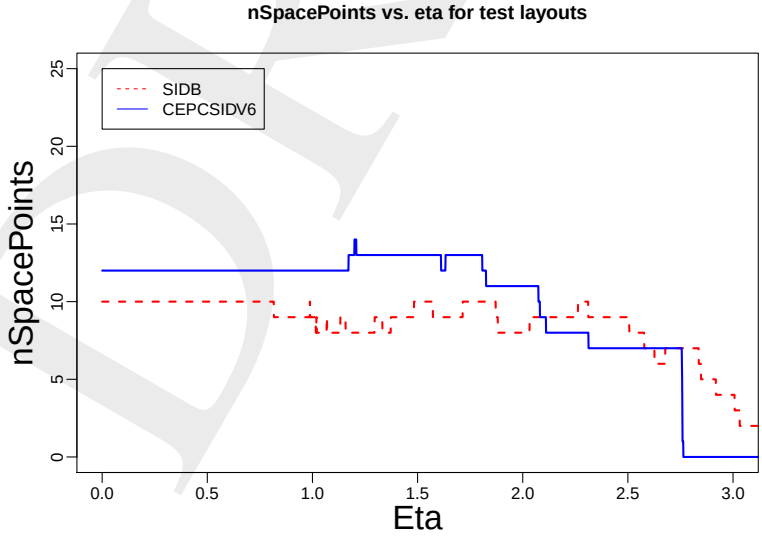

Figure 5.21: The number of expected hits are shown as function of track pesuro-rapadity.

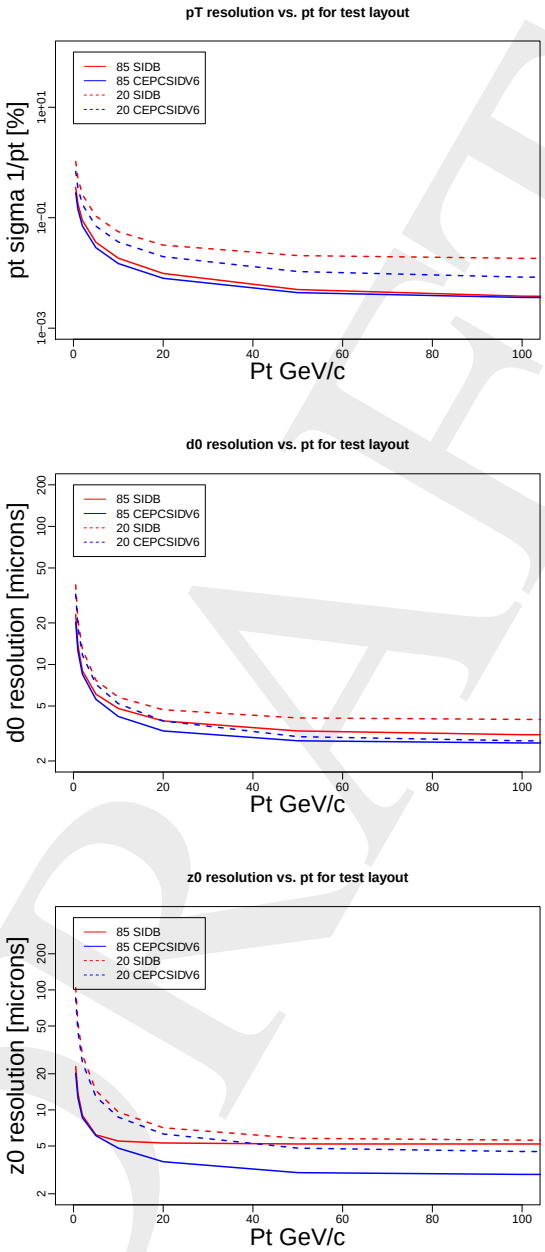

Figure 5.22: The expected p_T, d0, and z0 resolutions from the toy simulation (Idres) are compared as function of track p_T in GeV/c for tracks with $\theta = 85$ and 20 degree, respectively.

	CEPC-SID				SIDB			
Barrel	R (m)		±z (m)	Type	R (m)		±z (m)	Type
layer 0	0.153		0.368	D	0.344		0.793	S
layer 1	0.321		0.644	D	0.718		1.029	S
layer 2	0.603		0.920	D	1.082		1.391	S
layer 3	1.000		1.380	D	1.446		1.746	S
layer 4	1.410		1.840	D	1.820		2.107	S
layer 5	1.811		2.300	D				
Endcap	R_{in} (m)	R_{out} (m)	±z (m)	Type	R_{in} (m)	R_{out} (m)	±z (m)	Type
Disk 0	0.082	0.321	0.644	D	0.207	0.744	1.034	D
Disk 1	0.117	0.610	0.920	D	0.207	1.111	1.424	D
Disk 2	0.176	1.000	1.380	D	0.207	1.477	1.779	D
Disk 3	0.234	1.410	1.840	D	0.207	1.852	2.140	D
Disk 4	0.293	1.811	2.300	D				

Table 5.3: The proposed geometry parameters for the outer strip barrel layers and disks, where D and S stand for double and single-strip layer.

5.3.3 Detector simulation and reconstruction

In order to optimize the full silicon tracker detector for CEPC, we generate several benchmark processes that include single muon events, $e^+e^- \to ZH \to \nu\nu\mu\mu$, and $e^+e^- \to ZH \to \nu\nu GG$ (two gluon jets). The events are then simulated and reconstructed using different detector geometries, which are then used for the tracking performance studies.

5.3.3.1 CEPC-SID detector

The implement of geometry of full-silicon-tracker is based on a simulation tool Mokka[16]. The CEPC group have create a version of database cepc_v4 to build the preliminary design of CEPC detector [**?**], in which the tracker is composed of VXD, SIT, TPC, SET and FTD. In order to implement the full-silicon-tracker, the TPC is considered to be replaced with a new silicon-based strip tracker. Similarly, the new silicon tracker is also called as SIT, and the SET is removed at the same time, since the type of the old SIT, the new silicon-based strip tracker and the SET are based on the same design. Finally, a full-silicon-tracker including VXD, SIT and FTD is built on the basis of cepc_v4, as described above.

In order to improve the flexibility of design, a new package of SiTracker is implemented in Mokka which represents the silicon tracker by planar structure, which consists of a. thin layer of silicon with 150 μm thickness and 50 μm pitch size. For VXD and SIT, they are composed by several layers, and each layer is composed by several ladders, and each ladder is divided to several sensors. The SIT layer consist of double silicon layers mounted back to back with a stereo-angle of 7 degree. For FTD, it is composed by several pixel disks FTD_PIXEL and several double-side strip disks FTD_STRIP that are composed by petals. The strip FTD disk has two sensitive silicon sub-layers on each side with a stereo-

angle of 5 degree. The number of ladders/petals, the size and position of layers, and the sub-structure of layers can be modified easily in input file as globalModelParameter. In future, a XML structure is considered as the method to input parameters.

The lcio format is used to output the simulated signals from the full-silicon-tracker, same as other sub-detector system [17]. The digitization and clustering are done in reconstruction process. In the default version, a smearing technology based on truth information is used as a simple digitization and clustering, which is used for this study. Recently, a new digitization for silicon-based detector has been developed. It first finds out the pixel which the hit is located, and uses the center of the pixel or strip as the new position for the hit. And then those hits in same pixel or neighboring will be merged into single hit.

The silicon tracking algorithm is the same one used by CEPC-ILD [**?**], which are steered by a set of strategies. Each strategy represents a set of layers in the detector and tries to find combinations of hits that forms a helix within these layers. The algorithm starts by looking for a track seed by any combination of three hits that fulfils a helix fit. Once found, the track seed is extended by successively adding more hits that are consistent with the extrapolation of the seed helix. If fewer than the minimum required number of hits are found, the track candidate is discarded. If the tracks found in different strategies share more than one hit, only the track with the best fit is kept based on the χ^2 per degree of freedom and the number of hits on the track.

5.3.3.2 Optimized SID detector

For the SiD detector optimized for CEPC (or SIDB), events were simulated and reconstructed using a software developed for the International Linear Collider (ILC) [11, 13], but re-worked for the HepSim project [18, 19]. The response of the SiD detector to physics events is simulated using the "Simulator for the Linear Collider" (SLIC) 5.0 software [20] interfaced with the GEANT4 10.3p1 program [21]. The track reconstruction was performed with the LCSIM 4.0 package [17] using the "seed tracker" algorithm as for the SiD detector simulation. Track candidates with at least six hits in the silicon pixel and microstrip layers were considered. Only tracks with a minimum transverse momentum (p_T) of 100 MeV were accepted. The track-fitting was performed with the following requirements; maximum distance of closest approach (DCA) is $|DCA| < 6$ mm, $|z_0| < 10$ mm, and fit $\chi^2 < 10$. The reconstruction includes particle-flow algorithms (PFA) which enable identification and reconstruction of individual particles. The PFA objects can be reconstructed using the software algorithms implemented in the PANDORA package [22, 23].

The geometry of SIDB detector is implemented using the compact XML geometry description, which can load and built at runtime. The main changes over the ILC-SID detector include the reduced B-field from 5 Tesla to 3 Tesla. The outer tracker is scaled up by a factor of about 1.44 to the radius of 1.83 m and z of $\pm$ 2.3 m. The silicon module sizes were appropriately scaled. The first inner layer of the barrel vertex detector was positioned at 15 mm, just outside of the beam pipe. The outer barrel layer of the silicon vertex detector was moved to 100.3 mm (vs 59 mm for the SiD detector), while other barrel layers are equally spaced. The forward disks, together with the support structures, were appropriately scaled in z by a factor 1.37.

As for the SiD detector, the barrel tracker consists of five layers of silicon sensors with 50 μm pitch. The forward tracker has four disks of silicon sensors. The silicon pixel detector had 20 μm pitch, consisting of five layers in the barrel and six disks in the forward

region. The hadronic and electromagnetic calorimeters, as well as the muon detector, were optimized for CEPC physics as described in [24].

5.3.4 Tracking performance

After the detector simulation and reconstruction, the tracking performances are measured in terms of efficiencies, fake rates, momentum resolution, and the impact parameter resolutions using single muons or $e^+e^- \rightarrow ZH$ events. The tracking efficiency is defined as a fraction of stable charged particles that can be matched to well reconstructed tracks. The stable particles are defined as those charged particles with p_T >1 GeV/c in the detector fiducial region ($9 < \theta < 170$ degree), originated from the interaction point, and lived long enough to reach the calorimeter. A well reconstructed track is defined as sharing more than 50% of its assigned silicon hits originating from a single particle (truth hits). We define a truth hit fraction as ratio of truth hits over total assigned hits of the track using silicon hits only. A poorly reconstructed track is defined to have the truth hit fraction less than 50%. The fake rate is defined as the fraction of poorly reconstructed tracks out of total reconstructed tracks, but this requires a realistic detector simulation, which we are not there yet. The tracking performance in the CEPC (v_4) detector is also shown as the reference.

5.3.4.1 Single muon particle

Figure 5.23 shows the tracking efficiency for single muons in CEPC-SID as function of p_T. The tracking efficiency is close to 100% at high p_T and slightly lower at small p_T. The trend is the same for CEPC v_4 , which indicate both trackers are capable of finding tracks efficiently in the detector fiducial region.

The number of silicon hits found on the track and the fraction of truth hits are shown in Fig. 5.24 where the hit purity is reached more than 90% for both detectors.

Since the track resolution depends on the track angle θ, we divide the tracks in the barrel region with $40 < \theta < 140$ degree and in the endcap region with $7.25 < \theta < 40$ degree or $140 < \theta < 172.75$ degree. Figure 5.25 shows the track resolutions of p_T, d0, and z0 as function of track p_T in the barrel and endcap region. The resolutions for the low momentum tracks seem slightly better in the CEPC v_4 detector (TPC+Silicon) than an alternative full silicon tracker due to extra materia in the detector while they are compatible at the high p_T. The resolutions from the SIDB detector are also included in the comparision, which has a compatible momentum resolution while the d0 and z0 are slightly worse.

5.3.4.2 Di-muon mass resolution

Figure 5.26 shows the di-muon invariant mass distributions from $ZH \rightarrow \nu\nu\mu\mu$ decay between different detector configurations. The higgs mass used in CEPC simulation is 125 GeV/c^2 while 125.09 GeV is used in the SIDB simulation. The di-mass from CEPC-ILD seems shifted by 0.2 GeV from the input Higgs mass of 125 GeV/c^2 while other masses from CEPC-SID and SIDB agree with the expectation. The di-muon mass resolution from CEPC-SID has $\sigma = 0.21$ GeV/c^2 and seems 20% and 25% better than ones obtained from CEPC-ILD and SIDB, respectively.

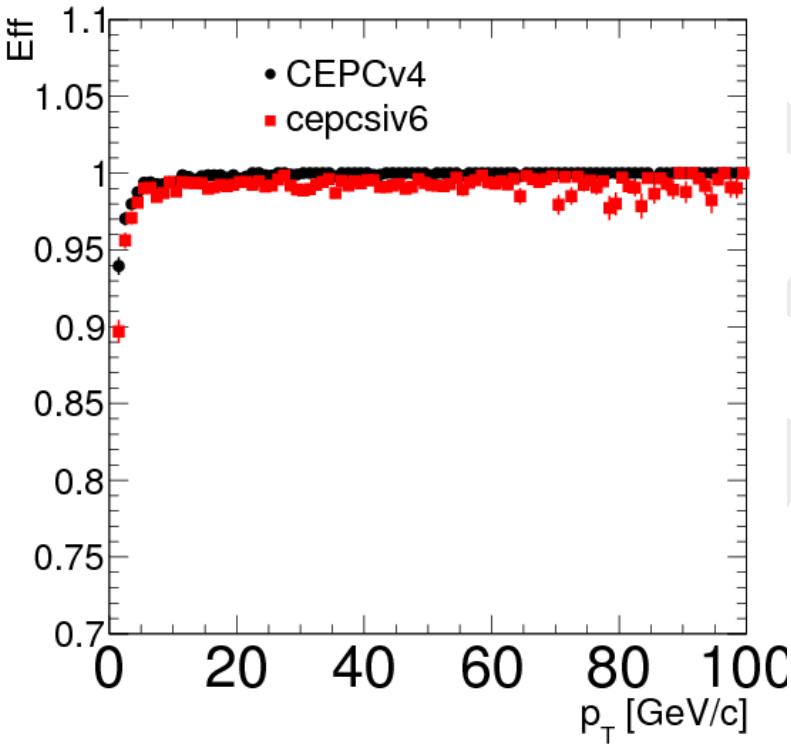

Figure 5.23: The tracking efficiencies are measured as function of p_T for single muons using CEPC v_4 and CEPC-SID detetcors.

5.3.4.3 Tracking inside the jets

In order to study the tracking performance inside the jets, we generated and simulated some Higgs decaying into two gluon jets (GG) in $zH \rightarrow \nu\nu GG$ events. Figure 5.27 shows the tracking efficiency inside the jets as function of track momentum. The average efficiency of finding tracks inside the jets is about 90% for CEPC-SID while about 97% for CEPC-ILD due to the excellent tracking in TPC. The full silicon tracking inside the dense of jets is not fully optimized in dealing with outliers in the fit, which requires a realistic detector simulation and clustering. The work is in progress to improve the tracking inside the jets.

5.3.5 Conclusion

We present a preliminary study of full silicon tracker option as an alternative design for CEPC tracking. Two approaches are considered for the design: the first is to keep the silicon detectors (VXD, SIT, FTD) in the CEPC-ILD detector and replacing TPC with additional silicon detectors, the second is to optimize the ILC-SID tracker to fulfil the CEPC tracking volume in order to achive the excellent momentum resolution using 3 Tesla B field. The new detector geometry has been implemented in the simulation and the track reconstruction has also been adoped for the full silicon tracker. The initial study of the tracking performance looks promising. There are still many improvements needed in the simulation and reconstruction in order to explore the full potential of the full-silicon tracker.

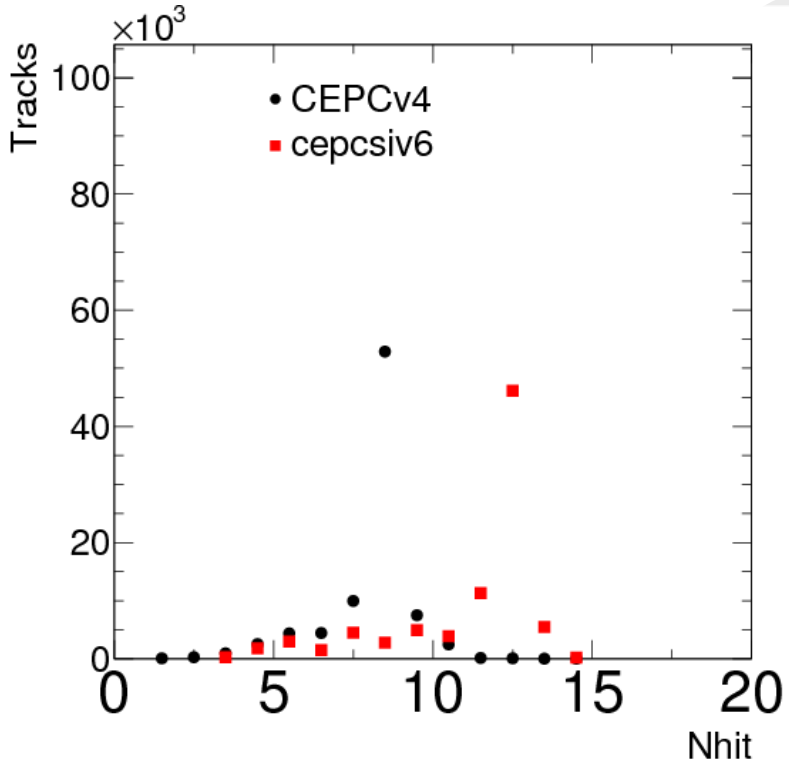

Figure 5.24: The distributions are shown for the number of silicon hits on the track (left) and the hit purity on (right).

5.4 Drift chamber tracker detector

5.4.1 Introduction

The drift chamber (DCH) is designed to provide good tracking, high precision momentum measurement and excellent particle identification by cluster counting. Main peculiarity of the drift chamber is its high transparency, in terms of radiation lengths, obtained thanks to the novel approach adopted for the wiring and assembly procedures. Original ancestor of the DCH design is the drift chamber of the KLOE experiment [25], more recently culminated in the realisation of the MEG2 [26] drift chamber .

5.4.2 Physics Requirements and Performance Goal

Main requirements imposed to the tracking system are high efficiency and state of the art momentum and angular resolutions for charged particles, of the order of $\sigma(1/p) \approx 2-3\times 10^{-5}\,GeV/c^{-1}$ and $\sigma(\theta,\phi) \approx 0.1\,mrad$ for 45 GeV muons Moreover, high transparency in terms of radiation length, and particle identification capabilities are a necessary requisite.

5.4.3 Overview

The DCH is a unique volume, high granularity, all stereo, low mass cylindrical drift chamber, co-axial to the 2 T solenoid magnetic field. It extends from an inner radius R_{in} = 0.35 m to an outer radius R_{out} = 2 m, for a length L = 4 m. It is made of 112 co-axial layers, at alternating sign stereo angles and arranged in 24 identical azimuthal sectors.

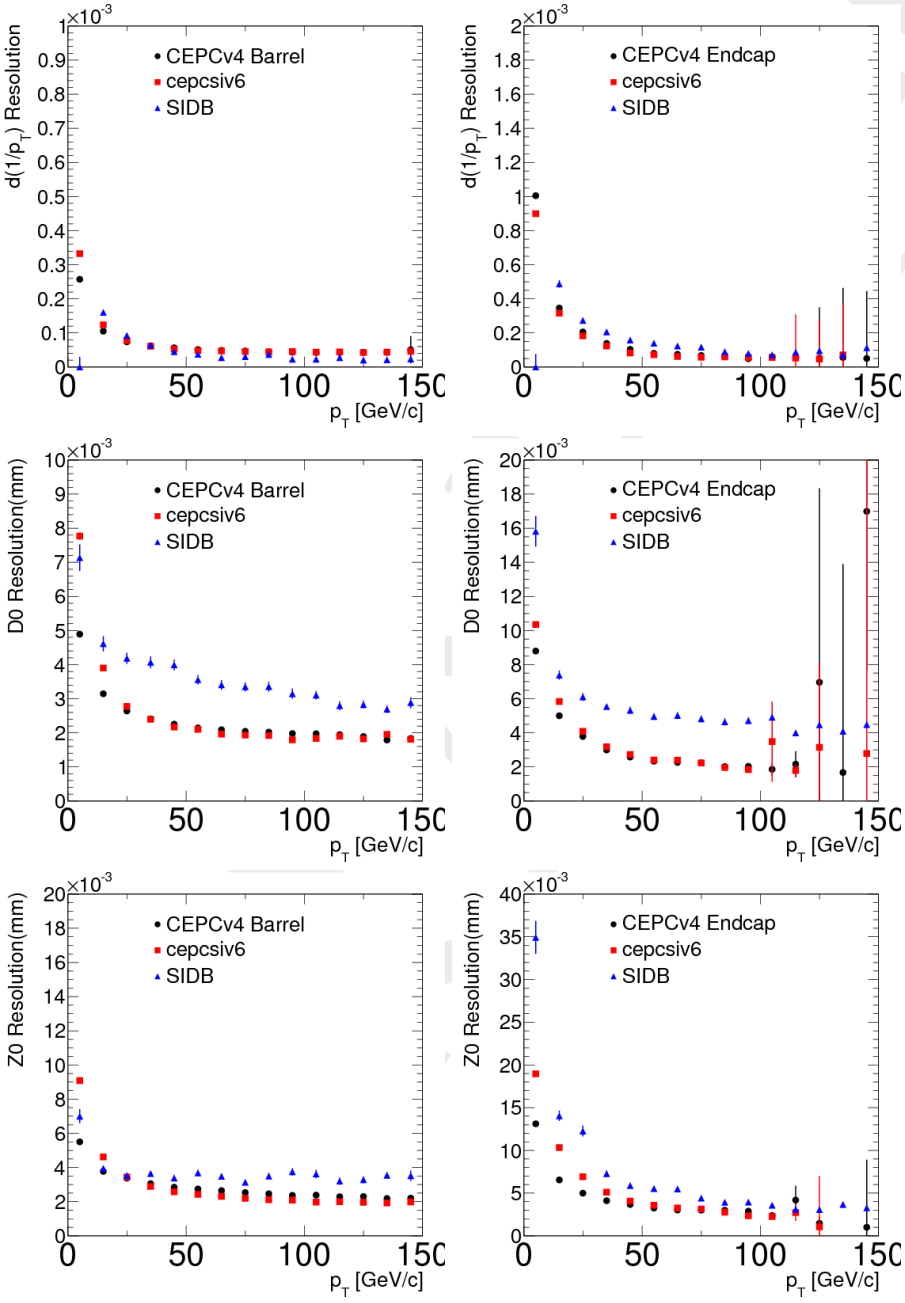

Figure 5.25: The tracking p_T, d0, and z0 resolutions are measured as function of p_T, ϕ, and θ using single muons, left in the barrel region and right in the endcap region. They are compared between CEPC v_4 and two full silicon detector concepts.

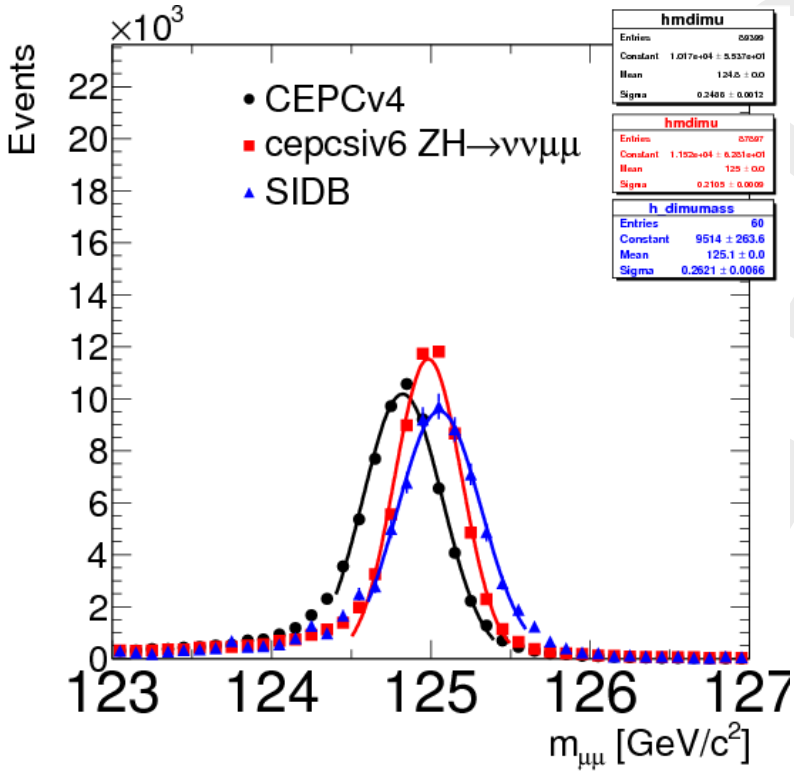

Figure 5.26: The di-muon mass distribution is compared from different detectors.

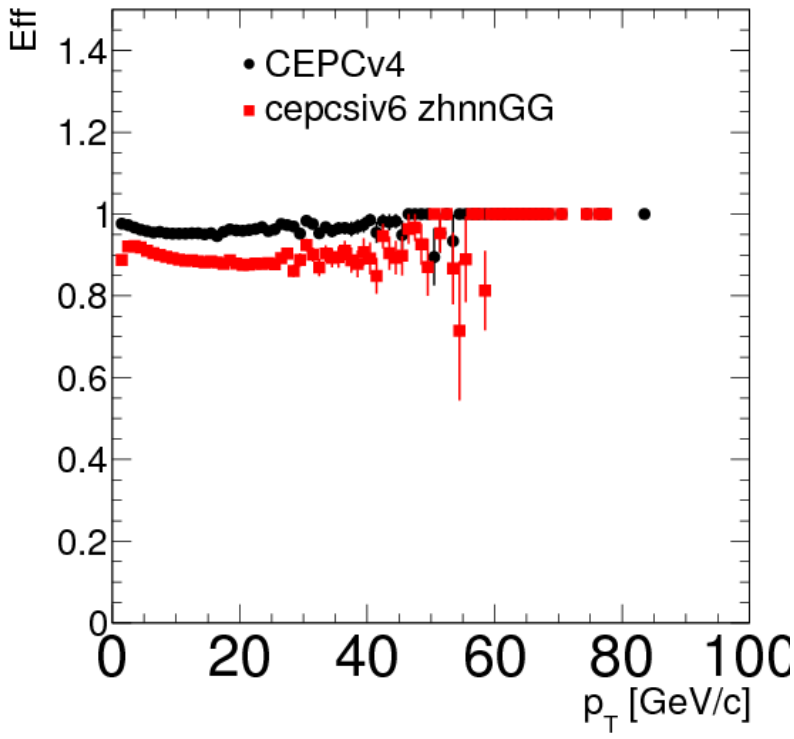

Figure 5.27: The tracking efficiencies for the stable particles inside the gluon jets as function of track p_T with CEPC v_4 and CEPCSID.

The square cell size varies between 12.0 and 14.5 mm. The total number of drift cells is 56,448. The angular coverage, for infinite momentum tracks originated at the origin and efficiently reconstructed in space, is 97%. The sense wires are read out from both ends in order to facilitate track finding through charge division and time propagation difference measurements.

5.4.4 Mechanical Design

A considerable reduction in the amount of material of the end plates can be obtained by the simple consideration of separating the gas containment function of the mechanical structure from the wire tension relief function. According to this scheme, the wires are anchored to a self-sustaining light structure (a "wire cage") surrounded by a very thin skin (a "gas envelope") of suitable profile to compensate for the gas differential pressure with respect to the outside. The "wire cage" is schematically made of a set of radial spokes (24 for the present proposal), extending from the inner radius of the chamber to the outer one. The drift chamber is, then, built by alternatively stacking, along the radius and between the spokes of the wire cage, printed circuit boards, to which the ends of the wires are soldered, and spacers, to set the proper cell width, in each of the 24 sectors. A cylindrical carbon fibre support structure guarantees the proper end plates separation, whereas, two thin carbon fibre domes, suitably shaped and free to deform under the gas pressure without affecting the wire tension, enclose the gas volume.

5.4.4.1 Layer Structure

The active volume of the drift chamber is divided in 14 co-axial super-layers, each one composed of 8 layers, at stereo angles of alternating signs, for a total of 112 layers, arranged in 24 identical azimuthal sectors. The innermost 8 layers, constituting the first super-layer, contain N_1 = 192 drift cells (8 per sector) each. In order to maintain an approximately constant cell size, the number of drift cells in each consecutive super-layer is incremented by 48 (2 in each sector): $N_i = 192 + (i-1) \times 48$, up to $N_{14} = 816$ (34 drift cells per sector), for a total of 56,448 drift cells. The width of the cell, approximately square, varies from about 12 mm at the innermost layer to about 14.5 mm at the outermost layer. The stereo angle is generated by stringing the wires between two points on the end plates at the same radius and mutually displaced by two sectors ($2\alpha_i = \pm 30°$, see Figure 5.28). Thus, the stereo angles increase linearly with the layer radius from 50 to 250 mrad. Because of this configuration, the cell size at the end plates ($z = \pm L/2$) results larger by about 3.5%, with respect to the cell size at $z = 0$, maintaining, however, its aspect ratio identical to 1 at any z. Each layer consists of three wire sub-layers: an inner and an outer cathode sub-layers made of 40 μm diameter Au coated Al field wires and a middle anode sub-layer made of alternating sense (20 μm diameter Au coated W) and field shaping (50 μm diameter Au coated Al) wires. Two consecutive layers are oriented at opposite stereo angles. The outer cathode sub-layer of each layer lies at the same radius as the inner cathode sub-layer of its radially adjacent layer, thus forming a dense equipotential mesh of cathode wires (Figure 5.29). Its envelope in space forms a rotational hyperboloid surface. The resulting large ratio of field to sense wires of $5:1$, besides assuring uniformity of response longitudinally, allows for thinner field wires, thus reducing the total mass of the chamber and the tension load on the end plates.

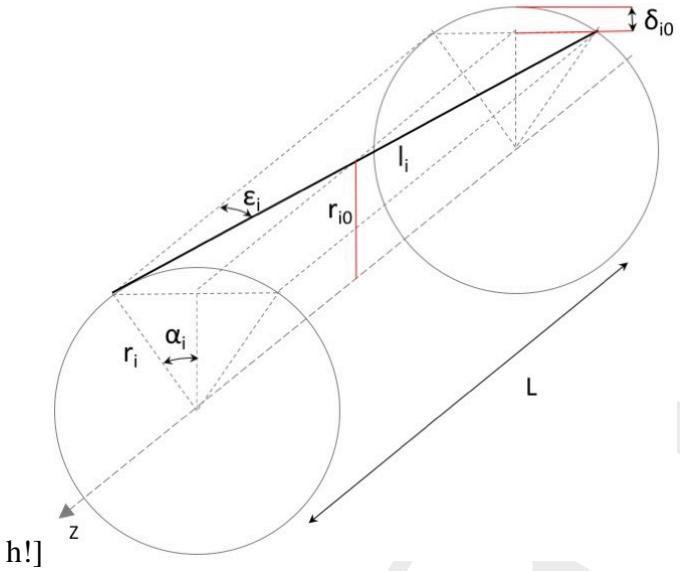

Figure 5.28: Arrangement of a stereo wire.

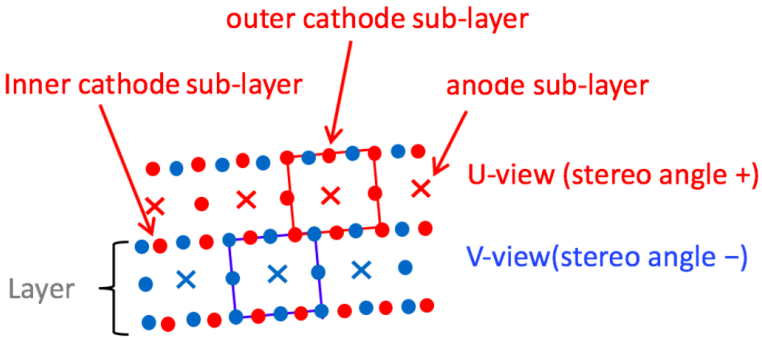

Figure 5.29: Stereo layers arrangement.

5.4.4.2 Drift Cell Structure

A reasonable single electron signal at the front end (pulse height of the order of 6 mV), with the configuration described in Figure 5.29 (sense to field wires capacitance C = 8 pF/m), is obtained at a gas amplification of 6×10^5, corresponding to 100 fCoul charge on the sense wire, or 10 nCoul/m linear charge density, if one assumes a charge spread of the order of 10 μm. These values are compatible with 1.25 kV sense wire positive potential with respect to the field wires. The necessary electric field of about 200 kV/cm on the sense wire surface is reached with a 20 μm diameter sense wire. In order to avoid generating uncorrelated noise due to positive ions amplification and to mitigate cathode ageing effects, the electric field on the surface of the field wires must be kept below 20 kV/cm. It is, therefore, necessary that the surface of all field wires surrounding a sense wire be, at least, ten times larger than the sense wires surface. In the described configuration of Figure 5.29, with five field wires per sense wire, the resulting diameter of all field wires must then be, in average, at least twice the sense wire diameter, i.e. 40 μm. In addition, since all field wires located at the same reasonadius as the sense wires exhibit for symmetry reasons a higher field, their diameter need be increased to 50 μm.

5.4.4.3 Wire Choice

Gas amplification considerations suggest the choice of 20 μm for the sense wires and 40 μm and 50 μm for the field wire diameters. Tungsten (W) is a good candidate for the sense wires because of its availability, due the ease of drawing, despite of its large density ($19.3\,g/cm^3$) and short radiation length ($0.35\,cm$). However, Molybdenum (Mo, $10.22g/cm^3$ density, $0.95\,cm$ radiation length) or Titanium (Ti, $4.54\,g/cm^3$, $3.56\,cm$), can be considered as viable options, provided the necessary prototype studies are successfully accomplished. Considerations about limiting multiple scattering contributions to momentum and angular resolution, particularly for low momentum particles, impose the choice of light metal alloys for the large number of field wires. Silver plated (0.3 μm thickness) Al5056 wires (40 μm and 50 μm diameter) produced by California Fine Wire company, similar to the ones used for the KLOE drift chamber - though their diameter was 80 μm - and exactly the same wires used for the MEG2 drift chamber have been chosen here.
This 40 μm wire presents an elastic limit at about $50\,g$ tension, corresponding to an elongation of $5\,mm/m$. Setting the operating mechanical tension at $20\,g$ tension, corresponding to a gravitational sagitta of approximately $400\,\mu m$, over $4\,m$ wire length, the resulting tension load on the "wire cage", including the 50 μm diameter field wires and the 20 μm sense wires, is of the order of $7.7\,Ton$. Heavier wire alloys would have required correspondingly higher loads.

5.4.4.4 Electrostatic Stability

Electrostatic stability condition for a sense wire of radius r, length L, at Voltage V_0 with respect to the surrounding field wires placed at distance $w/2$ and with mutual capacitance per unit length:

$$C = \frac{2\pi\epsilon}{\ln\frac{w}{r}}$$

is reached when the wire mechanical tension T is above a critical value T_c:

$$T_c \geq \frac{C^2 V_0^2 L^2}{4\pi\epsilon w^2} = \frac{\pi\epsilon V_0^2 L^2}{w^2 ln^2 \frac{w}{r}}$$

In this particular case, $V_0 = 1500\,V$, $L = 4\,m$, $w = 12\,mm$, $r = 10\,\mu m$ and $T_c \geq 0.16\,N$, which confirms the electrostatic stability of the chamber, since the plan is to tension the wires at about $0.25\,N$ (at this value, stability is reached up to a length $L \approx 5.0\,m$), being the elastic limit for the $20\,\mu m$ W sense wire equal to $0.48\,N$.
However, in case of high occupancy at the inner layers, which might require a local downsizing of the drift cells, let's say down to $w = 7\,mm$, $T_c \geq 0.48\,N$, equal to the sense wire elastic limit. One possible solution would be the shortening of the wires of the inner layers, though at the cost of a severe loss of angular coverage. Alternatively, one could increase the sense wire diameter

5.4.4.5 Gas Mixture

A helium-based gas mixture has been chosen to minimize multiple scattering and energy losses. Moreover, helium is fairly insensitive to X-ray background and exhibits a small Lorentz angle in magnetic field. The relevant properties of the gas mixture, either measured directly, or computed with transport equations, are listed in Table 5.4. The drift

Table 5.4: Properties of the $90\%He - 10\%iC_4H_{10}$ gas mixture.

Number of primary clusters (per m.i.p.)	$12.3\,cm^{-1}$
Number of total clusters (per m.i.p.)	$19\,cm^{-1}$
Drift velocity ($E = 0.4 \div 1.0\,KV/cm$)	$1.5 \div 2.4 cm/\mu s$
Lorentz angle ($E = 0.4 \div 1.0\,KV/cm$ and $B = 2\,T$)	$15° \div 20°$
Longitudinal diffusion	$170\,\mu m/\sqrt{cm}$
Radiation length	$1400\,m$

velocity as a function of the electric field is shown in Figure 5.30. The meager density of primary clusters produced in a helium based gas mixture affects in a biased way the spatial resolution, particularly for small impact parameters, however, it allows exploiting the possibility of correcting the bias, with statistical considerations, by measuring the arrival time of each individual ionization cluster, as illustrated in the next paragraph.

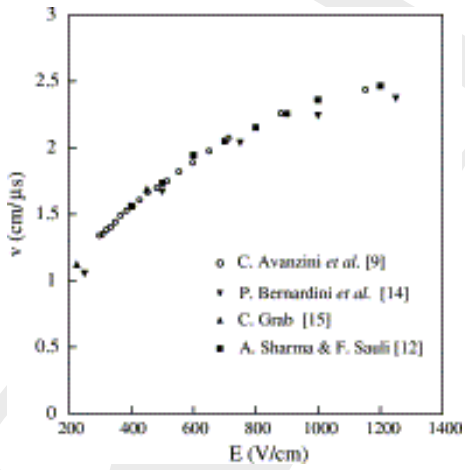

Figure 5.30: Drift velocity for $90\%He - 10\%iC_4H_{10}$ gas mixture.

5.4.5 Cluster Counting/Timing Techniques

5.4.5.1 Cluster Timing for improved spatial resolution

The left hand side of figure 5.31 shows the signal generated on a 20 μm sense wire by a m.i.p. crossing a 8 mm diameter drift tube (an illustration of the ionization process is presented inFigure 5.32), filled with $90\%He - 10\%iC_4H_{10}$ gas mixture, at a gain of 5×10^5 and read out by a 1 GHz, 2 GSa/s, 8 bit digitizer, after a $\times 10$ gain preamplifier. Single electron pulses, as well as multiple electron cluster pulses, are clearly identifiable by a peak finder algorithm (in the right hand side of Figure 5.31 is shown the result of PEAKFIT [**?**] software applied to the signal at left) and their amplitudes and times can reliably be reconstructed. From the ordered sequence of the electrons arrival times and from their amplitude, considering the average time separation between ionization clusters and the time spread due to diffusion, one can thus reconstruct the most probable sequence of the cluster drift times: $\left\{t_i^{cl}\right\}$ with $i = 1, N_{cl}$. The cluster timing technique, given such

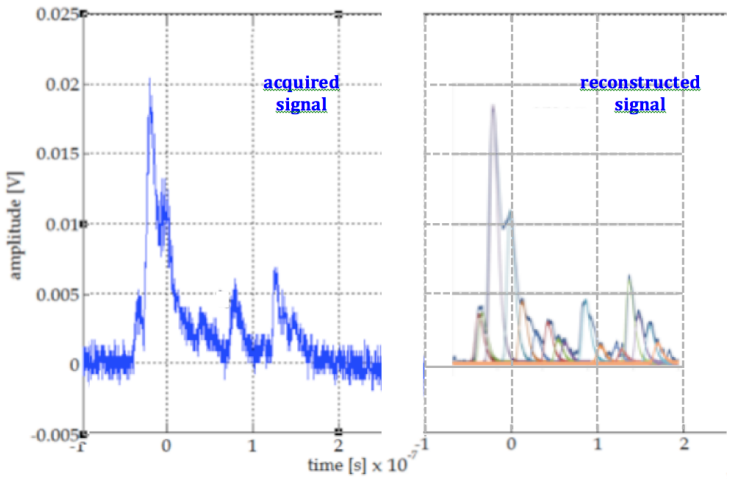

Figure 5.31: Left, drift tube signal generated in the setup described in the text. Right, software reconstructed signal.

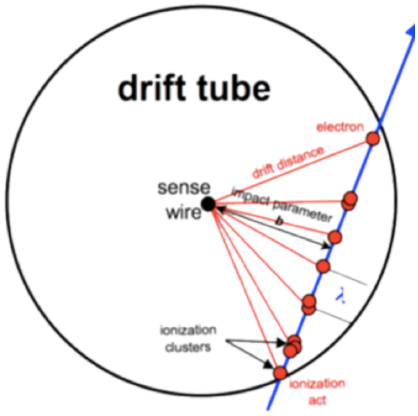

Figure 5.32: Schematic picture of an ionisation track in a drift tube.

a sequence, exploits the drift time distribution of all clusters to determine, with statistics based algorithms, the most probable impact parameter, thus reducing the bias and the average drift distance resolution with respect to those obtained by the first cluster method alone. In Figure 5.33, one can see the result of the application of several algorithms to the sequence of cluster times. The Maximum Possible Spacing (MPS) algorithm [**?**] is the

one that corrects the bias in the most effective way (by about 100 μm in the critical region around the sense wire).

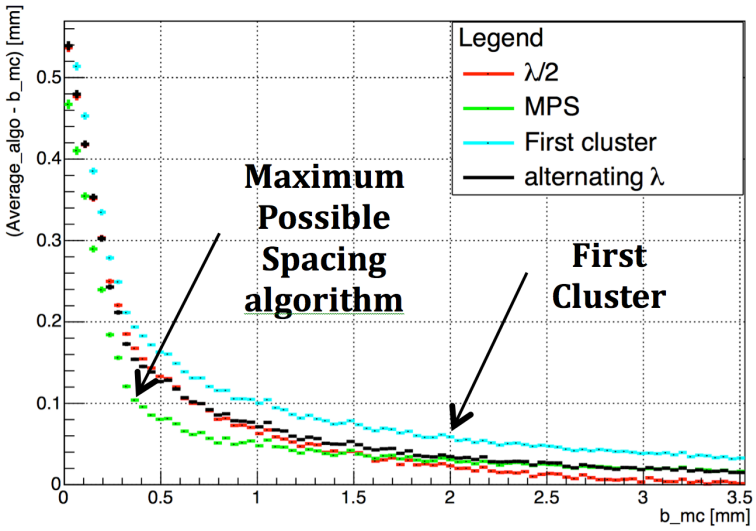

Figure 5.33: Drift distance bias correction, as function of the impact parameter, according to different algorithms.

5.4.5.2 Cluster Counting for particle identification

Thanks to the Poisson nature of the ionization process, by counting the total number of ionization clusters N_{cl} along the trajectory of a charged track in a drift chamber, one can, in principle, reach a relative resolution on $dN_{cl}/dx \propto 1/\sqrt{N_{cl}}$.

The data shown in Figure 5.34 and Figure 5.35, were taken in a 200 MeV/c momentum beam of muons and pions selected by time of flight. A 2.6 cm square drift tube, oriented at 45° with respect to the beam direction (to avoid corrections due to space charge effects), filled with a $95\%He - 5\%iC_4H_{10}$ gas mixture ($N_{cl} = 9/cm$), instrumented with a 25 μm sense wire (gas gain 2×10^5), readout through a high bandwidth (1.7 GHz, $\times 10$ gain) preamplifier and digitized with a 2 GSa/s 1.1 GHz, 8 bits digital scope, was used to collect the data. By merging together 100 different signals, belonging to a muon or to a pion, one is able to reproduce the effects of a 3.7 m long track ([**?**] and references therein). Figure 5.34 (a) and (b) show the typical Landau distribution of the integrated collected charge over a single signal, respectively for pions and muons. The best resolution in dE/dx one can achieve, under these conditions (gas at NTP), according to WalentaÕs parameterization [**?**] with n=100 samples and L = 3.7 m total sampled length, is $\sigma_{(dE/dx)}/(dE/dx) = 3.7\%$, corresponding to a $2.0\,\sigma$ μ/π separation. By truncating 20% of the largest dE/dx samples, in order to obtain normal distributed values, shown in Figure 5.34 (c) and (d), one gets experimentally, instead, $\sigma_{(dE/dx)}/(dE/dx) = 4.5\%$, corresponding to a $1.4\,\sigma$ μ/π separation.

The distribution of the number of clusters in the 3.7 cm samples is shown in Figure 5.35 (a) and (b), for pions and muons respectively. The misidentification of the Poisson distributed number of clusters is indicated by the asymmetric tails, both in the single 3.7 cm sample distribution (Figure 5.35 (a) and (b)) and in the distributions summed over 100 samples (Figure 5.35 (c) and (d)). This bears, as a consequence, the worsening of the resolution

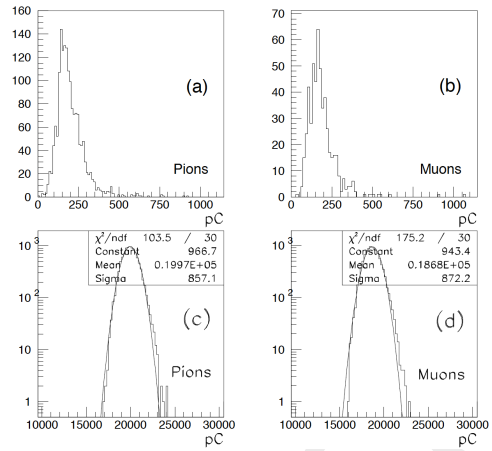

Figure 5.34: Pions (a) and muons (b) charge integral distribution (Landau) for single samples and pions (c) and muons (d) 20% truncated mean distributions summed over 100 samples. Sample size $3.7\,cm$ and particles momenta $200\,MeV/c$

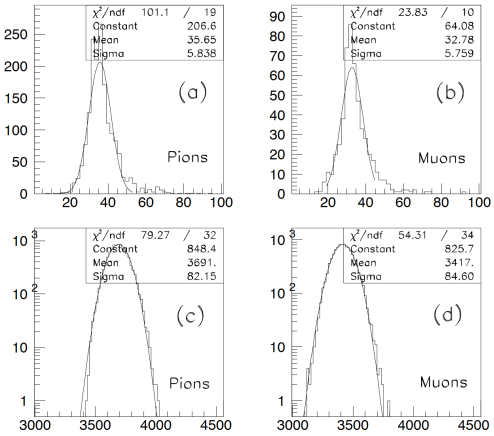

Figure 5.35: Distribution of counted clusters (Poisson) over single samples for pions (a) and muons (b) and the same distributions for pions (c) and muons (d) over the sum of 100 samples. Sample size $3.7\,cm$ and particles momenta $200\,MeV/c$

from a hypothetical theoretical value, $\sigma_{(dN_{cl}/dx)}/(dN_{cl}/dx) = 1.7\%$, corresponding to a $5.0\,\sigma$ μ/π separation, to the more realistic experimental value $\sigma_{(dN_{cl}/dx)}/(dN_{cl}/dx) = 2.5\%$, corresponding to a $3.2\,\sigma$ μ/π separation.
This simple exercise demonstrates the potentialities of the cluster counting method for

particle identification, able to achieve a relative resolution better by a factor two with respect to the traditional method of the dE/dx truncated mean.

5.4.5.3 Requirements for Cluster Timing/Counting

The use of helium based gas mixtures, thanks to the sparse number of primary ions per unit length and to the slower drift velocity, makes the application of the cluster counting/timing techniques particularly favourable. In these mixtures, average drift time difference between consecutive clusters goes from a few ns, for clusters close to the sense wire, where drift velocity is at its highest values, to tens of ns for clusters at several mm from the sense wire. As shown in Figure 5.31, a $\times 10$ gain high bandwidth preamplifier and at least 1 GHz, 2 GSa/s, 8 bit digitizer are, therefore, sufficient to guarantee an efficient cluster identification and, consequently, a sizeable improvement on spatial resolution (below 100 μm) and a very effective particle identification ($\sigma_{(dN_{cl}/dx)}/(dN_{cl}/dx) = 2.5\%$).

5.4.6 Front-end electronics

5.4.6.1 Signal amplifier and digitizer

In order to allow for an efficient detection of single ionization clusters, the front end electronics must be able to process high speed signals at a gain suitable for digitisation and acquisition. Given the very large number of readout channel and their high spatial density, low power consumption is required even in the presence of efficient cooling systems. Moreover, bandwidth adequate to the expected signal spectral density and fast pulse rise time response are necessary to exploit the cluster counting/timing techniques. As anticipated in the previous paragraph, digitisation at high sampling rates is mandatory to separate closely spaced clusters. In the proposed gas mixture, cluster separation in time goes from a few ns to tens of ns, as a function of the drift distance. However, electron diffusion from distant multi-electrons clusters may result in over counting. For an efficient cluster identification is, therefore, necessary to digitise the signals at fractions of a ns.

5.4.6.2 Data reduction and cluster analysis

5.4.7 Drift chamber material budget

5.4.7.1 Mechanical Structure

5.4.7.2 Gas mixture and wires contribution

5.4.8 Expected performance

5.4.8.1 Aging

One can extrapolate results from the aging studies performed for the MEG2 drift chamber [**?**]. By using an equivalent cell structure, wire size, gain, and a very similar gas mixture ($85\% He - 15\% iC_4H_{10}$), a gain drop:

$$R = -\frac{1}{G_0}\frac{dG}{dQ} \approx -0.1\%/(mC/cm)$$

has been observed after integrating approximately $0.32\,C/cm$ in the hottest region of the chamber, near the target, at a m.i.p. rate of $30\,kHz/cm^2$, corresponding to a 3 years exposure to a $7 \times 10^7 \mu/s$ beam. According to J. A. Kadyk's classification [**?**], this level

of aging is considered "moderate". However, it is worth noticing that a rate decrease of 30% can merely be compensated by roughly 5% increase in the applied high voltage.

5.4.8.2 Measured spatial resolution

5.4.8.3 Transverse momentum resolution

5.4.8.4 Angular resolutions

5.4.8.5 Momentum resolution

5.4.8.6 Particle identification

5.4.9 Simulation and Reconstruction

5.4.9.1 Simulation framework

5.4.9.2 Geometry description

5.4.9.3 Hit digitization

5.4.9.4 Vertex detector and pre-shower integration

5.4.9.5 Track finding and fitting

5.4.10 Predicted Performance

5.4.10.1 Beam related backgrounds

5.4.10.2 Cell occupancy from background and physics events

5.4.10.3 Discussion about geometry optimization based on occupancy

5.4.10.4 Efficiency with montecarlo truth and with track finding

5.4.10.5 Longitudinal and transverse impact parameter resolution

5.4.10.6 Momentum resolution

5.4.10.7 Angular resolutions

5.4.10.8 Particle identification

5.4.10.9 ZH events: Z and H invariant mass in dimuon

5.4.11 Conclusion

References

[1] CEPC-SPPC Study Group, *CEPC-SPPC Preliminary Conceptual Design Report. Volume I - Physics & Detector*, .

[2] Particle Data Group Collaboration, C. Patrignani et al., *Review of Particle Physics*, Chin. Phys. **C40** (2016) no. 10, 100001.

[3] J. E. Augustin et al., *A silicon envelope for the TPC*, .

[4] A. Affolder et al., *DC-DC converters with reduced mass for trackers at the HL-LHC*, JINST **6** (2011) C11035.

[5] S. Diez, *System Implications of the Different Powering Distributions for the ATLAS Upgrade Strips Tracker*, Phys.Procedia **37** (2012) 960–969.

[6] K. Klein et al., *DC-DC conversion powering schemes for the CMS tracker at Super-LHC*, JINST **5** (2010) C07009.

[7] A. Nomerotski et al., *Evaporative CO2 cooling using microchannels etched in silicon for the future LHCb vertex detector*, JINST **8** (2013) P04004, arXiv:1211.1176 [physics.ins-det].

[8] The ATLAS Collaboration, A. Affolder, *Silicon Strip Detectors for the ATLAS HL-LHC Upgrade*, Phys.Procedia **37** (2012) 915–922.

[9] V. Blobel, *Software alignment for tracking detectors*, Nucl.Instrum.Meth. **A566** (2006) 5–13.

[10] T. Abe et al., *The International Large Detector: Letter of Intent*, arXiv:1006.3396 [hep-ex].

[11] T. Behnke et al., *The International Linear Collider Technical Design Report - Volume 4: Detectors*, arXiv:1306.6329 [physics.ins-det].

[12] A. Savoy-Navarro, *Large Area Silicon Tracking: New Perspectives*, arXiv:1203.0736 [physics.ins-det].

[13] C. Adolphsen et al., *The International Linear Collider Technical Design Report - Volume 3. II: Accelerator Baseline Design* , 2013. arXiv:1306.6328 [physics.acc-ph].

[14] N. Calace and A. Salzburger, *ATLAS Tracking Detector Upgrade studies using the Fast Simulation Engine*, J. Phys.:Conf. Ser. **664** (2015) 072005.

[15] M. Regler et al., *The LiC Detector Toy program*, J. Phys.:Conf. Ser. **119** (2008) 032034.

[16] P. Mora de Freitas and H. Videau, *Detector simulation with Mokka/GEANT4: Present and future, LC-TOOL-2003-010, 623-627 (2002).*, (2002) .

[17] N. Graf and J. McCormick, *LCSIM: A detector response simulation toolkit*, in *2012 IEEE Nuclear Science Symposium and Medical Imaging Conference Record (NSS/MIC)*, p. 1016. Oct, 2012.

[18] S. V. Chekanov, *Public repository with Monte Carlo simulations for high-energy particle collision experiments*, PoS **ICHEP2016** (2016) 229, arXiv:1609.04455 [hep-ex].

[19] S. V. Chekanov, M. Beydler, A. V. Kotwal, L. Gray, S. Sen, N. V. Tran, S. S. Yu, and J. Zuzelski, *Initial performance studies of a general-purpose detector for multi-TeV physics at a 100 TeV pp collider*, JINST **12** (2017) no. 06, P06009, arXiv:1612.07291 [hep-ex].

[20] N. Graf and J. McCormick, *Simulator for the linear collider (SLIC): A tool for ILC detector simulations*, AIP Conf. Proc. **867** (2006) 503–512.

[21] J. Allison et al., *Recent developments in Geant4*, Nuclear Instruments and Methods in Physics Research A **835** (2016) 186.

[22] M. J. Charles, *PFA Performance for SiD*, in *Linear colliders. Proceedings, International Linear Collider Workshop, LCWS08, and International Linear Collider Meeting, ILC08, Chicago, USA, Novermber 16-20, 2008* . 2009. arXiv:0901.4670 [physics.data-an].

[23] J. S. Marshall and M. A. Thomson, *Pandora Particle Flow Algorithm*, in *Proceedings, International Conference on Calorimetry for the High Energy Frontier (CHEF 2013)*, pp. 305–315. 2013. arXiv:1308.4537 [physics.ins-det].

[24] S. V. Chekanov and M. Demarteau, *Conceptual Design Studies for a CEPC Detector*, Int. J. Mod. Phys. **A31** (2016) no. 33, 1644021, arXiv:1604.01994 [physics.ins-det].

[25] S. L. Glashow, *Partial Symmetries of Weak Interactions*, Nucl. Phys. **22** (1961) 579–588.

[26] S. Weinberg, *A Model of Leptons*, Phys. Rev. Lett. **19** (1967) 1264–1266.

CHAPTER 6

CALORIMETRY

6.1 Introduction to calorimeters

Calorimeters of the CEPC detector, including electromagnetic calorimeter (ECAL) and hadron calorimeter (HCAL), are employed for precise energy measurements of electron, photon, tau and hadronic jets. To fully exploit the physics potential about Higgs, W, Z and related SM processes, the jet energy resolution σ_E/E is required to reach 3%-4%, or $30\%/\sqrt{E}$ at energies below about 100 GeV. This resolution is about a factor of two smaller than the calorimeters used for the LEP detectors and currently operating calorimeters at the LHC. It significantly improves the separation of the W and Z bosons which decay into two jets, as shown in Figure 6.1. The basic requirements for ECAL and HCAL resolution are $16\%/\sqrt{E}$ and $50\%/\sqrt{E}$, respectively.

To achieve the required jet energy resolution, many R&D researches are carried out within the CALICE collaboration since 2000 [1]. The majority of these studies aim to develop extremely fine granularity and compact imaging calorimeters with several technology options shown in Figure 6.2. Imaging calorimeter is a rapidly developing novel particle detector which has excellent spatial resolution. It is capable to provide enormous position information of incident and showering particles, which makes it possible to reconstruct every single particle cluster. This is vital for Particle Flow Algorithm (PFA [2]) and help to significantly improve the energy resolution of hadrons. The basic idea of PFA is to distinguish charged (∼65%) and neutral particles (∼35%) inside the calorimeters. Charged particles measured in the inner tracker with high momentum resolution are matched to their energy depositions in the calorimeters. Energy depositions without matched inner tracks are considered to originate from neutral particles inside jets, among

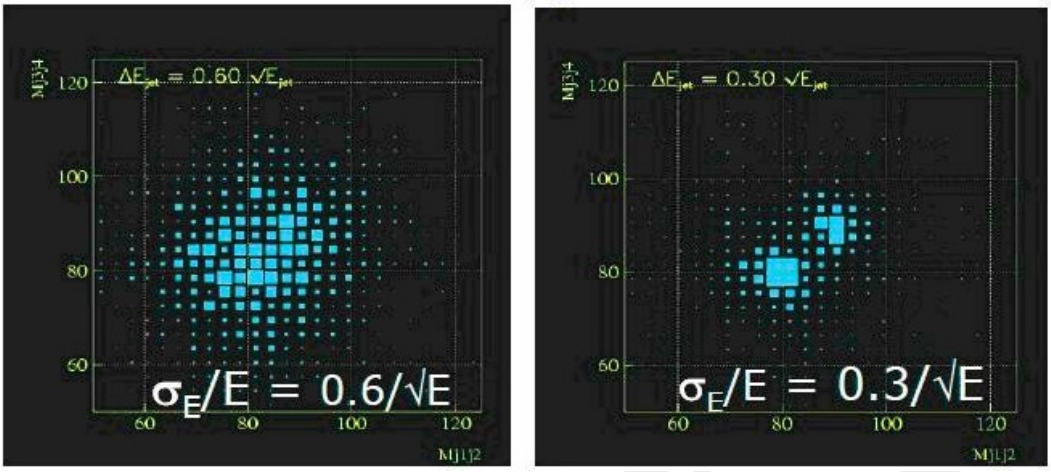

Figure 6.1: Separation of W and Z bosons with different jet energy resolutions.

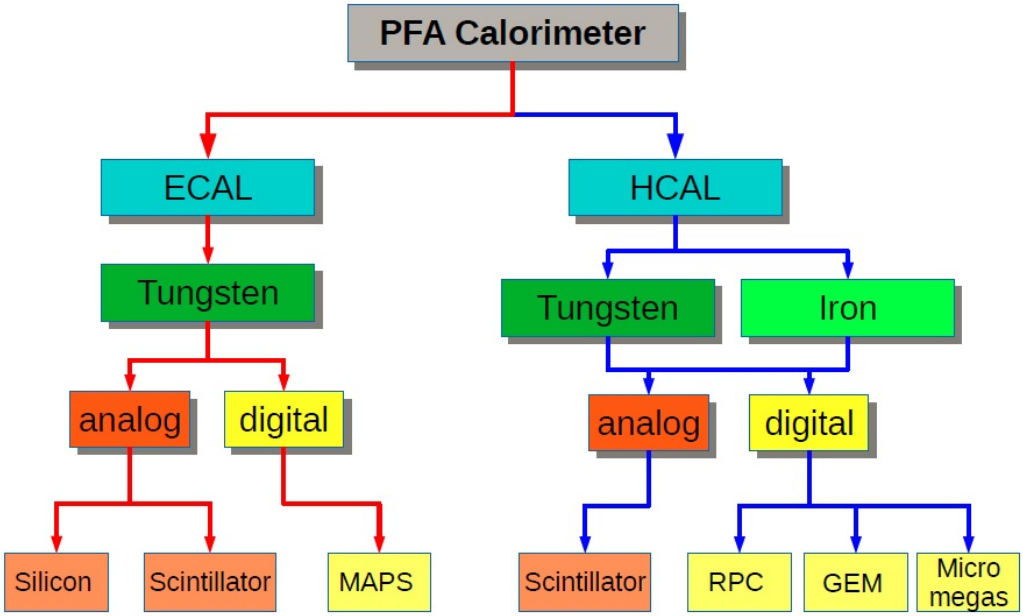

Figure 6.2: PFA: Imaging calorimeters being developed by the CALICE collaboration since 2000.

these neutral particles, about 25% of energy from photons are measured in the ECAL with good energy resolution, while the residual energy of merely 10% from neutral hadrons are measured by the calorimeters with poor energy resolution. Hence, the jet energy is determined by the charged track momenta of charged particles from inner tracker and energy depositions of neutral particles in the calorimeters. It has been demonstrated that significant improvement of the jet energy resolution is achievable based on MC simulations and test beam measurements. However, more efforts are needed to optimize the calorimeter design, to improve the PFA, and to develop the technologies for high granularity imaging calorimeters.

The calorimeter system includes two sub-detectors, an electromagnetic calorimeter (ECAL) which is optimized for the measurement of photons and electrons, and a hadronic

calorimeter (HCAL) which is employed to measure the energy deposit of the hadronic showers caused by the hadronic particles when they are absorbed in the HCAL detector. The two sub-detectors will be installed within the solenoid to minimize the inactive material in front of the calorimeters and to reliably associate tracks to energy deposits. The calorimeter system is divided into three parts, one cylindrical barrel and two end-caps.

The ECAL consists of layers of active sensors (such as silicon pads or pixels, or scintillator detector) interleaved with absorber tungsten plates. The digital HCAL (DHCAL) is expected to have stainless steel absorber plates with gaseous detectors such as glass Resistive Plate Chambers (gRPC) or GEM, or analog HCAL (AHCAL) using scintillator with SiPM readout as sensor. Both ECAL and HCAL are sampling detectors with very fine granularity and segmentations of electronic readout which is driven by excellent separations requirement between charged and neutral particles for the particle flow algorithms.

From Figure 6.2, there are more detector options with enormous worldwide R&D efforts ongoing within the CALICE collaboration. Another approach for high performance calorimeters is dual-readout calorimetry.

However, for this particular CDR, we have to be selective and focus on a few options with collaborators who expressed great interests so far. The CEPC detectors R&D is widely open for international collaboration with different detector options and new ideas.

6.2 Electromagnetic Calorimeter for Particle Flow Approach

The particle flow paradigm has tremendous impact on the design of the electromagnetic calorimeter detector. Separating overlap showers from each other is principal requirement of the detector. A calorimeter used for particle flow thus needs to be able to do pattern recognition in the shower. The electromagnetic section has lots of tasks to fulfill. It should be able to select photons from close-by particles. It should be able to reconstruct the detailed properties of the shower, such as shower shape, starting point and energy distribution. It should be able to distinguish early starting electromagnetic showers from hadronic ones. The imaging capabilities of the calorimeter are more important than the intrinsic single particle energy resolution, although the latter is still important to the particle flow performance for electron, photons and jets. Due to the reason that about half of the hadronic showers will start development inside the electromagnetic calorimeter, a calorimeter with excellent three dimensional granularity is of utmost importance. In order to have the ability of separate close-by showers in the calorimeter, the detector with small Moliere radius is required. A large ratio between interaction length and radiation length of the detector is advantageous to the separation between electromagnetic and hadronic showers. A small radiation length will make the start of the electromagnetic shower earlier in the calorimeter, while a large interaction length will reduce the fraction of hadronic showers starting in the calorimeter. At the same time, the calorimeter with a compact structure is favorable.

In this section, we focus on two detector options for the ECAL, which consist of layers of active sensors (silicon pads or pixels, or scintillator detector) interleaved with absorber tungsten plates.

6.2.1 Silicon-Tungsten Sandwich Electromagnetic Calorimeter

6.2.1.1 Introduction

The study of the Higgs is not the only goal of a machine at 250 centre-of-mass energy. It can be generalised to the multi boson physics (Z, W and H). The best way to use the excellent luminosity foreseen at CEPC, consist to tag the boson through their mass in their decays into $q\bar{q}$ (2 jets). Taking into account the natural width of the Z and W, it has been shown that this goal required to achieve a jet energy resolution of $30\%/\sqrt{E_{\mathrm{Jet}}}$, thus a factor two better than the energy resolution achieved for a typical detector at LEP.

It has been shown [3] that a method consisting to fully reconstruct every single particle could reach this goal (Particle Flow Algorithm); it requires both a high performance tracker, typically achieving $\delta p/p$ of $10^5 p/GeV$ associated with high granularity calorimeters able to separate the contribution from individual particles down to the MIP level. As a typical jet is contains fractions in energy of 65%, 25% and 10% of charged particles, photons and neutral hadrons respectively, a moderate calorimetric resolution is then sufficient to achieve the goal. In this framework, the electromagnetic calorimeter (ECal), is first devoted to measure photon(s) and to a lesser extent electron(s) and to make a full pattern of the deposited energy of the hadron, i.e. shower of hadron interacting in the ECAL. To avoid "blind region", the entire calorimeter has to be put inside the super-conductive solenoid. The compactness is therefore an important criterion.

The design of the calorimeters have to take the following guidelines into account [4]:

- Optimisation of the number of calorimeter cells (cell size and number of layers)
- Choice of the absorber material in order to insure a high level of compactness and the infra-structural components such as cooling, power supplies, readout cables and the very front end electronics.

For the electromagnetic calorimeter these criteria has led to the choice of Tungsten with a radiation length of Xo=3.5mm, a Moli?re radius of RM=9mm and an interaction length of $\lambda_{\mathrm{I}} = 96mm$.

6.2.1.2 Silicon sensors

Among several sensor techniques, high resistivity silicon pin diodes offer several unique intrinsic advantages:

- stability: under a reasonable bias voltage, completely depleted pin-diode have a gain of one, and a signal response to MIP mostly defined by the thickness of the sensor, with a very low dependence on temperature, radiation, humidity, ...
- uniformity: for the same reason, the control of the thickness over large batches (typically to less than a percent) ensures a uniformity of response within a wafer and between them. The nonsensitive area between wafers has recently been reduced by the use of laser cutting, thinned guard-ring design [5], and would benefit from the use of larger ingot size (8" becoming the standard).
- flexibility: the dimension and geometry of the cells are defined by the readout pad on the PCB.

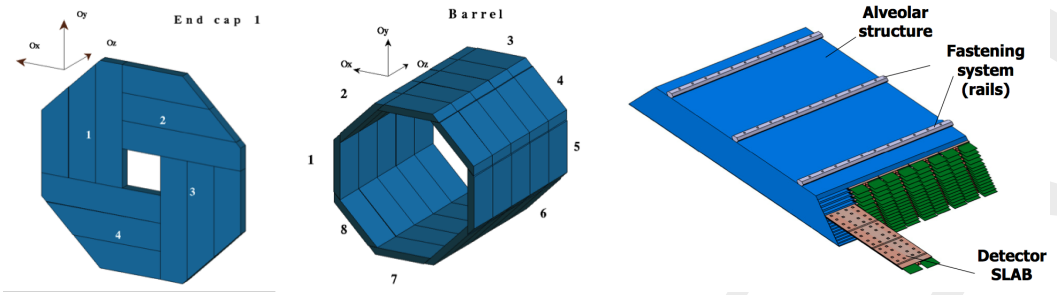

Figure 6.3: Left: Geometry of the SiW-ECAL Endcaps. Middle: Barrel Right: Geometry of the barrel modules.

- High Signal-to-Noise ratio: with $\simeq$ 80 electron-hole pairs created by linear mm of MIP track, MIPs tracks can easily be traced in the calorimeters, which is critical for the god performance of

The only real drawback of Silicon sensors remaining is their price, to be expected around $2 - 3\$/cm^2$.

By associating of Silicon sensors with Tungsten absorbers and Carbon Fibre structures, the SiW-ECAL offers an excellent option for PFA optimised calorimetry.

6.2.1.3 Constraints

High granularity calorimetry, and ECal especially, is technically challenging: the very number of channels calls for an embedded readout and zero suppression, to limits the amount of connections; in turn embedded readout power consumption should be as limited as possible to avoid large cooling systems which would degrade the capacity of the calorimeter. In the best case the cooling should stay passive at the heart of the calorimeters.

The design proposed for the CEPC SiW-ECal is very largely inspired by the one of the ILD detector for ILC as described in the Detector baseline Document [6]; it is influenced by the options studied for the CMS High-Luminosity upgrade endcap replacement HGCAL [7, 8], concerning cooling and electronics. In terms of luminosity and collision rates, the CEPC lies between the 2 options.

6.2.1.4 Mechanics & design

The geometry presented here reflects the current (october 2017) status on the realistic models developed for ILD. It differs slightly form the CEPC_v1 and CEPC_v4 models [9], mainly on ECAL thickness ($223mm$ vs $185mm$), and inner radius of the endcaps (226.8 and $245mm$ vs $400mm$).

6.2.1.5 Geometry

The geometry of the detector is based on ILD detector, where there is no blind zone between modules, but only "special zone", where it has been shown that performance of the reconstruction of jets or photon(s) is not downgraded significantly [10].
The figure below shows this octagonal geometry and the possible way to build the detector:

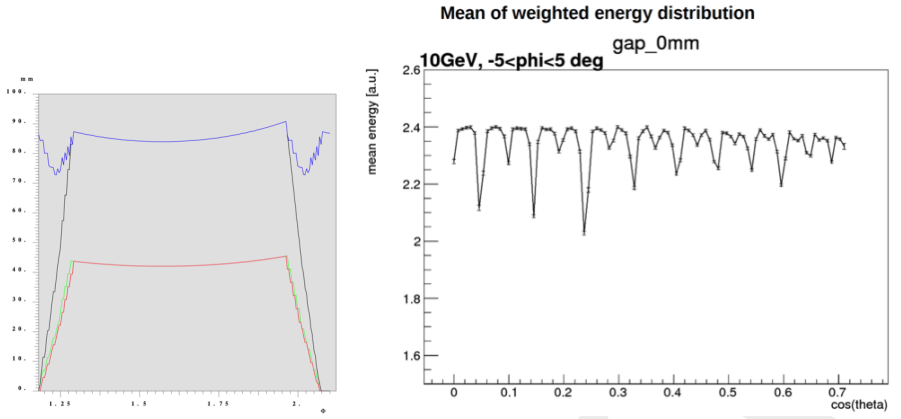

Figure 6.4: Left: Thickness of Tungsten seen as function of the polar azimuthal angle scan of one octant of the barrel. Right: Mean Theta angle scan

ECal thickness For a baseline design featuring 30 layers – split in 2 sections of 20 and 10 layers, holding each an equal amount of $12Xo$ of W – $525microns$ thick wafers, and a base plate of $20mm$ of carbon, the ECal thickness is estimated at $223mm$.

For a reduced number of layers, at 22 (with section of 14 and 8), but thicker wafers ($725microns$), the thickness becomes $191mm$.

ECal dimensions The Barrel consist of 8 staves of 5 trapezoidal modules. Each barrel module contains 5 columns of alveoli. The number of modules and alveoli is even in order to avoid any special region at the azimuthal angle $theta = 0$. The alveolus size is fixed to $186mm$ by mechanical limits and by cost optimisation considerations, to contain exactly two 6-inch wafers or one-and-a-half 8-inch wafer. Integrating the alveolus size, walls of modules and contingencies, the barrel length amount to $4700mm$. ($4900mm$ in CEPC simulations). A gap of typically $70mm$ ($100mm$ in simulation) is left between the barrel sides and end-cap front parts, whose precise dimension will depend on the amount of ancillaries needed to service the ECAL and trackers (power and DAQ cables, cooling pipes, patch panels).

The end-caps are made of quadrants of 2 modules of 4 and 3 alveoli columns. Their inner radius is fixed by the ECal ring at $400mm$. With 7 alveoli columns, the end-cap outer radius is $1755mm$. An overshoot of $32mm$ is left between the outer radius of the barrel and of the end-caps, in order to contain the EM shower impinging the region of overlap. see figure 6.4. This fixes the inner radius size of the ECal barrel at $1498mm$ or $1530mm$.

For such a geometry, summing the barrel (200) and end-caps (56), 256 alveoli columns are needed. For 22 (resp. 30) layers, and this yields 5632 (7680) alveoli, and as many detector slabs.

Slab geometry In each alveola of the modules, a slab is inserted. Slabs contains 2 symmetric layers of Silicon sensors glued on PCB, equipped with readout ASICs, high voltage distribution by a Capton foil and copper layers for passive cooling. The elements are chained on both sides of a Carbon fibre cradle taking the shape of an H, with a core of Tungsten, and shielded by an aluminium cover. This so-called H-Structure is illustrated below.

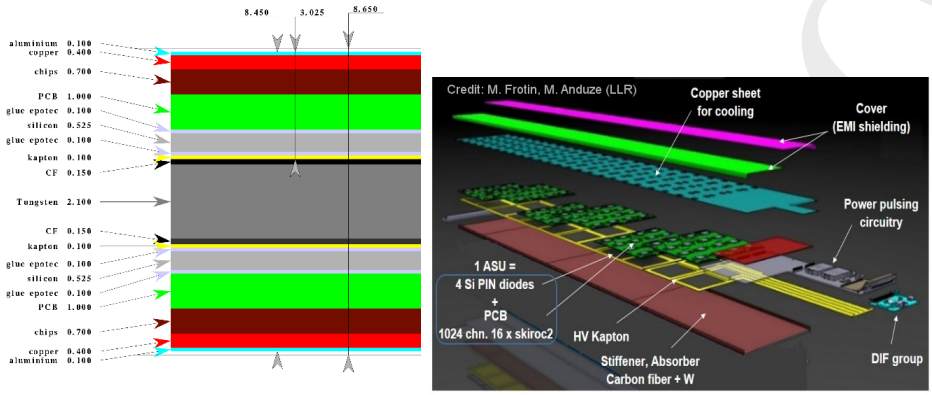

Figure 6.5: Left: Transverse cut through of a thin layer of the SLAB. Right: Exploded view of the top layer of a slab of the SiW-ECAL. The same structure is mirrored below the slab.

To insure scalability and industrial production, the design has been made as modular as possible: the basic unit is the ASU (Assembly Single Unit), made of a $18x18mm^2$ PCB onto which 4 wafers of $90x90mm^2$ wafers are glued. Each ASU would handle 256 cells with 4 ASICs, for cell surfaces of $11.25x11.25mm^2$.

The ASUs are chained together for the clock and configuration distribution and data collection. For a radius of $1498mm$ the longest (shortest) barrel slabs measure $1146mm$ ($955mm$).

6.2.1.6 Electronics

One of the most critical element of the CEPC calorimeters is the readout electronics which is defined by the dynamic range, the effective digitisation, mode of trigger, the rate of working and power consumption per channel.

Dynamic range: A MIP going through a $725microns$ diode would produce $\simeq 60000$ electron-pairs holes or a charge of $9.6fC$ as the most probable value (MPV). To record MIPs with an efficiency higher than 95% this ports the low-end of the dynamic range to a 1/3 of the MPV. The high-end is determined by the number of MIP equivalent at the core of the high-energy EM showers, which can reach up-to 10000 MPV or $96pC$ for $11x11mm^2$ cells.

Timing: Time measurement of deposits in the calorimeters can be useful to Particle Flow algorithms to help disambiguate particle contributions. For the CMS HGCAL it is planned to distinguish particle stemming from different interactions [7], by achieving a timing of $50 - 20ps$ on EM showers. For e^+e^- colliders, with a single primary vertex, precision timing of individual cells – or group of cells – could still be useful to reduced the confusion and improve the resolution. The required precision is uncertain and should be studied further. Recent version of the SKYROC2a ASIC, could be operated [11] on test board with a measure of time close to 1.4ns. The performance has to be measured in an integrated design.

Rates: The running conditions a circular collider preclude any pulsed operation as is planned for the linear ones, where clocks, pre-amps, digital conversion are powered sequentially at a few Hz. A partial in-time shut-off or local on-demand switch-on of the ADC and TDC parts can be envisaged, leaving the pre-amp as the single major power

consumer. As a point of reference, the current power consumption for SKIROC2 chips designed for the SiW-ECAL of ILD is of $5mW$ per channel in continuous mode.

Occupancy: The occupancy of the calorimeters should be very low. This pushes in the the direction of designing pre-amps with a very small consumption when there is no signal.

6.2.1.7 Power & Cooling

To the first order, the amount of power dissipates scales with the number of electronics channels. One important issue is to decide on the power scheme:

- a reduced number of channels using only passive cooling at the heart of the detector, such as planned at the ILD; a $400microns$-thick copper sheet will drain the heat to the end of the slab, where it is removed by a cooling system.
- keep a high granularity but include CO_2 cooling in the absorbers such as envisaged for the HGCAL.

The CEPC ECAL is at edge of both options, with a limit for the purely passive option of the order of $2x2cm^2$ cells for a increase of temperature limited to $\Delta T \sim 10°C$ at the remote-end of the slab.

Water cooling Current plans for the ILD SiW-ECAL is to use a leak-less water cooling system to extract the heat at the end of each slab from the copper. Details of implementation can be found in [12**?**].

CO_2 cooling HGCAL is preparing a biphasic CO_2 cooling system, with pipes circulating inside the absorber planes, made of an alloy of Tungsten and Copper.

A similar system adapted to the SiW-ECAL has been simulated [13]. The ILD $400microns$ passive colling are replaced by plates of $3mm$ of Copper, equipped with $1.6mm$ inner-diameter pipes for CO_2 circulation, glued on the ASICs, on both side of the slab. Assuming a fully transversally isolated system, with ASICs a sole heat source at equilibrium dissipating $0.64W$ ($10mW$ per channel times 64 channels), and a fixed working point of $20°C$ for CO_2 (i.e assuming perfect heat absorption), a doubled sided module of $252x252mm^2$ holding 32 chips cooled by $2x2$ pipes was simulated.

Very preliminary simulations in "ideal conditions" show a difference of $\Delta T \sim 2°C$ mostly centered on ASIC's ($0.3°C$ in the exchanger itself only).

6.2.1.8 Status of R&D

The performances of a Silicon-Tungsten ECAL have beed explored using the "physical prototype" of the CALICE collaboration, on numerous beam tests during the years 2005-2011 [14–16].

Some ASU, similar to the one foreseen for the ILD detector have been operated in two beam test campaigns: first at CERN in 2015, where 3 ASU mounted on test boards behaved as expected [17]; a signal to noise ratio (SNR) - defined as the Most Probable Value of a Landau fit on data, divided by the Gaussian width of the noise – reached typical values of 15-18, with a very limited number of masked channels.

More recently a campaign at DESY using 1-5 GeV electrons, punching through "short slabs", featuring all the elements of the slabs described in section 6.2.1.5 but limited to a

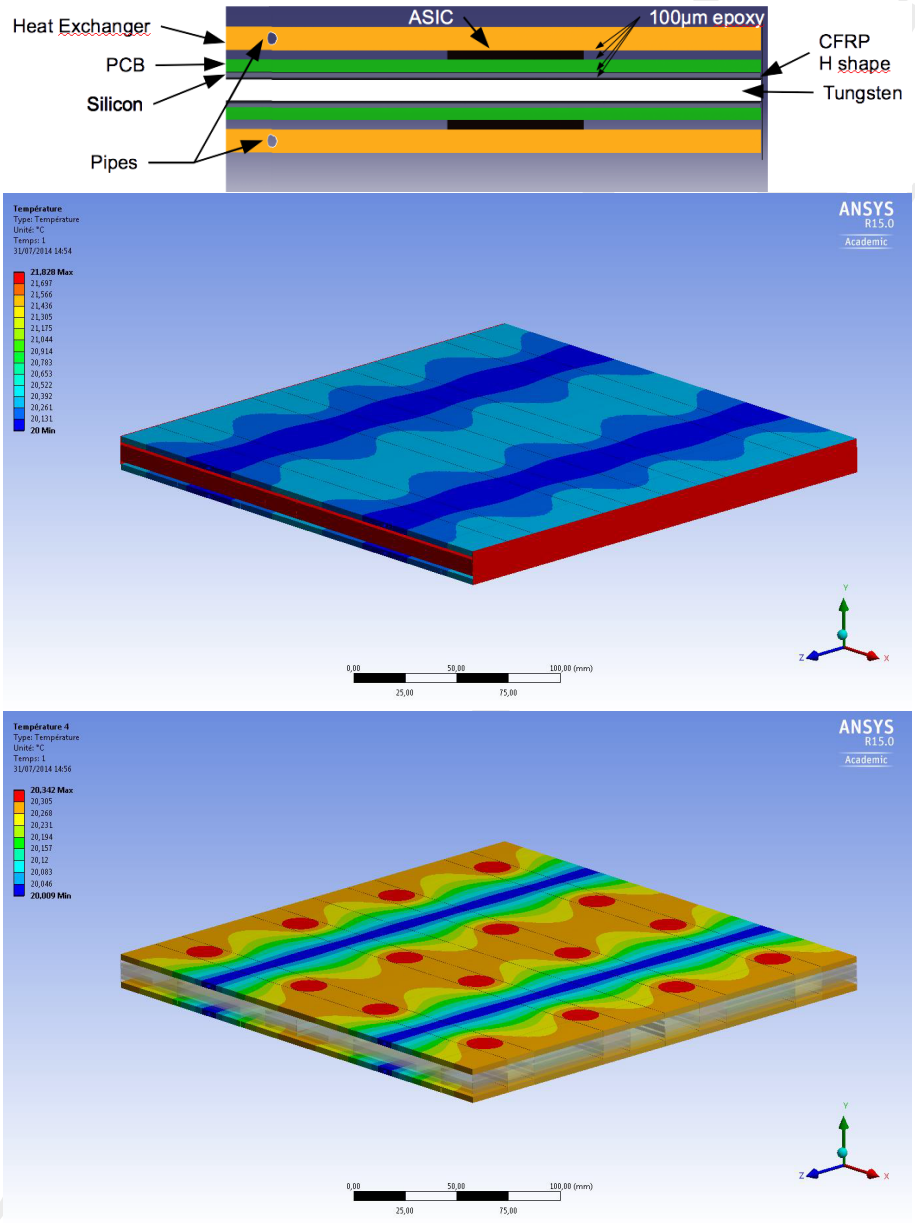

Figure 6.6: Top: Transverse section of slab equipped with CO_2 cooling pipes embedded in the cooling plates Left: Heat map over the full module. Right: heat map in the heat exchanger

single ASU on a single side, could reach a SNR of $\simeq 20$ in average [18].

The collected data is still under analysis for estimated calorimetric performances, but they are expected to be similar to the physics prototype.

The building of a "long slabs" is being actively pursued, and should be completed toward the end of year 2019; the R&D involves all the power, cooling and FE issues for an ILD near the ILC.

The results and design will have to be adapted for a circular collider, where operation *a priori* forbid power-pulsed operations.

6.2.2 Scintillator-Tungsten Sandwich Electromagnetic Calorimeter

6.2.2.1 Introduction

Alternatively, a sampling calorimeter with scintillator-tungsten structure is proposed. It can be built in a compact and cost effective way. The structure of the ScW ECAL is similar to the SiW ECAL. The major geometry parameters of the ScW ECAL are also studied and optimized, with the similar results of the SiW ECAL. The active layers of the ScW ECAL are consisting of $5\times45\text{mm}^2$ scintillator strips. The scintillator strips in adjacent layers are perpendicular to each other to achieve a $5\times5\text{mm}^2$ effective transverse readout cell size. Each strip is covered by a reflector film to increase collection efficiency and improve uniformity of the scintillation light. Photons from each scintillator strip are read out by a very compact photo-sensor, SiPM, attached at the end of the strip. The SiPM and highly integrated readout electronics make the dead area in the ScW ECAL almost negligible.

Plastic scintillator is a robust material which has been used in many high energy physics experiments. Production of the scintillator strips can be performed at low cost by the extrusion method. Moreover, the number of readout channels can also be significantly reduced due to the strip structure. So the total construction cost of the ScW ECAL is lower than the SiW ECAL. Some key issues which might affect the performance of the ScW ECAL were studied and optimized.

6.2.2.2 SiPM dynamic range study

Because each pixel on a SiPM can only detect one photon at once and a few nanoseconds are needed before recovery, the SiPM is not a linear photon detection device, especially in the case of high intensity light input. The application of the SiPM in the CEPC ScW ECAL is a challenge to its dynamic range, which need to be studied.

For a short time light pulse, the response of the SiPM can be theoretically calculated as

$$N_{fired} = N_{pixel}(1 - e^{-N_{pe}/N_{pixel}}) \tag{6.1}$$

However, for the ScW ECAL, the width of the light pulse should not be ignored, and some pixels of the SiPM can detect more than one photon in an event. The response of the SiPM should be modified as

$$N_{fired} = N_{eff}(1 - e^{-N_{pe}/N_{eff}}) \tag{6.2}$$

The N_{eff} stands for the effective number of pixels on a SiPM, which is relative to the width of the input light pulse. Response curve of 10000 pixel (10μm pitch size)and 1600 pixel (25μm pitch size) SiPM with different duration light have been tested. As shown in

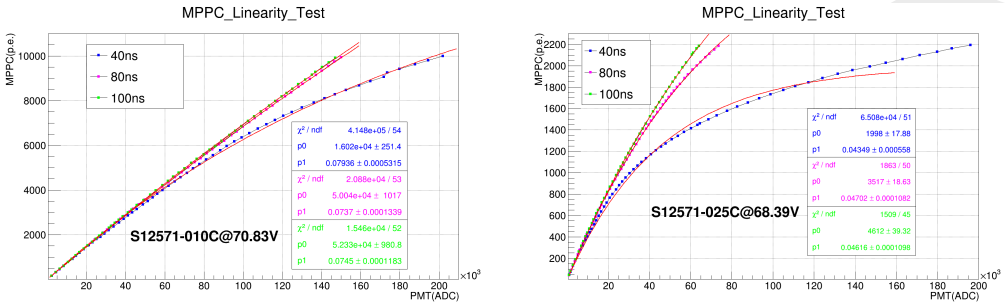

Figure 6.7: The response curve of 10000-pixel(left) and 1600-pixel(right) SiPM with different duration light.

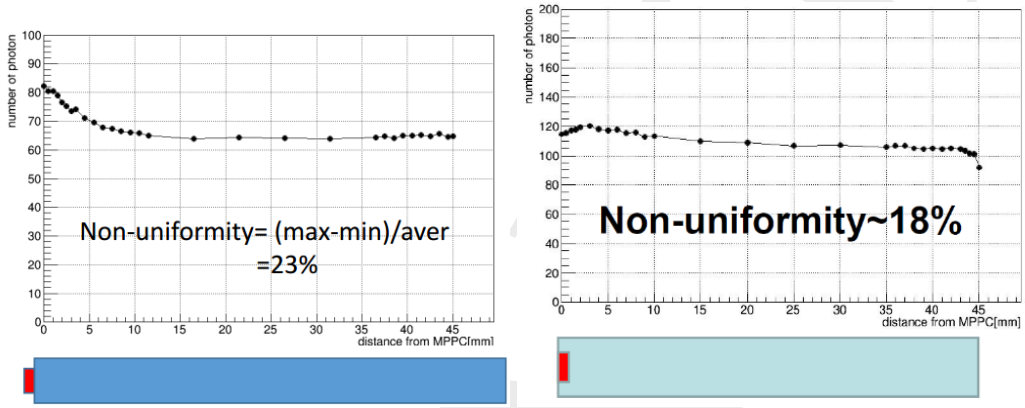

Figure 6.8: Scintillator module test results, with the SiPM coupled on the surface (left) or embedded into the strip(right).

Figure 6.7, the output linearity of the device is improved by the increase in the incident light width.

6.2.2.3 Scintillator strip test

Because the SiPM is coupled at one end of the scintillator strip, the light output will be non-homogeneous along the length of the scintillator, which will affect the performance of the ScW ECAL. By moving a Sr^{90} source along the length of the scintillator, we test the light pulses height read out by the SiPM to study the non-uniformity of the scintillator detector. Figure 6.8(left) is a typical test result of a scintillator module whose light output non-uniformity is 23%. The uniformity can be improved by optimizing the reflection material or the coupling methods of the SiPM to the scintillator strip. Figure 6.8(right) shows a result of a scintillator module with the SiPM embedded into the scintillator strip, and Figure 6.9 is the light output of another scintillator module with different reflector. Scintillators with ESR reflector can give much more light output. We have also test the light output of the scintillator coupled with the SiPM with different pitch size. Two kinds of SiPM have same sensitive area (1mm$\times$1mm), but have pitch size of 25μm and 10μm respectively. The light output of the scintillator with 25μm pitch SiPM is only about 1/3 of the scintillator with 10μm pitch SiPM, shown in Figure 6.10.

6.2.2.4 Beam test of a mini prototype

To study the layout, the coupling mode of the scintillator and the SiPM, and further test the minimum ionization particles (MIP). A mini prototype was constructed and tested by test

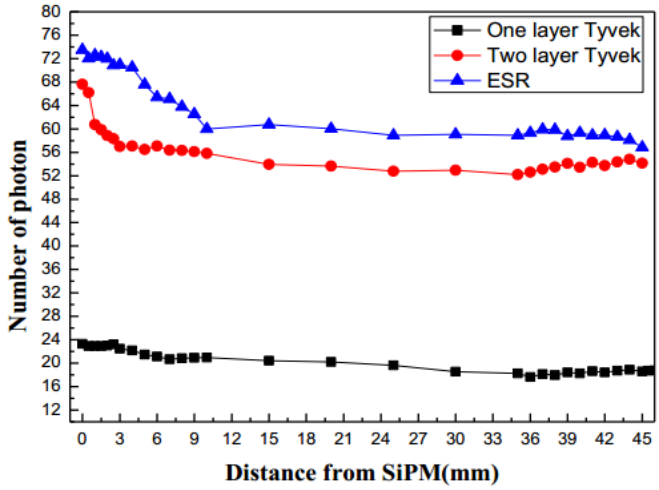

Figure 6.9: light output of scintillator with different reflector.

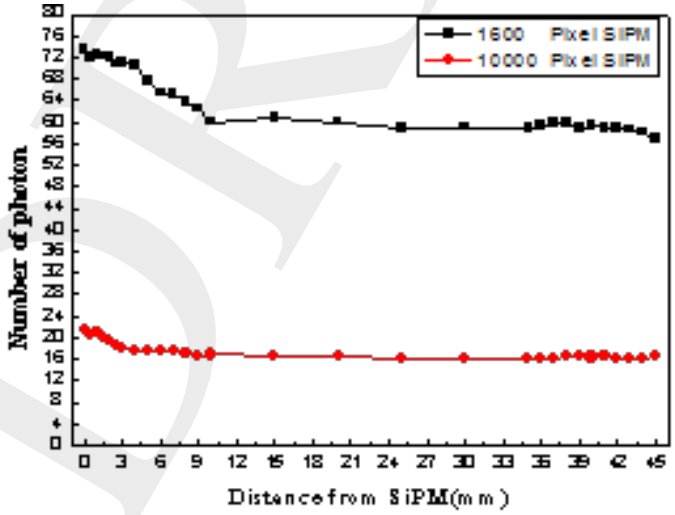

Figure 6.10: light output of the scintillator with different SiPM.

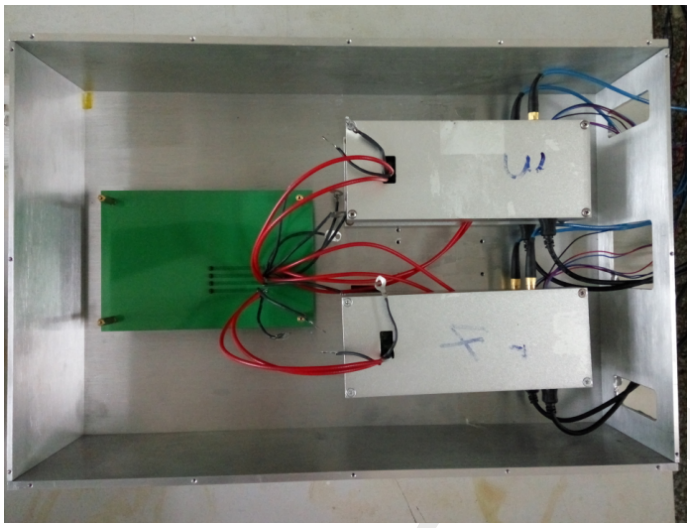

Figure 6.11: the picture of the prototype.

beam. The test was carried out at the E3 beam at the IHEP, which could provide proton and pion mixed irradiation. The momentum of the particles was adjusted from 400MeV to 1.1GeV in the test.

The prototype includes four scintillator modules attached tightly to each other, as shown in Figure 6.11. Each module is composed of a BC408 scintillator with a dimension of 45mm×5mm×2mm, and a Hamamatsu S12571-025P SiPM coupled at the end of the scintillator as a photoelectric conversion device. The prototype is put into an aluminum box for electro-magnetic and light shielding. Figure 6.12 shows the detector layout in the test beam and the schematic of the readout. The beams first pass through two time of flight detectors (TOF) with the distance of 3m for particle identification, and then go through two scintillator counters with the same dimension of total of the four scintillator modules used to estimate the efficiency of the prototype. The prototype is located between the two scintillator counters. The signals from the TOFs and the scintillator counters are directly sent to a wave sampling digitizer (CAEN DT5751). The SiPM from each modules of the prototype is connected to a Hamamatsu driver board (C12332-01), which not only amplifies the signals from the SiPM, but also can eliminate the gain changes of the SiPM caused by the fluctuation of the temperature during the test thanks to its temperature compensation circuit. The signals from the four driver boards are sent to another CAEN DT5751 module to be digitized.

Figure 6.13 are the energy spectrums of pions and protons with momentum of 400MeV/c, 700MeV/c and 1000MeV/c respectively after the system calibration, which indicate the energy deposition in a module. The dE/dx as a function of the momentum of the particles can be got from the energy spectrums of the module, as shown in Figure 6.14. The values of dE/dx of protons and pions are consistent with the expected ones with respect to the momentum of the particles. Based on the dE/dx of pions, we can know the signal of the MIPs from the scintillator module is about 50 photoelectrons.

6.2.2.5 Implementation Example for the Analog Calorimeter Readout

The readout electronics of the ECAL has to provide high dynamic range of energy, while showers of particle may deposit 1∼800 MIPs energy in single cell for 100GeV photon.

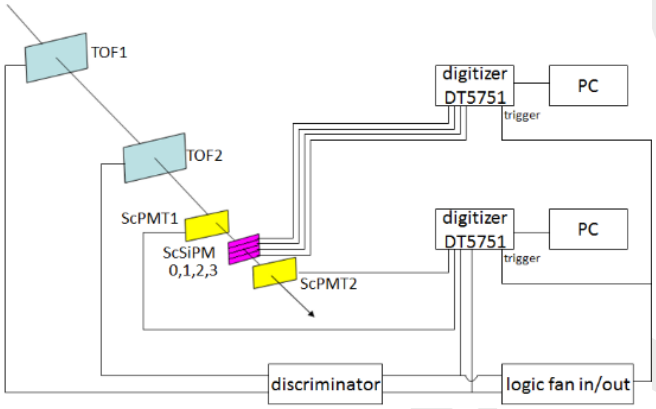

Figure 6.12: the schematic of the readout of the prototype.

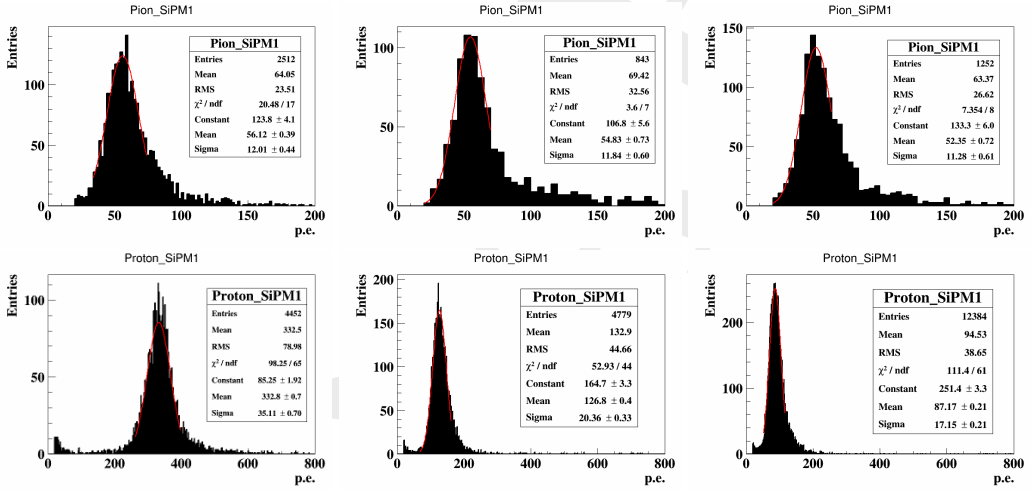

Figure 6.13: the energy spectrums of pions and protons with momentum of 400MeV/c, 700MeV/c and 1000MeV/c.

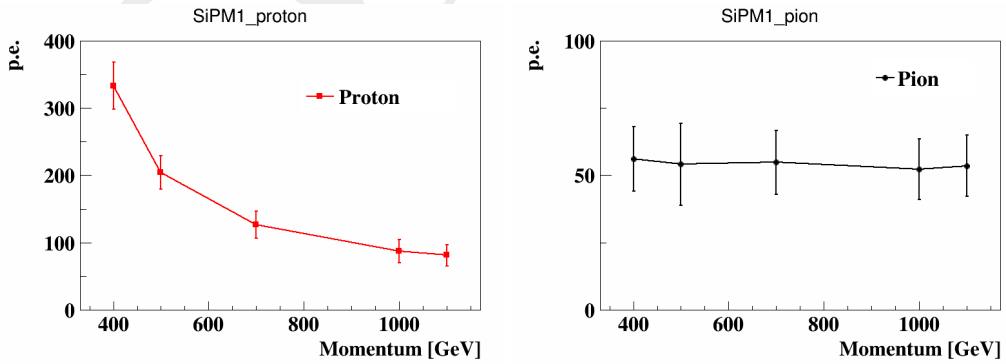

Figure 6.14: dE/dx of protons and pions change with the momentum.

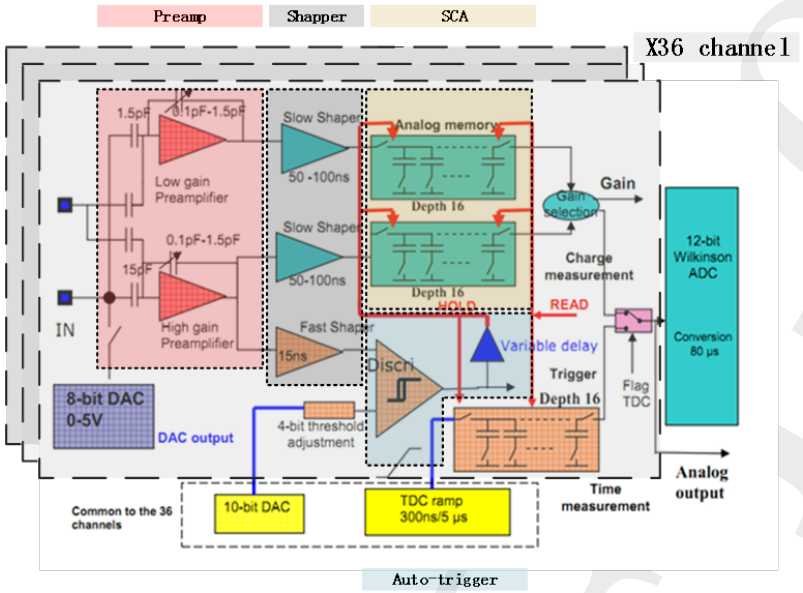

Figure 6.15: Schematic view of proposed readout ASIC.

As Particle Flow Algorithm (PFA) is being considered, high granularity requirement need be meet. Granularity of cells in ECAL need be finer than 10mm therefore a large amount of channels need be readout. So multiple-channels-readout-chip is considered.

Electronics consists of two parts: Front-End and Back-End. The Front-End-Electronics (FEE) is embedded into the layers of ECAL. It performs amplification, auto-triggering, digitization and zero-suppression, with local storage of data between the working phases. The Back-End-Electronics play the role of collecting data and configuring chip before system running.

Several studies and existing calorimeter readout electronics have shown that one can obtain optimized energy resolutions using a preamplifier-shaper and digitizing the pulse at peak. For instance, a preamp-shaper-SCA structure of analog circuit applied on ILC HCAL which implemented in ASIC. A similar approach can be applied at CEPC-ECAL. An ASIC named SPIROC2b is considered in present stage. The analog part is schematically depicted in Figure 6.15.

The basic principle consists of a readout chain with an amplifier-shaper using a RCn-CRp filter delivering a pulse length of about 50-200ns duration for a SiPM pulse signal. This signal is also shaped by a fast shaper in the same time to generate fast and narrow pulse for discriminating. Then the discriminator gives the trigger to Switched-Capacitor-Array (SCA) for locking the peak value of slow-shaped signal. The locked voltage value is corresponding to the charge that circuit received. A 12bits Wilkinson ADC is used for digitizing analog voltage in SCA. Future detailed implementations of the calorimeter front-end electronics for CEPC is still considered using ROC series ASIC but newer version.

The maximum data rate can be estimated as follows. Assuming signal keep coming consistently, SPIROC2b will be continuously switched between three states called Acquisition, AD Converting and Readout. Only in Acquisition state can SPIROC2b receive signal from SiPM and stored in SCA in the rate of about 5MHz. Another two states should be seen as âĂIJdead-timeâĂİ status. There is 16 depth in SCA, so 4us for Acquisition,

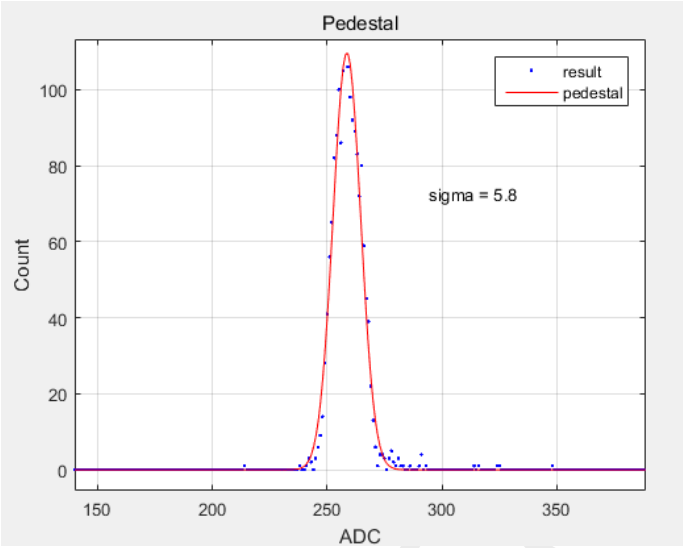

Figure 6.16: Pedestal noise.

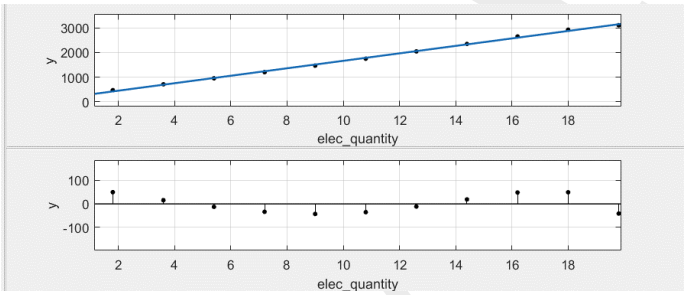

Figure 6.17: High gain calibration.

according to measurement, ∼4ms for ADC & Readout. So data rate is 16 events per 4ms which equals to 4 kHz. Each fulfilled data packaged is 2 Kbytes in size.

More chip in one layer will multiply the duration of Readout. Assuming that there are 4 chips in one layer. So there is 16ms for Readout. Maximum events rate is reduced to 1kHz and leads to about a transmission of 5Mbyte/s. This can easily be managed with 100M links.

The power consumption in the front-end will be dominated by ASIC and more specifically by analog part of ASIC. Opening all modules, one SPIROC2b is consuming 250.8mW of which about 150mW is consumed by analog part. In actual use, most of cycle is ADC and Readout. It leads to about 150mW power consumption per chip and 4mW per channels.

The electronic calibration and cosmic ray test have been done. From these electronic calibration Figure 6.16 - Figure 6.18, we can see that the noise of readout system is 46fC in RMS and high gain and low gain is 151/pC and 10.3/pC while maximum ADC range is 4096. So dynamic range that from 100fC-300pC of readout system is measured by electronic method. Cosmic ray results shows that the system can distinct MIPs signal from pedestal well and figure out that about 1pC.

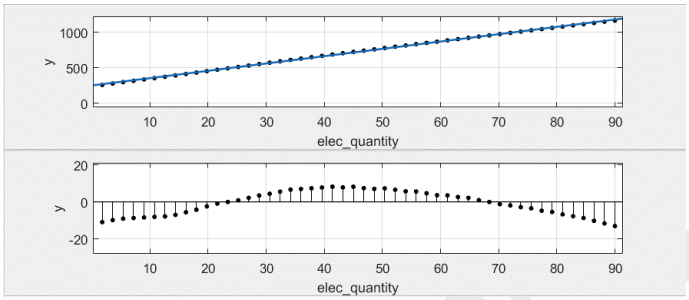

Figure 6.18: Low gain calibration.

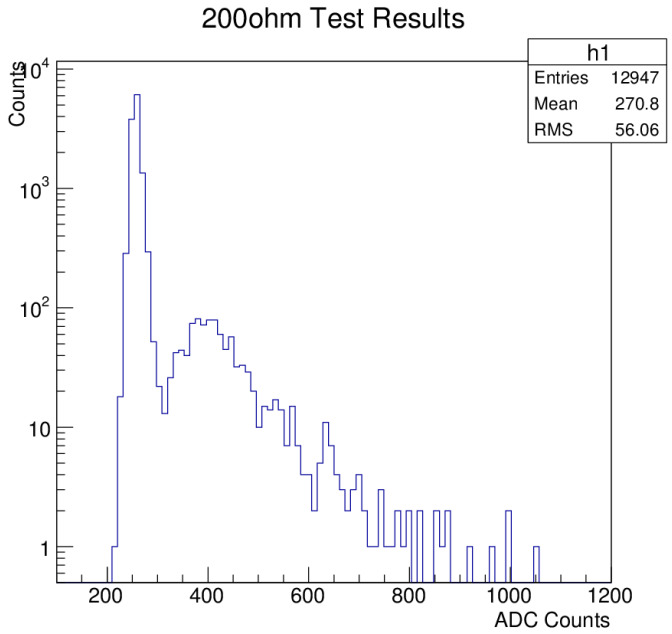

Figure 6.19: Cosmic Ray result.

6.3 Hadronic Calorimeter for Particle Flow Approach

6.3.1 Introduction

High-granularity hadronic calorimeter concept is to play an essential role in PFA-based experiments such as CEPC. It allows to separate the deposits of charged and neutral hadrons and to precisely measure the energy of the neutrals. The contribution of the neutrals to the jet energy, around 10% on average, fluctuates in a wide range from event to event, and the accuracy of the measurement is the dominant contribution to the particle flow resolution for jet energies up to about 100 GeV. For higher energies, the performance is dominated by confusion, and both topological pattern recognition and energy information are important for correct track cluster assignment. High-granularity hadronic calorimeter is thus needed to achieve excellent jet energy resolution.

HCAL are sampling calorimeters with steel as absorber and scintillator tiles or gaseous devices with embedded electronics for the active part. The steel was chosen due to its rigidity which allows to build self-supporting structure without auxiliary supports (dead regions). Moreover, the moderate ratio of hadronic interaction length ($\lambda_I = 17$ cm) to electromagnetic radiation length ($X_0 = 1.8$ cm) of iron, allows a fine longitudinal sampling in terms of X_0 with a reasonable number of layers in λ_I, thus keeping the detector volume and readout channel count small. This fine sampling is beneficial both for the measurement of the sizable electromagnetic energy part in hadronic showers as for the topological resolution of shower substructure, needed for particle separation.

The active detector element has very finely segmented readout pads, with 1×1 cm^2 size, for the entire HCAL volume. Each readout pad is read out individually, so the readout channel density is approximately 4×10^5/m^3. For the entire HCAL, with $\sim$100 m^3 total volume, the total number of channels will be 4×10^7 which is one of the biggest challenges for the HCAL system. On the other hand, simulation suggests that, for a calorimeter with cell sizes as small as 1×1 cm^2, a simple hit counting is already a good energy measurement for hadrons. As a result, the readout of each channel can be greatly simplified and just record 'hit' or 'no hit' according to a single threshold (equivalent to a '1-bit' ADC). A hadron calorimeter with such kind of simplified readout is called a Digital Hadron Calorimeter (DHCAL). In a DHCAL, each readout channel is used to register a 'hit', instead of measure energy deposition, as in traditional HCAL. In this context, gas detectors (such as RPC, GEM) become excellent candidates for the active element of a DHCAL. Another technology option is Analog Hadron Calorimeter (AHCAL) which is based on scintillator with SiPM as active sensor.

A drawing of the HCAL structure is shown in Figure 6.20, the barrel part is made of 5 independent and self-supporting wheels along the beam axis. The segmentation of each wheel in 8 identical modules is directly linked with the segmentation of the ECAL barrel. A module is made of 40 stainless steel absorber plates with independent readout cassettes inserted between the plates. The absorber plates consist of a total of 20 mm stainless steel: 10 mm absorber from the welded structure and 10 mm from the mechanical support of the detector layer. Each wheel is independently supported by two rails on the inner wall of the cryostat of the magnet coil. The cables as well the cooling pipes will be routed outside the HCAL in the space left between the outer side of the barrel HCAL and the inner side of the cryostat.

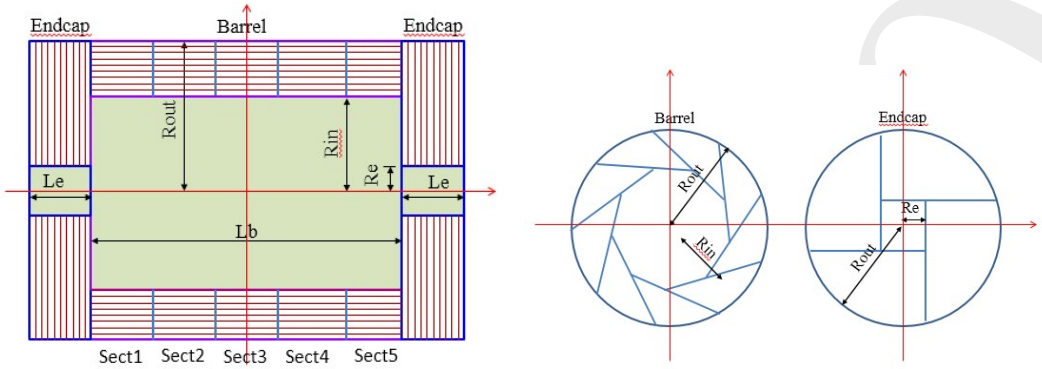

Figure 6.20: Longitudinal profile (Left) and transverse section (Right) of the HCAL.

6.3.2 Semi-Digital Hadronic Calorimeter (SDHCAL)

6.3.2.1 Introduction

For the CEPC, a SDHCAl based on gaseous detecor is proposed. This is motivated by the excellent efficiency and very good homogeneity the gaseous detectors could provide. Another important advantage of gaseous detectors is the possibility to have very fine lateral segmentation. Indeed, in contrast to scintillator tiles, the lateral segmentation of gaseous devices is determined by the readout electronics and not by the detector itself. Active layer thickness is also of importance for what concerns the CEPC hadronic calorimeter to be placed inside the magnetic field. Highly efficient gaseous detectors can indeed be built with a thickness of less than 3 mm. Other detectors could achieve such performance. However, gaseous detectors have the advantage of being cost-effective and discharge free. They are also known for their fast timing performance which could be used to perform 4D construction of the hadronic showers. Such a construction can improve on hadronic showers separation by better associating the energy depots belonging to the same shower from those of other showers. It can also improve on the energy reconstruction by identifying the delayed neutrons and assigning them a different weight.

To obtain excellent resolution of hadronic shower energy measurement a binary readout of the gaseous detector is the simplest and most effective scenario. However, a lateral segmentation of a few millimeters is needed to ensure good linearity and resolution of the reconstructed energy. Such a lateral segmentation leads to a huge number of electronic channels resulting in a complicated readout system design and a too large power consumption. 1x1 cm^2 cells are found to be a good compromise that still provides a very good resolution at moderate energies. However, simulation studies show that saturation effects are expected to show up at higher energies ($> 40\,\mathrm{GeV}$). This happens when many particles cross one cell in the center of the hadronic shower. To reduce these effects, the choice of multi-threshold electronics (Semi-Digital) readout is chosen to improve on the energy resolution by exploiting the particle density in a more appropriate way. These elements were behind the development of a Semi-Digital Hadronic CALorimeter (SDHCAL) that we propose to equip one of the CEPC future experiments.

Even with a 1x1 cm^2 lateral granularity of the readout system, a huge number of electronic channels is still needed. This has two important consequences. The first is the power consumption and the resulting increase of temperature which affects the behavior of the active layers. The other consequence is the number of service cables needed to

power, read out these channels. These two aspects can deteriorate the performance of the HCAL and destroy the principle of PFA if they are not addressed properly.

The R&D pursued by the CALICE SDHCAL groups has succeeded to pass almost all the technical hurdles of the PFA-based HCAL. The SDHCAL groups have succeeded to build the first technological prototype [19] of these new-generation calorimeters with 48 active layers of GRPC, $1m^2$ each. The prototype validates the concept of high-granularity gaseous detector and permits to study the energy resolution of hadrons one can obtains with such calorimeter.

In order to find out an appropriate option for the active detector of the SDHCAL, two parallel detector schemes, the Glass Resistive Plate Chamber (GRPC) and the Thick Gaseous Electron Multiplier (THGEM) are proposed for the active layers of the SDHCAL.

6.3.2.2 GRPC based SDHCAL

The GRPC scheme The structure of GRPC proposed as an active layer of the HCAL proposed for CEPC is shown in Figure 6.21. It is made out of two glass plates of 0.7 mm and 1.1 mm thickness. The thinner is used to form the anode while the the thicker forms the cathode. Ceramic balls of 1.2 mm diameter are used as spacers between the glass plates. The balls are glued on only one of the glass plates. In addition to those balls, 13 cylindrical fiber-glass buttons of 4 mm diameter are also used. Contrary to the ceramic balls the buttons are glued to both plates ensuring thus a robust structure. Special spacers (ceramic balls) were used to maintain uniform gas gap of 1.2 mm. Their number and distribution were optimized to reduce the noise and dead zones (0.1%).

The distance between the spacers (10 cm) was fixed so that the deviation of the gap distance between the two plates under the glass weight and the electric force does not exceed 45 microns. The choice of these spacers rather than fishing lines was intended to reduce the dead zones (0.1%). It was also aimed at reducing the noise contribution observed along the fishing lines in standard GRPC chambers. The gas volume is closed by a 1.2 mm thick and 3 mm wide glass-fiber frame glued on both glass plates. The glue used for both the frame and the spacers was chosen for its chemical passivity and long term performance. The resistive coating on the glass plates which is used to apply the high voltage and thus to create the electric field in the gas volume was found to play important role in the pad multiplicity associated to a mip [20]. A product based on colloids containing graphite was developed. It is applied on the outer faces of the two electrodes using the silk screen print method, which ensures very uniform surface quality. The measured surface resistivity at various points over a $1m^2$ glass coated with the previous paint showed a mean value of 1.2 $M\Omega/\square$ and a ratio of the maximum to minimum values of less than 2 ensuring a good homogeneity of the detector.

Another important aspect of this development concerns the gas circulation within the GRPC taking into account that for the CEPC SDHCAL, gas outlets should all be on one side. A genuine system was proposed. It is based on channeling the gas along one side of the chamber and releasing it into the main gas volume at regular intervals. A similar system is used to collect the gas on the opposite side. A finite element model has been established to check the gas distribution. The simulation confirms that the gas speed is reasonably uniform over most of the chamber area. The GRPC and its associated electronics are housed in a special cassette which protects the chamber and ensures that the readout board is in intimate contact with the anode glass. The cassette is a thin box consisting

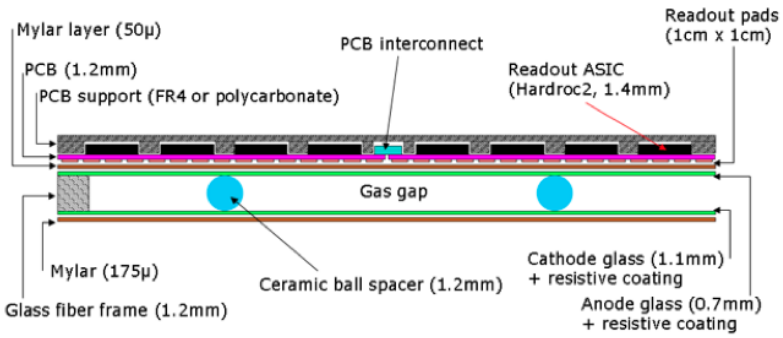

Figure 6.21: Cross-section through a 1 m^2 chamber.

of 2.5 mm thick stainless steel plates separated by 6 mm wide stainless steel spacers. Its plates are also a part of the absorber.

The electronics board is assembled thanks to a polycarbonate spacer which is also used to fill the gaps between the readout chips and to improve the overall rigidity of the detector. The electronics board is fixed on the small plate of the cassette. Thanks to tiny screws and the new set is fixed on the other plate which hosts the detector and the spacers. The whole width of the cassette is 11 mm with only 6 of them corresponding to the sensitive medium including the GRPC detector and the readout electronics.

GRPC technological prototype An SDHCAL prototype fulfilling the efficiency, robustness and the compactness requirements of the future PFA-based leptonic collider experiments [19] was built. 48 cassettes as the one described above were built. They fulfilled a stringent quality control. It is worth mentioning that 10500 HR ASICs were produced and tested using a dedicated robot for this purpose. The yield was found to be higher than 92%. The ASICs were then fixed on the PCBs to make a $1m^2$ and itself fixed on the cassette cover once successfully tested. The cassettes were inserted in a self-supporting mechanical structure that was conceived and built in collaboration with the Spanish group of CIEMAT. The structure is made of Stainless Steel plates of 1.5 cm each. The plates were machined to have an excellent flatness and well controlled thickness. The flatness of the plates was measured using a laser-based interferometer system. It was found that the flatness of the plates are less than 500 microns. This results guarantees that for the SDHCAL V structure proposed for ILD, a tolerance of less than 1mm is achievable. The prototype construction lasted less than 6 months. A commissioning test at CERN in 2011 allowed to understand the whole system behavior. In April 2012 the prototype was exposed to pion, muon, electron beams of both the PS and the SPS of CERN Figure (6.22). Power-pulsed mode was applied to the whole prototype using the beam cycle structure (0.3 ms time duration for the PS beam and 9 s for the SPS beam every 45s). The data were collected continuously in a triggerless mode. Figure 6.23 shows the efficiency (left) and pad multiplicity (right) of the prototype's GRPC chambers measured using the muon beam. Figure 6.24 shows a display of two events collected in the SDHCAL. One is a produced by a pion interaction (left) and the other by an electron interaction (right).

The SDHCAL prototype results obtained with a minimum data treatment (no grain correction) show clearly that excellent linearity and good resolution [21] could be achieved on large energy scale as can be shown in Figure 6.25 where results obtained in two different beam lines are obtained using the same detector configurations. Useless to mention that

the high granularity of the SDHCAL allows one to study thoroughly the hadronic showers topology and to improve on the energy resolution by, among others, separating the electromagnetic and the hadronic contribution. The separation between close-by showers will also get big benefit thanks to the high granularity on the one hand and to to the very clean detector response (< 1 Hz/cm^2) on the other hand. The results obtained with the the SDHCAL [22] confirm the excellent efficiency of such separation thanks to the SDHCAL performance. In addition, the high-granularity of the SDHCAL allows to extract the track segments of hadronic showers in a very efficient way [23]. The track segments (Figure 6.26) are then used to study the detector behavior in-situ. This is a simple but powerful control and calibration tool for a running calorimeter.

The quality of data obtained during several campaigns of data taking at the CERN PS and SPS beam lines validates completely the SDHCAL concept. This is especially encouraging since no gain correction was applied to the electronics channels to equalize their response. Still, improvement was further achieved by applying gain and threshold correction schemes in terms of the calorimeter response homogeneity.

A digitizer describing the response of the GRPC within the SDHCAL was developed [24]. It allows to study the SDHCAL behavior in a realistic manner in the future experiments.

In parallel to the prototype construction, a single cassette was tested in a magnetic field of 3 Tesla (H2 line at CERN) applying the power-pulsed mode. The TB results [25] indicated clearly that the use of the power-pulsed mode in such a magnetic field is possible. The behavior of the detector (efficiency, multiplicity..) was found to be similar to those obtained in the absence of both the magnetic field and the power-pulsed mode.

Readout electronics To read out the SDHCAL an ASIC called HARDROC2 was developed. To solve the problem of connections related to the high number of electronic channels, the option of a detector embedded electronics using the DAISY chain scheme was chosen and Printed Circuit Board (PCB) were conceived for the readout of large detectors GRPC.

- **Front-end ASIC**: The HARDROC2 chip (HR) implements a multi-threshold readout which integrates the functionalities of amplification, shaping, digitization, internal triggering and local storage of the data. Each of its 64 channels consists of a fast low impedance current preamplifier with 8-bit variable gain (in the $[0, 2]$ range) followed by 3 fast shapers (15 ns shaping time). A low offset discriminator is present on each path and the three corresponding thresholds establish the multi-level readout. The thresholds are set using three integrated 10-bit Digital to Analog Converters (DAC). The outputs of the three discriminators are then encoded and stored in an internal digital memory latched by a trigger event. A trigger is generated when one of the lowest level discriminators is fired but can also be configured on the other thresholds. A frame consists of the 64 encoded discriminator outputs, plus a 24-bit time-stamp and a chip identifier is stored after a trigger is received. Noisy channels could be easily masked via the configuration parameters control. In order to avoid fake triggers produced by noisy channels, the output of each discriminator can be switched off from the trigger generator logic via the configuration parameters control (Slow Control hereafter) commands. The response of all the channels can be calibrated by injecting an analog signal through an integrated 2 ± 0.02 pF input test capacitor; this is a useful tool to make the response of the different channels as uniform as

possible [20]. The ASIC contains a 127-frame long digital memory. This allows to work in a triggerless mode and keep all the data accumulated during the bench crossing.

Once the memory is full the acquisition is stopped, the readout is performed and the ASIC can start acquisition again. The Gray-coded time-stamp is derived from an external 5 MHz clock. An essential feature of the HR is the possibility to be operated in the power-pulsing mode (PP) that consists of switching off almost all power-consumption functionalities in between the bench crossings (BC) of the electron beams. In the case of CEPC this mode may allow a moderate reduction of the power consumption but this is not enough to prevent the detector heating due to the power consumption. Therefore an embedded active cooling system is needed.

- **Active Sensor Units**: To read out the 1 m^2 detector of the SDHCAL prototype, an electronic board with the same size is needed. This electronic board is an important piece in the present design. It hosts both the pick-up pads and the ASICs in addition to the connections between the pads and the ASICs and those linking the different ASICs. To ensure good transmission qualities and low cross-talk, 50 cm $\times$ 33 cm, 8-layer Printed Circuit Board (PCB) is designed. Each of these ASUs hosts 24 chips to read out 48$\times$32 pads of 1cm ^{2} each. This dressed PCB is dubbed Active Sensor Unit (ASU). The routing of each input signal from its own pad up to chip pin has been carefully optimized to reduce the cross-talk. The rooting was conceived so two of the ASUs can be associated to form one slab hosting 48 ASICS. Each slab is then connected to one Detector InterFace board (DIF). The connection between the DIF and the slab as well as the connection of the two ASUs is performed thanks to tiny connectors allowing the different clocks, signals as well as the power to circulate between the two ASUs. Three slabs are then assembled to form the required electronics board. To ensure the same electric reference level for the six ASUs, the GND layer of the six ASUs is connected thanks to a copper gasket on all the common sides. Similar schemes could be proposed for GRPC detectors with larger size.

- **Front-end and back-end boards**: The interface between the ASUs and the data acquisition system (DAQ) is realised by the DIF. The main elements of the DIF is an FPGA and USB, HDMI and SAMTEC connectors. It manages the control signals (*e.g.* clock, busy/ready, external/internal trigger, power-pulsing) and supply power to the ASICs and also performs the readout of the ASIC memories. DIFs are read out by other FPGA-based boards called Data Concentrator Cards (DCC). They can be connected up to 9 DIFs through HDMI links and are controlled by a synchronous DCC (or SDCC). The SDCC can connects to up to 9 DCCs to which it distributes the clock and the commands. It is also connected to the computer network for the user to control the DAQ.

- **Data Acquisition software**: To exploit the data collected by the SDHCAL detectors an acquisition software was developed. This software is organized in three parts. The first one allows to access the hardware devices (DIF, SDCC) through an FTDI chip associated to each of these devices. It transmits the configurations parameters to ASICs through these devices and collect the data as well. The second part is the configuration data base. It gives the possibility to store and retrieve all parameters needed by the DAQ system. The database itself is hosted on an Oracle server. To interface this SQL database with the DAQ software and to allow users to insert and query data without knowledge of SQL, a C++ library has been written. A special care was taken to allow to download the parameters associated to a given parameters of the prototype (roughly 550000 parameters) in few seconds. The third part concerns the data collection. Data from different DIFs may be readout at a different times but will have the same Bench Crossing IDentifier (BCID)

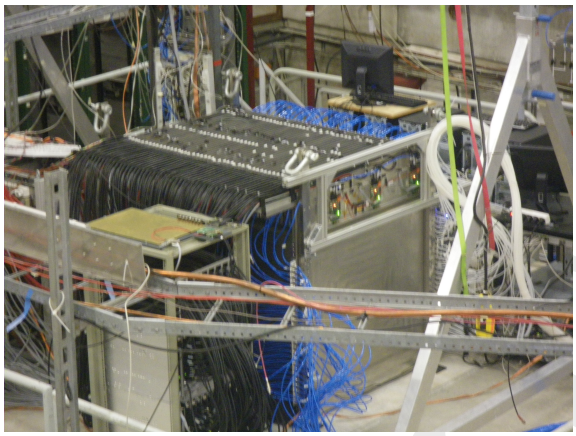

Figure 6.22: The SDHCAL prtototype in beam test at CERN.

for a given trigger. The logical way to keep synchronicity is to store in a BCID indexed map the buffers of all read DIFs but it requires to man-age memory allocation, access and cleaning. This was achieved thanks to the abilities offered by recent Linux kernels to use file based shared memory. In addition, whenever several computers are involved in the data taking, as it is the case for the SDHCAL prototype, a communication framework is needed. The CMS data acquisition XDAQ framework was chosen. This provides communication tools, an XML description of the computer and software architecture, a web-server implementation of all data acquisition application and a scalable event builder. A monitoring system was also developed to have an online follow-up of the acquisition during data collection.

Preparation for future experiments A genuine self-supporting mechanical structure to host the hadronic calorimeter of future PFA-based leptonic collider experiments was fully studied. The structure (called V-structure) was conceived to eliminate the projective holes and cracks so none of the particles produced close to the detector centre could escape detection. The V-structure has additional advantages. It eliminates in principle the space between the barrel and the Endcaps avoiding the shower deformation which results not only because of this space but also of the different cables and services needed in CMS-like mechanical structures. In this structure the different services such as the gas tubes, data collection and electric cables of both the barrel and the Endcaps are taken out from the outer radius side.Detailed studies have shown that the deformation of this structure is extremely low and its robustness was verified experimentally with the SDHCAL technological prototype built with a self-supporting structure respecting the spirit of the V one. Services and Integration issues were also worked out. Besides, realistic costing was performed , based on the prototype experience.

current SDHCAL R&D Large GRPC of $1m^2$ were developed and built for the technological prototype. However, larger GRPC are needed in the SDHCAL proposed for future leptonic collider experiments. These large chambers with gas inlet and outlet on one side need a dedicated study to guarantee a uniform gas gap everywhere notwithstanding the angle of the plate. It is necessary also to ensure an efficient gas distribution as it was done for the 1m2 chambers. To obtain this different gas distribution systems were studied. A new scheme with two gas inlets and one outlet was found to ensure an excellent homo-

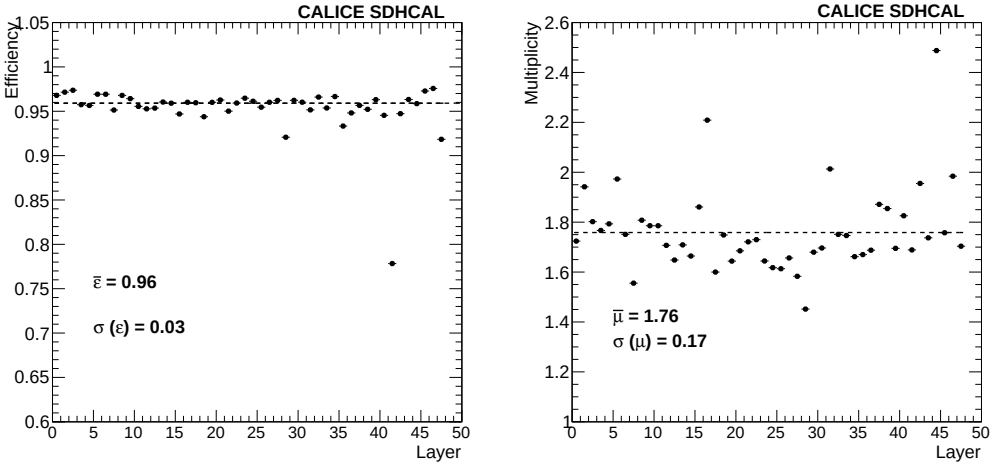

Figure 6.23: Left: Efficiency of the GRPC detectors of the SDHCAL. Right: the pad multiplicity of the GRPCs. One third of the chamber 42 was not instrumented.

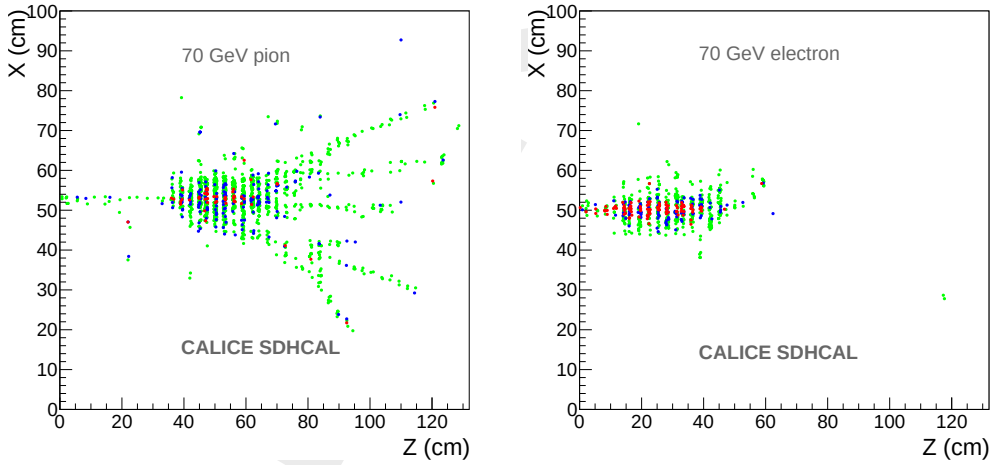

Figure 6.24: Left: event display of an 70 GeV pion interaction in the SDHCAL prototype. Right: Event display of a 70 GeV electron interaction in the SDHCAL prototype.

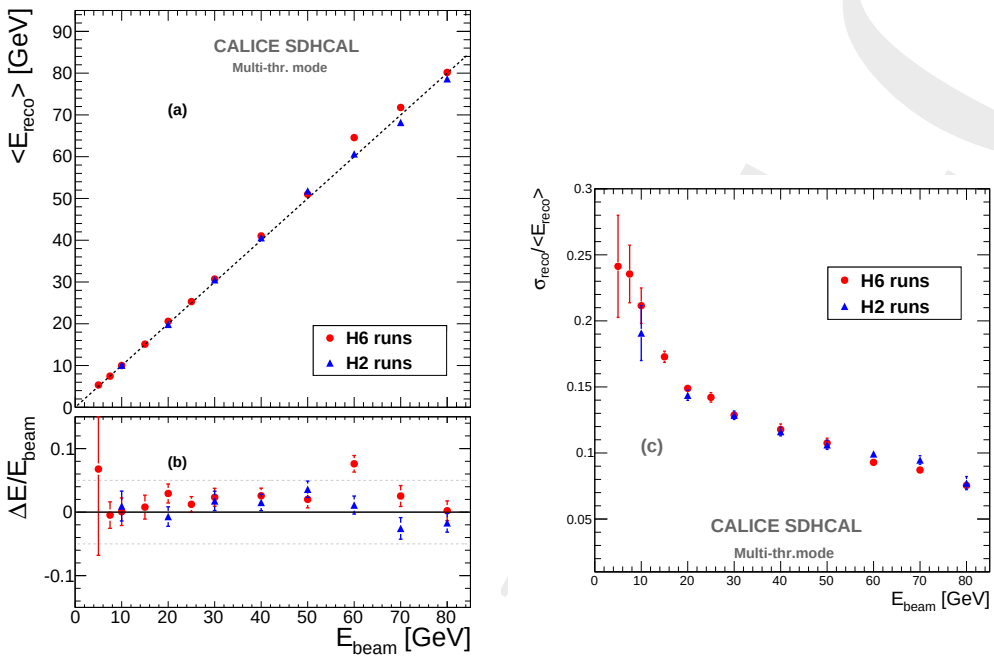

Figure 6.25: Left: a) Reconstructed energy of the hadronic showers collected in both H2 and H6 SPS beamlines. b) the relative deviation of the reconstructed energy with respect to the beam energy. Right: Relative energy resolution of the reconstructed hadronic shower.Pion beam of H6 beamline is largely contaminated by protons at high energy (>50 GeV).

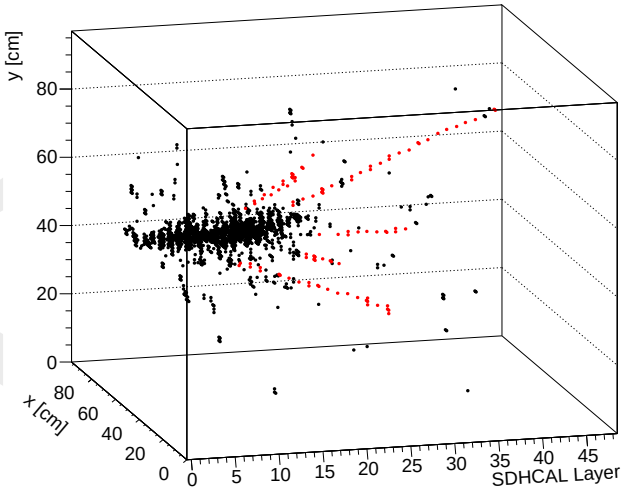

Figure 6.26: A 3D event display of a pion interaction event showing the track segments extracted by applying a hough transform technique.

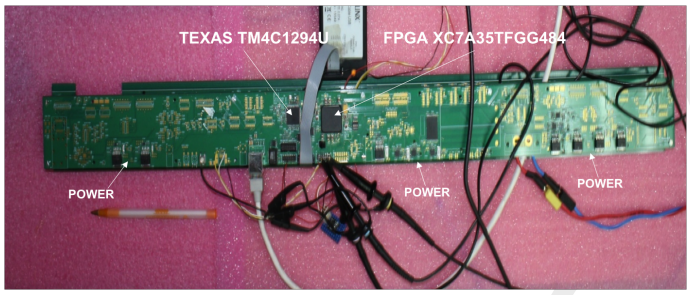

Figure 6.27: A new Detector InterFace (DIF) allowing to address up to 432 ASICs of 64 electronic channels each.

geneity of the gas distribution. This system will be used in the near future to build large detectors exceeding $2m^2$. The readout of such chambers needs also to be as efficient as the one of the technological prototype $1m^2$. An upgrade of the HR ASIC allowing larger dynamic range (01-50 pC) was conceived, produced and successfully tested. The new ASIC (HR3) allows to be directly addressed and easily bypassed in case of failure thanks to the I2C protocol. In addition and contrary to the HR2, the 64 channels of the new ASIC are independent which allows a better calibration procedure. Furthermore, a new interface board (DIF) is conceived to control the ASICs synchronization and data transfer. Indeed, the space left between the active layer of one module and the cryostat maybe very short in future leptonic experiments (< 5 cm). This means that the DIF components should be optimized to cope with the volume availability. A new design with new functionalities of the DIF is proposed. A TPC/IP protocol is adopted for data transfer and a TTC one for the clock synchronisation. A microprocessor implemented on the new DIF is in charge of the communication between the ASICs and the DIF's FPGA. The new DIF shown in Fig. 6.27 is capable to address up to 432 ASIC. A new PCB design that allows to assemble few boards to cover up to 3 m^2 GRPC detector was also conceived. Care is taken to ensure robust and flexible but still tiny connection between the different PCB to build a large one. Fig. 6.28 shows a picture of such a PCB equipped with the HR3 ASICs. Finally a new technique based on electron beam welding is being tested to build a mechanical structure. This intends to reduce the steel quantity used to assemble the absorber plates while guaranteeing a minimum deformation. First attempts have taken place at CERN recently 6.29 and more study is ongoing to determine the best protocol one should follow to obtain optimal results. Finally, to cope with the heating produced by the embedded readout system in case of limited or even the absence of use of the Power Pulsing system, a new active cooling system is being studied. Figure 6.30 shows a study of a water-based cooling system to absorb the excess of heat in the SDHCAL. The cooling system is very simple but very effective as well. It allows to keep the average temperature as well as the temperature dispersion of the GRPC well under control.

6.3.2.3 THGEM-based DHCAL

The THGEM scheme The THGEM can be built in large quantities at low cost, which might make them suitable for the large CEPC HCAL. THGEM detectors can provide flexible configurations, which allow small anode pads for high granularity. They are robust and fast, with only a few nano-seconds rise time, and have a short recovery time which allows a higher rate capability compared to other detectors. They are operated at a relatively low voltage across the amplification layer with stable high gain. The ionisation

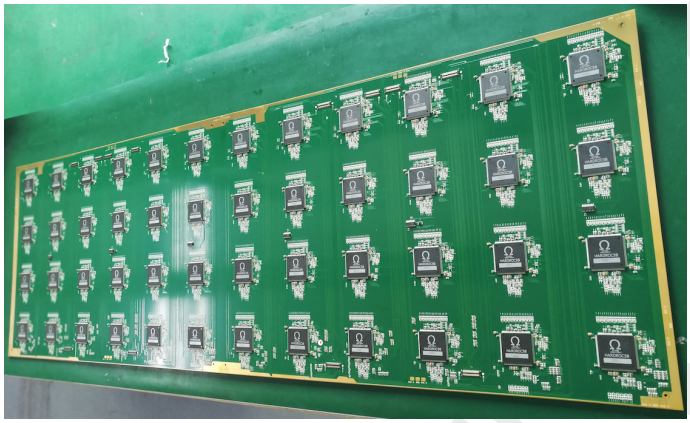

Figure 6.28: A new PCB equipped with he HR3 ASICs. The PCB is 100 cm $\times$ 33.3 cm. Several PCBs could be connected thanks to tiny flexible connectors to read out very large GRPC detectors.

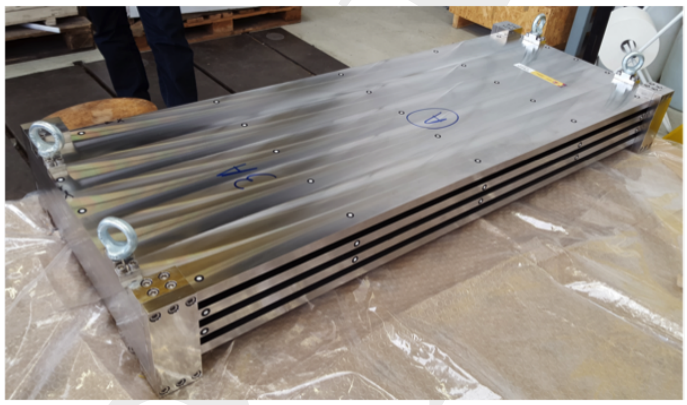

Figure 6.29: A prototype of an SDHCAL mechanical structure assembled using the electron beam welding technique.

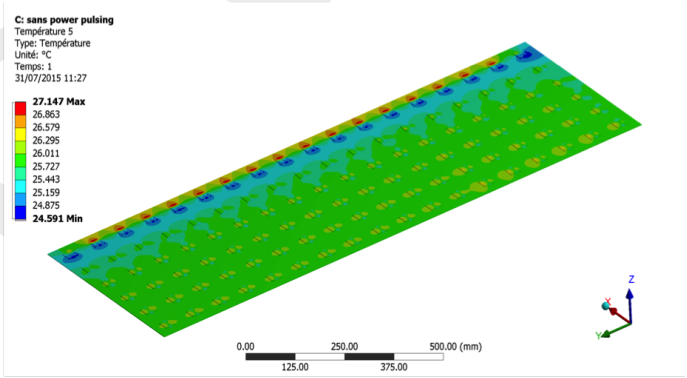

Figure 6.30: Temperature distribution in an active layer of the SDHCAL operated with no power-pulsing. The cooling system is made of a circulating water inside copper tubes in contact with the ASICs.

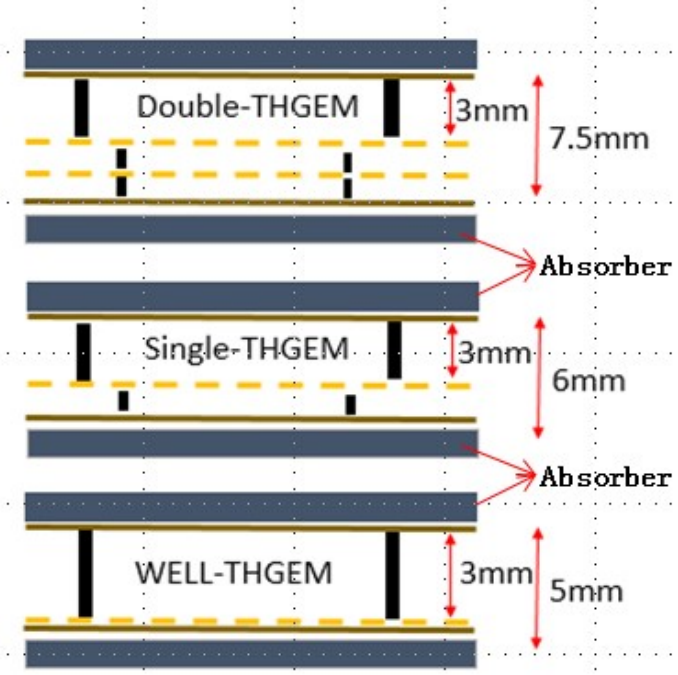

Figure 6.31: Structure of THGEM based detector for DHCAL.

signal from charged tracks passing through the drift section of the active layer is amplified using a sigle layer or WELL-type THGEM structure. The amplified charge is collected at the anode layer with pads at zero volts. As the HCAL is located within the coil, WELL-THGEM, a single layer structure with thinner thickness, as shown in Fig. 6.31, can be considered as the sensitive medium, to keep the HCAL compact.

Digital readout has been proposed to limit the total amount of data, which simplifies the data treatment without comprising the energy resolution performance. The readout electronics of the DHCAL will be integrated into the sensitive layer of the system, thus minimising dead areas. Large electronics boards are assembled together to form extralarge boards before being attached to the THGEM. The board assembly will utilise a mechanical structure made of 4 mm stainless steel plate. In addition, to keep the HCAL as compact as possible, the fully equipped electronic boards are designed to be less than 2 mm thick in total.

A THGEM based detector for DHCAL has been designed with 40 layers in total. Each layer contains 2.0 cm thick stainless steel, 0.8 cm thick THGEM and readout electronics with 1×1 cm^2 readout pads. As THGEM production technology matures, the maximum area of THGEM is limited only by the size of the CNC drilling area. Its low price, robustness against occasional discharges, high gain and count rate capability of up to 10MHz/cm^2 make THGEM very attractive for building the DHCAL. THGEM is cheaper and more robust than GEM, and has a higher counting rate capability than GRPC. As illustrated in Fig. 6.31, the total thickness of the sensitive medium is 5 mm, which consists of 3 mm drift gap, 1 mm transfer gap and 1 mm induction gap. The absorber between the active layers is made of 20 mm thick stainless steel. The thickness of the readout electronics board is about 3 mm, and the total thickness of a single sensitive layer is less than 10 mm. Each layer corresponds to about 1.2 radiation length and 0.65 nuclear interaction

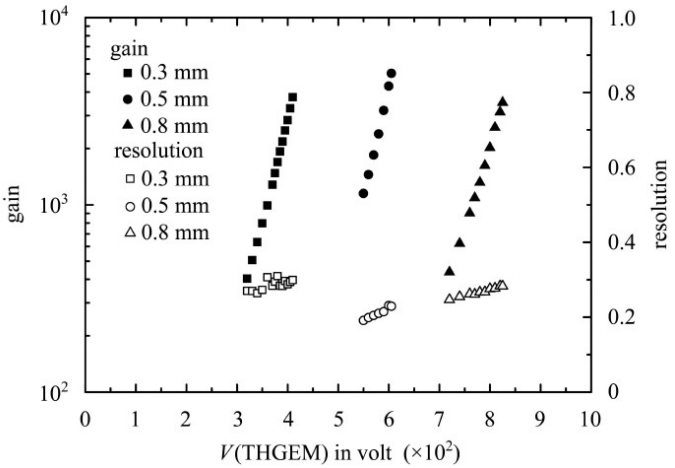

Figure 6.32: Gain and energy resolution of THGEM detector obtained with ^{55}Fe.

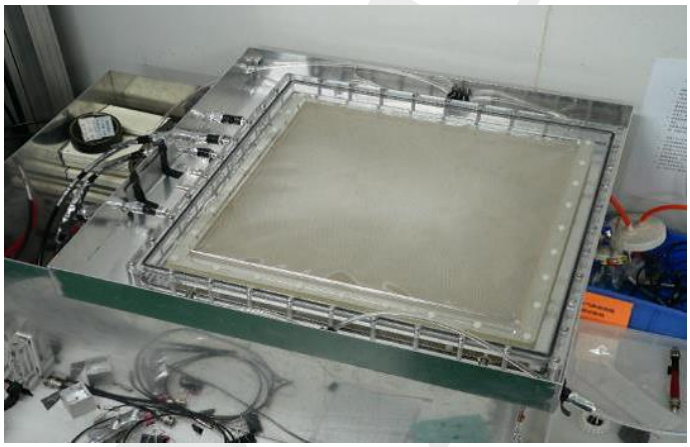

Figure 6.33: The maximum size of THGEM produced in domestic currently (40×40 cm^2).

length. The whole DHCAL detector is evenly divided into 40 layers, with a total stainless steel absorber thickness of 4.7 nuclear interaction lengths.

THGEM prototype A THGEM with an area of 40×40 cm^2 has been successfully fabricated, as shown in Fig. 6.33, and a gain of 2×10^5 has been achieved with a double THGEM, with an energy resolution of about 20%. The THGEM produced has the following features: 1)standard PCB processes are used, which keeps the cost low; 2) excellent performance in terms of energy resolution, gas gain and stability (as shown in Fig. 6.32); 3) Rim around the hole formed by full-etching process, the size of which can be varied between 10 μm and 90 μm, as depicted in Fig. 6.32 - this allows adjustment according to gas requirements.

Fig. 6.34 shows the schematic diagram of a new THGEM detector, where a micro-plate directly attached to the readout plate, since the micro-porous structure similar to a well, known as the well-type THGEM (WELL-THGEM). This structure contains of a single-layer THGEM, so that the thickness of detector can be reduced to $4 \sim 5$ mm, and the total thickness of the detector including ASIC electronics could be lowered to about 6 mm.

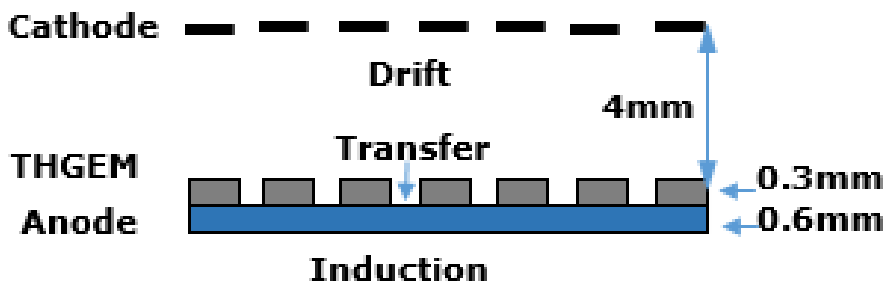

Figure 6.34: The schematic diagram of the WELL-THGEM.

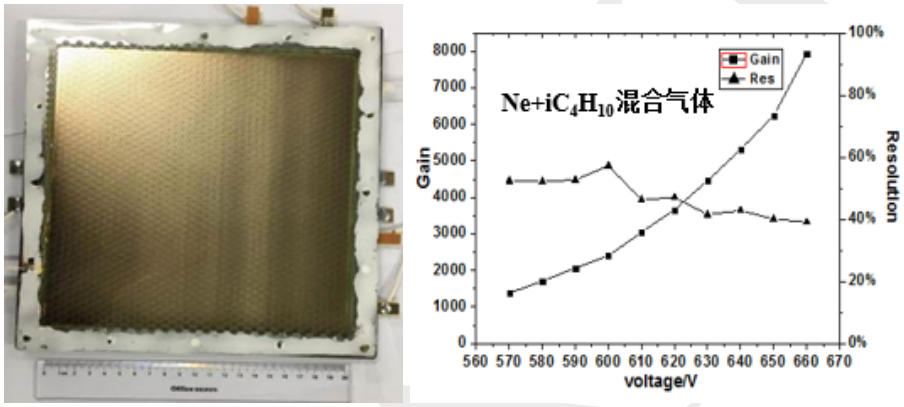

Figure 6.35: The photograph(left) and performance (right) of the WELL-THGEM detector.

A $20cm \times 20cm$ WELL-THGEM detector using thin-type THGEM have been developed, and the basic performances such as the gain curve, uniformity and energy resolution were studied and shown in Fig. 6.35.

In addition, Researches on large THGEM detectors have been carried out. Single THGEM detectors and Well-THGEM detectors are being developed to reduce detector instability and inefficiency. Gas recycling systems are built to lower gas consumption and pollution. The achieved THGEM detection rate of 1 MHz/cm^2 with efficiency greater than 95% already meets the CEPC requirements.

THGEM digital readout system A MICRO-mesh gaseous structure Read-Out Chip (MICROROC), which is developed at IN2P3 by OMEGA/LAL and LAPP microelectronics groups was used to read out the THGEM-based SDHCAL. The MICROROC is a 64-channel mixed-signal integrated circuit based on 350 nm SiGe technology. Each channel of the MICROROC chip contains a very low noise fixed gain charge preamplifier which is optimized to cover a dynamic range from 1 fC to 500 fC and allow a input detector capacitance of up to 80 pF, two gain-adjustable shapers, three comparators for triple-threshold readout and a random access memory used as a digital buffer. Otherwise, it have a 10-bit DAC, a configuration register, a bandgap voltage reference, a LVDS receiver shared by 64 channels etc. A 1.4 mm total thickness is achieved by using the Thin Quad-Flat Packaging (TQFP) technology.

The readout system structure as shown in Fig. 6.36 is developed on the Scalable Readout System (SRS), which is proposed by the RD51 Collaboration. It is composed of a front-end board (FEB), a detector interface board (DIF) and a data acquisition card (DAQ).

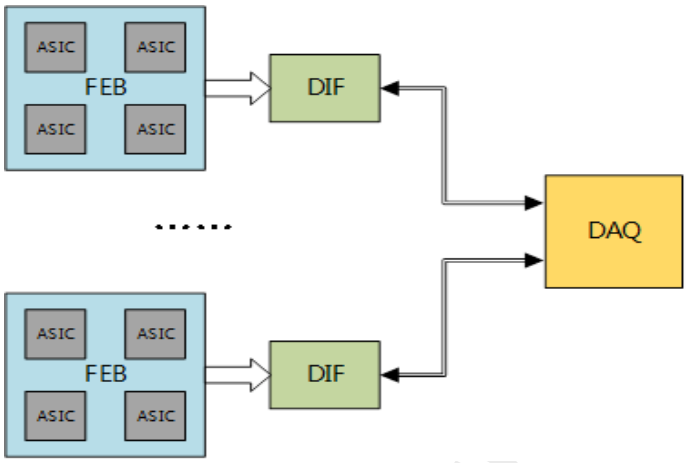

Figure 6.36: The schematic diagram of the readout system.

The FEB (also called ASU-Active Sensor Unit) carries all the front-end ASIC, together with the readout plane of GEM detector. The DIF in charge of ASIC control and data connection, plugs to the FEB using high density connector. The DAQ card is designed to serve several DIF boards. It distributes the clock, command and trigger to different DIF and gather the data from DIF boards.

The FEB is the combination of readout pads of GEM detector and readout ASICs. In order to minimize the dead-area of the detector, the FEB is designed to use blind and buried via technology. Considering the signal integrity and costs, $8 \sim 10$-layer PCB is a suitable choice. The thickness of this kind of PCB can be as thin as 1.2 mm. This means contain the 1.4 mm MICROROC, the total thickness of FEB can be made within 3 mm. Limited by PCB manufacturing technology, a well-performance FEB can be made as large as $50cm \times 50cm$. If a $1m^2$ prototype is made, it necessary to combine 4 FEB into one detector layer.

The DIF controls the FEB and gather the data of ASIC and can be tailored to the particular front-end ASIC with the particular application, giving the users the freedom of choice for the front-end circuit. Just changing the ASIC and DIF, the same design can be used both in ECAL and HCAL. Considering the data rate and costs, the master device of DIF can be some low-cost FPGA and the communication interface to the DAQ can be both USB type C or fiber-optical.

The DAQ card accesses the command from a server and controls several DIF. The design goal of the DAQ card is a universal controller for both ECAL and HCAL. Once a mature DAQ card is finished, it can be in common use even if we change the front-end ASIC.

Besides the readout ASIC and card, the clock synchronization design is an important block of the system. There are two kinds of clock source in the readout system, local clock and global clock (Usually, this kind of clock may be hundreds or thousands of meters from calorimeters). The local clock goes through the PLL and low-skew fan-out chip to the DIF, then the DIF distribute the clock to the FEB for local synchronization. If a global clock source is used, it is necessary to module there clock to optical signal and distribute the clock through fiber-optical. Another circuit call Clock and Data Recover (CDR) is needed for clock rebuild. The rebuild clock is global synchronized and can be used as local clock in one DAQ card.

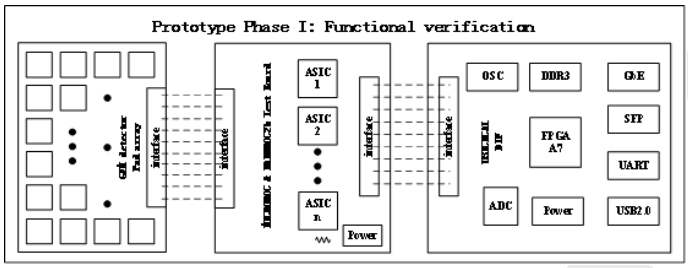

Figure 6.37: The diagram of the phase I design.

Figure 6.38: Pictures for the phase I design.

A phase I design (in Fig. 6.37 and Fig. 6.38) is completed to verify this kinds of readout structure and to test the performance of the MICROROC chip. In this design we separate the front-end ASIC from the detector readout plane for single test the ASIC. It contains the readout array of the GEM detector, front-end ASIC board and DIF board. The structure of the design is shown in figure 2. The GEM detector is $30cm \times 30cm$, and the readout pad detector is 1 cm^2. To ensure signal integrity and low cross talk the readout plane is designed 8-layer PCB with 4 ground plane to separate the signal and shield. The pads signal is connector to the front-end ASIC board via soft-board made from kapton. The front-end ASIC board composed by 4 ASIC controlled in daisy chain. The DIF board controls the front-end ASIC board and transmit data to the upper monitor. The main controller of DIF is Xilinx A7 100T series, a low cost FPGA. The data can be readout via USB2.0 or fiber-optical or Giga-bit Ethernet. We also reserve an ADC on DIF for monitoring the analog test signal. Figure 3 shows the picture of these three board. The primary performance studies for this design have been carried out. For all the ASIC channel, the maximum noise is 0.35 fC, which means it beyonds the best performance of this ASIC distinguishing at least 2fC signal. The linear region of the high gain shaper reaches to $\sim$ 140 fC, and the low gain shaper is $\sim$ 500 fC. All the result shows that this ASIC can work well with the detector and the readout scheme is effective.

In order to optimize the design, a next stage design (shown in Figure 6.39) based on the test results have been proposed and put into effort. In this version, the MICROROC chips are planed to be mounted on the bottom side of the readout plane, utilizing blind buried via technology. A 10-layer PCB with 3 ground plane and 2 power plane will ensure good signal integrity and low crosstalk. Considering the cost and performance, we choose 2 kinds of blind via (Layer1 - Layer2 and Layer9 - Layer10) and 1 kinds of buried via (Layer2 - Layer9). This board is the real FEB in the system structure. The design diagram is shown in figure 4. Besides FEB, the design of the DIF board is going on the same time. The DIF can plug to FEB directly or through a soft-board made from kapton. After the DIF design, we will consider the design of DAQ board. We can share the same DAQ board with ECal readout system. The DIF is connected to DAQ through USB type C wire

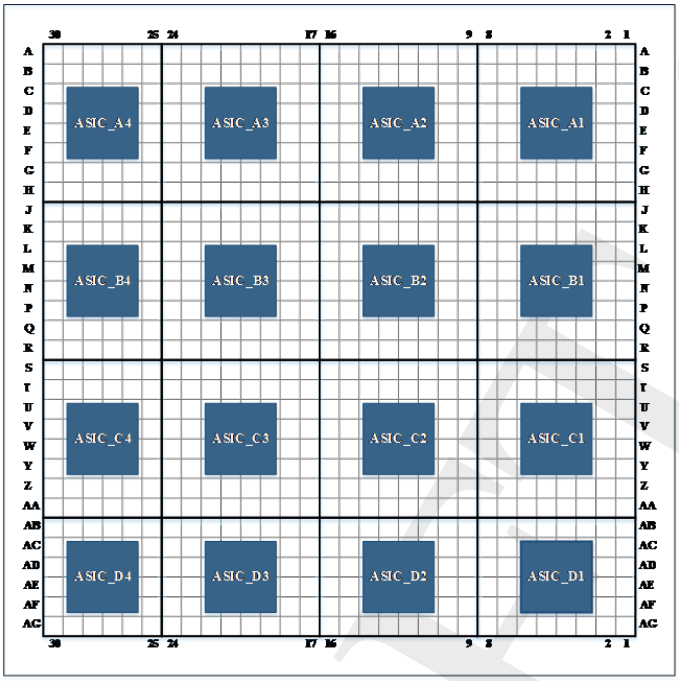

Figure 6.39: The Design scheme for next stage FEB.

or fiber-optical. Besides the SRS readout structure, a new system name FELIX is under research, which can made the whole system trig less readout.

6.3.3 Analog Hadronic Calorimeter based on Scintillator and SiPM

A high-granularity hadronic calorimeter plays an essential role in PFA-based experiments such as CEPC. It allows separation of the energy deposits from charged and neutral hadrons. The contribution of the neutrals to the jet energy, around 10% on average, fluctuates over a wide range from event to event. The HCAL is a sampling calorimeter with steel as the absorber and scintillator tiles with embedded electronics. The moderate ratio of hadronic interaction length (I=17cm) to electromagnetic radiation length (X_0 = 1.8 cm) of steel, allows a fine longitudinal sampling in terms of X_0 with a reasonable number of layers.

Various calorimetry options are being developed to address challenges from the stringent performance requirements on future lepton collider experiments for precision measurements of the Higgs boson and for searches of physics beyond Standard Model. Within the CALICE collaboration, a large technological prototype using scintillator tiles and SiPMs is currently being built to demonstrate the scalability to construct a final detector via automated mass assembly. Though this prototype is aimed for the future International Linear Collider (ILC), the outcome of CALICE-AHCAL R&D activities can be an essential input for the conceptual design of the hadron calorimeter system at the future Circular Electron Positron Collider (CEPC).

6.3.3.1 AHCAL geometry and simulation

The AHCAL consists 40 sensitive and absorber layers, and the thickness is about 100cm. The AHCAL barral consists 32 supper module, each super module consists 40 layers, fig-

ure6.40 shows the AHCAL structure. Figure6.41 shows the AHCAL one layer structure. The scintillator tiles wrapped by reflective foil are used as sensitive medium, interleaved with stainless steel absorber. The thickness of active layer is 4 mm to 5 mm, it depend the thickness of scintillator thickness.

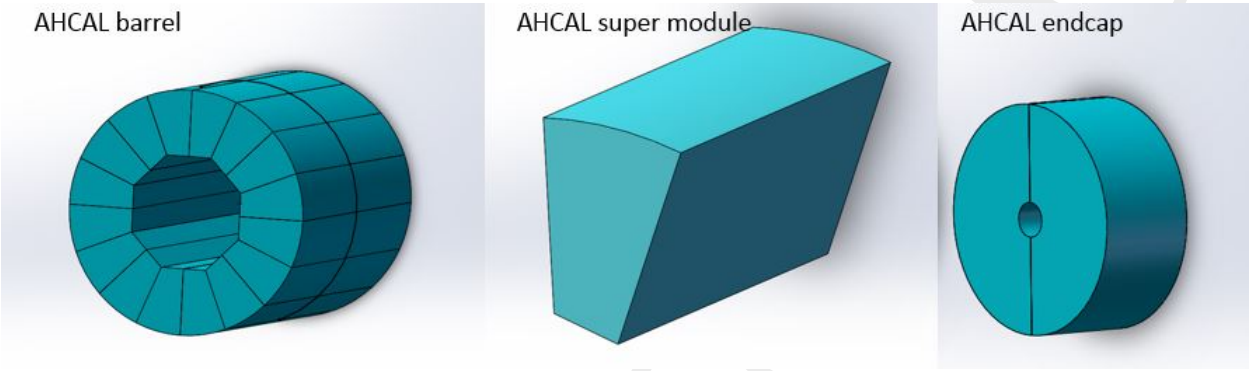

Figure 6.40: Side view of one layer in AHCAL

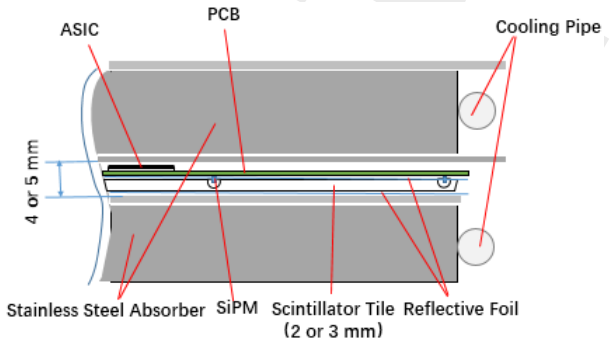

Figure 6.41: Side view of one layer in AHCAL

The structure of scintillator tiles is shown in Figure 6.42. A dome-shaped cavity was processed in the center of the bottom surface of each tile via mechanical drilling and polishing. The diameter and height of cavity are 6mm, 1.5mm, respectively, as shown in Figure 6.42 (right). This design of cavity can improve response uniformity and decrease the dead area of HCAL.

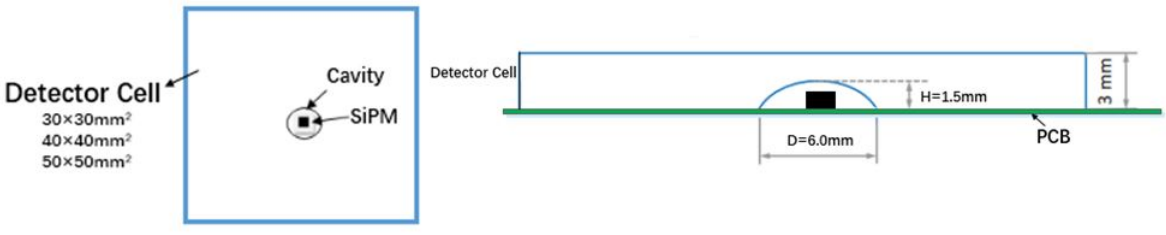

Figure 6.42: Top view of a detector cell (left) and sectional view of a detector cell with a dome-shaped cavity (right)

The AHCAL prototype detector simulated by Geant4 which was encapsulated in toolkit including several models. The detector model used here was CEPC_v1 detector model and the sub detector was SiCal. The geometry information was extract by Mokka at

runtime and the generated events was stored in Slcio, which contains primary information regarding the energy deposition, hit position, time and Monte Carlo particle causing the energy deposition. It can read out by Marlin and translate into Root files for analyzing. The ECAL was simulated 30 layers. The HCAL is a structure of 40 active layers interleaved with 20 mm steel absorber plates. Each active layer is assembled from 3mm plastic scintillator, also the readout layer thickness is 2mm PCB, detector cell size is 30×30×3 mm^3. And the TCMT, we simulate 20 layers and each layer is the same component and material as HCAL. Their structure is shown in Figure 6.43.

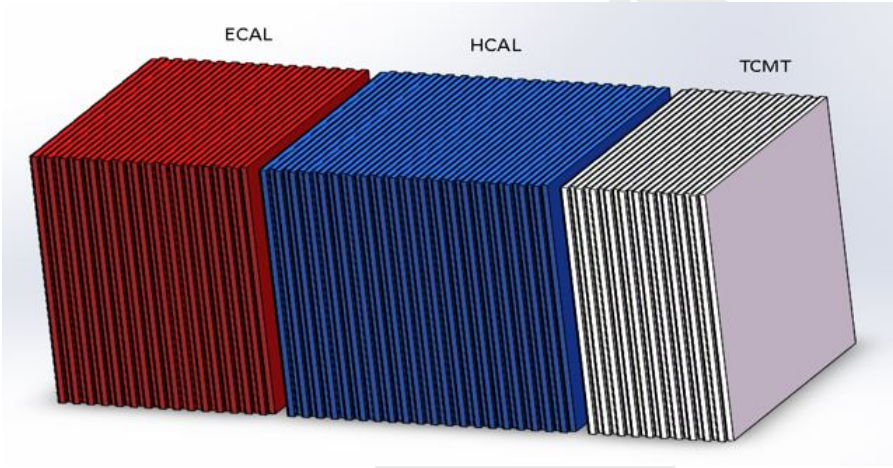

Figure 6.43: The structure of simulated calorimeters which is a part of the simplify geometry. Red part is the ECAL, Blue part is the HCAL, and white part is the TCMT

$$E_{REC} = a \times E_{ECAL} + b \times E_{HCAl} \tag{6.3}$$

For getting the resolution of calorimeters (ECAL and AHCAL) which structure was show in figure 6.43. Formula 6.3 is the energy reconstruction formula, the coefficients a and b in this formula represent ECAL and HCAl calibration constant. After optimization, the calibration constants are a=44.4 and b=44.2 respectively which were corrected by energy of 60GeV. Calibration constants can correct the energy leakage from the calorimeters. So it can be used formula 6.4 for calculating the resolution. The energy resolution result shows in figure 6.44. For the resolution is better than the result of CALICE, the reason should be simulation ignore the response difference between detector cells. For the energy linearity, the slope value is 0.99, which means the reconstruction energy is essentially linear.

$$\frac{\sigma}{E} = \frac{p_0}{\sqrt{E}} + p_1 \tag{6.4}$$

6.3.3.2 Plastic Scintillator cell measurement

The basic tile size was optimized with respect to particle separation capability and found to be 30 × 30mm^2. The simulation results suggest that it is possible to use the detector cells of larger sizes. For example, it will reduce nearly two-thirds electronics channels by using 50 × 50mm^2 size detector cell instead of 30 × 30mm^2 size. Therefore, the construction

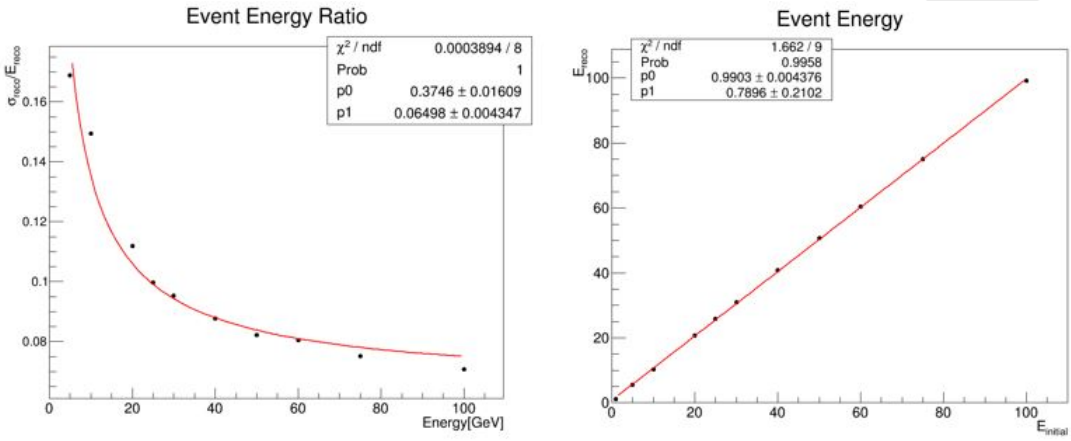

Figure 6.44: Left figure is energy resolution, right figure is the result of reconstruction energy linearity

costs can be greatly reduced if the larger detector cells can meet the physics requirements. Two larger sizes of detector cells were considered. Four kinds of scintillator (BC408) tiles with different sizes were fabricated and tested, and they are $30 \times 30 \times 3\text{mm}^3$, $40 \times 40 \times 3\text{mm}^3$, $50 \times 50 \times 3\text{mm}^3$ and $30 \times 30 \times 2\text{mm}^3$.

The SiPM is soldered onto a readout Printed Circuit Board (PCB) and the scintillator tile wrapped by ESR reflective foil is directly glued onto the PCB. Such a cavity design provides enough space for the SiPM package and improves collection efficiency of the light produced by incident particles penetrating the tile at different positions. The SiPM is readout by the Hamamatsu electronic readout board (C12332-01) which has the function of temperature compensation. The time instability of signal amplitude (ADC channel) of SiPM is from 17.59% to 2.38% in the range of 22^{o}C to 30^{o}C owing to temperature compensation from the board, as shown in Figure6.45.

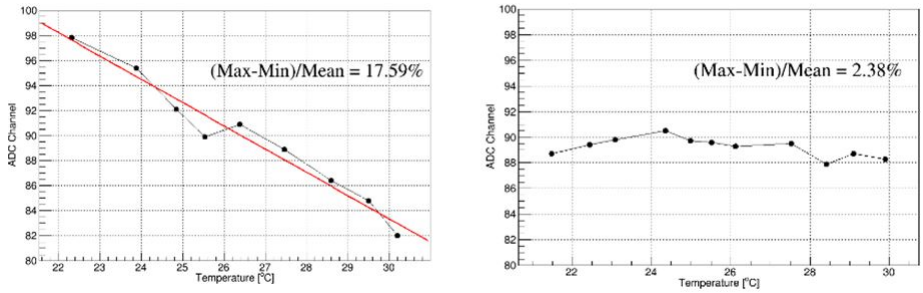

Figure 6.45: SiPM signal amplitude varies with temperature, before (left) and after (right) temperature compensation electronics (Hamamatsu C12332-01)

Uniformity measurement:A strongly non-uniform tile response can lead to a distortion of the energy reconstruction in a complete calorimeter, and also compromises the calibration of the detector cells based on single particle signals [4]. The response uniformity of a SiPM inside the cavity of a scintillator tile has been measured with a 90Sr source, as shown in Figure 6.46. The trigger scintillator ($5\times5\times3\text{mm}^3$) and 90Sr source were fixed. A detector cell, which was mounted on a step motor, can be finely moved between 90Sr source and the trigger scintillator. Uniformity scans were accomplished by

horizontally translating the detector cell in a step size of 5×5 mm^2. The electronics data acquisition system is shown in Figure 6.47.

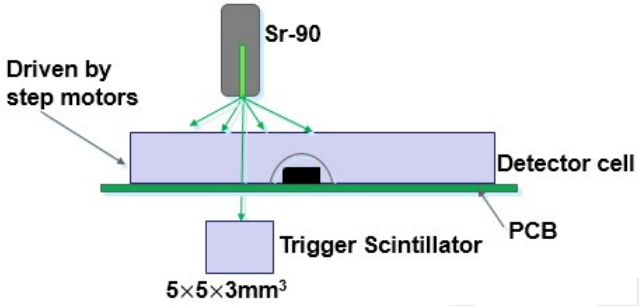

Figure 6.46: Setup of uniformity measurement

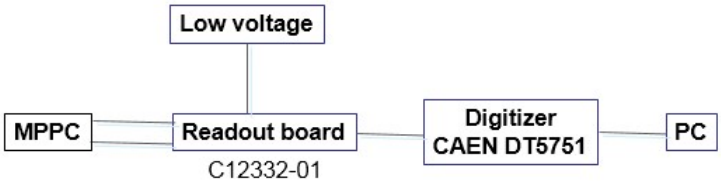

Figure 6.47: Block diagram of data acquisition

Three different sizes tiles ($30\times30\times3$mm^3, $30\times30\times2$mm^3 and $50\times50\times3$mm^3) were tested by the Hamamatsu MPPC S12571-025P and S13360-025PE. The photosensitive area of module MPPC S12571-025P is 1×1 mm^2 containing 1600 pixels, and each pixel is 25 μm$\times$25 μm in size. The MPPC S13360-1325PE whose sensitive area is 1.3mm$\times$1.3mm contains 2668 pixels. The spatial distribution of p.e. (photon equivalents) number with different detector cell areas are shown in Figure 6.48. So the p.e. number presents signal amplitude of different tile areas. It can be seen that the number of p.e. in the center area is a little higher than that of the surrounding area because the MPPC is placed in the center area and there is less self-absorption in the area close to the MPPC. The global mean response is around 32.2p.e. and 100% of the cell area is within 10% deviation from the mean value for $30\times30\times3$mm^3 cell. The global mean response is around 34.29p.e. and 100% of the cell area is within 10% deviation from the mean value for $30\times30\times2$mm^3 cell. The three detector cells show good response uniformity. The global mean response is around 8.57p.e. and 94% of the cell area is within 10% deviation from the mean value for $50\times50\times3$mm^3 cell.

Cosmic-ray measurement: The cosmic-ray test setup for measuring responses of scintillator cells to muons is shown in Figure 6.49 . The detector cell is placed between two trigger scintillators ($20\times20\times3$mm^3) tiles. A lead is placed between the detector cell and bottom trigger scintillator to select higher energy cosmic ray events. The coincidence of two trigger signals ensures a muon track passing though the detector cell. Four kinds of tiles with different sizes ($30\times30\times3$mm^3, $40\times40\times3$mm^3, $50\times50\times3$mm^3 and $30\times30\times2$mm^3) were measured.

The single photon spectrum of SiPM was used to calibrate the test system, as shown in Figure 6.50 (left). The cosmic-ray MIP response spectrum is shown in Figure6.50 (right). It is fitted by a Landau convoluted with Gaussian distribution.

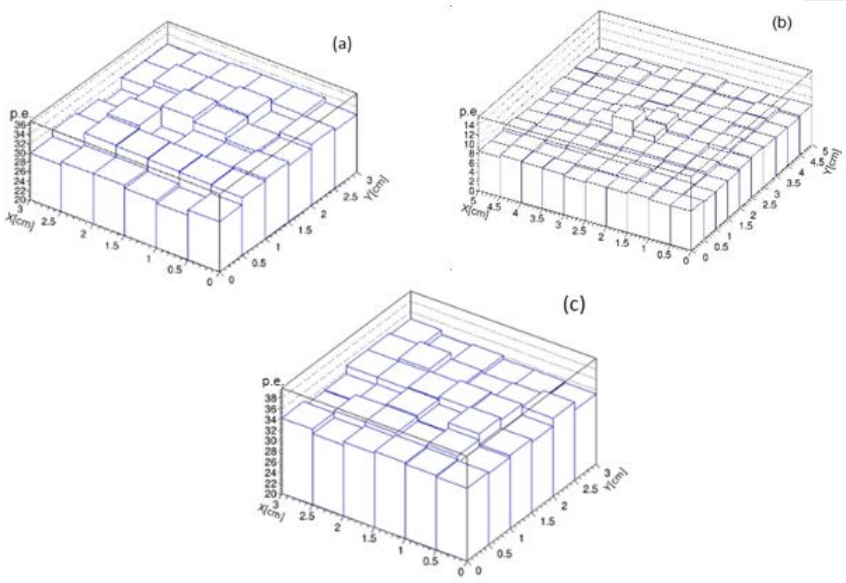

Figure 6.48: The uniformity measurement result of $30\times30\times3mm^3$(a), $50\times50\times3mm^3$(b)and $30\times30\times2mm^3$(c)detector cell

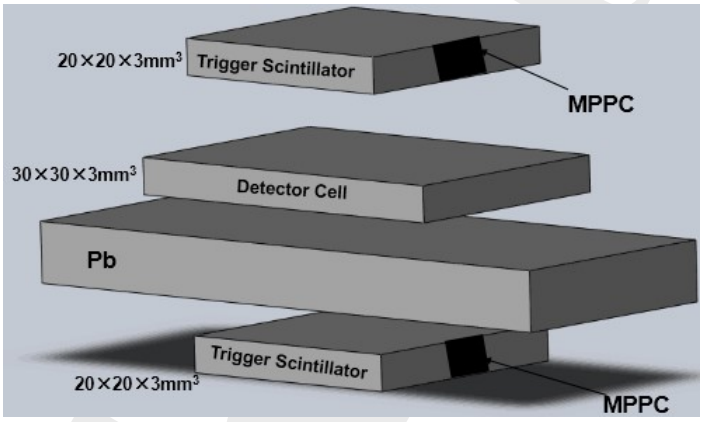

Figure 6.49: Schematic diagram of cosmic-ray measurement setup

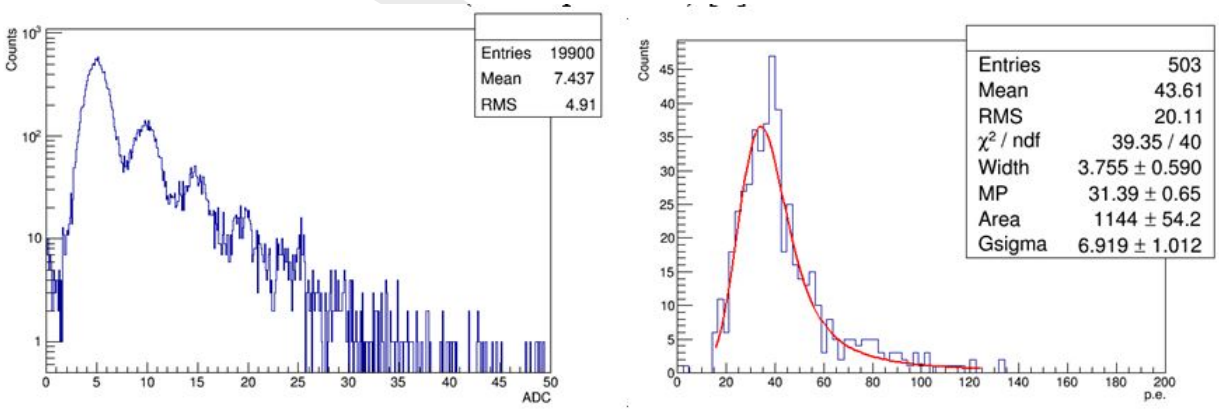

Figure 6.50: Single photon spectrum of MPPC (left) and responses to muons of $30\times30\times3mm^3$ detector cell (right)

Seven detector cells of different sizes, polishing methods and wrapping foil types were measured and summarized in figure 6.51. The larger the area of the cell is, the less p.e. are detected, and the results of same size cells varied greatly because of the polishing methods. As is shown in the table that the ESR foil performs better than the TYVEK reflective foil. The cell with the size of $30\times30\times2mm^3$ detected 33.89 ± 0.49 p.e. because of the larger photosensitive area of MPPC.

No.	Detector Cell	MPPC Type	Reflective Foil Type	Mean $N_{p.e.}$	Polishing Methods
1	$30\times30\times3mm^3$	S12571-025P	ESR	31.39 ± 0.65	Ultra Precise Polishing
2	$30\times30\times3mm^3$	S12571-025P	ESR	22.55 ± 0.7	Precise Polishing
3	$30\times30\times3mm^3$	S12571-025P	ESR	18.92 ± 0.39	Rough Polishing
4	$30\times30\times3mm^3$	S12571-025P	TYVEK	13.63 ± 0.33	Precise Polishing
5	$40\times40\times3mm^3$	S12571-025P	ESR	14.89 ± 0.73	Precise Polishing
6	$50\times50\times3mm^3$	S12571-025P	ESR	9.87 ± 0.43	Precise Polishing
7	$30\times30\times2mm^3$	S13360-1325PE	ESR	33.89 ± 0.49	Precise Polishing

Figure 6.51: Cosmic-ray measurement results of detector cells with different sizes

MIPs Detection efficiency: The detection efficiency of $30\times30\times3mm^3$ and $50\times50\times3mm^3$ were measured by the cosmic ray test. The detection efficiency of $30\times30\times3mm^3$ and $50\times50\times3mm^3$ cells are 99%, 98.2%, respectively. According the cosmic-ray test result, the detection efficiency of $30\times30\times2mm^3$ with S13360-025PE MPPC also can reach to 98

Several size plastic scintillator detector cells of AHCAL were tested. The response uniformity, cosmic-ray responses and detection efficiency of detector cells were measured. The good response uniformity and high detection efficiency results show that both $30\times30\times3mm^3$ and $50\times50\times3mm^3$ cells are acceptable for AHCAL. The size of detector cell will be decided by the simulation result.

6.3.3.3 NDL EQR-SiPM for CEPC AHCAL

SiPM with epitaxial quenching resistors (EQR SiPM) is one of the main SiPM technologies now under development [16,17]. This kind SiPM was developed in China. As shown in Figure6.52, each APD cell (pixel) forms a high electric field, composing an enriched region between N-type epitaxial silicon substrate and P++ cap layer, and it employs the un-depleted region in the epitaxial silicon layer below P/N junction as the quenching resistor. Compared to conventional SiPM configurations that employ poly-silicon quenching resistors on the device surface, it is easier to achieve high density and small micro APD cells, thus obtaining a small junction capacitor; it is also easy to realize low resistance for the quenching resistors, simply based on the resistivity of the epitaxial layer and the geometrical scale. As a result, a low RC time constant of the pixel, or a short recovery time and fast counting rate for the EQR SiPM, can be expected. In addition, thanks to the high geometrical fill factor of the EQR SiPM with a high density of micro APD cells, both wide dynamic range and adequate PDE can be realized at the same time, which satisfactorily resolves the conflict between dynamic range and PDE existing in most commercial SiPMs with poly-silicon stripes as quenching resistors.

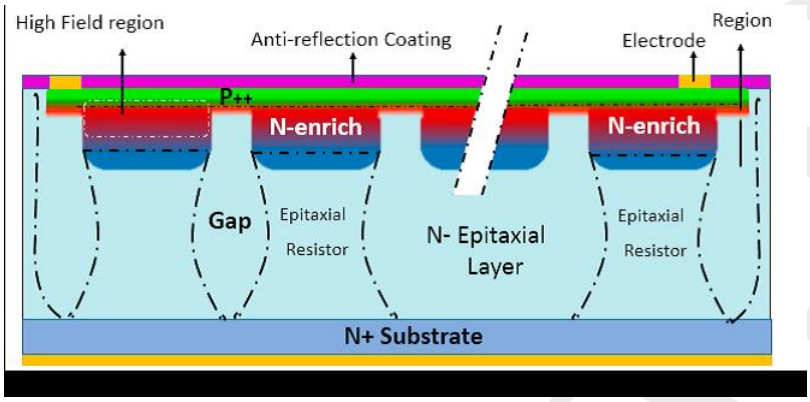

Figure 6.52: Schematic structure of EQR SiPM; APD cell consists of N-enriched regions forming high electric fields between the N-type epitaxial silicon wafer and the P++ surface layer, the un-depleted region in the epitaxial silicon layer below the P/N junction as the quenching resistor, and the APD cells are isolated from each other by the Gap depletion region.

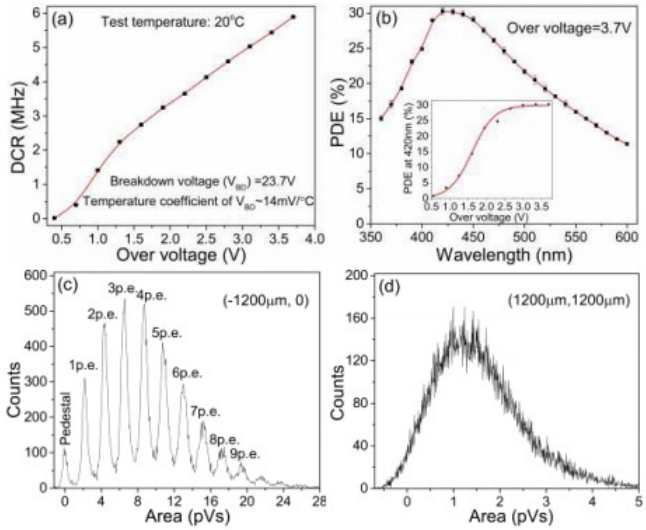

Figure 6.53: Characteristics of NDL EQR PS-SiPM. (a) DCR vs over voltages. (b) PDE vs the wavelength of 360nm-600nm at over voltage of 3.7V; peak PDE is at 420nm and is improved with the increase of over voltage as shown in the inset. (c), (d) show the pulse area distribution collected by cathode at the incident light positions of (1200um, 0) and (1200um, 1200um) respectively. Because of the pedestal electronic noise, the pulse area is starting at negative values.

Furthermore, the fabrication technology of NDL EQR-SiPM is simple, it omits the fabrication steps for producing quenching resistors on the surface; thus, the price of NDL EQR-SiPM is low. Its good property and low price can meet AHCAL requirement, and it will be tried to be used on CEPC-AHCAL detector. Figure 6.53 show some performance of NDL EQR-SiPM, and figure 6.54 show the performance compare between NDL EQR-SiPM and Hamamastu MPPC.

6.3.3.4 Electronics and DAQ

Front-end electronics ASIC: High-density electronics is indispensable to instrumentation of high-granularity calorimetry. An ASIC chip named SPIROC, developed by the OMEGA group, is capable to handle 36 SiPMs. For each channel, it can be operated in

NDL EQR-SiPM VS Hamamatsu MPPC

	NDL SiPM		Hamamatsu MPPC	
Effective Active Area	11-3030 B-S	22-1414 B-S	S13360-3025PE	S13360-1325PE
	3.0×3.0 mm²	1.4×1.4 mm² (2×2 Array)	3.0×3.0 mm²	1.3×1.3 mm²
Effective Pitch	10 μm	10 μm	25 μm	25μm
Micro-cell Number	90000	19600	14400	2668
Fill Factor	40%	40%	47%	47%
Breakdown Voltage (V_b)	23.7±0.1V	23.7±0.1V	53±5V	53±5V
Measurement Overvoltage (V)	3.3	3.3	5	5
Peak PDE	27%@420nm	35%@420nm	25%@450nm	25%@450nm
Max. Dark Count (kcps)	< 7000	<1500	1200	210
Gain	2×10^5	2×10^5	7.0×10^5	7.0×10^5
Temp. Coef. For V_b	17mV/° C	17mV/° C	54mV/° C	54mV/° C

Figure 6.54: Performance compare between EQR SiPM and Hamamatsu MPPC with similarly high micro-cell density.

an auto-trigger mode and has a dual-gain charge preamplifier with high dynamic range. It allows to measure for each channel the charge from 1 to 2000 photo-electron and the time within 1 ns using a 12-bit digitizing circuit. With one 8-bit 5V input DAC per channel, the bias voltage for each SiPM can be adjusted to reach its optimum. In each channel, there are 16 analogue memory cells that can buffer both charge and timing signals to be digitized afterwards consecutively. The digitization circuit is shared for both charge and timing measurements to minimize the power consumption, which needs to be as low as $25\ \mu W$ per channel. The latest version SPIROC2E has been improved in many aspects and its packaging has changed to a thinner BGA, which ensures a compact design for HBU and allows better automated mass soldering.

HCAL Base Unit: A merit of the AHCAL electronics is flexibility. One full AHCAL active layer can be constructed by connecting several base units (namely HBUs) via connectors, each with 12×12 channels in a square plate of $36 \times 36\ cm^2$. The exact granularity is being optimized for CEPC to balance between the detector performance and the number of total channels. To achieve a compact HCAL design, the PCB for each HBU should be thin enough and a 6-layer PCB within 1 mm thickness is proved to be feasible.

As a semiconductor detector, SiPM is intrinsically sensitive to environmental changes, especially temperature. Thus each SiPM needs on-site calibration, which requires an on-board LED circuit for each channel. There is an LED circuit at each channel of an HBU, which can emit UV light to a scintillator tile. Using these photons, the gain of a SiPM can be extracted and monitored.

Detector interface: ASIC chips are controlled by an interface board named DIF (Detector Interface). One DIF board handles a full HCAL active layer (a long slab with up to 6×3 HBUs), corresponding to 72 ASICs in total. The expected data rate per DIF can be estimated based on the event rate at HCAL, which depends on the beam structure at CEPC.

LED calibration board: A dedicated LED calibration board is needed to control all LED circuits in an HCAL active layer. It can send trigger signals for the proper SiPM calibration.

Power board: SiPM operation relies on a proper reversely bias voltage. Therefore, between power supplies and ASIC chips, a power board is required to distributing the bias voltage to each SiPM. This power board can also play an important role in regulating voltages for protection and smooth working of SiPMs. Like the DIF board, it would be feasible to use only one such board for an active HCAL layer (up to 6×3 HBUs).

6.3.3.5 DAQ system

DAQ hardware: DAQ system is also required to be compatible to the final detector layout, where two hardware parts are essential. One part is so-called LDA (Link to Data Aggregator), which collects all the data via DIFs from active layers in an HCAL segment and transmit them to a back-end PC for further processing or storage. Smart units like FPGAs are equipped on this board for data packaging and transmission. Modern FPGAs integrated with RAMs are an ideal option to have a capability of data buffering and some advanced feature like system on chip.

The other key hardware part is so-called CCC (Clock and Control Card), which provide a global clock signal and synchronize DIFs. Control signals are also sent to DIFs including starting and stopping acquisition.

DAQ software: The DAQ software is being developed in the framework of EUDAQ supported by AIDA2020, aiming for a generic solution for a combined setup with several detectors, which is important in test-beam activities during the prototyping phase. The latest version EUDAQ2 has made much progress during extensive beam tests for various combinations of detectors and can be considered as a solution for further HCAL prototyping and beam-test campaigns for CEPC.

6.4 Dual-readout Calorimetry

6.4.1 Introduction

Till now, the performance obtained in hadronic energy measurements has been by far worse than for the electromagnetic ones, since showers from single hadrons or jets develop an electromagnetic component (em fraction, f_{em}), from π^0 and η production, that exhibits large event-by-event fluctuations and dependence on the particle type and energy [26].

As a matter of fact, the em fraction changes as a function of the particle initiating the shower (e.g., π, K, p) since, for example, impinging $\pi^{\pm}$ mesons can undergo a charge-exchange reaction with a nucleon as first interaction and generate a pure em shower, while a p can't do that.

Moreover, since π^0 production happens at any stage of shower development, the f_{em} increases with the energy as well as with the depth ("age") of the shower.

The em and $non-em$ components of a hadronic shower are normally sampled with very different sensitivity, producing large differences in the measured signals, heavily affecting the energy resolution capability.

To overcome the problem two methods have been exploited: compensation and dual readout (DR). The first relies on equalising the detector response to electromagnetic and

non-electromagnetic shower particles but requires the integration of the signals over large volumes (and long time) and leads to limited resolution for electromagnetic showers. The DR method allows to avoid these limitations by measuring and accounting for the f_{em}, on event-by-event basis. The showers are sampled through two independent processes, namely scintillation and Čerenkov light emissions. The former is sensitive to all ionizing particles, while the latter is produced by highly relativistic particles only, almost exclusively found inside the em shower component. By combining the two measurements, energy and f_{em} of each shower can be simultaneously reconstructed. The performance in hadronic calorimetry may be boosted toward its ultimate limit.

Over the last 15 years, the DREAM/RD52 collaboration at CERN has deeply investigated both homogeneous and sampling DR solutions [27]. The first don't suffer from sampling fluctuations and have, in principle, much higher light yields.

Nevertheless, the two signals are mixed together and must be separated by means of optical filters and/or timing properties. Last but not least, the cost of building a fully-homogeneous hadronic calorimeter looks prohibitive.

On the other hand, in sampling calorimeters, the two signals (from scintillation and Čerenkov light) are separated by construction since they are measured in independent detector elements. The results obtained so far show that a sampling fibre calorimeter may reach resolutions close to $10\%/\sqrt{E}$ for em showers and better than $\sim 30 - 40\%/\sqrt{E}$ for hadronic showers, coupled with strong standalone particle-ID capabilities. This allows $W \rightarrow jj$ separation from $Z \rightarrow jj$ by invariant mass, high-precision missing ν three-vector by subtraction, e-μ-π separation and tagging.

The intrinsic high granularity, exploited with Silicon Photo-Multipliers (SiPM) single-fibre readout, may as well provide powerful input to particle flow algorithms.

Indeed, while the DR concept has been extensively proven and experimentally validated in a series of beam tests, the use of standard Photo-Multiplier (PM) tubes to read out the Čerenkov and scintillation light has so far limited its development towards a full-scale system compliant with the integration in a particle detector at a colliding beam machine. These limitations can be overcome using SiPM, low-cost solid-state sensors of light with single photon sensitivity, magnetic field compliance and design flexibility. Concerning devices built on materials other than silicon, a relevant advantage in the detection of the Čerenkov light could in principle come from the development of sensors based on Silicon Carbide (SiC), essentially because of its UV sensitivity and visible-light blindness.

6.4.2 Dual-Readout Calorimetry

The independent sampling of hadronic showers, through scintillation and Čerenkov light emission, allows to fully reconstruct, at the same time, energy and f_{em} of hadronic showers. In fact, the total detected signals, measured with respect to the electromagnetic energy scale, can be expressed as:

$$S = E\,[\, f_{em} + \eta_S \cdot (1 - f_{em})\,] \tag{6.5}$$

$$C = E\,[\, f_{em} + \eta_C \cdot (1 - f_{em})\,] \tag{6.6}$$

where $\eta_S = (e/h)_S$ ($\eta_C = (e/h)_C$) is the relative yield of the scintillation (Čerenkov) signal for the em to the hadronic component of the shower. The system can be easily solved giving:

$$\frac{C}{S} = \frac{[\, f_{em} + \eta_C \cdot (1 - f_{em}) \,]}{[\, f_{em} + \eta_S \cdot (1 - f_{em}) \,]} \tag{6.7}$$

$$E = \frac{S - \chi C}{1 - \chi} \tag{6.8}$$

where:

$$\chi = \frac{1 - \eta_S}{1 - \eta_C} = \cot\, \theta \tag{6.9}$$

This is the simplest formulation of hadronic calorimeter response: an em part with relative response of unity, and a $non - em$ part with relative response η.

There are two unknowns for each shower, E and f_{em}, and two measurements S and C. The electromagnetic fraction, f_{em}, is determined entirely by the ratio C/S, and the shower energy calculated as in Eq. (4). Both C and S (e/h) ratios have event-by-event fluctuations and should be considered stochastic variables, nevertheless the average $<e/h>$ values are essentially independent of hadron energy and species [28–30]. The global parameter χ can be extracted with a fit to calibration data:

$$\chi = \frac{E_0 - S}{E_0 - C} \tag{6.10}$$

$$S = (1 - \chi)E_0 + \chi C \tag{6.11}$$

where E_0 is the beam energy.

The geometrical meaning of the θ angle can be understood by looking at the scatter plor of C versus S signals. In Figure 6.55, there are both (a) a prediction for the normalised scatter plot for protons and pions, and (b) the observed scatter plot for 60 GeV pions, in the RD52 lead/fibre calorimeter.

The plot in Figure 6.55(b) shows the data points located on a locus, clustered around a line that intersects the C/S = 1 line at the beam energy of 60 GeV. χ is the energy-independent slope of the event locus. This is to be expected. In first approximation, the signal generated in the Čerenkov fibers is produced only by the em components of the hadron showers. The larger the em fraction f_{em}, the larger the C/S signal ratio. Events in which (almost) the entire hadronic energy is deposited in the form of em shower components give signals very similar to those from 60 GeV electrons and are, therefore, represented by data points located near (S=60, C=60) in the plot.

All signals are relative to the em scale meaning that both the Čerenkov and the scintillation responses have to be calibrated with electrons only, i.e. no hadronic calibration is required. This is one of the most qualifying point of dual-readout calorimetry.

The effectiveness of this approach has been probed by the DREAM/RD52 collaboration over a 15-year research program with a variety of detector solutions. Results and simulations [31–36] provide, so far, confidence that a fibre-sampling calorimeter, even without longitudinal segmentation, may meet the requirements of the CepC physics programme in a cost-effective way. Linearity and energy resolution, for both em and hadronic showers, $e/\pi/\mu$ separation, spatial resolution, all show adequate performance.

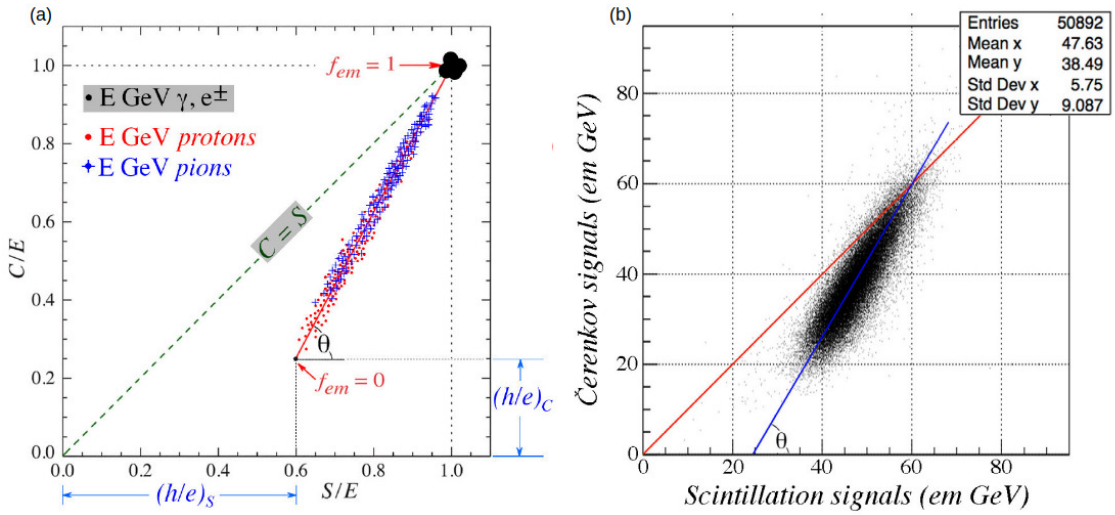

Figure 6.55: (a) Scatter plot of C/E versus S/E in a dual-readout calorimeter for p and π; (b) scatter plot of C versus S signals for 60 GeV pions in the RD52 dual-readout lead/fibre calorimeter.

6.4.3 Layout and Mechanics

6.4.3.1 Layout

A possible projective layout has been studied by the 4th Detector Collaboration and described in its LoI [37]. Assuming the converter to be copper, the calorimeter is a copper matrix loaded with 1 mm diameter, 1 mm apart, alternate scintillating and clear (for Čerenkov light detection) fibres. About 200 cm (10 λ) long, projective towers cover (at $\theta \sim 90°$) about 1.4° in both ϕ and θ, with of the order of 2000 fibres per tower. The dimensions of the inner faces in the barrel section depend on θ, and increase going in the forward direction. The sampling fraction is kept constant by fibres starting at different depths inside each tower.

This layout has been already imported in the simulations for the CepC detector and will be validated in the next months.

6.4.3.2 Mechanics (Material Choice and Machining)

Both lead and copper have been used as absorber materials by the DREAM/RD52 collaboration. Their main properties are:

$$Lead : \rho = 11.3\ g/cm^3,\ X_0 = 0.56\ cm,\ \rho_{Mol} = 1.60\ cm,\ \lambda_{int} = 170\ mm \quad (6.12)$$

$$Copper : \rho = 8.96\ g/cm^3,\ X_0 = 1.44\ cm,\ \rho_{Mol} = 1.56\ cm,\ \lambda_{int} = 151\ mm \quad (6.13)$$

meaning that, for hadronic showers, a full-coverage solution with lead will give broader and longer showers and a total mass 42% heavier than using copper. A full-containment $3 \times 3 \times 10\ \lambda^3$ prototype will need about 5 tons of material with lead and 2.8 tons with copper.

An even stronger reason in favour of copper is the fact that, being the Čerenkov light almost exclusively produced by the em shower components and the (e/mip) ratio 50% higher for copper than for lead, the Čerenkov light yield should be significantly higher in copper, resulting in a better hadronic resolution.

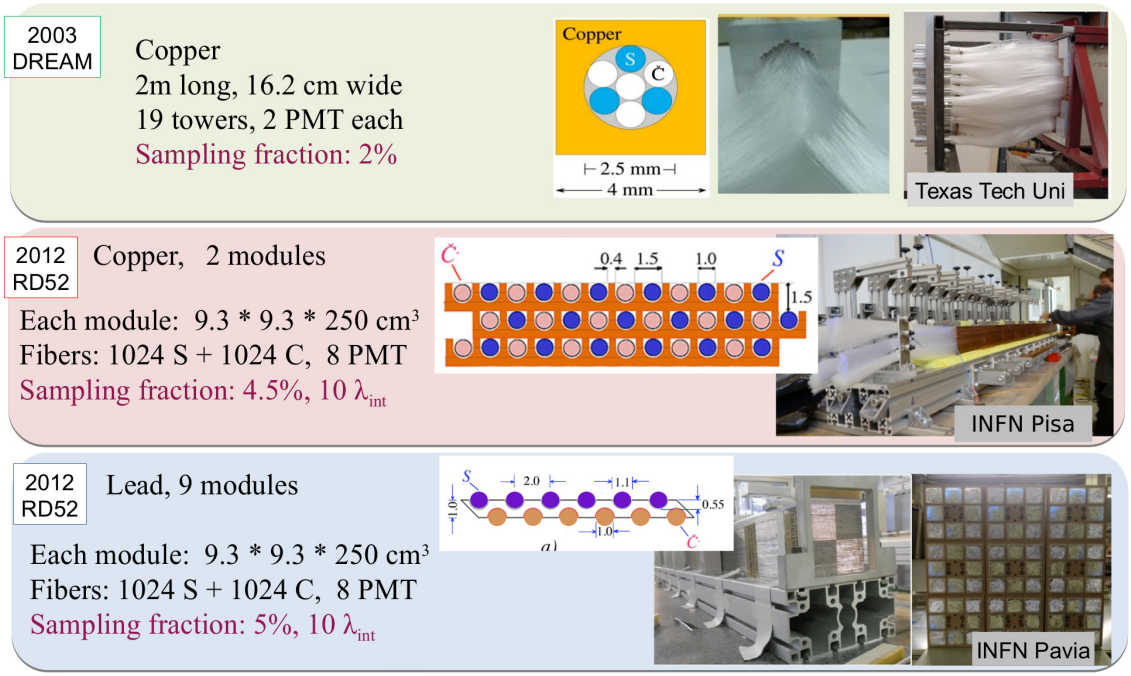

Figure 6.56: The DREAM calorimeter (top), built in 2003, and the RD52 prototypes, with copper (middle) and lead (bottom), built in 2012.

On the other hand, copper extrusion, with the required tolerances in planarity and groove parallelism, is not yet an established industrial process. A variety of techniques (extrusion, rolling, scraping and milling) for machining the converter layers have been tested, essentially by John Hauptman and collaborators at Iowa State University and by Fabrizio Scuri at INFN-Pisa. None has been qualified for a large-scale production and identifying an industrial and cost-effective process, including moulding, is a relevant issue.

In the 3-year R&D INFN program, under discussion, the identification of an industrial procedure to produce the converter layers is one key point.

Alternative copper alloys (brass, bronze) will be investigated as well, both for addressing the production process issues and for optimising the detector performance.

6.4.4 DREAM/RD52 Prototype Studies

Different prototypes were built and studied by the DREAM/RD52 collaboration, with copper or lead as absorber. A summary of the most significant results [31–36] is given, in particular for the matrices built in 2012: a matrix of 9 lead modules and a matrix of 2 copper modules, each module $9.3 \times 9.3 \times 250\ cm^3$ (see Figure 6.56 for the mechanical details, the first DREAM calorimeter built in 2003 is also shown on the top). From the readout point of view, the calorimeter was arranged as in Figure 6.57.

6.4.4.1 Electromagnetic Performance

In Figure 6.58 the linearity of the response for both matrices is shown. The range of measurement is different for the two (spanning 6-60 GeV for Cu and 60-150 GeV for Pb). The deviations for the very first points ($\lesssim 10\ GeV$) are likely due to the spread of the energy of the beam particles.

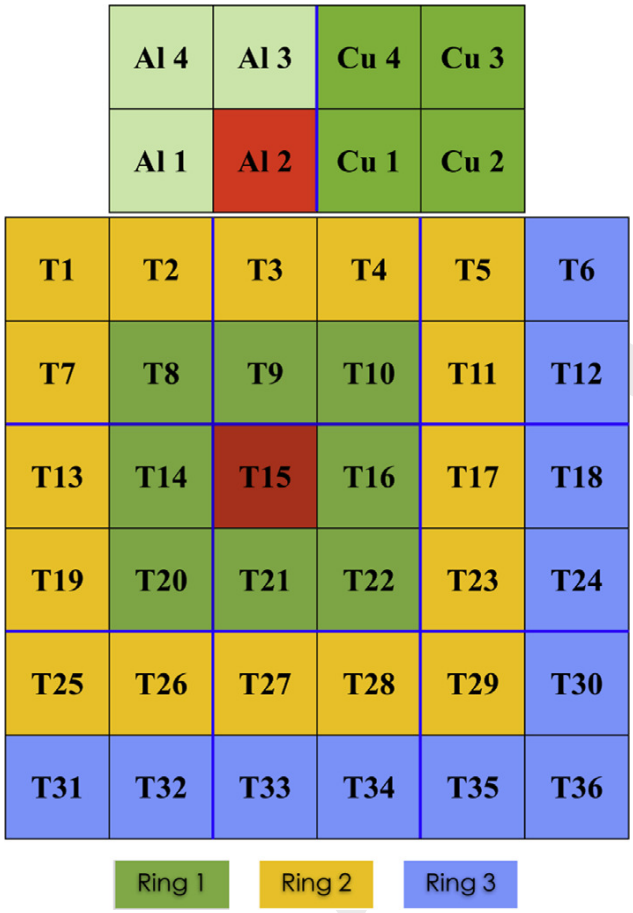

Figure 6.57: The RD52 calorimeter as tested at the end of 2012. It consisted of 9 lead-based modules, each consisting of 4 towers (towers 1-36), and 2 copper-based modules, placed on top of the lead array. Each tower was readout by two photomultipliers, one for scintillation and one for Čerenkov light detection. The left copper module (of which the towers are marked as âĂIJAlâĂİ) was equipped with Čerenkov fibres with an aluminised upstream end face. For the measurements described in this paper, the particle beams were typically steered in the center of tower T15.

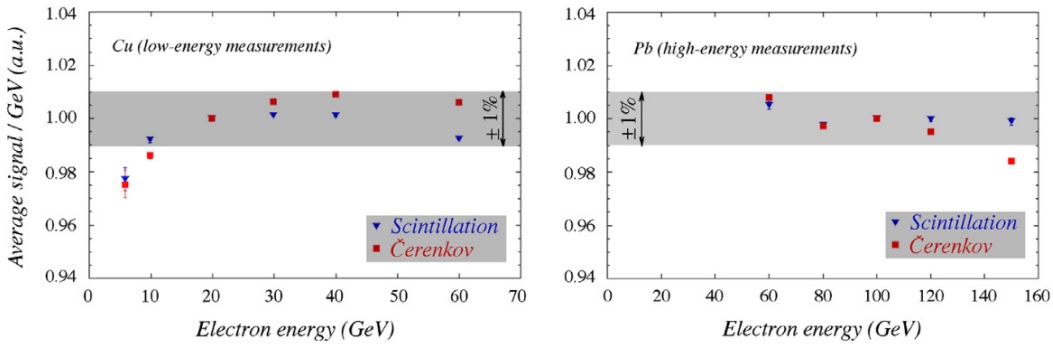

Figure 6.58: The linearity of the copper (left) and lead (right) based fibre calorimeters for em shower detection in the scintillation and Čerenkov channels.

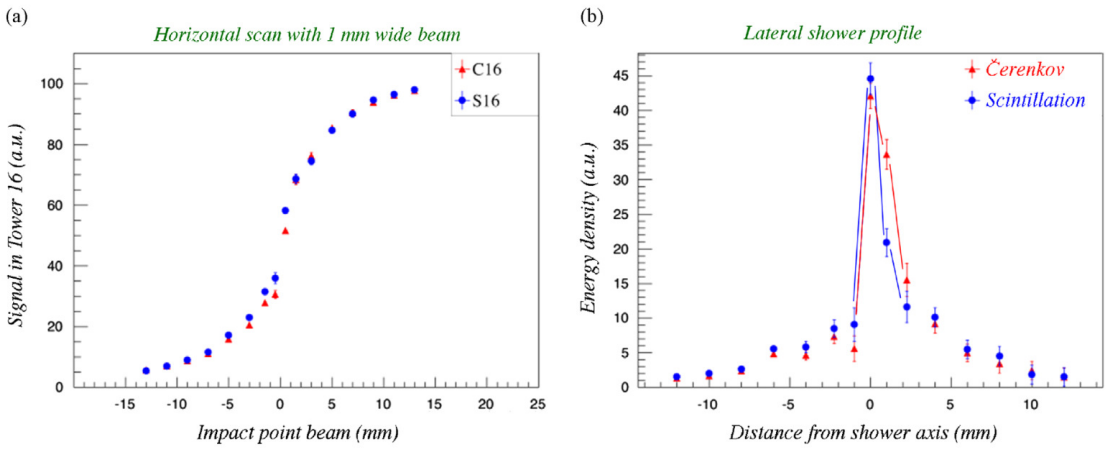

Figure 6.59: The signal from a 1 mm wide beam of 100 GeV electrons, as a function of the impact point (a), and the lateral shower profiles derived from this measurement (b).

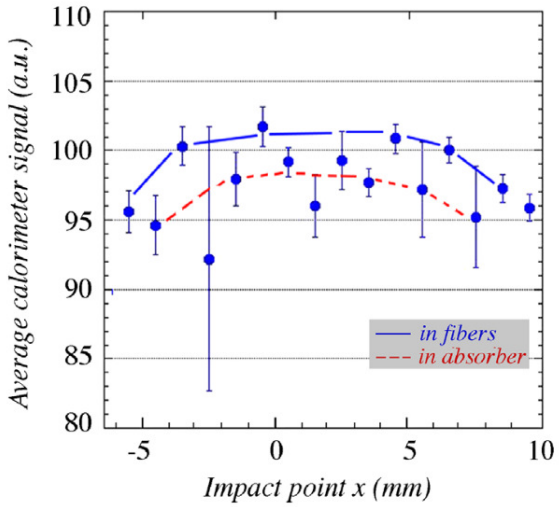

Figure 6.60: The scintillation signal for 100 GeV electrons developing showers in the lead matrix as a function of the beam impact point.

Figure 6.59 shows the radial shower profile and the sensivity to the impact point: the core of the signal spans just few mm. Figure 6.60 shows the dependence of the S signal on the impact point for particles entering parallel to the fibres. This introduces a constant term in the resolution that can be avoided with a small tilt of the fibre axis. In the C fibres, the problem doesn't show up since the early (collimated) part of the shower produces photons outside the numerical fibre aperture.

For the reconstruction of the energy of em showers, C and S signals provide independent uncorrelated measurements, with different sensitivity of the response. They are affected by different problems: S signals have a photo-electron statistics of at least one order of magnitude higher than C signals, and their fluctuations are largely dominated by the sampling fluctuation of the energy deposits. C signal fluctuations are generally dominated by the limited photo-electron statistics, expecially at low energies. Nevertheless, for C signals, the constant term is negligible giving a better resolution at high energies. Averaging the two measures improves the resolution up to a factor of $\sqrt{2}$. Separate and

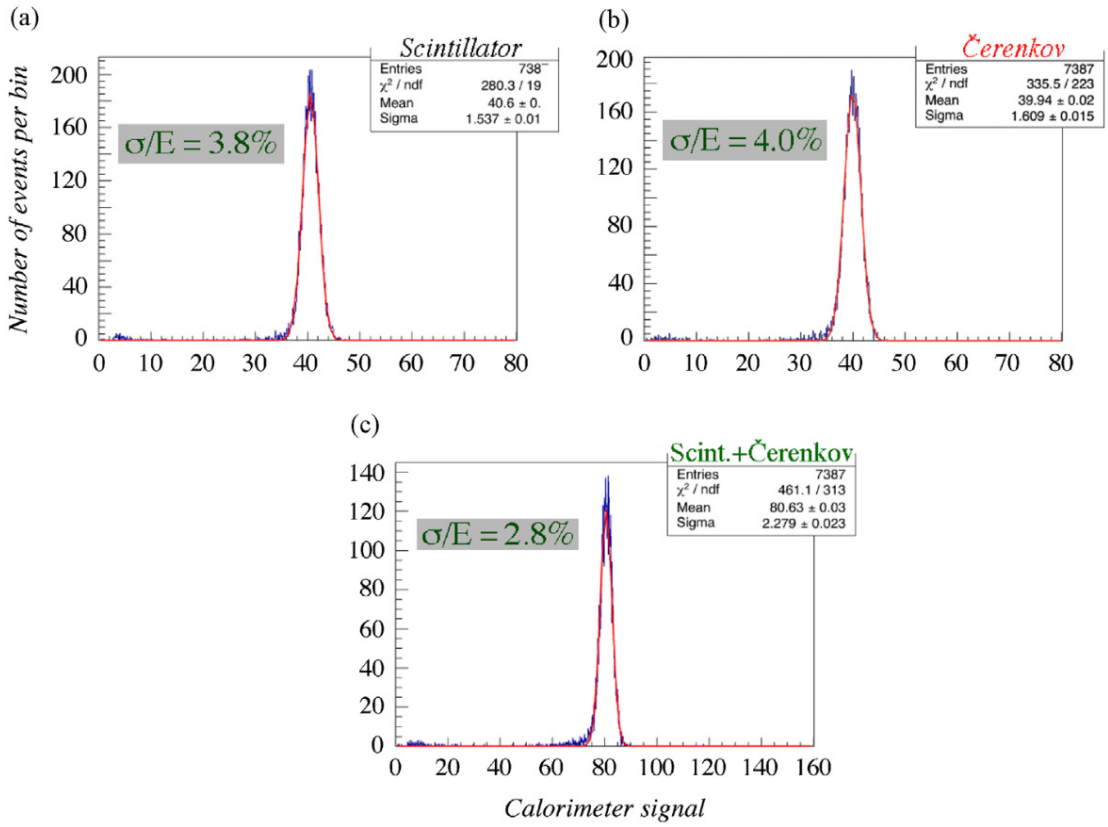

Figure 6.61: Signal distributions for 40 GeV electrons in the copper-fibre calorimeter: from the sum of the scintillating fibres (a), of the Čerenkov fibres (b), of all fibers (c). The angle of incidence of the beam particles ($\theta,\ \phi$) was $(1.5°, 1.0°)$. The size of the beam spot was $10 \times 10\ mm^2$.

combined (unweighted) results for the copper matrix are shown in Figure 6.61 for 40 GeV electrons.

In Figure 6.62, the electromagnetic resolution is shown for the 2 matrices.

6.4.4.2 Hadronic Performance

The RD52 lead matrix response was studied with pion and proton beams [36]. High-multiplicity events ("jets") were also generated by means of a target. The energy was reconstructed with the dual-readout relation (Eq. 4), that restores a gaussian behaviour and linearity of the response (Figure 6.63 and Figure 6.64).

The comparison of p and π signals at 80 GeV is shown in Figure 6.65, confirming that the method largely compensates for the differences in shower composition.

The limited lateral size of the matrix (about 1 λ) allows to collect, in average, $\sim 90\%$ of the shower energy so that leakage fluctuations dominate the resolution capability. Leakage counters were used to select events about fully contained (that of course, tend to have a higher f_{em}). The resolution improves by a factor of almost 2 in this case (Figure 6.66). A second effect affecting resolution is the light attenuation in the fibres, that causes early starting showers to be observed at lower signal values. The hadronic resolution, to be corrected for both effects, was reconstructed to be $\sim 70\%/\sqrt{E}$.

Geant4 simulations point at a possible resolution of $\sim 30\%/\sqrt{E}$, allowing sensible separation of the W/Z decays to jet pairs (Figure 6.68). The figure summarizes the situ-

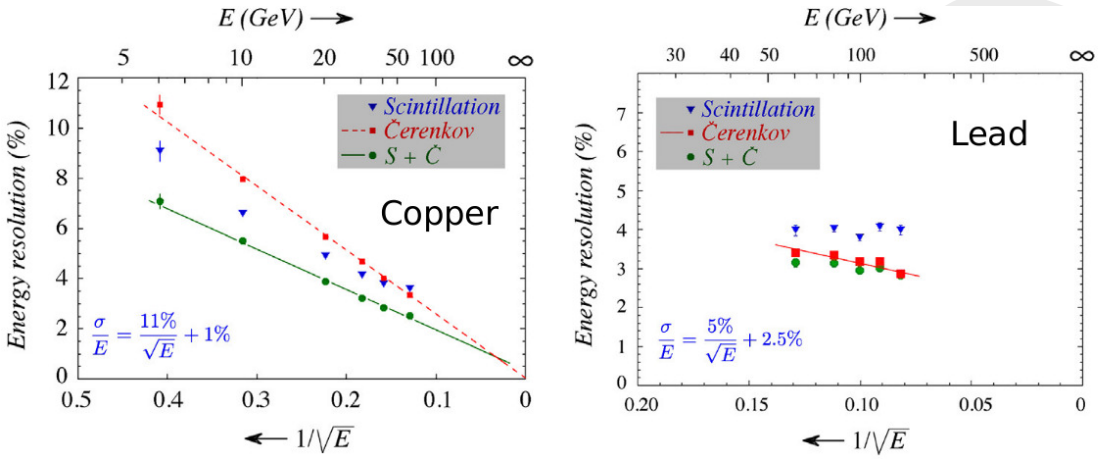

Figure 6.62: The energy resolution for electrons in the copper-fibre module (left) and in the lead-fibre module (right), as a function of the beam energy. Shown are the results for the two types of fibres, and for the combined signals. The angle of incidence of the beam particles (θ, ϕ) was $(1.5°, 1.0°)$. The size of the beam spot was $10 \times 10\ mm^2$.

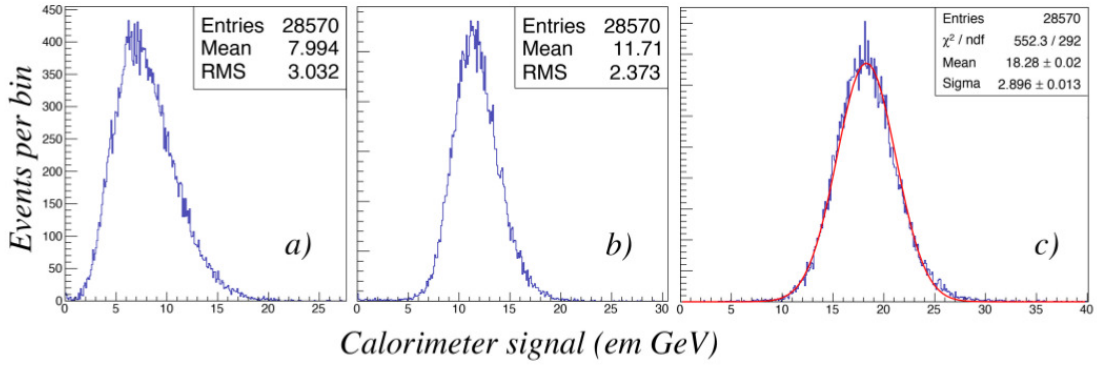

Figure 6.63: Signal distributions for 20 GeV π^- particles. Shown are the measured Čerenkov (a) and scintillation (b) signal distributions as well as the signal distribution obtained by combining the two signals according to Equation 4, with $\chi = 0.45$ (c).

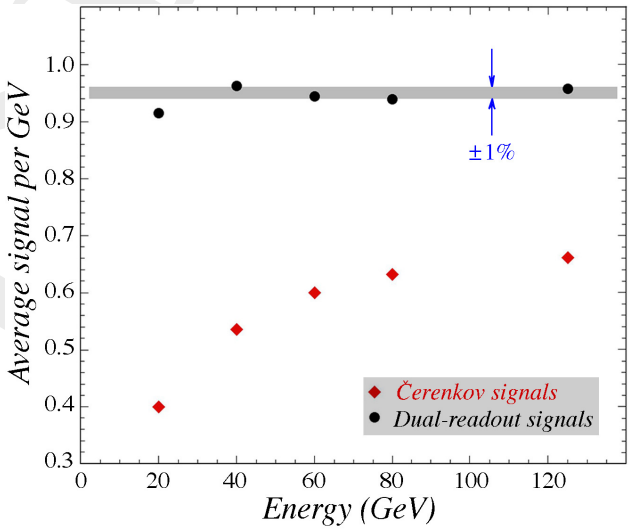

Figure 6.64: The hadronic response for single pions. Shown are the average Čerenkov signal and the dual-readout signal (Eq. 4) per unit deposited energy, as a function of the pion energy.

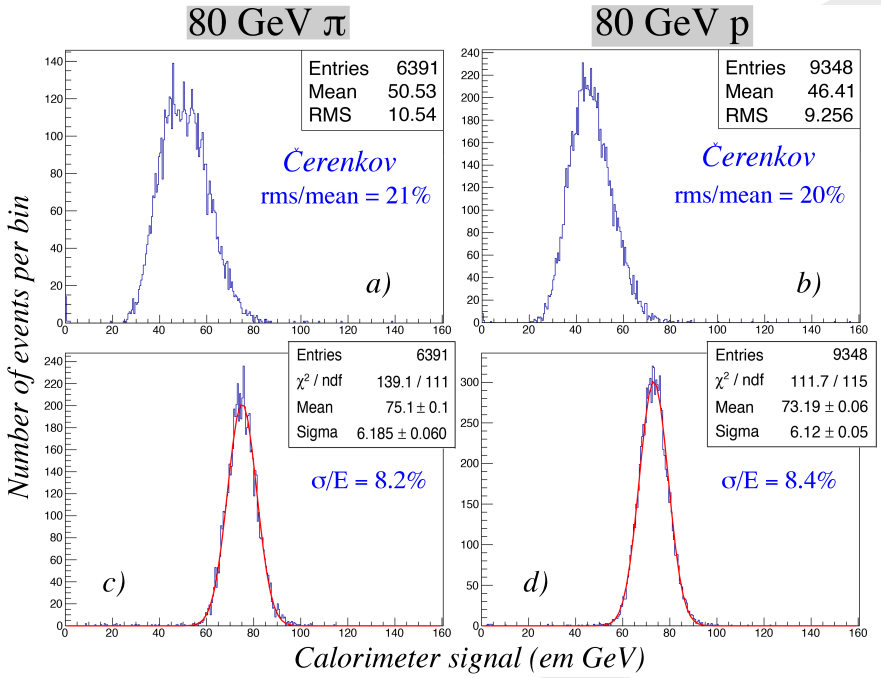

Figure 6.65: Signal distributions for the Čerenkov signals from 80 GeV π^+ (a) and protons (b), as well as the dual-readout total signals for 80 GeV π^+ (c) and protons (d).

ation concerning the hadronic energy resolution, for single pions. Experimental data on hadronic performance compared to GEANT4 simulations are shown in Figure 6.68(a). The experimental data obtained with the original DREAM fibre calorimeter, which had a lateral cross-section of $820\ cm^2$, are compared [35] with simulations using the standard FTFP_BERT hadronic simulation package for the geometry of that detector. The improvement expected for a larger detector ($65 \times 65\ cm^2$ lateral cross-section) with the RD52 geometry is also shown, both for the standard FTFP_BERT package and for the high-precision version of this package. For comparison, the record setting experimental data reported by SPACAL [38] are also shown, as well as a curve representing an energy resolution of $30\%/\sqrt{E}$.

6.4.4.3 e/π Separation

Four discriminating variables were identified for implementing e/π separation: the fraction of energy in the central tower, the Čerenkov/scintillation light signal ratio, the signal starting time, the total charge/amplitude ratio, shown in Figure 6.69. A multivariate neural network analysis showed that the best e/π separation achievable for 60 GeV beams was 99.8% of electron identification efficiency with 0.2% pion misidentification. Further improvements may be expected by including the full time structure information of the pulses, especially if the upstream ends of the fibers are made reflective.

6.4.5 Sensors and Readout Electronics

Separately read out the signals from the Čerenkov and scintillation fibre forest and avoid oversampling of late developing showers is an issue that may be successfully addressed through the use of Silicon Photo-Multipliers (SiPM), allowing the separate reading of each fibre and magnetic field insensitivity. This, in principle, assuming powering and cooling

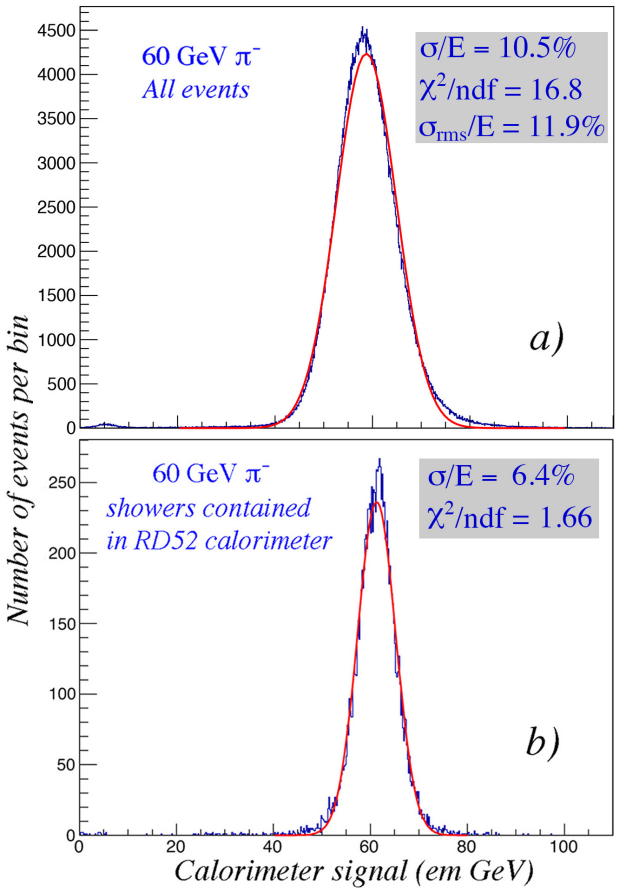

Figure 6.66: Total signal distributions for 60 GeV $\pi^?$, measured with the dual-readout method. Shown are the distributions for all events (a) and for events fully contained inside the calorimeter, i.e., for which no energy leakage was measured in the leakage counters (b).

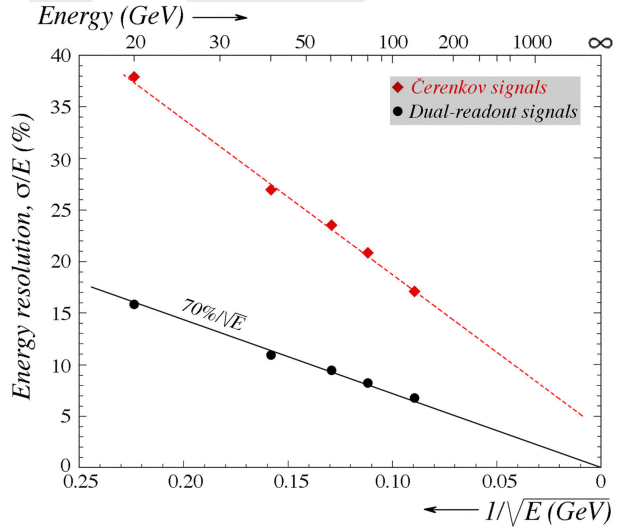

Figure 6.67: The hadronic energy resolution of the RD52 lead-fibre dual-readout calorimeter, for single pions. Shown are the results for the Čerenkov signals alone, and for the dual-readout signals.

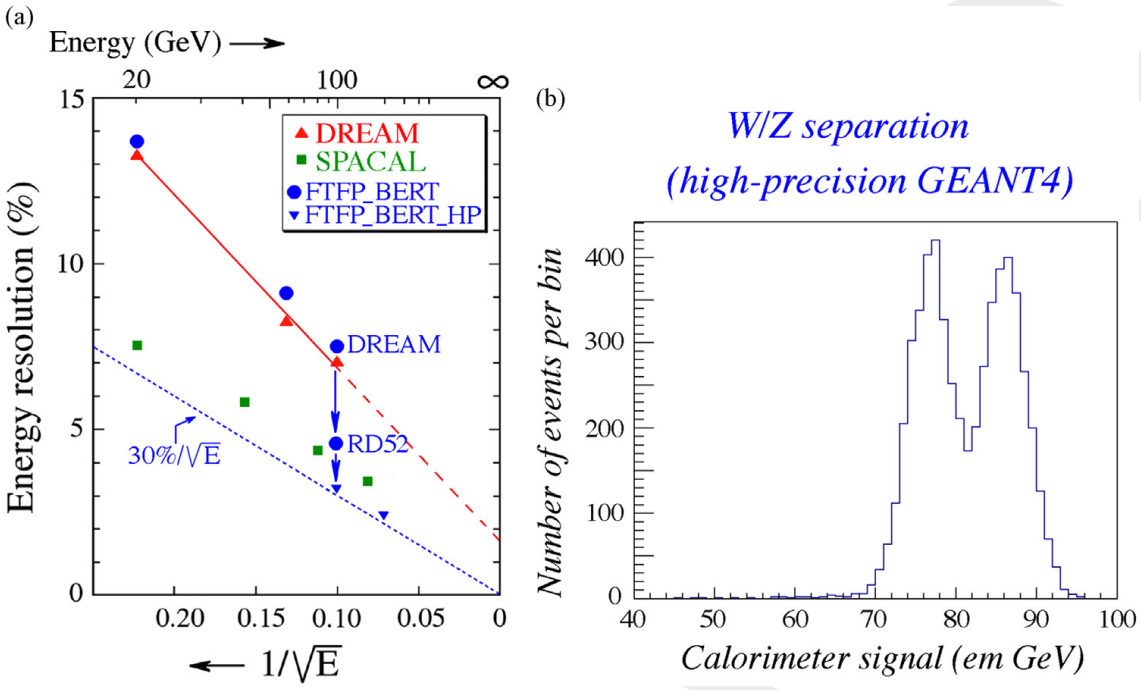

Figure 6.68: Experimental data on hadronic performance compared to Geant4 simulations (a). See text for details. Diagram (b) shows the results of a simulation for a mixture of hadrons with the energies of the W and Z vector bosons, using the high-precision hadronic shower simulation package.

don't pose issues, allows for a transversal segmentation as small as possible. SiPM are low-cost solid state light sensors with single photon sensitivity that underwent an impressive development over the last years. Tests done in the last 2 years by the RD52 collaboration show that effective solutions for small scale prototypes are very close already now. Thanks to their higher photon detection efficiency wrt standard PM, the Čerenkov light signal should be improved with a gain in the resolution for hadronic showers. On the other hand, the scintillation light spans a very large dynamic range and saturation and non-linearity effects were observed already for low-energy em showers. In Figure 6.70, the number of photoelectrons per GeV measured in July 2017, with a very small module ($1cm^2$ section, 32 + 32 fibres) is shown. The most relevant technical specifications of the sensors were 1600, $25 \times 25\ \mu m^2$, cells, and a 25% nominal detection efficiency.

C signals show a linear response with about 30 p.e./GeV while S signals shows a decreasing sensitivity starting at around 1000 p.e./GeV, for 10 GeV electron showers. It should be mentioned the fact that the shower containment is around 40%. Last but not least, the problem of serious light leaks of the S signals to the neighbouring C SiPM, observed in the first 2016 tests, looks solved thanks to a staggered readout of the C and S fibres (Figure 6.71).

6.4.5.1 Sensor Choice

As far as the scintillation light detection is concerned, saturation or non linearity should largely disappear with higher density devices (e.g. with 10000, $10 \times 10\ \mu m^2$, cells). The definition of the optimal dynamic range and the qualification of existing silicon photomultipliers in that regard, will be likely addressed in a short-term $R\&D$ phase.

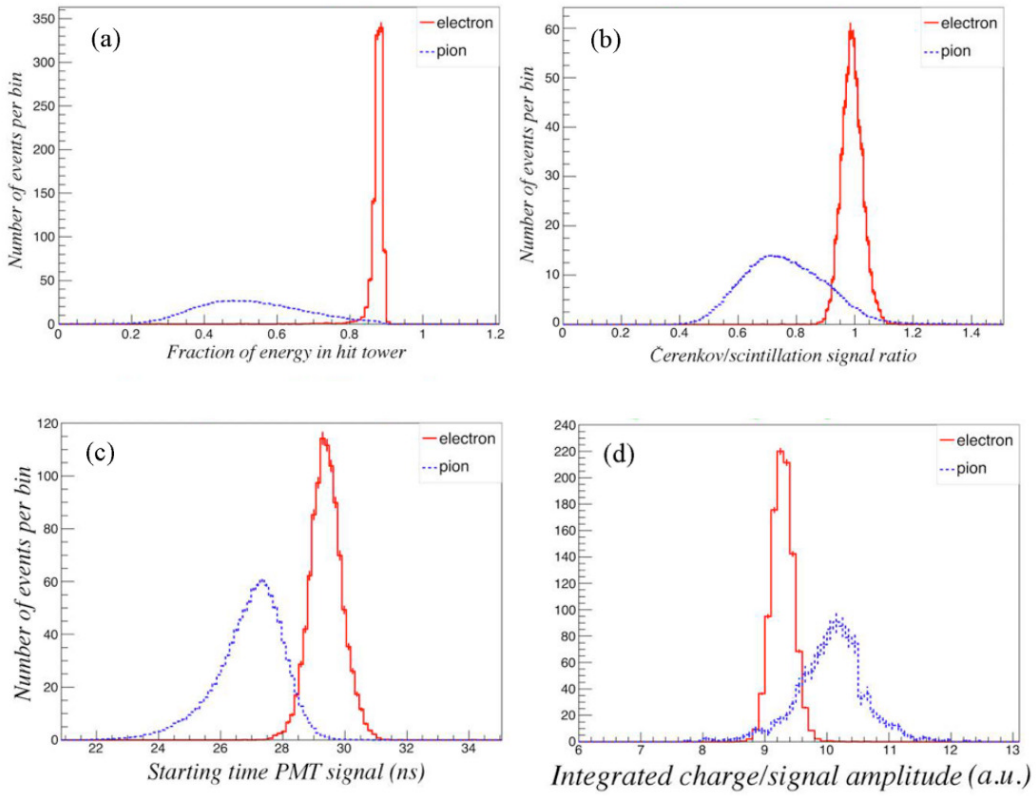

Figure 6.69: Distribution of four discriminating variables: energy fraction deposited in the hit tower for the (a), C/S signal ratio in the hit tower (b), starting time of the PM signal (c), ratio of the integrated charge and the amplitude of the signals (d), for electron and pion showers.

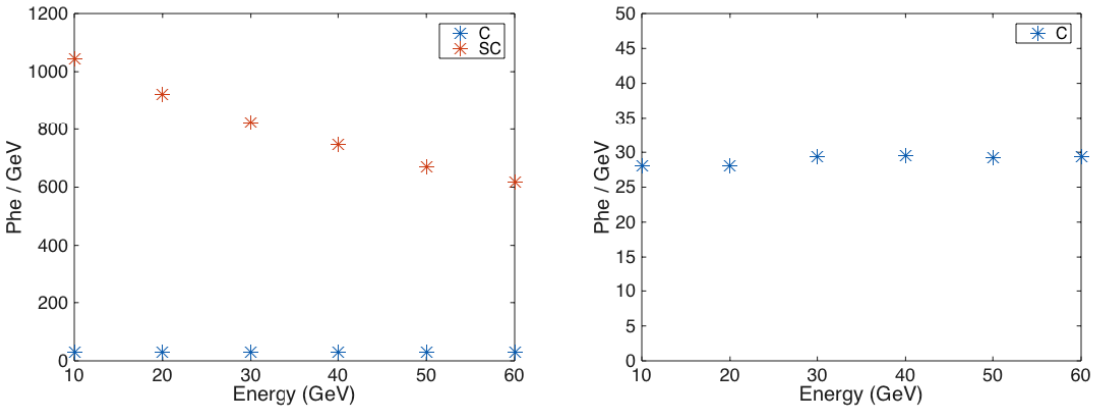

Figure 6.70: Number of photoelectrons per GeV for both the scintillation and the Čerenkov signals (left) and for the Čerenkov signal only (right), as a function of the electron energy. The main sensor specifications were 1600, $25 \times 25\ \mu m^2$, cells, and a 25% nominal PDE.

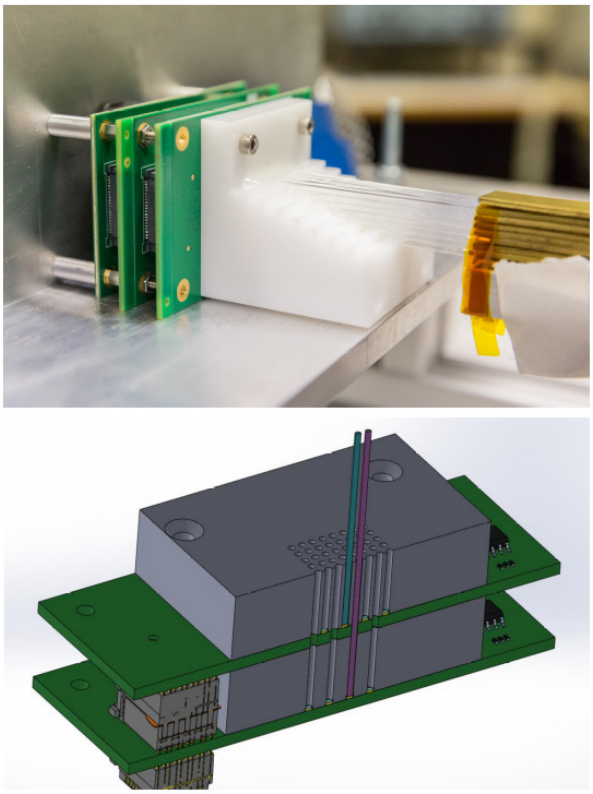

Figure 6.71: Staggered readout scheme: the scintillation and Čerenkov fibres are readout at different planes to avoid light leakage into neighbouring channels.

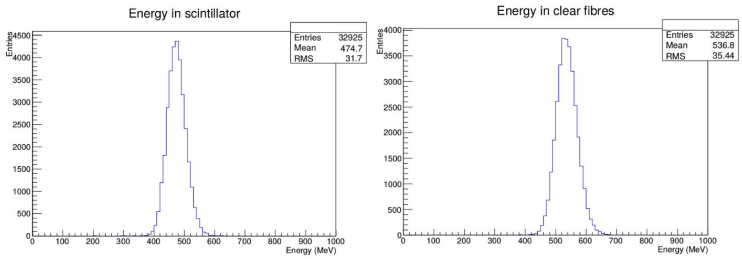

Figure 6.72: Energy deposited in scintillating (a) and Čerenkov (b) fibres, by 20 GeV electrons.

For the Čerenkov light, improvements of the photon collection may come with the development of Silicon Carbide (SiC) sensors, that are expected to provide exclusive UV sensitivity (i.e. visible-light blindness). It must be said that the R&D of these device is at a very early stage and they still miss a proof that they will really give a significant improvement in the Čerenkov light detection. A program for the development and qualification of SiC sensors is under discussion at INFN.

6.4.5.2 Front-End Electronics and Readout

Concerning the front-end, the development shall certainly evaluate the use of Application Specific Integrated Circuits (ASIC), to handle and reduce the information to be trasferred to the DAQ system. A major question is finding the optimal way for summing signals from a plurality of sensors into a single output channel. Available ASICs will have to be analysed, compared and qualified with the goal to select the optimal one and/or define the specification for a dedicated design to be pursued at a later stage. The development and usage of a feature-extracting processor has to be considered, in particular for addressing the problem of disentangling overlapping em and hadronic showers.

6.4.6 Monte Carlo Simulations

Geant4 simulations (version 10.02.p01-10.03.p01, with FTFP_BERT_HP physics list) are under development and analysis for understanding the performance of both testbeam modules and a 4π calorimeter integrated in a detector, with magnetic field, tracking and preshower elements.

6.4.6.1 em Performance

A $31 \times 31 \times 100\ cm^3$ Cu matrix, with 1 mm fibres at 1 mm distance, has been simulated for the evaluation of the electromagnetic performance. PMMA clear fibres and Polystirene scintillating fibres, with a 3% thick cladding (C_2F_2 Fluorinated Polymer for clear and PMMA for scintillating fibres), were the sensitive elements.

A small ($\lesssim 1°$) tilt angle was introduced to avoid large non gaussian tails in the scintillation signal due to channeling and oversampling.

The energy containment for 20 GeV electrons was estimated to be $\sim 43.4\%$, with sampling fractions of 5.3% and 6.0% (see Figure 6.72), for scintillating and clear fibres, respectively.

Given the integral sampling fraction of about 11.3% and the 1 mm thick fibres, the contribution to the energy resolution due to sampling fluctuations can be estimated to be around:

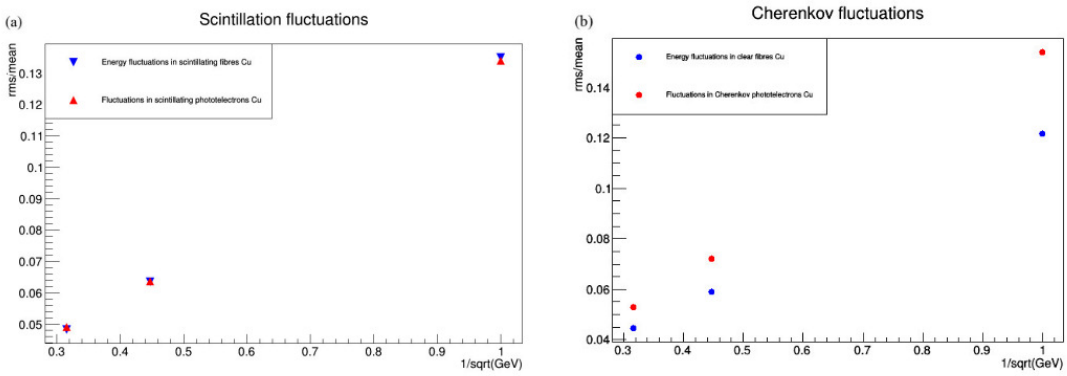

Figure 6.73: Relative fluctuation of the total signal detected in the scintillating (a) and Čerenkov (b) fibres, for both the energy deposit and the number of photoelectrons.

$$\frac{\sigma}{E} = 2.7\% \times \frac{\sqrt{1/0.113}}{\sqrt{E}} = \frac{8.0\%}{\sqrt{E}} \tag{6.14}$$

ultimate limit on the em resolution.

One of the main (blocking) issue was the cpu time needed for the light propagation up to the photodetectors, dominated by the scintillating photons. Nevertheless the analysis has shown that the fluctuations in the detection of the scintillating light (about 5500 photoelectrons/GeV) are largely dominated by the energy sampling fluctuations (Figure 6.73(a)). This is not true for the Čerenkov light signals (Figure 6.73(b)), which sensitivity is estimated to be of about 108 photoelectrons/GeV.

So, the propagation of the scintillation light has been switched off without biasing the detector performance while for the Čerenkov photons a parameterization has been introduced, convoluting the effect of the light attenuation, the angular acceptance and the Photon Detection Efficiency (PDE). The performance obtained in this way with a single thread over a 2.0 GHz processor ranges from $\sim 11.3s$ at 40 GeV up to $\sim 72s$ at 250 GeV.

In Figure 6.74 the resolutions are shown for both C and S signals, separately, and for the unweighted average value of the two.

The fit to the data points gives:

$$S\ only: \frac{\sigma}{E} = \frac{10.1\%}{\sqrt{E}} + 1.1\% \tag{6.15}$$

$$C\ only: \frac{\sigma}{E} = \frac{17.3\%}{\sqrt{E}} + 0.1\% \tag{6.16}$$

$$combined: \frac{\sigma}{E} = \frac{10.1\%}{\sqrt{E}} + 0.4\% \tag{6.17}$$

A sligthly better result using a weighted average is under evaluation.

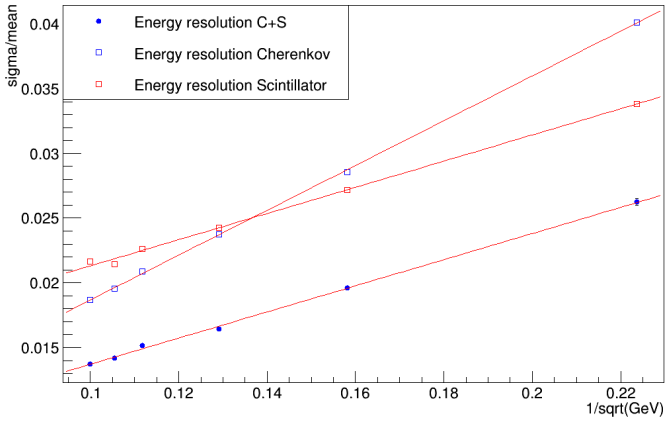

Figure 6.74: Relative resolution for em showers for the C and S signals, independently, and for the average of the two.

6.4.6.2 Short Term Planning and Open Issues

The performance for single hadrons, jets and τ.s has to be understood and the work has just started. For validation, the comparison with the data taken with the Pb matrix (the only recent prototype with a sensible hadronic shower containment) is planned.

About the em simulations, the priority will be the comparison with the 2017 testbeam data and the calibration of the absolute photoelectron scale for the Čerenkov light.

In general, an understanding of light attenuation effects is also needed, for a $\sim 2 - 2.5m$ long detector, that affect the hadronic resolution as a function of the shower development point (late starting showers will give bigger and faster signals). The evaluation of pro/cons of filters (to dump the short attenuation-lenght components) and mirrors (to increase the number of photons that may reach the photodetectors) may be relevant in this context.

The effects of the integration of a preshower detector have to be evaluated and the e/π separation assessed and quantified, for both isolated particles and within jets.

About physics, a (non exhaustive) list of benchmark channels to be studied is: $H \to \gamma\gamma$, $H \to \tau\tau$, $H \to gg$, $Z \to jj$, $W \to jj$, $H \to ZZ^* \to 4j$, $H \to WW^* \to 4j$.

6.4.7 Final Remarks

After a 15-year long research program on dual-readout calorimetry of the DREAM/RD52 collaboration, this technology looks mature for the application in future experimental programs. The results show that the parallel, independent, readout of scintillation and Čerenkov light, makes possible to cancel the effects of the fluctuations of the electromagnetic fraction of hadronic showers, dominating the energy resolution of most calorimeters built so far. In conjunction with high-resolution em and hadronic energy measurements, excellent standalone particle-id capability has been demonstrated as well.

Those results give increasing support to the convinction that a a matrix of alternating scintillating and clear fibres, inserted in copper strips and readout by Silicon PhotoMultipliers (SiPM), should be able to provide performance more than adequate for the physics programs at the proposed future CepC collider.

Nevertheless, there is a series of technical and physics issues that needs to be solved in order to arrive up to the design of a realistic 4π detector. An INFN project, with a 3 year programme, is going to be discussed in the next weeks, aiming at addressing the main problems:

a) The industrial machining of foils of copper (or some other material) with the required precision.

b) The readout of the high granularity matrices of SiPM that, in order to be effective, will require the development of a dedicated Application Specific Integrated Circuit (ASIC). Possible aggregations of more fibre outputs into a single channel have also to be implemented and studied.

c) The development of a modular solution and the assessment, at all levels, of its performance, through beam tests of small modules and simulations. An intensive program of simulations is already ongoing, with the target of the CepC CDR. The response to single particles and jets is under study, in standalone configurations. The work for understanding the behaviour of a calorimeter integrated in a full detector, with a tracking and a magnetic system, has also started. This will include, as well, the evaluation of the combined performance with a preshower detector in front.

References

[1] CALICE Wikipage. https://twiki.cern.ch/twiki/bin/view/CALICE/.

[2] J.-C. Brient, *Improving the jet reconstruction with the particle flow method: An introduction*, 2004. Calorimetry in particle physics. Proceedings, 11th International Conference, CALOR 2004, Perugia, Italy,.

[3] H. Videau and J. C. Brient, *Calorimetry optimised for jets*, in *Proc. 10th International Conference on Calorimetry in High Energy Physics (CALOR 2002), Pasadena, California* [39].

[4] H. Videau and J. C. Brient, *A Si-W calorimeter for linear collider physics*, in *Proc. 10th International Conference on Calorimetry in High Energy Physics (CALOR 2002), Pasadena, California* [39], pp. 309–320.

[5] CALICE Collaboration, R. Cornat, *Semiconductor sensors for the CALICE SiW EMC and study of the cross-talk between guard rings and pixels in the CALICE SiW prototype*, in *Proceedings CALOR'08*, vol. 160, p. 012067. 2009.

[6] ILD Collaboration, T. Behnke et al., *International Linear Collider – Detector Baseline Document*, , DESY / FERMILAB / CERN, 2013. https://edmsdirect.desy.de/edmsdirect/file.jsp?edmsid=D00000001021295.

[7] CMS Collaboration, A. M. Magnan, *HGCAL: a High-Granularity Calorimeter for the endcaps of CMS at HL-LHC*, JINST **12** (2017) no. 01, C01042.

[8] CMS Collaboration, A. Martelli, *The CMS HGCAL detector for HL-LHC upgrade*, in *5th Large Hadron Collider Physics Conference (LHCP 2017) Shanghai, China, May 15-20, 2017*. 2017. arXiv:1708.08234 [physics.ins-det].

http://inspirehep.net/record/1620207/files/arXiv:1708.08234.pdf.

[9] H. Zhao, *PFA Oriented ECAL Simulation and Geometry Optimization for the CEPC*, in *proceeding of the International Conference on Calorimetry for the High Energy Frontier (CHEF 2017)*. 2017.

[10] D. Jeans, *Simalution of the SiW-ECAL for ILD*, in *proceedings of LCWS 2017*. 2017.

[11] T. S. et al., *Performance study of SKIROC2/A ASIC for ILD Si-W ECAL*, in *proceeding of the International Conference on Calorimetry for the High Energy Frontier (CHEF 2017)*. 2017.

[12] D. Grondin, J. Giraud, and J.-Y. Hostachy, *CALICE Si/W ECAL: Endcap structures and cooling system*, in *Proceedings, International Workshop on Future Linear Colliders 2016 (LCWS2016): Morioka, Iwate, Japan, December 05-09, 2016*. 2017. arXiv:1702.03770 [physics.ins-det]. http://inspirehep.net/record/1513187/files/arXiv:1702.03770.pdf.

[13] V. Boudry, *SiW ECAL R&D*, in *Fourth International Workshop on Future High Energy Circular Colliders (CEPC2014)*. 2014. http://indico.ihep.ac.cn/event/4338/session/2/contribution/35/material/slides/0.pdf.

[14] CALICE Collaboration, J. Repond et al., *Design and Electronics Commissioning of the Physics Prototype of a Si-W Electromagnetic Calorimeter for the International Linear Collider*, JINST **3** (2008) P08001, arXiv:0805.4833 [physics.ins-det].

[15] C. Adloff et al., *Response of the CALICE Si-W electromagnetic calorimeter physics prototype to electrons*, Nucl. Instrum. Meth. **A608** (2009) 372–383.

[16] CALICE Collaboration Collaboration, R. Poschl, *A large scale prototype for a SiW electromagnetic calorimeter for a future linear collider*, in *Proceedings of International Workshop on Future Linear Colliders (LCWS11) 26-30 Sep 2011. Granada, Spain*. 2012. arXiv:1203.0249 [physics.ins-det].

[17] V. Balagura et al., *SiW ECAL for future e^+e^- collider*, in *Proceedings, International Conference on Instrumentation for Colliding Beam Physics (INSTR17): Novosibirsk, Russia*. 2017. arXiv:1705.10838 [physics.ins-det]. http://inspirehep.net/record/1601898/files/arXiv:1705.10838.pdf.

[18] A. Irles, *Latest R&D news and beam test performance of the highly granular SiW-ECAL technological prototype for the ILC*, in *proceeding of the International Conference on Calorimetry for the High Energy Frontier (CHEF 2017)*. 2017.

[19] G. B. *et.al.*, *Conception and construction of a technological prototype of a high-granularity digital hadronic calorimeter*, JINST **10** (2015) P10039.

[20] M. B. *et al.*, *Performance of Glass Resistive Plate Chambers for a high granularity semi-digital calorimeter*, JINST **6** (2011) P02001.

[21] C. Collaboration, *First results of the CALICE SDHCAL technological prototype*, JINST **11** (2016) P04001.

[22] C. Collaboration, *Separation of nearby hadronic showers in the CALICE SDHCAL prototype detector using ArborPFA*, CAN-054 (2016) .

[23] C. Collaboration, *Tracking within Hadronic Showers in the CALICE SDHCAL prototype using a Hough Transform Technique*, JINST **12** (2017) P05009.

[24] C. Collaboration, *Resistive Plate Chamber Digitization in a Hadronic Shower Environment*, JINST **11** (2016) P06014.

[25] L. Caponetto*et al.*, *First test of a power-pulsed electronics system on a GRPC detector in a 3-Tesla magnetic field*, JINST **7** (2012) P04009.

[26] R. Wigmans, *Calorimetry, Energy Measurement in Particle Physics*, vol. 168 (second edition). International Series of Monographs on Physics, Oxford University Press, 2017.

[27] All publications and other results obtained in the context of the RD52 project can be found at the website(s): http://www.phys.ttu.edu/ dream or http://dream.knu.ac.kr.

[28] C. Patrignani et al. (Particle Data Group) Chin. Phys. C **40** (2016) 479–482.

[29] D. E. Groom, *Energy flow in a hadronic cascade: Application to hadron calorimetry*, Nucl. Instrum. Methods A **572** (2007) 633–653.

[30] D. E. Groom, *Erratum to "Energy flow in a hadronic cascade: Application to hadron calorimetry" [Nucl. Instr. and Meth. A 572 (2007) 633âĂŞ653]*, Nucl. Instrum. Methods A **593** (2008) 638.

[31] N. Akchurin et al., *Particle identification in the longitudinally unsegmented RD52 calorimeter*, Nucl. Instrum. Methods A **735** (2014) 120.

[32] N. Akchurin et al., *The electromagnetic performance of the RD52 fiber calorimeter*, Nucl. Instrum. Methods A **735** (2014) 130.

[33] N. Akchurin et al., *Lessons from Monte Carlo simulations of the performance of a dual-readout fiber calorimeter*, Nucl. Instrum. Methods A **762** (2014) 100.

[34] C. Cardini et al., *The small-angle performance of a dual-readout fiber calorimeter*, Nucl. Instrum. Methods A **808** (2016) 41.

[35] R. Wigmans, *New results from the RD52 project*, Nucl. Instrum. Methods A **824** (2016) 721.

[36] S. Lee et al., *Hadron detection with a dual-readout fiber calorimeter*, Nucl. Instrum. Methods A **866** (2017) 76.

[37] 4th Detector Collaboration Letter of Intent: http://www.4thconcept.org/4LoI.pdf.

[38] D. Acosta et al., *Electron, pion and multiparticle detection with a lead/scintillating-fiber calorimeter*, Nucl. Instrum. Methods A **306** (1991) 481.

[39] *10th International Conference on Calorimetry in High Energy Physics (CALOR 2002), Pasadena, California, 25-30 Mar 2002*. March, 2002.

CHAPTER 7

DETECTOR MAGNET SYSTEM

CEPC website [1]

7.1 General Design Considerations

The CEPC detector magnet system is designed to provide an axial magnetic field over the tracking volume, a diameter 6.8 m over a length of 8.05 m, particle detectors within this volume will measure the trajectories of charged tracks emerging from the collisions. Based on the study of the compensating magnet of CEPC, a 3 T central field of detector superconducting solenoid is more reality to construct the CEPC compensation solenoid which making full cancelation to avoid disturbance to the beam with technologies to be developed in coming years, comparing the 3.5 T solenoidal field proposed in pre-CDR.

This chapter contains all the activities related to the design of field distribution, solenoid coil, specific superconductor, cryogenics, quench protection and power supply, and the yoke. In this report, for the first time, we explored the possibility of using HTS to build CEPC detector magnet. Benefit from the development of high Tc superconductor in recent years, the advantages by using YBCO winding is higher operating temperature, better stability to resist transient disturbances when operating the magnet.

We also discussed on the choice between iron yoke design and dual solenoid scenario. The baseline design iron yoke consists of barrel yoke and end yoke, it has three main functions: first is shielding the magnetic field; second is providing the install space for the muon detector which sandwiched between the iron plates; in addition, the yoke serves as the main mechanical structure of the CEPC detector. However, the active shielding design has been widely used in commercial MRI magnets, this scenario will not use iron yoke, and it has large impact on muon detector design.

7.2 The Magnetic Field Requirements and Design

7.2.1 Main parameters

The CEPC detector solenoid main parameters are given in the Table 7.1. The 7.6 m long CEPC detector coil is composed of 5 modules. It batches the construction easiness and risks including superconducting wire selection, fabrication of the external support, winding and impregnation, transport and handling. The design enables the possibility to use shorter unit lengths of superconducting conductor (1.65 km) and join them in known positions and in low field regions on the outer radius of the solenoid. The difference compared to PreCDR is that the central magnetic field changes from 3.5 T to 3 T. The geometry size is the same with 3.5 T design, as shown in Figure 7.1. There are five

The solenoid central field (T)	3	Working current (kA)	15779
Maximum field on conductor (T)	3.485	Total ampere-turns of the solenoid (MAt)	20.323
Coil inner radius (mm)	3600	Inductance (H)	10.46
Coil outer radius (mm)	3900	Stored energy (GJ)	1.3
Coil length (mm)	7600	Cable length (km)	30.35

Table 7.1: Main parameters of the solenoid coil

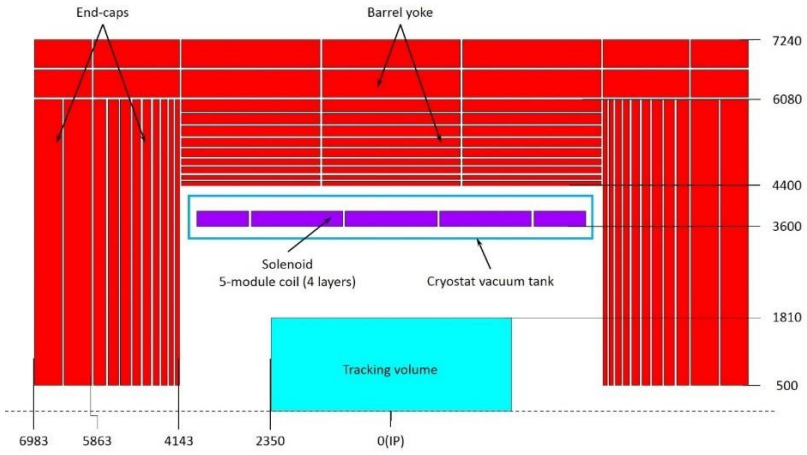

Figure 7.1: 2D layout of CEPC detector magnet (mm)

modules of the coil. Each module contains 4 layers. The three middle modules contain 78 turns per layer. The end two modules contain 44 turns per layer. Table 7.2 shows the coil parameters.

7.2.2 Magnetic field design

In the calculation we use the superconducting cable as Figure 7.2. The NbTi Rutherford cable is in the center, the pure aluminum stabilizer and aluminum alloy reinforcement are around. The figure shows the parameters of the cable. This model has been used for magnetic field calculation, stress analysis of the coil and quench analysis of the magnet.

Figure 7.3 shows the magnetic field map of the magnet. The central field is 3 T. The maximum magnet field is 3.5 T. Figure 7.4 gives the main component BZ of the field

Coil number	layers	Turns per layer
1	4	44
2	4	78
3	4	78
4	4	78
5	4	44

Table 7.2: Coil parameters

along the beam axis. Figure 7.5 shows the magnetic flux line distribution of the magnet. The non-uniformity of Tracking Volume (diameter 3.62m, length 4.7m) is 9.11%. Figure 7.6 shows the magnetic field distribution of the Tracking Volume.

$$B_p = \frac{Bmax - Bmin}{Bcenter} = 9.11\%$$

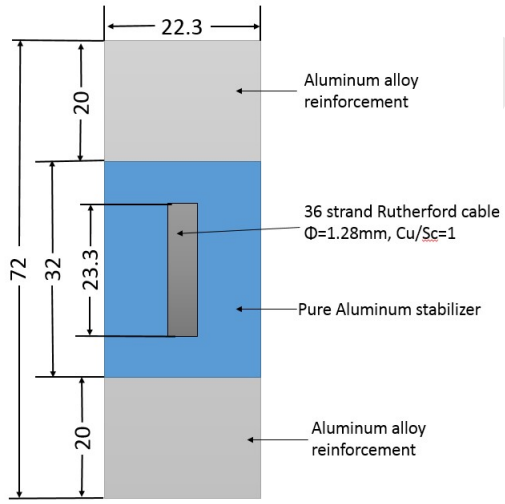

Figure 7.2: Sketch figure of cable cross section

The maximum magnetic field on the cable is 3.5 T located on the pure aluminum stabilizer. This can be seen in Figure 7.7 The magnetic field distribution on NbTi Rutherford cable is shown in Figure 7.8. The maximum field on the NbTi cable is about 3.485 T. Figure 7.9 shows the magnetic field distribution on the yoke.

The stray field of the detector magnet is shown in table 7.3 and Figure 7.10. The stray field range of 50 Gs and 100 Gs are marked out.

7.2.3 Coil mechanical analysis

Introduction:

There are two kind of stress act on the coil: thermal mechanical force caused by inconsistent of the material expansion coefficient and magnetic force. The cable used is shown in Figure 7.2. The stress analysis is divided into two conditions: coil at 4.2 K; coil energized: 4.2 K, 15779 A, 3 T. A magnetic FEA was performed to calculate the thermal

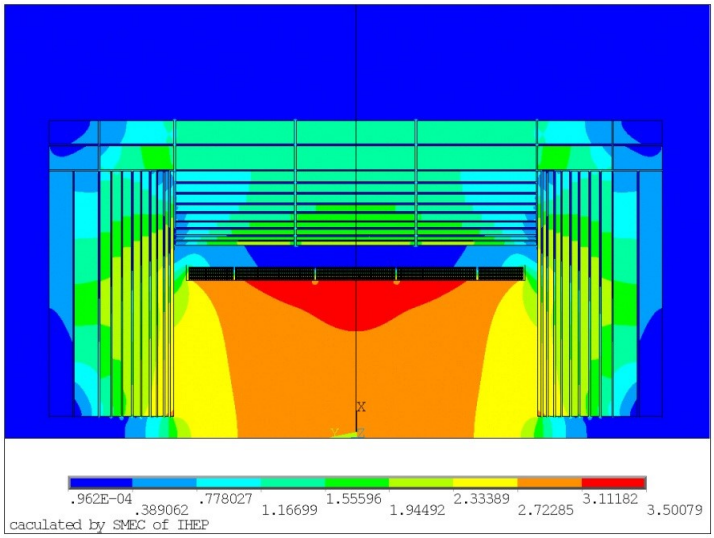

Figure 7.3: Field map of the magnet (T)

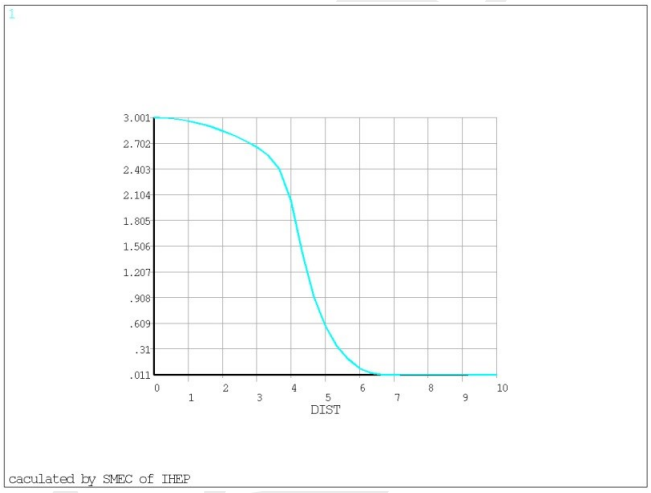

Figure 7.4: The calculated magnetic field Bz along the detector axis

Stray field	3 T
50Gs R direction	13.6 m
50Gs Z direction	15.8 m
100Gs R direction	10 m
100Gs Z direction	11.6 m

Table 7.3: Leak field parameters

mechanical force and Lorentz force. 2-D axisymmetric mechanical analyses are carried out according to the coil. In the model there are some approximations have been made: the barrel yoke and end-cap yokes are transformed into cylinders; the hole of the chimney in the barrel has been neglected; the current (15779 A) in the winding has been modelled as uniformly distributed in the Rutherford cable. The thickness of the support is 50 mm, which is the same with al-alloy used in the cable.

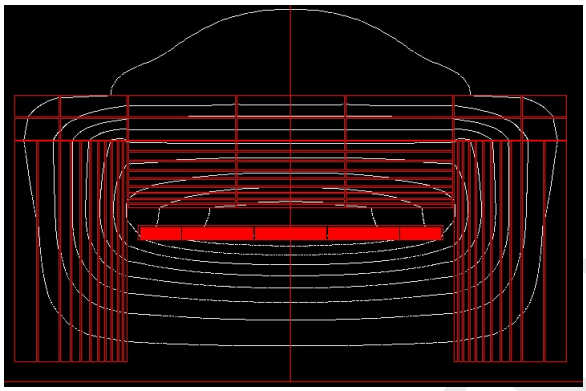

Figure 7.5: Magnetic flux line distribution of the magnet

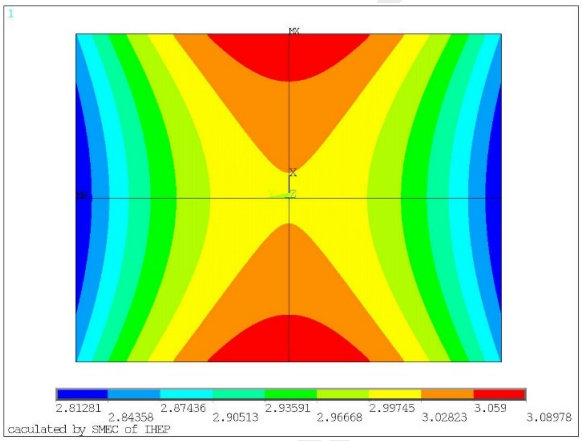

Figure 7.6: The magnetic field distribution of tracking volume

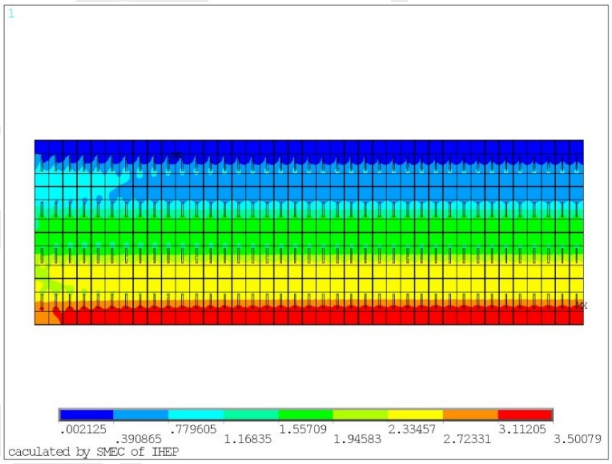

Figure 7.7: Magnetic field distribution on the cable of the center model

The properties of the different materials are given in Table 7.4 and Table 7.5. Table 7.4 gives the properties of every material used in the FEA. Table 7.5 shows mean integral thermal expansion coefficients used in the FEA.

The mechanical FE model:

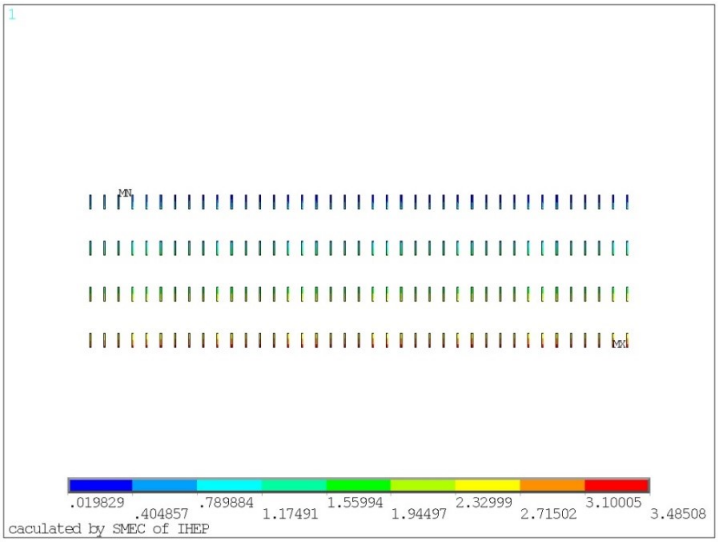

Figure 7.8: Magnetic field distribution on the center NbTi cable

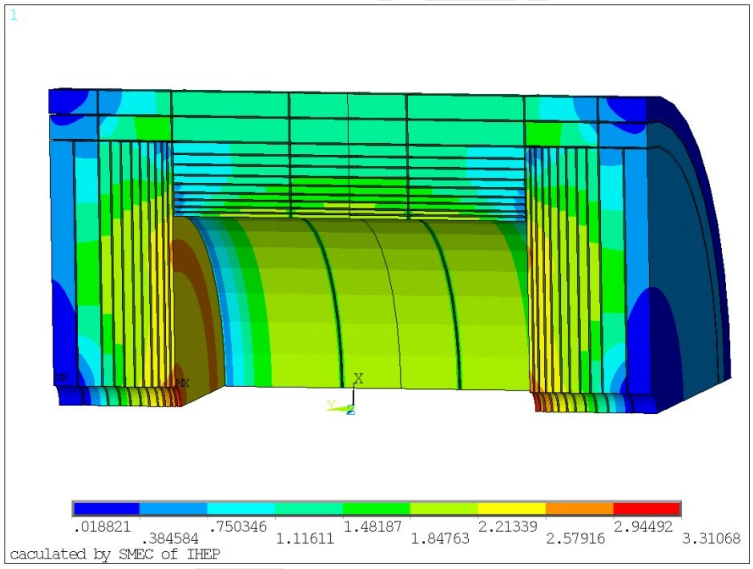

Figure 7.9: Magnetic field distribution on the yoke

Material	Temperature(K)	Young's Modulus (GPa)	Poisson's ratio
Al	4.2	0.8	0.49
Al-Alloy	4.2	77.7	0.327
Sc strand	4.2	130	0.3
Fiber glass epoxy	4.2	12.5	0.21

Table 7.4: Material properties used in the FEA

The coil has been simulated with an elasto-plastic 2-D axisymmetric FE model. Figure 7.11 shows the coil with aligned turns. Different materials are shown with different colors. Figure 7.12 shows the mesh grid distribution of the model. Stress FEA results:

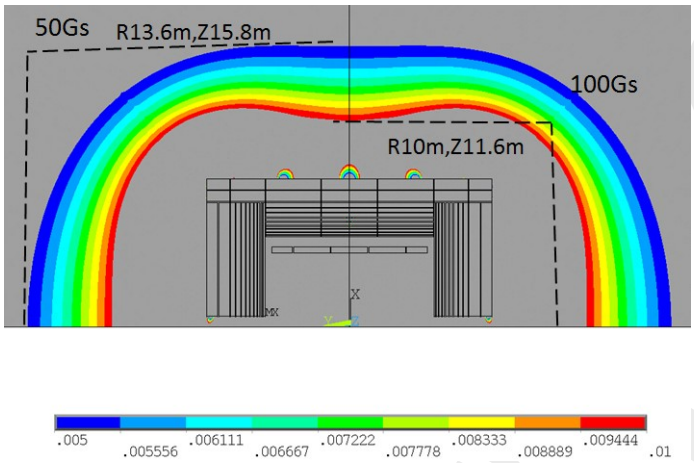

Figure 7.10: Stray field distribution outside the magnet (the field is given in T)

Material	Mean integral thermal expansion coefficient 293K-4.2K
Aluminum	14.23e-6
Al-alloy	14.16e-6
Sc strand	8.79e-6
Fiber glass epoxy	25.5e-6

Table 7.5: Mean integral thermal expansion coefficients used in the FEA

Figure 7.11: Coil with aligned turns

The Von Mises criterion has been used for all ductile materials present in the winding. A summary of the results is given in Table 7.6 and Table 7.7. From Figure 7.13 to Figure 7.18 show the Von Mises of every part of coil when in the load cases of the coil at 4.2 K

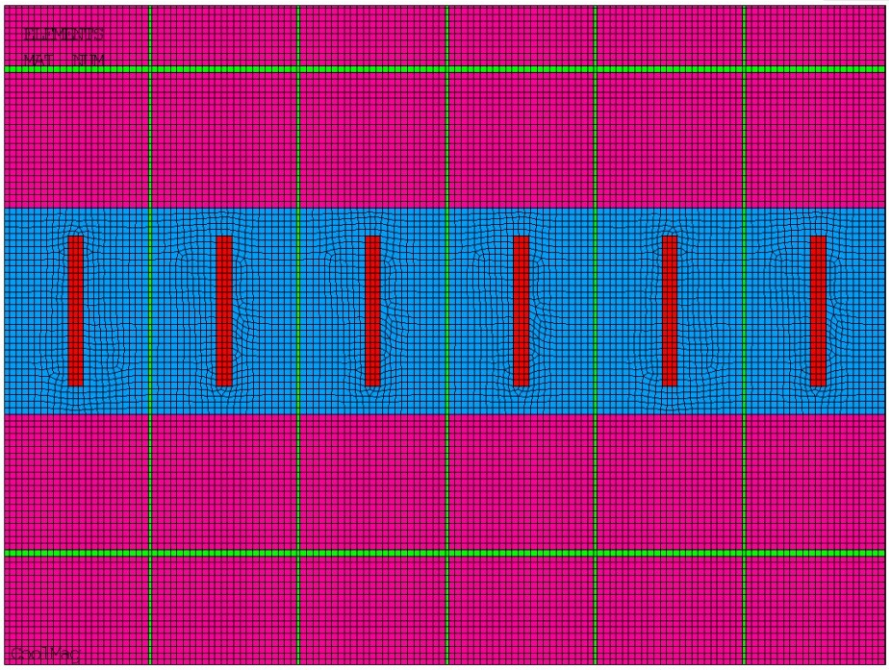

Figure 7.12: Mesh grid of the model

and energized. It seems that cooling down gives the largest contribution to the stress field in SC cable and aluminum alloy.The effect of magnetic force seems to be relatively small.

Material	Von Mises stress MPa End coil	Von Mises stress MPa Middle coil	Von Mises stress MPa Central coil
Coil at 4.2 K			
Pure Aluminum	0-7.2	0-6.8	0-7
SC cable	189-205	190-201	189-200
Al alloy	2.2-44	5-39	5-43
Coil at 4.2 K, energized			
Pure Aluminum	0-9.3	0-8.5	0-9.3
SC cable	85-142	62-95	66-106
Al alloy	40-94	74-103	65-103

Table 7.6: Maximum Von Mises of conductors

	End coil	Middle coil	Central coil
Coil at 4.2 K			
Von Mises(MPa)	21-60	19-59	21-59
Shear Stress(MPa)	1.2	8.8	1.3
Coil at 4.2 K, energized			
Von Mises(MPa)	29-85	30-84	29-79
Shear Stress(MPa)	12.4	9.0	13.1

Table 7.7: Shear stress and Von Mises of the insulation

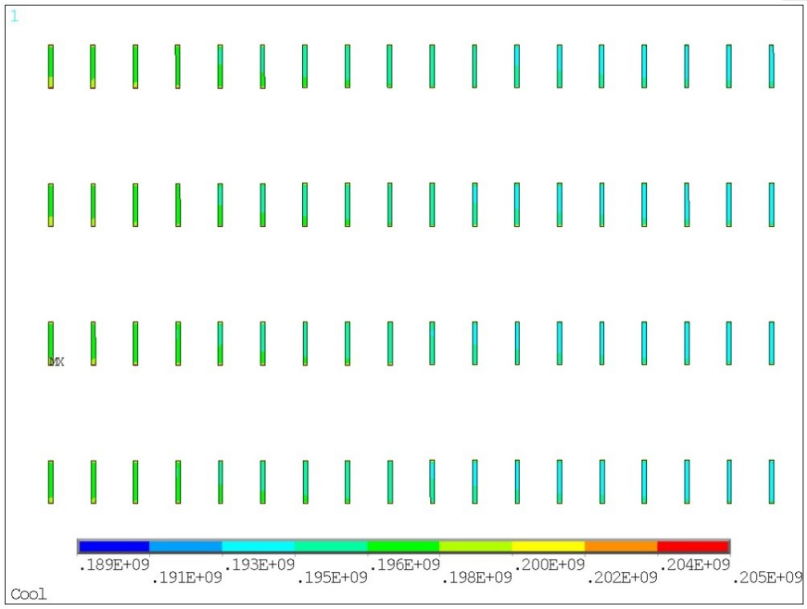

Figure 7.13: Coil at 4.2 K, Von Mises distribution of the end coil SC cable

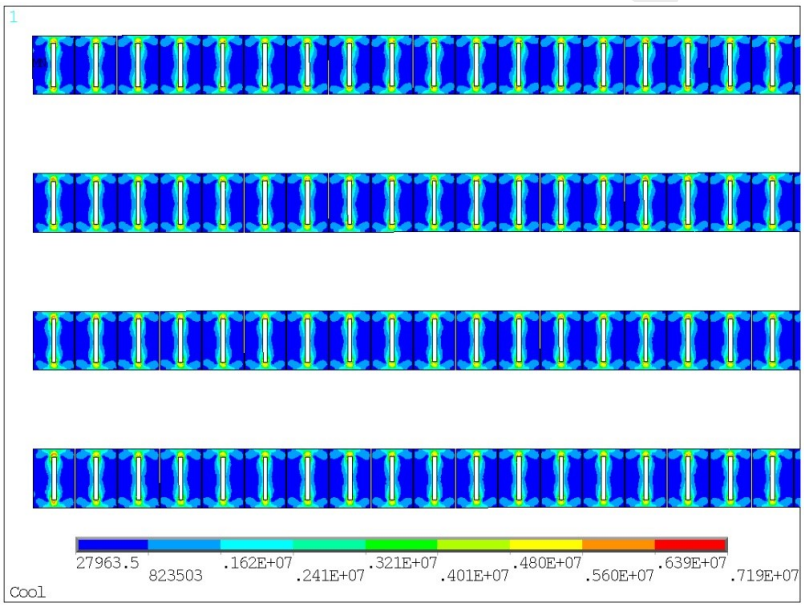

Figure 7.14: Coil at 4.2 K, Von Mises distribution of the end coil pure Aluminum

7.2.4 Preliminary quench analysis

Introduction: CEPC coil quench protection system, as shown in Figure 7.19, is based on a dump resistor concept. During a fast dump the power dissipated in it, effectively contributes to driving the whole winding to a normal state. The quench calculation is based on Finite Volume Method (FVM). Use Matlab to simulate the quench propagation in the coils, analyses the hot point temperature and the terminal voltage with timečőIn the analysis, the coils are just divided into four layers. The inductance is 10.4 H. The operating

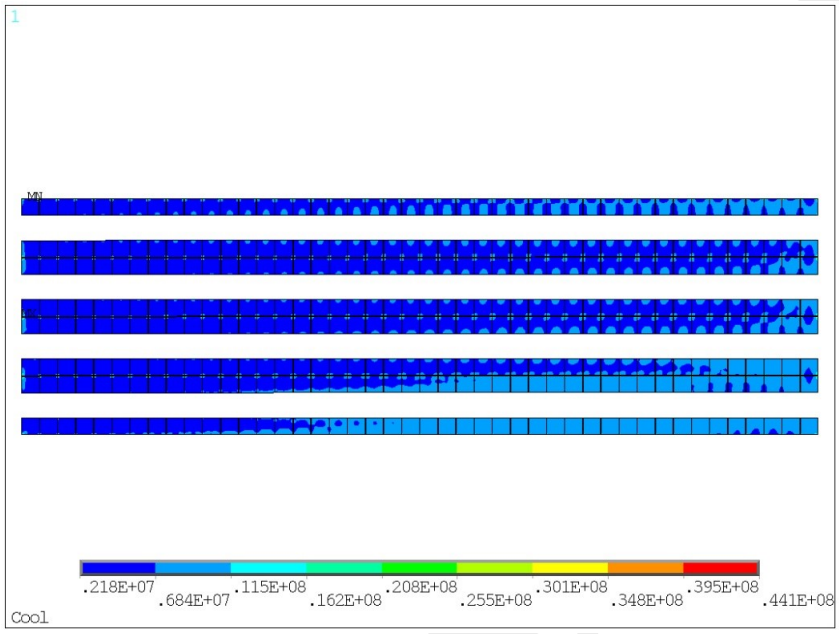

Figure 7.15: Coil at 4.2 K, Von Mises distribution of the end coil Aluminum alloy

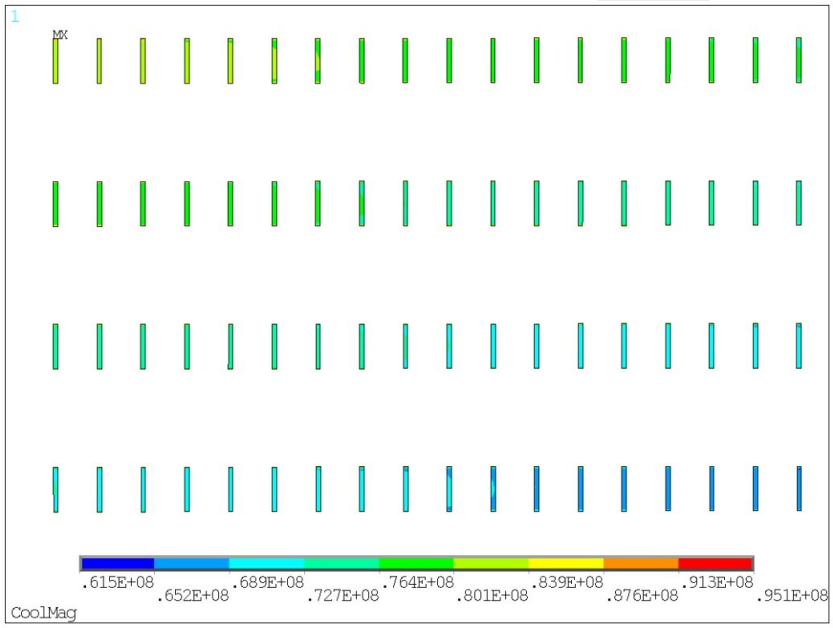

Figure 7.16: 6.16 Coil at 4.2 K, energized, Von Mises distribution of the central coil SC cable

current is 15779A. The insulation between layers is 1 mm thickness, and between turns is 0.5 mm thickness.

Two different scenarios have been considered: normal external fast dumping and failure of the protection system. The quench starts at the end of first layer, given the temperature of 9 K. Three conditions of dump resistorčž1, the protection system failure, Rp=0;2, Rp=0.05Ω; 3, Rp=0.1Ω.

Calculation process: All the materials we used are: G-10 CR (Fiberglass Epoxy), 1100 pure aluminum, 6061-T6 aluminum alloy, OFHC Copper RRR=100, NbTi. The curves of the magnet parameters under these three conditions are given in the figures from

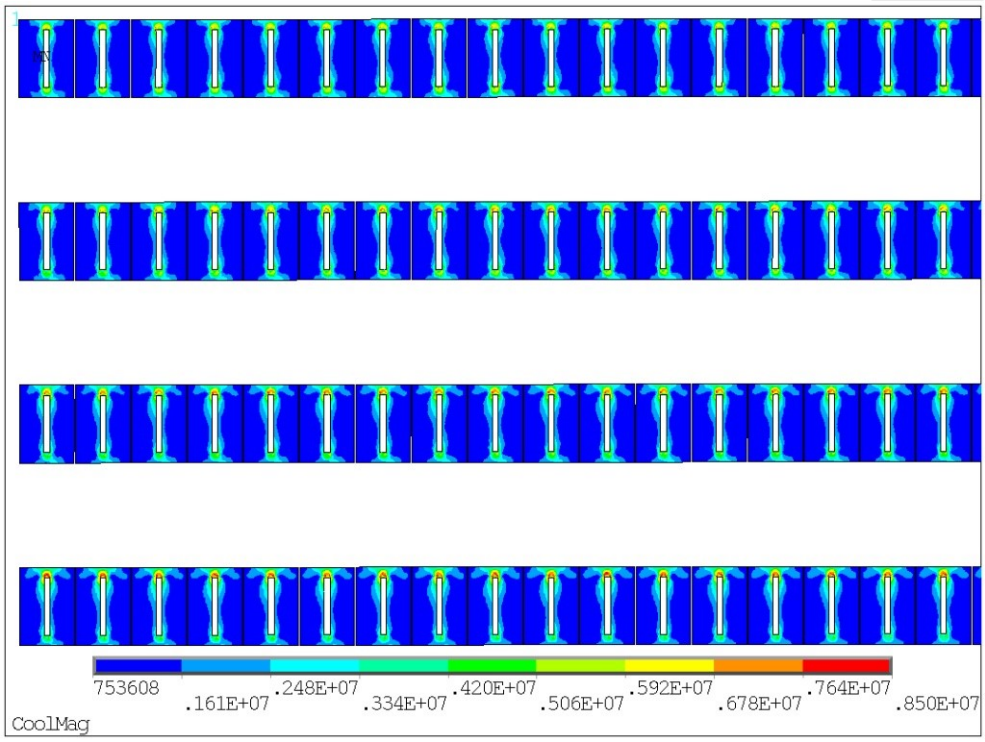

Figure 7.17: Coil at 4.2 K, energized, Von Mises distribution of the central coil pure Aluminum

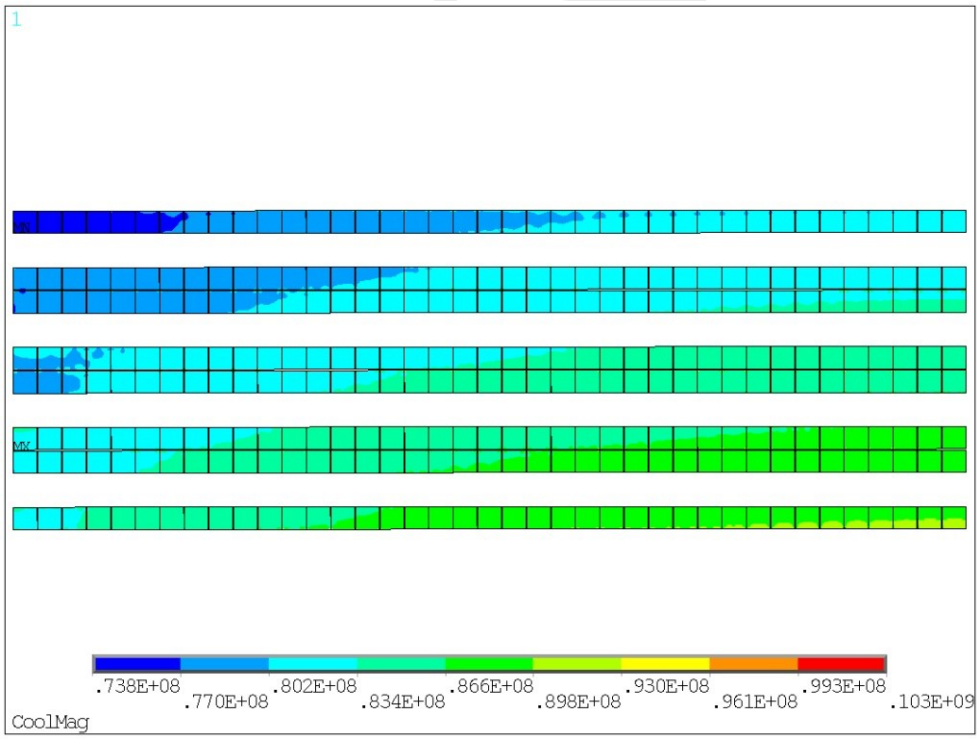

Figure 7.18: Coil at 4.2 K, energized, Von Mises distribution of the central coil aluminum alloy

Figure 7.20 to Figure 7.23. Current, resistance, hot temperature and voltage of the magnet are shown. Table 7.8 gives the summary of the quench calculation.

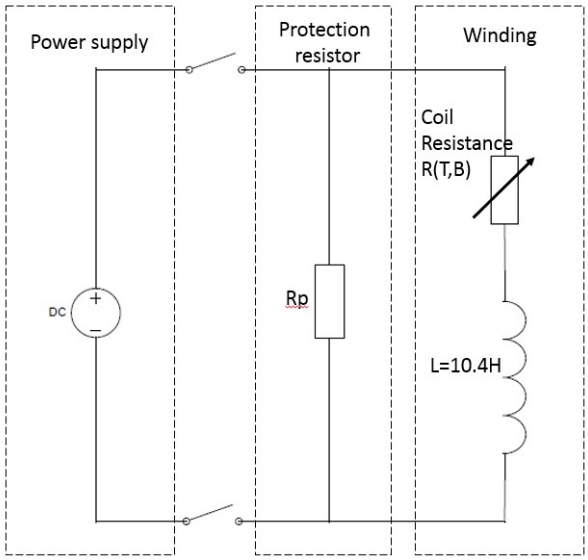

Figure 7.19: Equivalent electrical circuit of the quench protection of CEPC

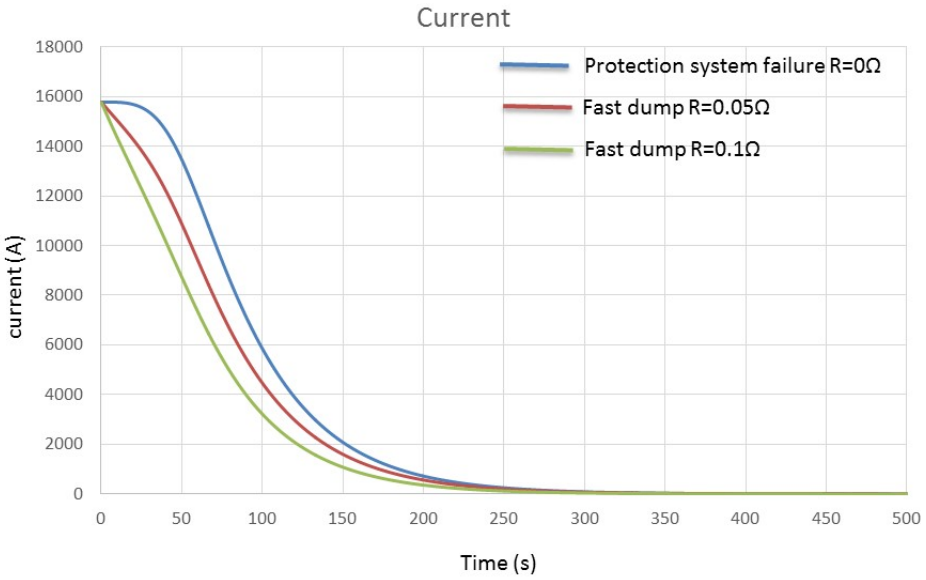

Figure 7.20: Comparison of the current profile with protection system failure and with different fast dump resistors

7.3 HTS/LTS Superconductor Options

7.3.1 HTS plan background

The center magnetic field strength of CEPC detector magnet is 3 T; the length of the magnet is about 15 meters; inner diameter is 7 m. If we use LTS (low temperature superconducting) plan, it is easier and more mature, but high temperature superconductor is the trend of the superconducting development, especially in the high strength field (greater than 16 T) detector magnets and accelerator magnets, which is only the HTS can achieve. So we need to accelerate the research of high temperature superconducting applications,

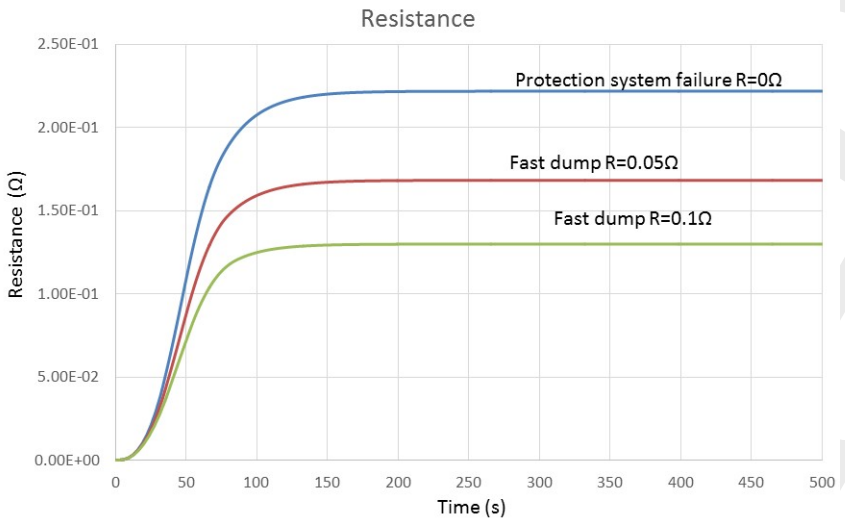

Figure 7.21: Comparison of the coil resistance profile with protection system failure and with different fast dump resistors

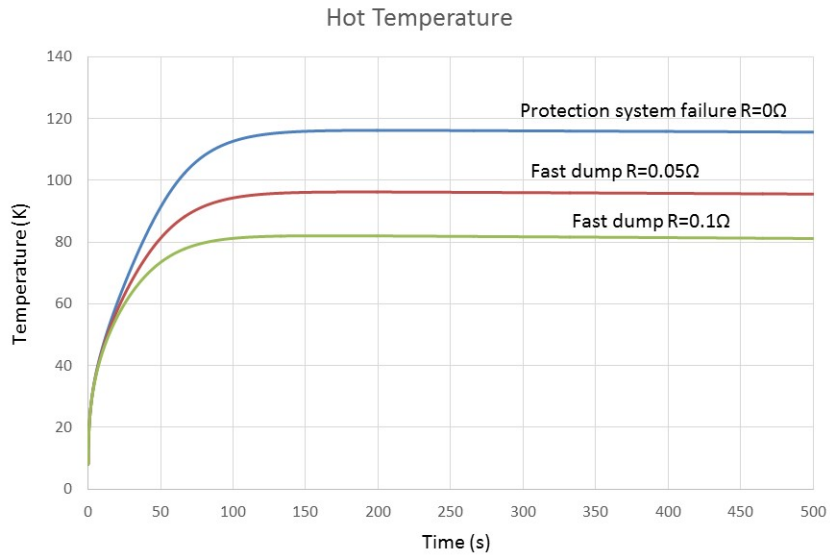

Figure 7.22: Comparison of temperature profile with protection system failure and with different fast dump resistors

accumulate high temperature superconducting magnet processing experience, and grasp the magnet processing technology. Compared with the use of low temperature superconducting, the high temperature superconducting detector has the following advantages: 1. the cost of the magnet will probably be reduced; 2. the security residual is large, the magnet is stable and not easy to quench; 3. HTS is not affected by irradiation; 4. Less material of HTS; 5. Coil winding is relatively easy. The coil can be made into a single pancake or double pancake, and then spliced; 6. Working at a relatively high temperature (20 K), the cooling structure is easy to do; 7. Use YBCO in bulk to reduce YBCO cost and promote the development of high temperature superconducting technology and related enterprises; 8. Lay the foundation for future high field magnets.

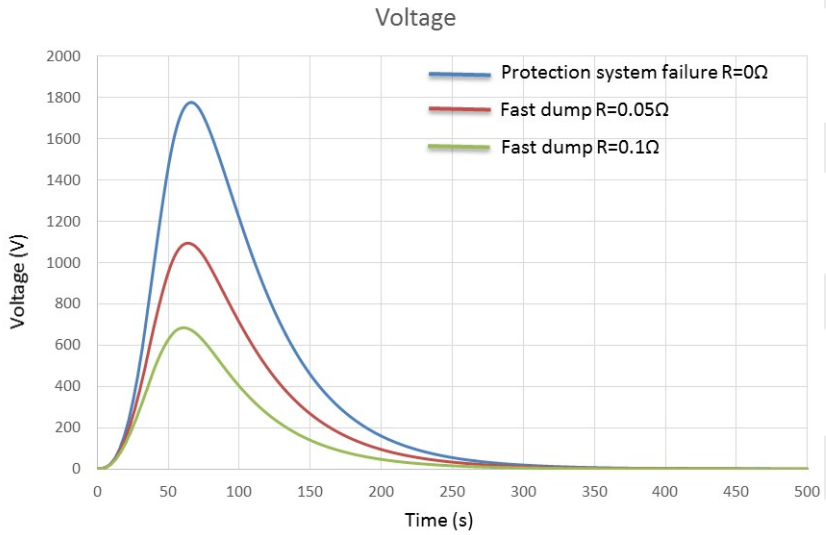

Figure 7.23: Comparison of the coil voltage profile with protection system failure and with different fast dump resistors

Fast dump resistance Rp	0 Ω	0.05 Ω	0.1 Ω
Average final coil temperature	136 K	113K	96K
Effective time constant(the current is I=I0/e=6833A)	90s	80s	68s
Magnet final resistance	0.25 Ω	0.19 Ω	0.15 Ω
Max voltage	2323 V	1478 V	946 V
Extracted energy	0	8.27e8 J	1.279e9 J
Extracted energy ratio	0	46%	71%

Table 7.8: Influence of Rp on quench characteristics

The second generation of practical HTS conductors, chemical formula YBa2Cu3O7 (YBCO). It is mainly produced by coating method (CCC - coated conductor composite): using chemical deposition or physical coating methods coating a layer of YBCO superconducting film on the alloy substrate. The cost of this kind of conductor is low. Figure 7.24 shows the structure diagram of YBCO (from Shanghai superconductor Company)

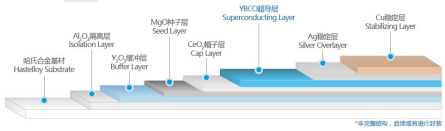

Figure 7.24: The structure diagram of YBCO

The high temperature superconducting YBCO has a huge advantage in the high field. The relationship between the critical current and magnetic field of various superconducting materials can be seen from figure 7.25 The advantage of HTS is very obvious when the magnetic field is greater than 20 T. When it is greater than 25 T, we can only use YBCO and 2212 HTS wires. The CEPC detector magnet is also an application of HTS. Because

the field is not high, the working temperature can be increased to 20K or even higher, then the requirements for the refrigeration system can be reduced.

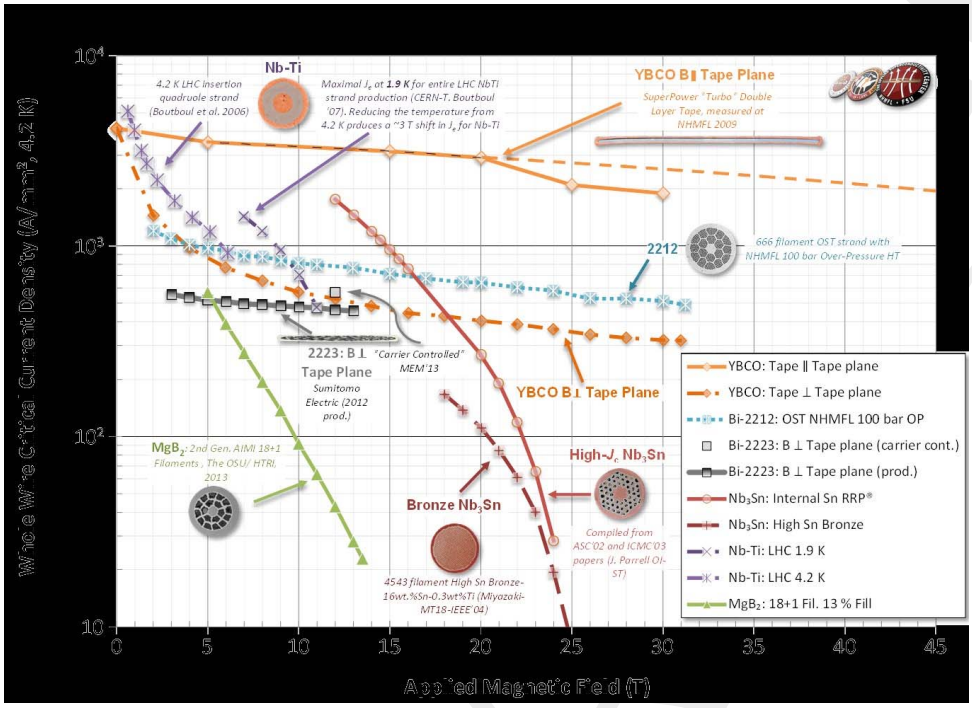

Figure 7.25: The relationship between critical current and applied magnetic field of different superconducting materials

7.3.2 The latest development of high temperature superconducting cable

Why do we need to study high temperature superconducting cable? What are the advantages of high temperature superconducting cable? Large detector magnet, accelerator magnets and other magnets generally use cable to wind, its advantages are: 1, increase the reliability of the coil, when one wire or a few wires of the cable quench, other wires can also shunt the current of the cable. Then the magnet would not quench due to a small disturbance; 2. The cable has a lower demand for power supply, and the inductance of single superconducting wire is very large, so we need a higher voltage of the power supply, and the cost of large power supply is very high; 3. Less demands of HTS wire. If the cable is used, the single length of the superconducting wire can be reduced to the order of 100 meters, which can greatly reduce the cost of the superconducting wire.

Some institutes have been developing high-temperature superconducting cables, and so far there has not been a mature, mass-used two-generation high temperature superconducting YBCO cable. Different institutes have different schemes, each has its own advantages and disadvantages, suitable for different types of magnets. Figure 7.26 shows different YBCO cables, TSTC (Twisted Stacked-Tape Cable) by MIT, CORC (Conductor on Round Core) by ACT (Advanced Conductor Technologies LLC) and RACC (Roebel Assembled Coated Conductor) by General Cable Superconductors Ltd. These cables are

also in the lab phase, not in batch applications. For large detector magnets, suitable cables need to be studied.

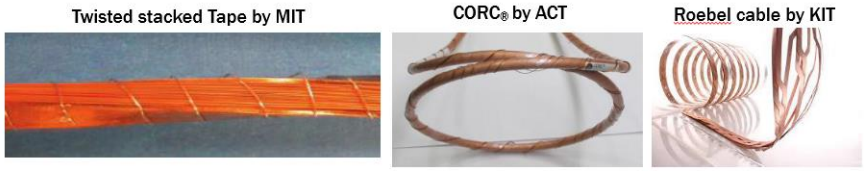

Figure 7.26: different YBCO cables

The advantages of TSTC are simple, high engineering current density, high length ratio of cable to tape length and isotropic J(B). The disadvantage is that it is suitable for winding compact small size magnets. The advantages of CORC cable is the round cable that can be bend freely and isotropic J(B). The disadvantages are low cable conductor length ratio and relatively lower engineering current density. The advantages of Roebel cable are flat cable and high engineering current density. The disadvantages are conductor waste and anisotropic J(B). It is also suitable to wind large detector magnet.

The requirement of detector magnets is long time stable. In this way we can develop a new kind of cable based on HTS strips, welding the HTS strip with solder to form a kind of stack form. For example, we use YBCO strip with 12mm width and 0.5mm thickness to weld ten layers together to form a 12mm wide and 5mm thick YBCO cable. If each trip can carry 800 A current, then 10 layers cable can carry 8000 A current. The disadvantage of this cable is that when excitation or demagnetization, this cable has a strong coupling effect, if the current changes too fast, it can affect excitation or demagnetization. We can use slow excitation or demagnetization to avoid strong electromagnetic coupling. Figure 7.27 shows the YBCO stack cable diagram. This kind of cable is easy to produce. We also need to study the stack cable, if it is suitable to wind the large detector magnet.

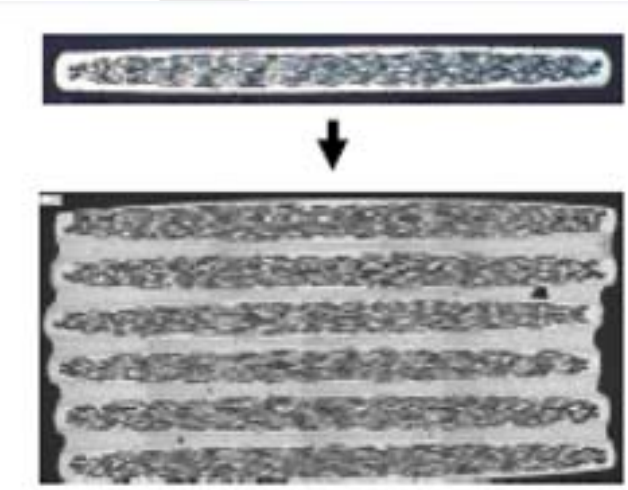

Figure 7.27: HTS stack cable

As for the selection of HTS cables, we need do further research on which type of cable is suitable for our large detector magnets. The following calculation is based on the simplest stack cable.

7.3.3 HTS magnetic design

The YBCO strip selection, for example Table 7.9 gives the parameters of Shanghai superconductor Co. We use 12 mm width YBCO strip. Figure 7.28 is the critical current of the strip at different temperatures and magnetic fields. Table 7.10 is the critical current at different fields. We select the working current 800 A for each strip and 8000 A for each cable.

series	ST-02-E	ST-03-E	ST-04-E	ST-05-L	ST-05-E	ST-06-L	ST-10-E	ST-12-L
Post-processing	Copper-plated	Copper-plated	Copper-plated	Laminated	Copper-plated	Laminated	Copper-plated	Laminated
Average Ic (77K s.f.)	45-60A	75-100A	80-120A	45-120A	120-160A	120-160A	200-350A	200-350A
Wire Width	2mm	3/3.3mm	4mm	4.8mm	5mm	5.8mm	10mm	12mm
Wire Thickness	55-95 μm	55-95 μm	55-95 μm	175-350 μm	55-95 μm	175-350 μm	55-95 μm	175-350 μm
Crit.Tensile Stress	>400Mpa	>400Mpa	>400Mpa	>400Mpa	>400Mpa	>400Mpa	>400Mpa	>400Mpa
Crit.Tensile Strain	0.4%	0.4%	0.4%	0.4%	0.4%	0.4%	0.4%	0.4%
Current Uniformity	±5-10%	±5-10%	±5-10%	±5-10%	±5-10%	±5-10%	±5-10%	±5-10%
Min Bending Diameter	11-15mm	11-15mm	11-15mm	15-20mm	11-15mm	15-20mm	11-15mm	15-20mm

Table 7.9: Parameters of YBCO strip made by Shanghai superconductor Co.

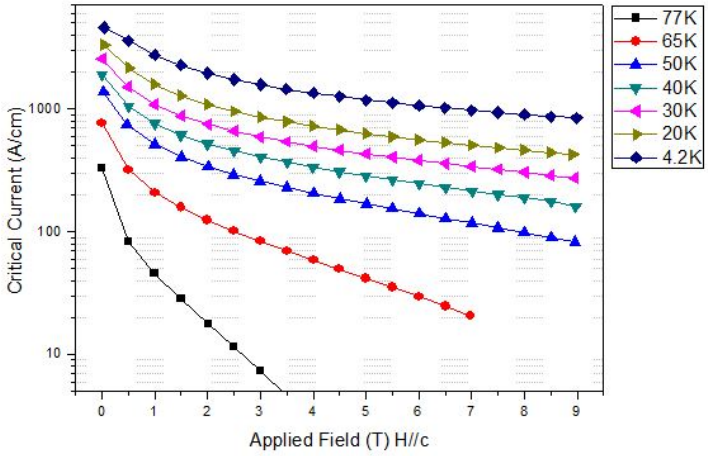

Figure 7.28: Critical current at different temperatures and magnetic fields

Magnetic field	Ic (4.2K)
2T	2000A
3T	1700A
5T	1200A

Table 7.10: critical current at different magnetic field

The superconducting coils are in the form of multiple double pancakes, with a total of 500 turns and 7.5 meters in length. Radial direction can be divided into five YBCO stack cables, each stack cable contains 10 of 12 mm wide YBCO strips, and the thickness is about 50 mm. Table 7.11 is the parameters of HTS magnet. Figure 7.29 shows the magnetic field distribution and Figure 7.30 is the magnetic flux distribution. Table 7.12 and Figure 7.31 show the stray field distribution.

Central magnetic field	3 T	Working current	7970 A
Maximum vertical field on cable	2.7 T	Ampere-turns	20000000
Inner diameter of coil	3.6 m	Inductance	38.36 H
Outer diameter of coil	3.7 m	Stored energy	1.2 GJ
Length of the coil	7.5 m	Operating temperature	Less than 20 K

Table 7.11: Parameters of CEPC detector magnet

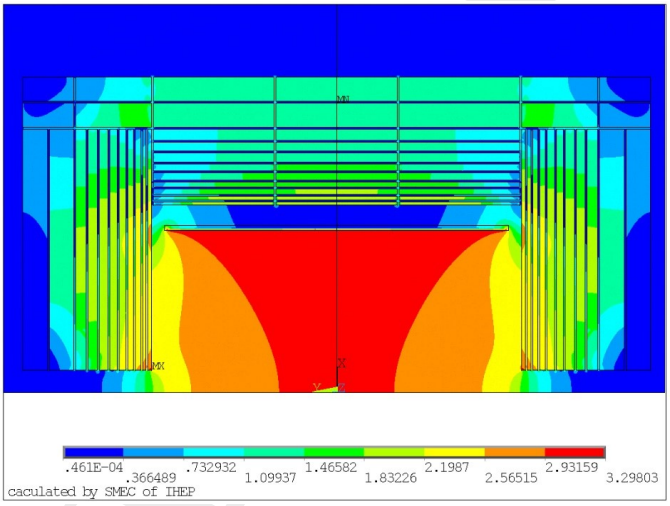

Figure 7.29: Magnetic field distribution

Stray field distribution:

	axial direction	radial direction
50Gs	15m	13m
100Gs	11m	9m

Table 7.12: Stray field region

7.3.4 Future work of HTS plan

I) YBCO cable research. Select proper HTS cable or develop new cable for large detector magnet. II) Study of HTS coil winding process. How to wind the YBCO coil? III) Quench

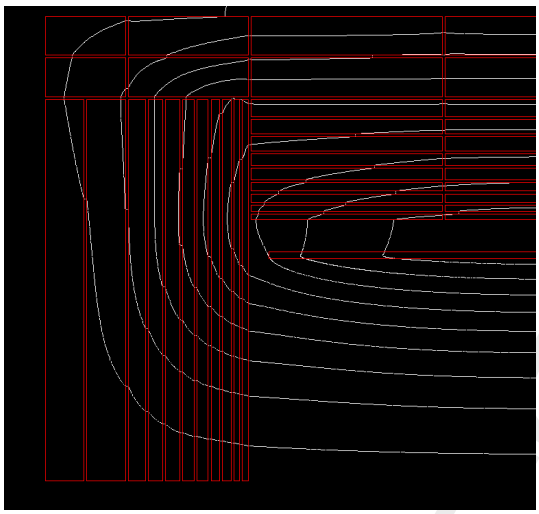

Figure 7.30: Magnetic flux distribution

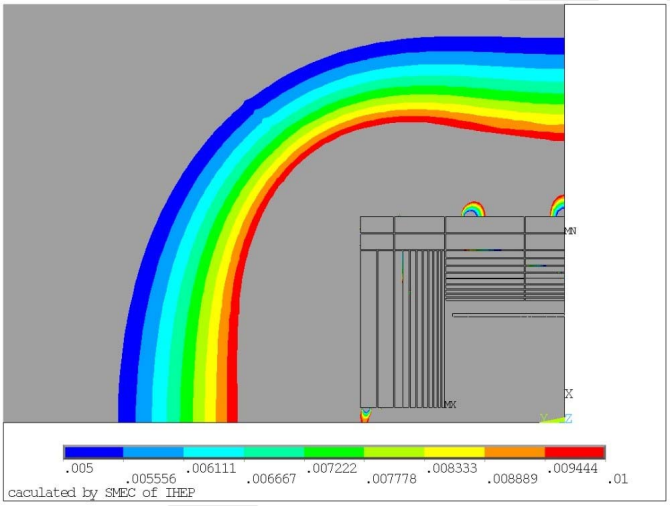

Figure 7.31: Stray field distribution of 50 Gs and 100 Gs

analysis. Study the quench detection, transmission and protection of the HTS coil. IV) Prototype HTS coil development.

7.4 Solenoid Coil Design

7.4.1 Solenoid Coil Structure

The coil has a 4 layer geometry to obtain the 3T center field with a reasonable nominal current, similarly to CMS. The solenoid has 5 modules, which will reduce the degree of difficulty of coil manufacture.

The coil is wound with inner winding technique. The aluminum alloy support cylinder is used as an external mandrel for the winding. The support cylinder is also used as a

mechanical mandrel for the coil and the quench circuit. The cooling tubes welded on the outer radius of the mandrel, where liquid helium circulates, to ensure the temperature of the coil.

A horizontal cryostat was developed for the superconducting magnet, consisting of a vacuum tank and thermal shields (inner and outer) covered with multiple layers insulation (MLI). The stainless steel vacuum vessel is 8.05 m length and 4.25 m outer radius. Two service towers are on top of the vessel to install current leads and phase separator. The vacuum tank, is cantilevered from the central ring of the barrel yoke.

7.4.2 R&D of Superconducting Conductor

The conductor design is similar to that of CMS. As the forces induced in the conductor by the magnetic and thermal loads are beyond the yield stress of pure aluminium, a mechanical strengthening is envisaged. This consists of a superconducting Rutherford cable, which is sheathed in a stabiliser and mechanically reinforced. Two aluminium alloy profiles are welded by electron beam to the central conductor stabiliser, which is made of high purity aluminium. The Rutherford cable will be made with NbTi superconducting strands. It is proposed to use cables with similar characteristics to the CMS superconductor, with a slightly decreased number of strands in the cable. The superconductor characteristics are shown in the table 7.13.

Superconducting strand in virgin state	
Strand diameter	1.2 mm
Cu/NbTi	1.3
SC strand critical current density	$\geq$ 2700A/mm2 @4.2K,5T
Filament diameter	About 55 um
RRR of copper matrix	$\geq$ 100
Twist pitch	1.3
Rutherford cable	
Number of strand	32
Cable transposition pitch	120mm
Compacting ratio	0.87
Final conductor	
Ic degradation during manufacturing	<10%
Nominal design current	16KA
Critical current at 4.2K and 5 Tesla	50KA
Total length of conductor	31km

Table 7.13: Superconductor characteristics

The initial critical current density of strands have a maximum degradation of 5% . The initial RRR of copper matrix of strands have a degradation of 1/3 due to the stranding process, as demonstrated on the tests by IHEP and Toly Co. The shear strength between copper and pure Al have a minimum value of 30MPa after the inserting process. And

other parameters of the superconductor due to the inserting process are test now. Samples are shown in Figure 7.32

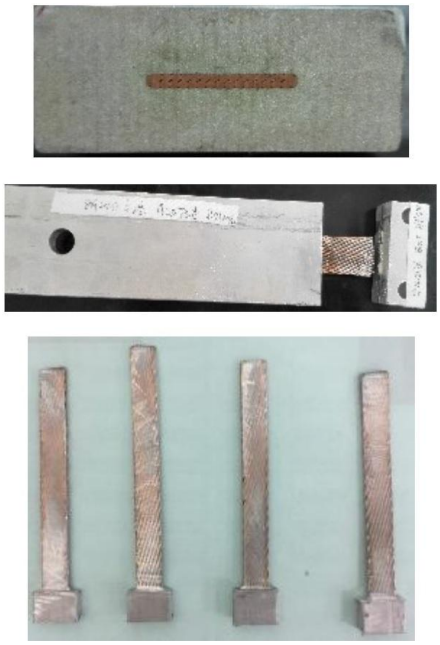

Figure 7.32: Samples of shear strength test

7.4.3 Coil fabrication and assembly

1.The coil supporting cylinder machining

The coil supporting cylinder consist of five modules, three longer modules in the middle and two shorter ones at the end. All modules are built with aluminium alloy 5083, which inner surfaces are high precision machined and cooling tubes are welded on outer surface. The three longer modules have two flanges and tube joints at each end. The two shorter ones have only one flange at the end and the tube joints at this side too, and the support rods are arranged on the other side.

2.coil winding

The coil is wound with the so-called inner winding technique, where the support cylinder is used as an external mandrel for the winding with a vertical axis. The five modules will be wound, immersed and cured individually.

3.coil assembly

The five coil modules are assembled together by the assembly tooling in the vertical position. They are assembled from one side to the other side. First, one short module is put on the assembly tooling in the vertical position, and then a longer one is put on it, and the flanges of the two modules are connected and the tube joints are welded, thus the two modules are assembled together. According to this method, the other three modules will be assembled together one by one.

7.5 Magnet Cryogenics Design

7.5.1 Preliminary Simulation of the Thermosyphon Circuit

7.5.1.1 Computational model and mesh

CEPC Detector Superconducting Magnet is cooled by the welding U-shaped pipe outside the coil, which using the thermosyphon principle. The thermosyphon circuit consists of three parts: the supplying pipe, the cooling pipe and the returning pipe. The liquid helium absorbs the heat in the cooling pipe and phase change occurs. The pressure in the cooling pipe changes and a gas-liquid two-phase flow is formed under the pressure difference between the two sides of the circuit. In order to study the phase transition process of helium in the circuit, the original circuit is simplified and the constant mass flow is used instead of the original pressure driving flow. So a single tube model is established (shown in Figure 7.33). Figure 7.33 a shows a 10:1 scale model and Figure 7.33 b shows a schematic diagram of 1:1 scale model. The entire circuit uses a uniform diameter of 14mm, the circuit place vertically and direction of gravity is downward vertically.

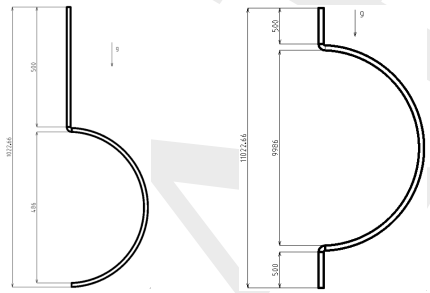

Figure 7.33: a. The 10:1 scale model b. The 1:1 scale model (schematic diagram) The computational model (mm)

ANSA is used to generate the mesh of the above three-dimensional model with a total number of 9.84 million for 10:1 scale model and 3.74 million for 1:1 scale model (still in the test stage), the mesh shape is shown in Figure 6.5.2. Because the scale of the latter is bigger than the former, the mesh setting of the 10:1 scale model is not applicable to 1:1 scale model and the simple simulation of 10:1 scale model was started early. In order to capture the accurate phase transition process and obtain accurate simulation results, a smaller mesh and time step is needed. Meanwhile, the mesh density increase near the wall is required to accurately compute the fluid boundary layer, as shown in Figure 7.34. The distribution of the boundary layer affect directly the heat transfer, phase change and two-phase flow process in the cooling pipe.

7.5.1.2 Computation settings for all scales

According to the data, set the inlet flow of 2.5g/s, using the flow calculation formula,

$$m = \rho V A$$

The fluid inlet velocity is 0.13 m / s. And then using Reynolds number calculation formula,

$$Re_D = \frac{\rho V D}{\mu}$$

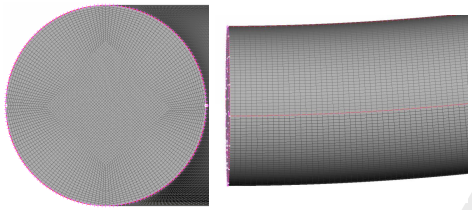

Figure 7.34: a. Cross-section mesh b. Lateral mesh The mesh shape

The result is $Re_D = 71830$. It is found that the Reynolds number of the flow in the thermosyphon circuit is much larger than the critical Reynolds number ($Re_{D,C} = 2300$), thus the flow in the thermosyphon is turbulent flow, using turbulence model to simulate it.

The phase transition of liquid helium and the two-phase flow process in the thermosyphon are simulated by VOF method to capture the two-phase interface. The liquid and gas properties of the helium are shown in Table 7.14, the difference between the standard state enthalpy (hs) of gas and liquid represents the latent heat required for phase transformation of liquid helium.

The physical properties	Liquid helium	Gas helium
T(K)	4.18	4.21
$\rho(kg/m^3)$	124.972	16.627
H_s	-864.648	82709.986
Tboil(K)	4.2	
$\rho(mN/m)$		0.096

Table 7.14: The physical properties

The settings of the simulation boundary conditions are shown in Table 7.15. The heat of the evaporator is simplified as a constant heat flux density, which is initially set to 12.4W/m2. Then, the heat flux density is adjusted according to the flow heat transfer condition so that the gas mass fraction is less than 10% in the final stable gas-liquid two-phase flow, to ensure the safety and stable of the entire circuit.

Positions	Boundary conditions	Parameters
Inlet	Velocity inlet	$V = 0.13m/s, T = 4.18K$
Outlet	Pressure outlet	$P = 101325Pa, T = 4.18K$
The heat wall	Constant heat flux density	$q = 12.4W/m^2$
Other walls	Adiabatic wall	$q = 0$

Table 7.15: The physical properties

7.5.2 Preliminary results for 10:1 scale model

More mesh number and smaller time step make the simulation slowly. Two-phase flow in the cooling pipe has not reached a steady state yet. The latest transient result is t=6.012s as shown in Figure 7.35 and 7.36. The temperature distribution of the circuit comprised as shown in Figure 7.35. At t=1s, the temperature of the cooling pipe is gradually raised from the initial temperature of 4.2K under the heating of the constant heat source. At this time, all the working fluid in the circuit is liquid helium as shown in Figure 7.36. At t = 5.042s, the liquid helium reaches the boiling point (4.23K) in the upper part of the cooling pipe, because it is kept heated during the upward flow process from the initial time. Therefore, the overall temperature of the upper part of the cooling pipe was shown in Figure 7.35; meanwhile, phase change occurs in the upper part of the cooling pipe, as shown in Figure 7.36. As the time goes by, the heat canąt be transferred immediately in the upper part, the temperature will gradually increase. In addition to that, the simulation of 1:1 scale model was still in the test of mesh generation.

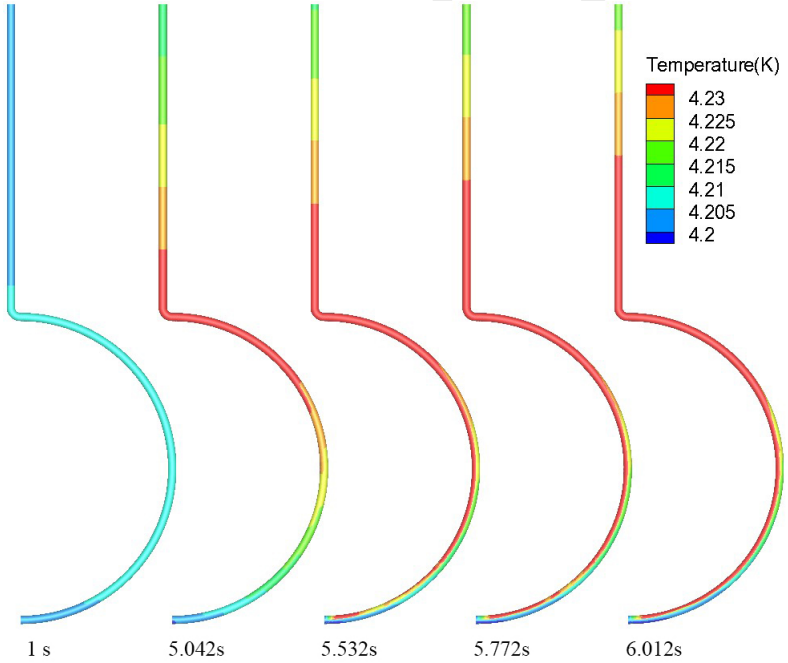

Figure 7.35: The comparison of the temperature distribution

Figure 7.37 shows the blue box part of Figure 7.36 (ie, the upper part of the cooling pipe). The helium bubbles emerged in the inner wall of the cooling pipe initially and then move outward because of the occurrence of buoyancy, part of the small bubbles gathered into a larger bubble in the vicinity of the outer wall, and followed to the outlet by the fluid.

7.5.3 Experiment of a small-sized He thermosiphon

7.5.3.1 Experimental Set-up

As shown in Figure 7.38, the experimental facility consists of a vertical oriented one meter long cryostat insulated by vacuum space and two cold shields which are conducted by cold head to minimize radiation and conduction heat transfer from the environment. The loop is mainly composed of two vertical tubes joined in a U shape with the upper

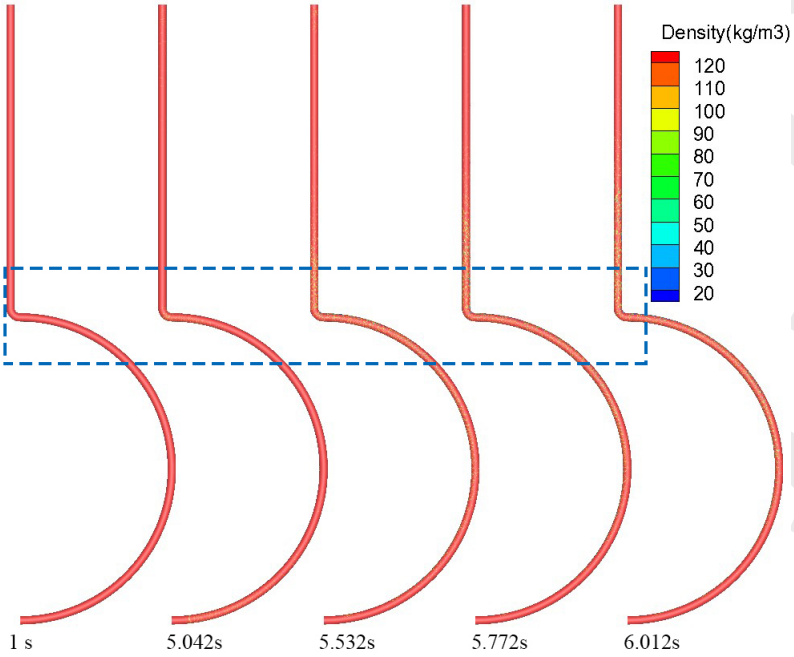

Figure 7.36: The comparison of the density distribution. (red: liquid helium, blue: gas helium)

ends connected to the phase separator, and the phase separator is connected directly to the second cold head. The cooling power is 1.0W@4.2K.

As shown in Figure 7.39,the schematic of experimental measures circulation loop. Five thermometers distributed along the tube were used for measurement of local inner wall temperature to deduce the corresponding heat transfer coefficient. The sensors have a measurement sensitivity of 0.1K between 2.5K to 25K.

7.5.3.2 Experimental result and analysis

As shown in Figure 7.40, when the heat flux is 137W/m2,the helium pressure increases from 0.3MPa to 1.8MPa,then descend to near 1.1MPa ,after that following up and down under the filling ratio of 26%.When the filling ratio is 52% and 87%,the pressure in thermosiphon maintain constant in general,as for ratio 87%,the pressure is a little higher than 52%.

In the beginning of the experiment, ΔT_w increases linearly with heat flux at low heat fluxes. Before $q_A = 25W/m^2$ at point A on Figure 7.41 and Figure 7.42, the heat transfer is identified as single phase natural convection. After point A, the temperature difference show difference between Figure 7.41 and Figure 7.42,the reason is that heat transfer intensity in exit section is higher than that in entrance, this leads to the upper comes to dry out earlier, then develop to the bottom with heat increase. a) Before $q_A = 25W/m^2$ at point A, the heat transfer is identified as single phase natural convection. b) Between points A and C is in the developing nucleate boiling regime. c) The transition from nucleate boiling to film boiling occurs at point C. d) After point E helium enters its supercritical state.

Calculation formula of heat transfer:

$$h = fracqT_w - T_f$$

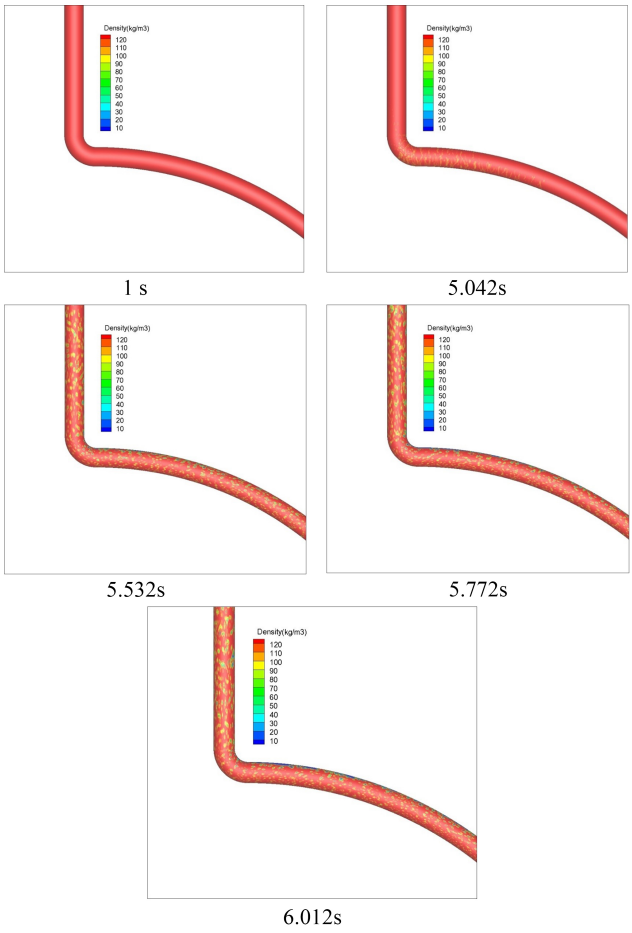

Figure 7.37: The comparison of the density distribution in the upper part of cooling pipe. (red: liquid he,blue: gas he)

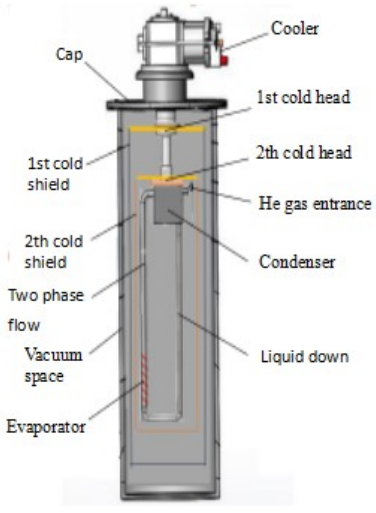

Figure 7.38: the main component structure of the experimental cryostat

Where T_w and T_f are, respectively, the wall and fluid temperatures, we assume $T_4 = T_f$. a) h changes almost linearly with q in the whole regime, at location $z = 6.5cm$. b)

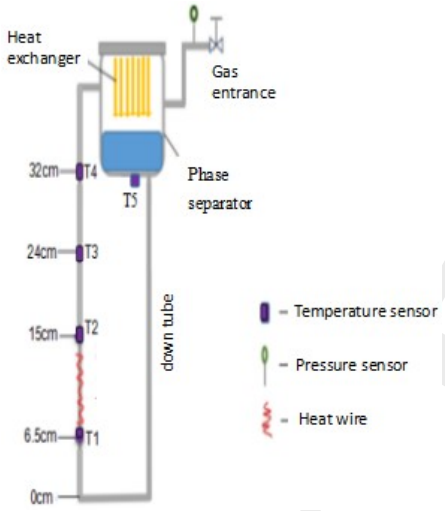

Figure 7.39: Schematic of the experimental measures circulation loop

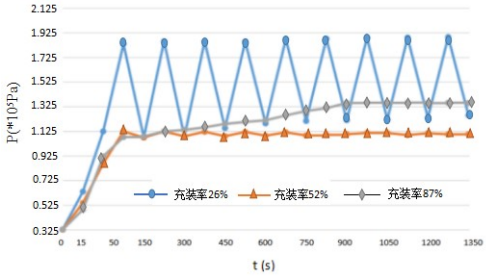

Figure 7.40: the saturation pressure of different filling ratio varies with time in heat flux $137W/m^2$

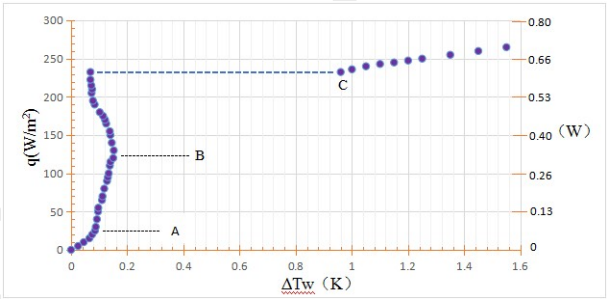

Figure 7.41: Boiling curve at $Z = 6.5cm$ in the entrance

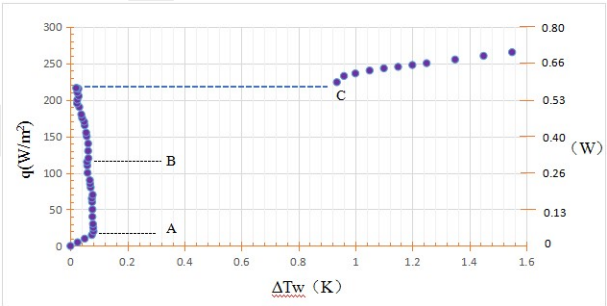

Figure 7.42: Boiling curve at $Z = 32cm$ in the exit section

The heat transfer is better in the upper part ($z < 24cm$) of the testing tube than the lower locations($z < 6.5cm$) where boiling is less developed. c) When the heat flux becomes higher than point C, heat transfer fall off quickly, since a large amount of vapor cannot be liquefied immediately, the heating surface is covered by a film of vapor.

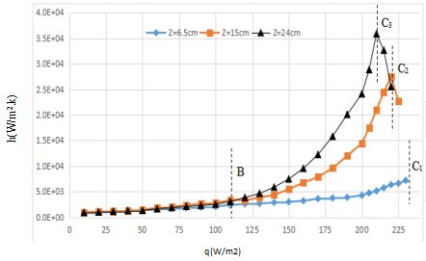

Figure 7.43: Heat transfer coefficient at different locations of the tube

7.5.4 Cryogenic System

7.6 Quench Protection and Power supply

7.6.1 power supply

The power supply for the solenoid is DC stabilized current supply with low voltage and high current, which should be adjusted slowly and evenly. In order to have a steady field, the ripple of the power supply should be lower. It is provided with a free-wheel diode systems and needs demineralized water cooling. Figure 7.44 is the main ciruit topology diagram.

The system consists of 2 stage 12 pulse diode parallel rectifier + post stage 4 group IGBT chopper circuit in parallel, in the post stage chopper circuit, the IGBT switching frequency is 10kHz, and the output power is 80kHz by phase shift frequency doubling control. In parallel chopper circuit, there is current sharing loop, plus balanced filter inductance, EMI filter is added to the power input to effectively reduce the pollution of the power supply to the grid. The main circuit uses the laminated busbar design process, to reduce the circuit stray inductance, weaken the skin effect and proximity effect of high-frequency current. Figure 7.45 is the main ciruit topology diagram.

7.6.2 control and safety systems

The safety system and the control system are independent, but exchange information between each other. The safety system measures magnet status in order to prevent operation in dangerous condition. The safety signals coming from quench detectors and voltage taps are transferred to the main switch in the circuit directly and trigger a fast discharge of the magnet. Also the quench detectors are used to protect the bus bars and the current leads. In addition, a substantial amount of instrumentation is required to monitor the operational status of the magnet and to provide diagnostic data such as temperature, stress, position and etc. The control system provides the controls needed to execute the automatic processes of the various running mode of the magnet system. It is based on PLC and control software.

Quench protection Plan: to provide quench protection system for cepc magnet, including signal acquisition, quench judgment,Energy release device. Pre research content:

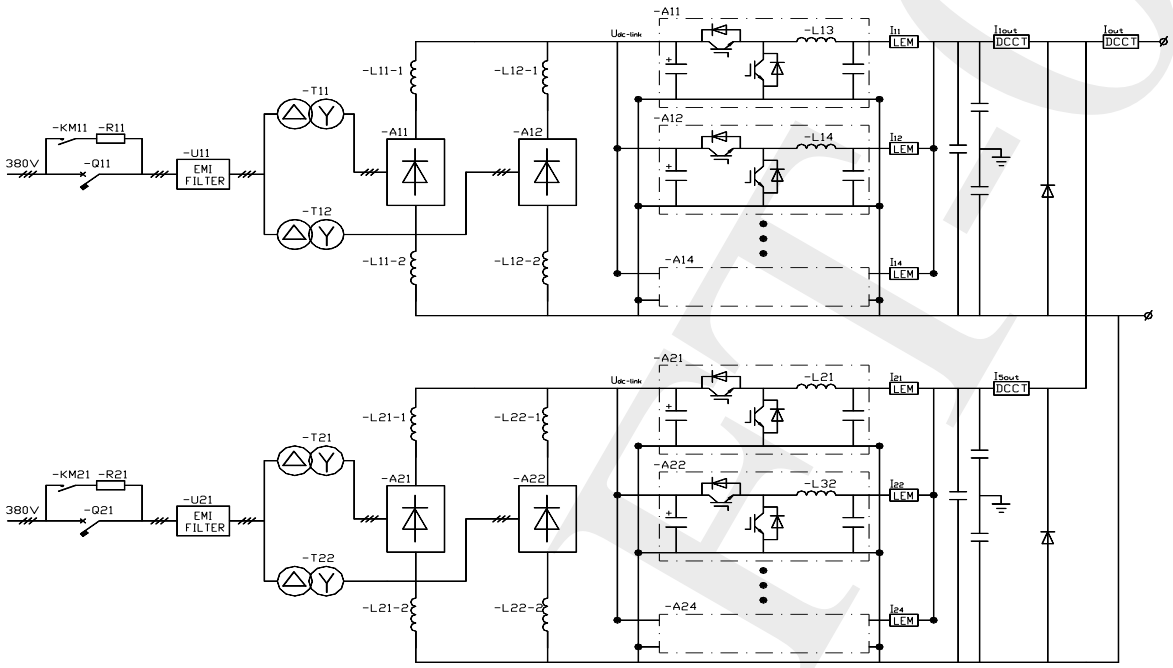

Figure 7.44: Main circuit topology diagram

Design quench protection system, including design of quench detector, quench protection-Circuit, write out judgment program, investigate energy release device, including water cooling part.

Magnet parameter monitoring Plan: monitoring the magnet parameters, radial and axial rod, low temperature, vacuum, bus Temperature, valve box temperature and vacuum, power supply parameters monitoring, including current, voltage,Internal temperature, cooling water flow, etc.. Pre research content: because the monitoring parameters are mainly weak voltage and small current, multi-channel instrument is investigatedTables and PLC acquisition signals, design optimization collection program and program design Meter.

7.7 Iron Yoke Design

According to the physical design, the CEPC detector solenoid magnet need to provide a 3.0 T field for precise trajectory measurement for charged particles. The CEPC solenoid consists mainly of three parts, which are a superconducting coil, a vacuum tank with a thermal shield and a magnet yoke. Figure 7.46 shows the structure of the CEPC detector solenoid magnet and yoke. The solenoid magnet will produce an axial field and the magnet yoke will take responsible for the return of the magnetic flux and reducing the outside stray field to an acceptable level. At the same time, the magnet yoke must match

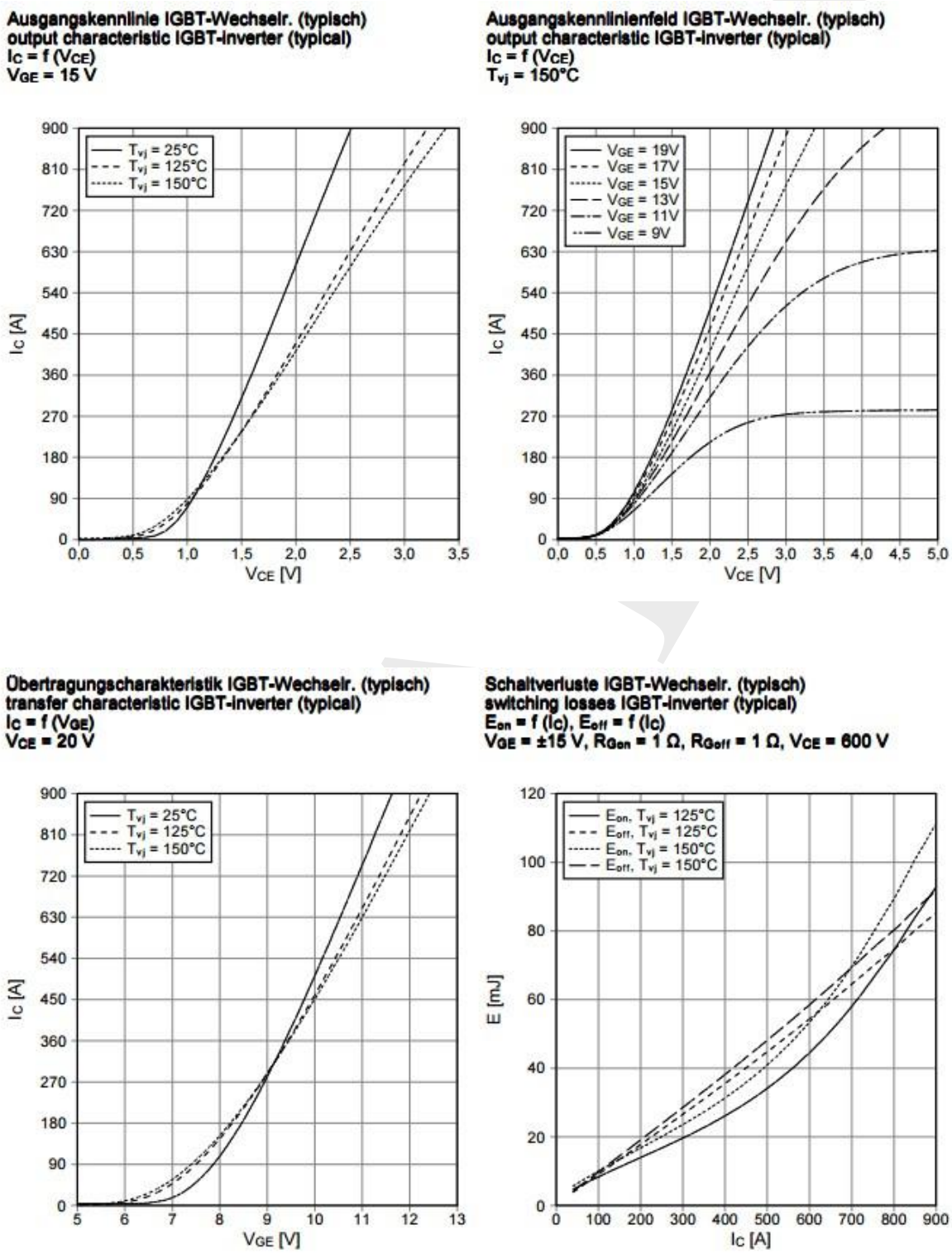

Figure 7.45: IGBT Performance schematic diagram

several other design requirements. Firstly, the yoke will provide mechanical support for sub-detectors so that they can be positioned accurately. Secondly, the yoke will provide room for muon detectors which will be set between layer and layer of yoke. Thirdly, the yoke will provide space for data cable, cooling pipes , gas pipes and so on. According

to the general design of the CEPC detector, the magnet yoke is divided into a cylindrical barrel and two endcap yokes. Taking into account of both mechanical performance and magnetic requirements, high permeability material need to be developed as the yoke material. Preliminary design of the yoke will be described as following.

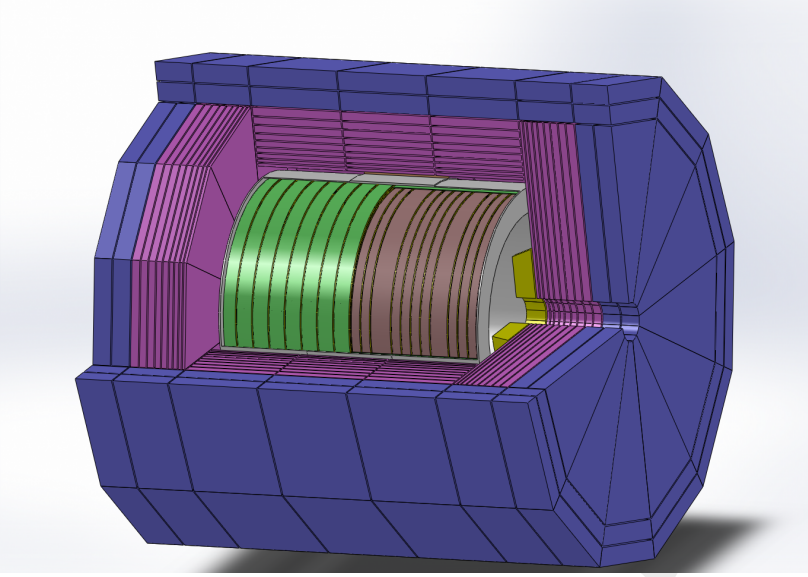

Figure 7.46: iron and magnet

7.7.1 The Barrel Yoke

The barrel yoke will have a length of about 8200 mm and with a dodecagonal shape. The inscribed circle diameter of the outer dodecagon will be about 13300 mm, and the inscribed circle diameter of the inner dodecagonal will be about 7800 mm. The barrel yoke will be composed of 3 rings, each ring will consist of 7 layers. There will be two 100 mm gaps between the rings which are designed to supply space for the data cables and services. The thickness of inner 4 layers are 100 mm and outer 3 layers are 450 mm. There will be 100 mm space between layers for muon detector. Figure 7.47 shows the schematic design of the barrel yoke.

7.7.2 The Endcap Yoke

There are two endcap yokes. Figure 7.48 shows the overall dimensions of them. The endcap yokes have a dodecagonal shape too. The inscribed circle diameter of the outer dodecagon will be 13300mm. The total thickness of the endcap will be 3150 mm. Each endcap yoke will consist of 7 layers. The thickness of the inner first layer is 600mm. The second layer to the fourth layer is 100 mm. The outer 3 layers are 200 mm. There will be 100 mm space between layers for muon detectors.

7.7.3 Yoke assembly

The total weight of the yoke will be about 10000 tons. Each ring of the barrel yoke and each endcap yoke will be composed of 12 segments. The maximum weight of the segments of the barrel yoke and endcap yoke will no more than 150 and 200 tons, respec-

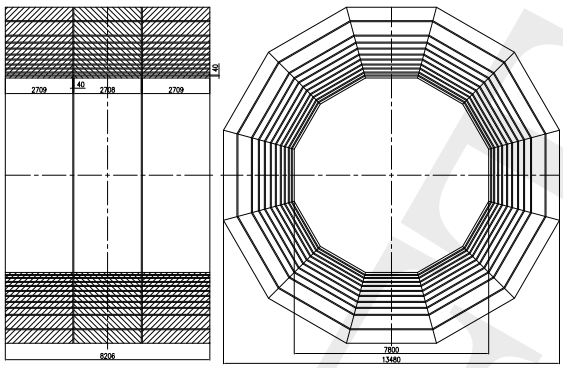

Figure 7.47: iron design

tively. The yoke will be preassembled at the manufacturer. Then they will be transported to the experimental site as segment. If there will be enough space, the yokes will be assembled at the IR hall. Otherwise they will be assembled in the surface building above the IR hall. The middle ring will be assembled together with the solenoid magnet. It will be the biggest one part to be lowered into the IR hall. Its weight will be about 3000 tons. A temporary gantry crane will be equipped. The time used for assembly at the IR hall will longer than that of assembly in the surface building.

7.8 Dual Solenoid Scenario

The active shielding design has been applied widely for commercial MRI magnets. Comparing to the one solenoid and yoke design, this design achieves a similar performance while being much lighter and more compact, which has been improved by FCC previous studies [1, 2]. Key to the choice of such magnets, in addition to their cost and complexity, is their ability to allow high-quality muon tracking. This is crucial for studying the properties of the Higgs boson, for example, and any additional new fundamental particles that await discovery. We will provide the active shielding conceptual design for Physicists to estimate its ability to allow high-quality particles tracking.

The active shielding design features two concentric antiseries connected superconducting solenoids, with the same room temperature bore as the one solenoid magnet mentioned in the chapter 8.2.1. The main solenoid provides 5 T central field over an obstruction-free room temperature bore of 7.2 m and a length of 7.6 m. The outer solenoid provides -2 T central field, with a radius of 6.5 m and a length of 10 m. The cold mass

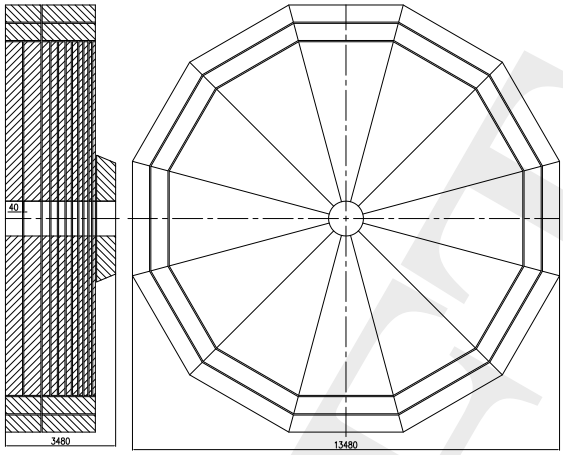

Figure 7.48: iron design

consists of two support cylinders for the main solenoid and shield solenoid (Figure 7.49). The available areas for muon chambers are marked in the figure. The field map of the magnet is showed in Figure 7.50, for consultation of particles tracking.

Figure 7.49: Sketch figure for the half cross section of the active shielding magnet, with the available areas for muon chambers

References

[1] CEPC project website. http://cepc.ihep.ac.cn.

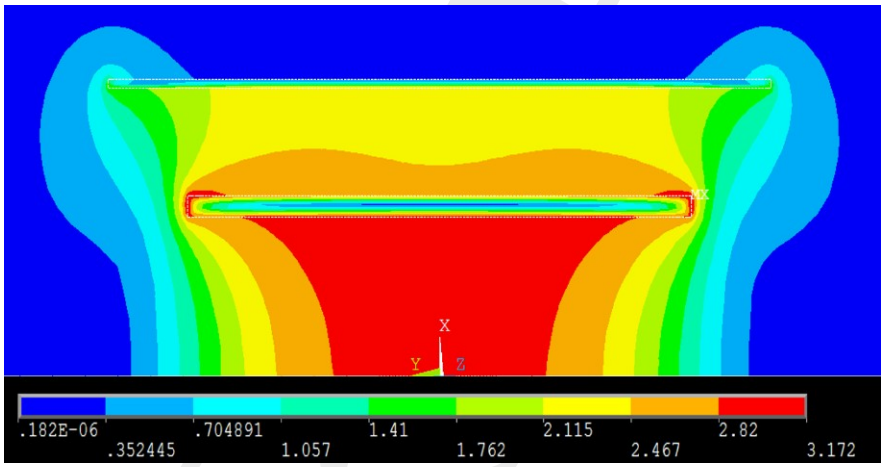

Figure 7.50: Field map of the active shielding magnet

CHAPTER 8

MUON SYSTEM

As described in pre-CDR [1], the CEPC muon system acts as the muon identifier, the solenoid flux return yoke and the support structure for the whole spectrometer. High muon detection efficiency, low hadron mis-identification rate, modest position resolution and large coverage are the main concerns of the design. The muon system plays an important role in measuring physics processes involving muon final states, e.g. $e^+e^- \to ZH$ with $Z \to e^+e^-$ or $\mu^+\mu^-$. In addition, it compensates for leaking energetic showers and late showering pions from the calorimeters, which is important to improve the relative jet energy resolution[2].

8.1 Baseline Design

The CEPC muon system is the outermost component of the whole detector. It is divided into barrel and end-caps, as shown in Fig. 5.1. Both the barrel and end-caps consist of segmented modules. The segmentation is constrained by the maximum sizes of the module and sensitive unit (more segments are required for a larger detector), dodecagon segmentation is selected for the baseline design of the CEPC muon system. All baseline design parameters are summarised in Table 8.1. These parameters will be further optimised together with the inner detectors, in particular the ECAL and the HCAL.

The number of sensitive layers and the thickness of iron (or tungsten) in the absorbers are two critical parameters. For the baseline design, the total thickness of iron absorber is chosen to be 8λ (the nuclear interaction length of iron) distributed in 8 layers, which should be sufficient for effective muon tracking. Gaps of 4 cm between neighbouring iron layers give adequate space for installing sensitive detectors.

Table 8.1: The baseline design parameters of the CEPC muon system

Parameter	**Possible range**	**Baseline**
Lb/2 [m]	3.6 – 5.6	4.0
Rin [m]	3.5 – 5.0	4.4
Rout [m]	5.5 – 7.2	7.0
Le [m]	2.0 – 3.0	2.6
Re [m]	0.6 – 1.0	0.8
Segmentation	8/10/12	12
Number of layers	6 – 10	8
Total thickness of iron	6 – 10λ ($\lambda = 16.77$ cm)	8λ (136 cm) (8/8/12/12/16/16/20/20/24) cm
Solid angle coverage	(0.94 – 0.98)$\times 4\pi$	0.98
Position resolution [cm]	$\sigma_{r\phi}$: 1.5 – 2.5	2
	σ_z : 1 – 2	1.5
Detection efficiency ($E_\mu > 5$ GeV)	92% – 99%	95%
Fake($\pi \to \mu$)@30GeV	0.5% – 3%	$< 1\%$
Rate capability [Hz/cm^2]	50 – 100	$\sim$60
Technology	RPC μRWell	RPC (super module, 1 layer readout, 2 layers of RPC)
Total area [m^2]	Barrel	$\sim$4450
	Endcap	$\sim$4150
	Total	$\sim$8660

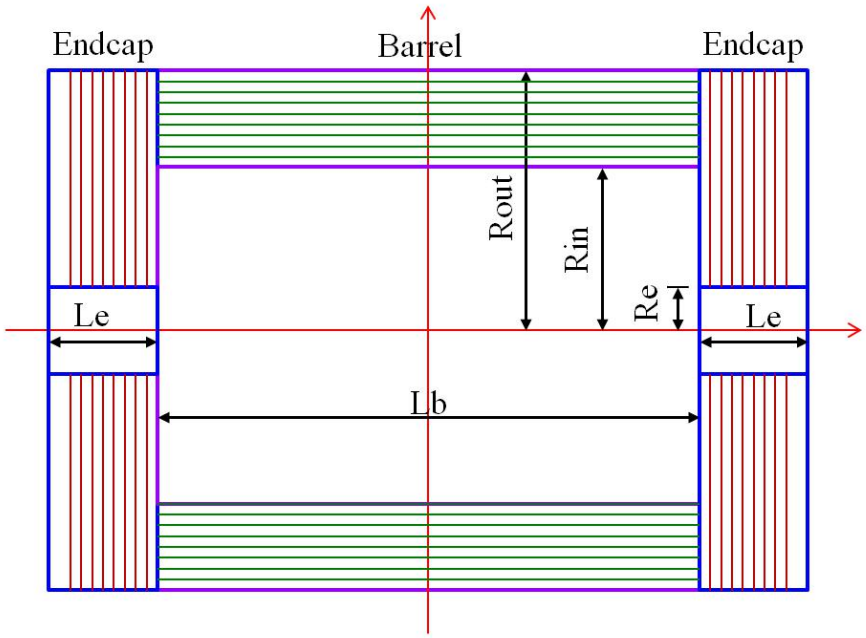

Figure 5.1: The basic layout of the muon system.

The solid angle coverage of the CEPC muon system should be up to $0.98 \times 4\pi$ in accordance with the tracking system. Position resolutions of $\sigma_{r\phi} = 2.0$ cm and $\sigma_z = 1.5$ cm are also required. Since the particle flow algorithm calorimetry provides very good particle identification capabilities, the detection efficiency of 95% ($E_\mu > 5$ GeV) of the CEPC muon system should provide enough redundancy in muon detection for most physics processes related to muons. Based on the dimensions and segmentation of the baseline design, the total sensitive area of the muon system amounts to 8600 m^2.

8.2 The Resistive Plate Chamber technology

Resistive Plate Chamber (RPC) is suitable for building large area detectors with milimeter spatial resolution. It has been applied in muon systems for experiments including BaBar [3], Belle [4], CMS [5] , ATLAS [6], BESIII [7], and Daya Bay [8]. It provides a common solution with the following advantages: low cost, robustness, easy construction of large areas, large signal, simple front-end electronics, good time and spatial resolution. It is chosen as the baseline design of the CEPC muon system.

RPCs can be built with glass or Bakelite, and run in avalanche or streamer mode. Bakelite RPCs of about 1200 m^2 and 3200 m^2 were produced for the BESIII and Daya Bay muon systems, respectively. Compared with glass RPC, Bakelite RPC has the advantages of easier construction, lower density, larger cell size and lower cost, especially if the event rate is below 100 Hz/cm^2 as required by the CEPC muon system. The characteristics of Bakeliete and glass RPCs are compared in Table **??**. Further improvements are required for Bakelite RPCs, however, in terms of long-term stability, detection efficiency, readout technologies, lower resistivity ($< 10^{10}$) and higher rate capability.

Table 8.2: Comparison of Bakelite and glass RPC.

Parameters		Bakelite	Glass
Bulk resistivity [$\Omega\cdot$ cm]	Normal	$10^{10} \sim 10^{12}$	$> 10^{12}$
	Developing	$10^{8} \sim 10^{9}$	
Max unit size (2 mm thick) [m]		1.2×2.4	1.0×1.2
Surface flatness [nm]		< 500	< 100
Density [g/cm^3]		1.36	2.4∼2.8
Min board thickness [mm]		1.0	0.2
Mechanical performance		Tough	Fragile
Rate capability [Hz/cm^2]	Streamer	100@92%	
	Avalanche	10K	100@95%
Noise rate [Hz/cm^2]	Streamer	< 0.8	0.05

8.3 The μRWell technology

The μRWell is a compact, spark-protected and single amplification stage Micro-Pattern Gas Detector (MPGD). In the μRWell technology an additional discharge resilience with respect to the triple-GEM detectors is foreseen as well as a simplified assembly geometry. A μRWell detector [**?**] is composed of two PCBs: a standard GEM Drift PCB acting as the cathode and a μRWell PCB that couples in a unique structure the electron amplification (a WELL patterned matrix) and the readout stages 8.2a). A standard GEM 50 μm polyimide foil is copper clad on one side and Diamond Like Carbon (DLC) sputtered on the opposite side. The thickness of the DLC layer is adjusted according to the desired surface resistivity value (50-200 M$\Omega/\square$) and represents the bottom of the WELL matrix providing discharge suppression as well as current evacuation. The foil is then coupled to a readout board 8.2b). A chemical etching process is then performed on the top surface of the overall structure in order to create the WELL pattern (conical channels 70 um (50 um) top (bottom) in diameter and 140 μm pitch) that constitutes the amplification stage 8.2c). The high voltage applied between the copper and the resistive DLC layers produces the required electric field within the WELLs that is necessary to develop charge amplification. The signal is capacitively collected at the readout strips/pads. Two main schemes for the resistive layer can be envisaged: a *low-rate* scheme (for particles fluxes lower than 100 kHz/cm^2) based on a simple resistive layer of suitable resistivity; and an *high-rate* scheme (for a particle flux up to 1MHz/cm^2) based on two resistive layers intra-connected by vias and connected to ground through the readout electrodes. Finally, a drift thickness of 3-4 mm allows for reaching a full efficiency while maintaining a versatile detector compactness.

A distinctive advantage of the proposed μRWell technology is that the detector does not require complex and time-consuming assembly procedures (neither stretching nor gluing), and is definitely much simpler than many other existing MPGDs, such as GEMs or MicroMegas. Being composed of only two main components, the cathode and anode PCBs, is extremely simple to be assembled. The engineering and the following indus-

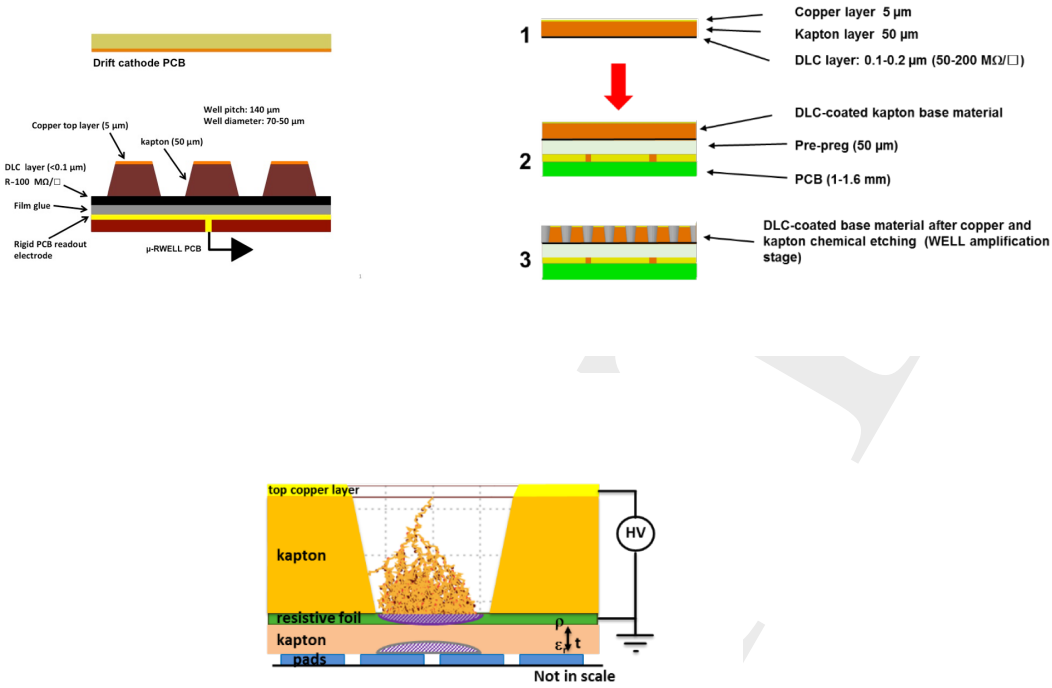

Figure 8.2: a) Layout of a μRWell detector module; b) Coupling steps of the μRWell PCB c) Amplification stage directly coupled with the readout.

trialization of the u-RWell technology is one of the most important goals of the project. The engineering of the detector essentially coincides with the technological transfer of the manufacturing process of the anode PCB to a suitable industrial partner. The main advantage of the μRWell technology with respect to other MPGD technologies (such as GEM or MM) is that in principle most of the manufacturing steps are already available by a typical company working on rigid and flexible PCB technology. In particular, the anode PCB manufacturing, apart from the DLC coating and the etching of the holes on the thin polyimide foil, the technology and the know-how are already available at the ELTOS Company (an Italian company located in the industrial area around Arezzo, specialized in rigid PCB). While the DLC dry sputtering will probably still be performed by a specialized external company (at the moment this is done by a Japanese firm), the polyimide etching to realize the micro-hole pattern, currently in the hand of the PCB-Workshop of CERN, will be the object of a technological transfer to the industrial partner. The technology is suitable for large area tracking devices and compact digital hadron calorimetry in HEP experiments; for X-ray and neutron imaging in industrial applications, medical and in particular for homeland security, where muon tomography requires very large area coverage. The technology could also be a much better option to cope with the more stringent requirements introduced in future experimental scenarios by dealing with those high luminosity high energy beams foreseen in the next generation particle accelerators, as CEPC or FCC.

8.3.1 Large size μRWell detectors

Modern HEP experiments, as well as some specific applications of gaseous detectors, require for large area coverage. In particular the upgrade of the experiments at the HL-LHC at CERN needs to cover large regions with high precision rad-hard tracking devices.

Figure 8.3: Top) Picture of the CMS GE1/1-μRWell prototype. Bottom) Picture of the CMS GE2/1 sector with two M4 μRWell prototypes.

The single-resistive layer μRWell is a mature technology that has been proposed as tracking device for the CMS Phase2 upgrade of the muon detector. The upgrade in the end-cap region called GE2/1, foresees several $\sim 2 \times 1$ m^2 trapezoidal chambers to cover a global area of about 140 m^2. In this framework an R&D for the engineering, construction and test of large size single-resistive layer μRWells has been pursued. The task has been accomplished in strict collaboration with an Italian PCB Company (ELTOS SpA, http://www.eltos.com/).
As a first step a $\sim 1.2 \times 0.5$ m^2 μRWell (GE1/1-μRWell prototype) was designed, built and characterized in a beam test at the H8-SPS area at CERN, smaller than the final GE2/1, but $\sim$40 times larger than every μRWells prototype previously built (fig. 8.3 Top).

The GE1/1 prototype had a resistive DLC surface resistivity of about 70 MΩ□ (in the *low-rate* schema configuration). The strips pitch was 800 μm and the chamber was equipped with VFAT2 front-end electronics. The gas mixture used was $Ar/CO_2/CF_4$ (45/15/40), with a drift gap of 7 mm. Due to different used geometries for the amplification stage, the prototype was divided into two sectors (left and right) of slightly different gain. Both sectors were tested for efficiency and time resolution and the results compared with the performance of small μRWell prototypes (10 cm x 10cm, built in the *high-rate* configuration) used into the same experimental setup and equipped with the same electronics. Figure 8.4a) shows the efficiency as a function of gain for the GE1/1 size prototype and two small (10x10 cm^2) μRWell prototypes: one can observe that the three detectors have an identical behavior. Figure 8.4b) shows the time resolution as a function of gain: a resolution better than 6 ns is obtained for all three μRWell prototypes for a gain of about 10000.

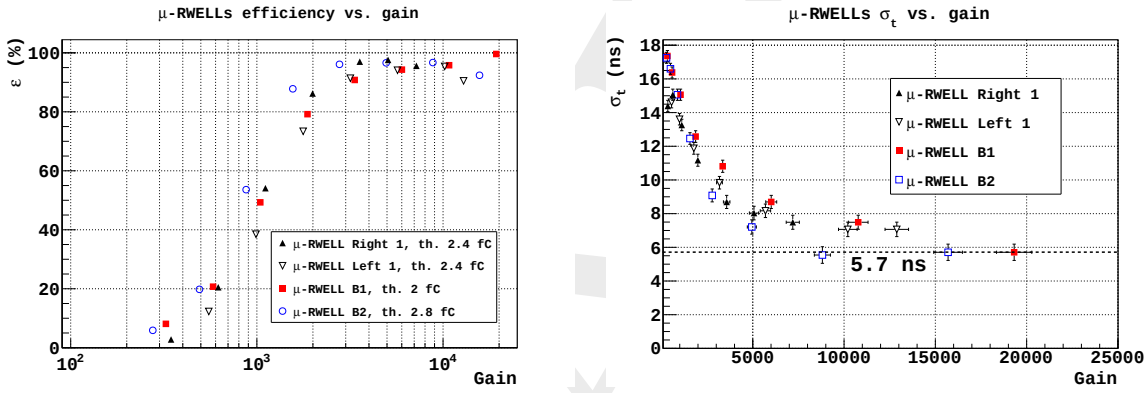

Figure 8.4: a) Efficiency vs Gain. b) Time resolution vs Gain.

In July 2017, the first GE2/1 20 degree sector equipped with two large area M4 μRWell detectors (each of dimensions ∼50x60 cm^2) was assembled. It was subsequently exposed to a muon beam at the H4 test beam at CERN. The detector was placed on a remotely controllable moving platform in order to allow to scan the surface of the detector across the muon beam, as can be seen in figure 6. Only one half of one M4 was equipped with readout electronics and horizontal scans across one half of the M4 at the time were performed. The GE2/1 sector was flushed with an $ARCO_2$ 70-30 gas mixture. The beam line was equipped with a tracker composed of two GEM detectors and two small size μRWell prototypes. The efficiency of the GE2/1 sector was defined as the number of triple coincidences GE21xGEM1xGEM2 divided by the double coincidence GEM1xGEM2. In figure fig. 8.3Bottom a picture of the GE21 sector equipped with two large are M4 detectors is shown in the H4 beam line at CERN.

As operating voltage 530 V was chosen, that is in the middle of the HV plateau. The nominal gain at this operating voltage is about 10000. Two horizontals scans were then performed at this voltage across the whole surface of one M4 detector: the two scans were performed at two vertical positions separated by 20 cm in height, in order to illuminate the whole surface of the detector. Figure 8.5 shows the efficiency obtained in the various points of the two horizontal scans. All points are within 98-99% efficiency, therefore showing the excellent uniformity achieved by the detector over all its surface.

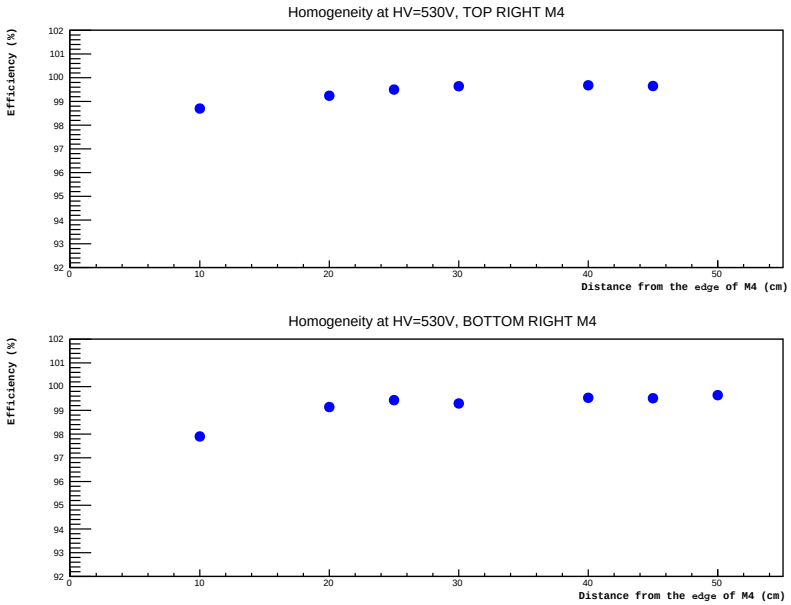

Figure 8.5: GE21 efficiency across the whole surface of one M4 detector. Two horizontal scans were performed in two vertical positions separated by 20 cm in height. All points are within 98-99% efficiency providing an excellent uniformity.

8.3.2 Applications for a Muon detection system for a CepC experiment

The μRWell technology, especially in its *low-rate* version, is a mature solution, with whom single detectors of a 0.5 m^2 have been realised and succesfully operated in the laboratory as well as in test beams. They can withstand particle rates up to a few tens of kHz/cm^2, providing a position resolution as good as $\sim$60 μm wuth a time resolution of 5-6 ns. Moreover the μRWell technology is a robust solution, intrinsically safer against sparks than, for example, the widely used GEM detectors. In comparison with the GEM detectors the construction is much simpler, involving no stretching of the kapton foils and only one amplification stage instead of the three stages of the triple-GEM solution. This makes the cost of a μRWell detector typically less than half the cost of a triple-GEM detector of the same size and the same strip pitch. A few industries have already started collaborating and producing some of the components of the μRWell detectors, and in a very short time, all the needed μRWell detector components will be produceable by industry. This technology could therefore be very effectively used for realizing a muon detection system for CepC. In particular this detector, which would have dimensions of a few thousand m^2 could be realised by using tiles of μRWell detectors of a size 50x50 cms^2. Each tile woud have a relatively small gas volume of $\sim$1 l. This would make the whole muon detector very modular with components bought directly from industry. The needed assembly and quality control of the μRWell detectors could then be efficiently realised by the collaborating institutes. A CepC muon detector made of μRWell tiles could consist of the three successive muon stations, each equipped with a couple of layers of μRWell detectors in order to provide a very precise, of the order of 200μm, position resolution on the coordinates of a muon track. The time resolution would be 5-6 ns. This precise position resolution, together with the three stations, would allow to have an independent muon tracking that could then also be associated back to the tracks measured

by the central tracker. This would make for a very robust and efficient muon detection system. A muon trigger system, albeit probably not essential for a CepC detector, could be easily implemented. A similar muon detection scheme, could be envisaged also for a SppC detector, eventually using the *high-rate* μRWell detectors in the regions where the highest particle rates are foreseen.

8.4 Future R&D

The baseline conceptual design and most promising technologies for the CEPC muon system have been discussed. Future R&D requires detailed studies of different technologies and further optimization of baseline design parameters. Several critical R&D items have been identified, including:

- **Long-lived particles optimization**: Explore new physics scenario of long-lived particles and exotic decays. Optimize detector parameters and technologies.
- **Layout and geometry optimization**: Detailed studies on the structure of the segments and modules need to be carried out to minimise the dead area and to optimise the interface for routing, support and assembly. The geometry and dimensions need to be optimized together with the inner detectors, in particular the ECAL and the HCAL.
- **Gas detectors**: Study aging effects, improve long-term reliability and stability.
- **All detectors**: Improve massive and large area production procedures, readout technologies.

References

[1] CEPC-SPPC Study Group, *CEPC-SPPC Preliminary Conceptual Design Report. 1. Physics and Detector*. IHEP, 2015. http://cepc.ihep.ac.cn/preCDR/volume.html.

[2] CALICE Collaboration, *Construction and performance of a silicon photomultiplier/extruded scintillator tail-catcher and muon-tracker*, JINST **7** (2012) no. 04, P04015, arXiv:1201.1653. http://stacks.iop.org/1748-0221/7/i=04/a=P04015.

[3] Babar Collaboration, *The BaBar detector*, Nucl. Instrum. Meth. **A479** (2002) 1–116, arXiv:hep-ex/0105044.

[4] A. Abashian et al., *The Belle Detector*, Nucl. Instrum. Meth. **A479** (2002) 117–232. KEK-PROGRESS-REPORT-2000-4.

[5] CMS Collaboration, *The CMS muon project: Technical Design Report*. Technical Design Report CMS. CERN, Geneva, 1997. http://cds.cern.ch/record/343814.

[6] ATLAS Collaboration, *ATLAS muon spectrometer: Technical Design Report*. Technical Design Report ATLAS. CERN, Geneva, 1997. http://cds.cern.ch/record/331068.

[7] Y.-G. XIE, J.-W. ZHANG, Q. LIU, J.-F. HAN, S. QIAN, N. YAO, J.-B. ZHAO, J. CHEN, and J.-C. LI, *Performance Study of RPC Prototypes for the BESIII Muon Detector*, Chinese Physics C **31** (2007) no. 01, 70–75. http://cpc-hepnp.ihep.ac.cn:8080/Jwk_cpc/EN/abstract/abstract7618.shtml.

[8] J.-L. Xu, M.-Y. Guan, C.-G. Yang, Y.-F. Wang, J.-W. Zhang, C.-G. Lu, K. McDonald, R. Hackenburg, K. Lau, L. Lebanowski, C. Newsom, S.-K. Lin, J. Link, L.-H. Ma, and P. Viktor, *Design and preliminary test results of Daya Bay RPC modules*, Chinese Physics C **35** (2011) no. 9, 844. http://stacks.iop.org/1674-1137/35/i=9/a=011.

CHAPTER 9

READOUT ELECTRONICS AND DATA ACQUISITION

This [1] is an example with plots, please edit ...

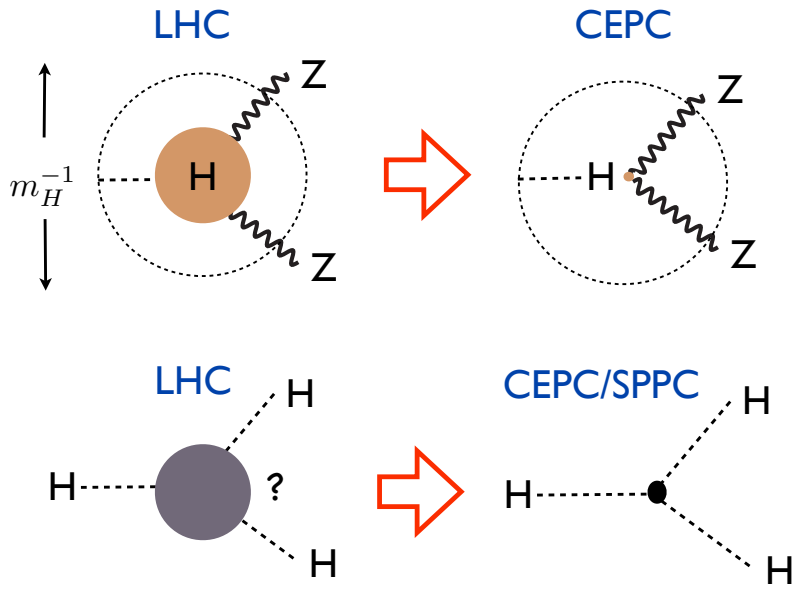

Figure 9.1: A sketch of two of the central goals of the CEPC and SPPC. The CEPC will probe whether the Higgs is truly “elementary", with a resolution up to a hundred times more powerful than the LHC. The SPPC will see, for the first time, a fundamentally new dynamical process — the self-interaction of an elementary particle — uniquely associated with the Higgs.

9.1 New Colliders for a New Frontier

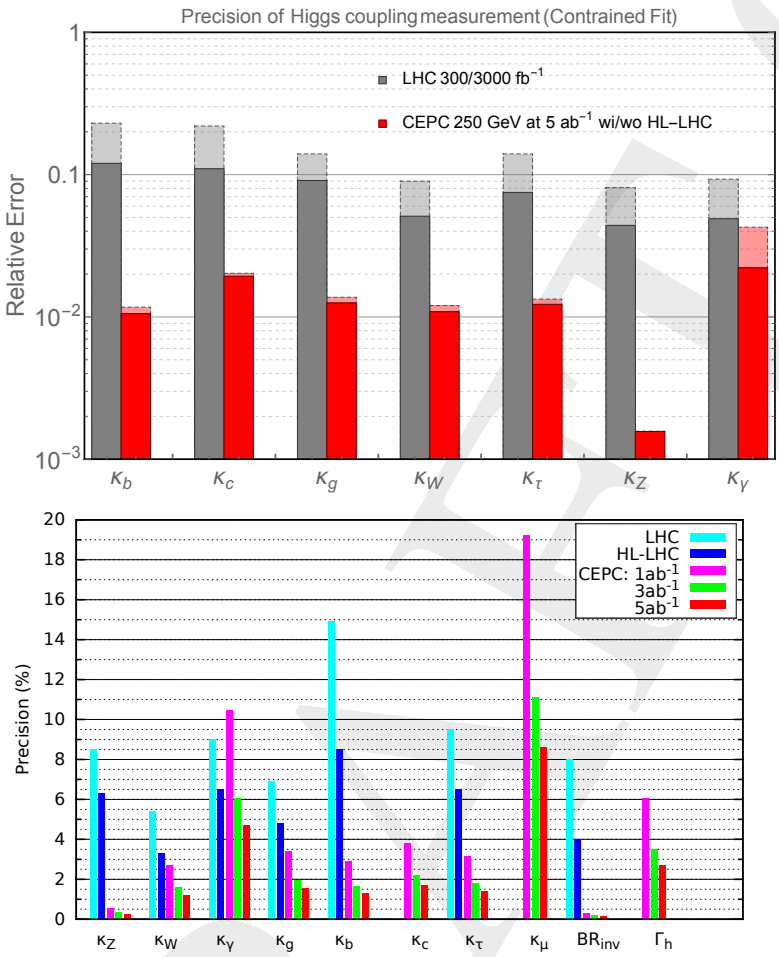

Figure 9.2: Top: The 7 parameter fit, and comparison with the HL-LHC, discussed in detail in Chapter 11. The projections for CEPC at 250 GeV with 5 ab^{-1} integrated luminosity are shown. The CEPC results without combination with HL-LHC input are shown with dashed edges. The LHC projections for an integrated luminosity of 300 fb^{-1} are shown in dashed edges. Bottom: Comparison between the LHC and several benchmark luminosities of the CEPC.

References

[1] CEPC project website. http://cepc.ihep.ac.cn.

CHAPTER 10

CEPC INTERACTION REGION AND DETECTOR INTEGRATION

The machine-detector interface (MDI) represents one of the most challenging topics for the CEPC projects. It shall cover common issues related to both machine and detector designs. Topics described in this chapter include the interaction region layout, detector backgrounds, luminosity instrumentation, and concerns regarding machine and detector integration. Comprehensive understandings are necessary to address properly relevant issues and achieve optimal, along with compromises, overall performance of the machine and detector combined.

10.1 Interaction region layout

The interaction region (IR) receives several updates to cope with the recent double-ring design of the machine. It features an increased focal lengthen ($L^* = 1.5$ m $\rightarrow$ 2.2 m), defined as the distance between the final focusing magnet (QD0) and the interaction point (IP). This allows enlarged separation between to the two single apertures of the QD0. Compensating magnets, positioned in front of the QD0 and surrounding both QD0 and OF1 and constructed with superconducting coils, are introduced to cancel out the impacts of the detector solenoid on the beam. The outer radius of the magnets defines the detector acceptance of $|\cos\theta| \leq 0.993$ in the forward region. The luminosity calorimeter ("LumiCal"), located in front of the compensating magnet, is designed to measure the integrated luminosity to a precision of 10^{-3}. The tracking disks in the forward region are re-located to cope with the limited space and shall be re-optimized with more studies.

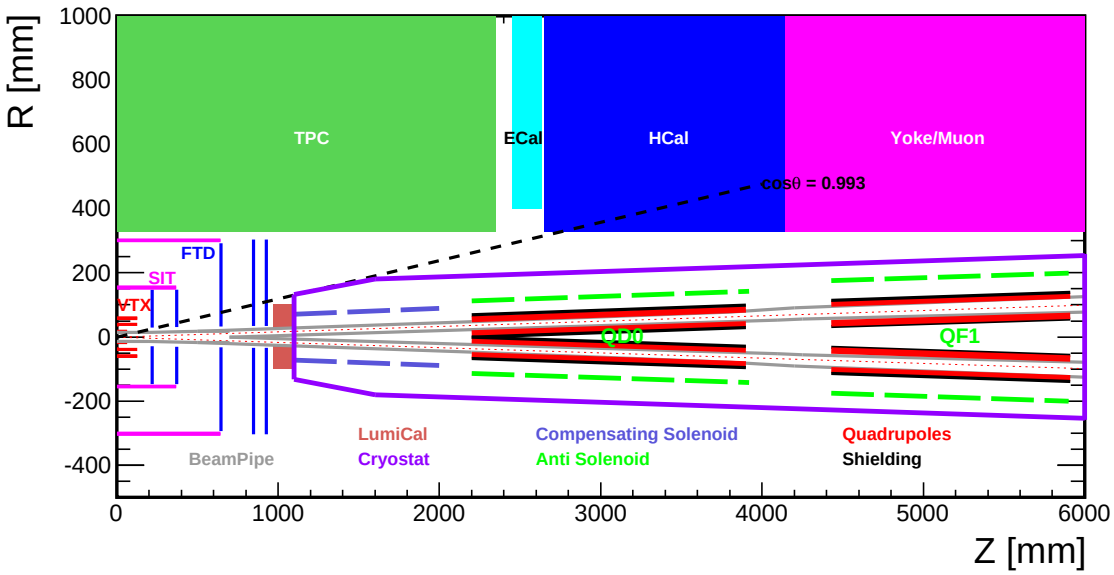

Figure 10.1: Layout of the interaction region.

10.2 Final focusing magnets

The two final focusing quadrupoles, QD0 and QF1, are inside the CEPC detector given the short focal length, and must operate in the background field of the detector solenoid. QD0 is the quadrupole magnet closest to the interaction point, with a distance of 2.2 m and 1.73 m in length. It is designed as double-aperture superconducting magnet realized with two layers of cos-theta quadrupole coil using Rutherford cable without iron yoke. The total four coils are clamped with stainless steel collars. It shall deliver a gradient field of 151 T/m and control the filed harmonics in the sensitive area to be below 3×10^{-4}. The cross-sectional view of the single aperture of the QD0 is depicted in Fig. 10.2.

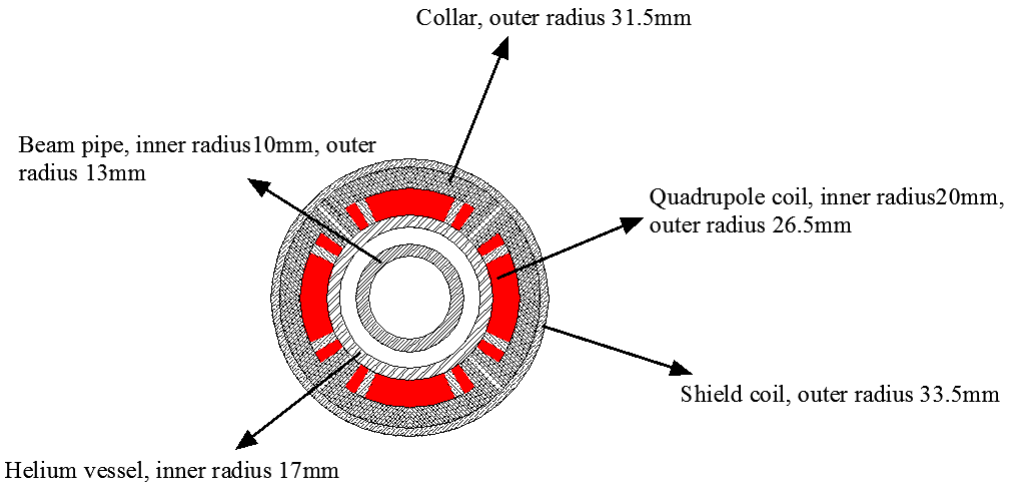

Figure 10.2: Schematic view of the single aperture of the QD0 superconducting magnet.

10.3 Detector backgrounds

Backgrounds will impose significant constraints on the detector design and technologies to be adopted. Different backgrounds can give rise to primary particles that can enter the detector directly, or generate secondary particles that ultimately reach the detector. They can cause radiation damages to detector and electronics components, and degrade their particle detection performance. Moreover, backgrounds of high rate can increase the detector occupancy, and thus exaggerate the data-taking capability of the impaired detector. It is desirable to characterize backgrounds originating from different sources, and mitigate their impacts with effective and sufficient detector protection. Thorough studies with Monte Carlo simulation, together with lessons and experience learned from previous experiments, shall provide necessary guidance for detector and machine design optimization. Main backgrounds from synchrotron radiation, beam-beam interactions, radiative Bhabha scattering, beam-gas interactions are described.

10.3.1 Synchrotron radiation

Synchrotron radiation is always considered one of the most critical backgrounds at circular machines. Optimization of the bending magnets and careful tuning of the beam parameters are necessary to weaken the unwanted synchrotron radiation. In addition, collimators and masks are often introduced to avoid sensitive detector components being bombarded directly by high rate energetic synchrotron radiation photons. To further prevent synchrotron radiation photons impinging the vulnerable vertex detector, additional gold plating of beam-pipe might have to be introduced but this can lead to degraded tracking performance. Synchrotron radiation backgrounds have been evaluated with the BDSim software package, which utilizes the Geant4 toolkit to simulate both the transport of particles in an accelerator and their interaction with the machine the components.

10.3.2 Radiative Bhabha scattering

Backgrounds with beam lost particles, in particular due to radiative Bhabha scattering ($e^+e^- \rightarrow e^+e^-\gamma$), are considered dominant for the Belle-II detector [**?**]. Electrons (positrons) after the radiative Bhabha scattering continue to travel along the ring but can be eventually kicked off their orbits after loosing energy more than $>$1.5% of the nominal beam energy (as defined by the accelerator acceptance). If getting lost close enough to the interaction region, they can interact with machine and/or detector components and cause particle showers. However, this type of detector backgrounds can be effectively suppressed with collimators along the ring, which should not disturb the beams.

Radiative Bhabha events with small angles are simulated with the BBBREM program [**?**]. Particle tracking with the outgoing electrons or positrons along the accelerator ring is performed with SAD [**?**]. Particles entering the interaction region and interacting with detector components (including the beam pipe and the final focusing magnets) are simulated with Geant4 [**?**]. Backgrounds formed by beam lost particles are symmetric in x, and the averaged maximum values toward the $+x$-direction are taken for the background estimation. A safety factor of 10 is always applied in background estimation unless explicitly stated elsewhere.

Fig. 10.3 demonstrates that after introducing collimators of small size aperture, detector backgrounds, as characterized by the hit density and the annual total ionization dose

(TID) at the vertex detector layers, can be reduced dramatically to ∼1.5 hits/cm^2·BX and 2 MRad/yr, respectively. In addition, beam lost particles due to beamstrahlung are also effectively suppressed with the same collimators, which result in almost negligible detector backgrounds.

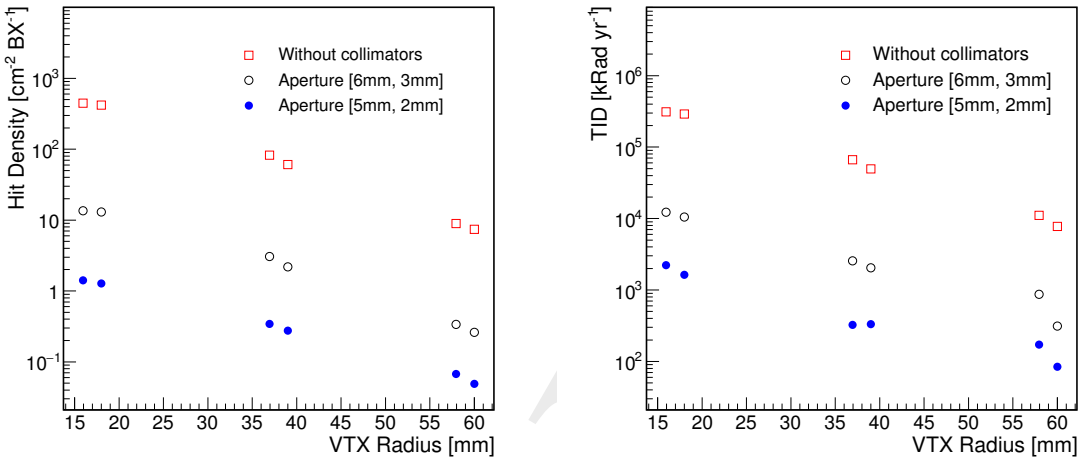

(a) (b)

Figure 10.3: Comparison of the hit density (a) and the annual total ionization dose (b) at the VTX detector layers at located different radii, before and after introducing collimators of different aperture sizes.

10.3.3 Beam-beam interactions

Beamstrahlung is considered the dominant background at the International Linear Collider (ILC). Although beams are less destructive at the CEPC, such background needs to be carefully evaluated. This process has been studied with the Monte Carlo simulation program GUINEA-PIG [**?**], which takes into account dynamically changing bunch effects, reduced particle energies and their impacts on the fields. Machine parameters for operation at $E_{\rm cm} = 240$ GeV, as listed in Table 10.1, serve as input to the simulation. It should be noted that compared to other consequent processes, electron-positron pair production generates most significant detector backgrounds and can be categorized as:

- Coherent Production: e^+e^- pairs are produced via the interaction of virtual or real photons (e.g. beamstrahlung photons) with the coherent field of the oncoming bunch. Particles can be highly energetic but are dominantly produced with small angle and confined in the beam pipe.
- Incoherent Production: e^+e^- pairs are produced through interactions involving two real and/or virtual photons. Most of the particles are confined in the beam pipe by the strong detector solenoid field. However, a small fraction of them are produced with high transverse momentum and large polar angle.

Figure 10.4(a) shows that the hit density imposed by pair production accounts for ∼1 hit/cm^2·BX at the first vertex detector layer ($r = 1.6$ cm), which is of similar size to

Table 10.1: Higgs machine design parameters fed to the GUINEA-PIG simulation.

Machine Parameters	Unit	Value
Beam energy	GeV	120
Particles per bunch		1.29×10^{11}
Beam size σ_x/σ_y	μm	20.9/0.086
Beam size σ_z	μm	3480
Normalized Emittance $\varepsilon_x/\varepsilon_y$	mm·mrad	284.1/0.845

the contribution from radiative Bhabha scattering after collimation. However, Fig. 10.4(b) shows that radiative Bhabha leads to much higher TID, which can be understood that charged particles of higher energies are generated following this process.

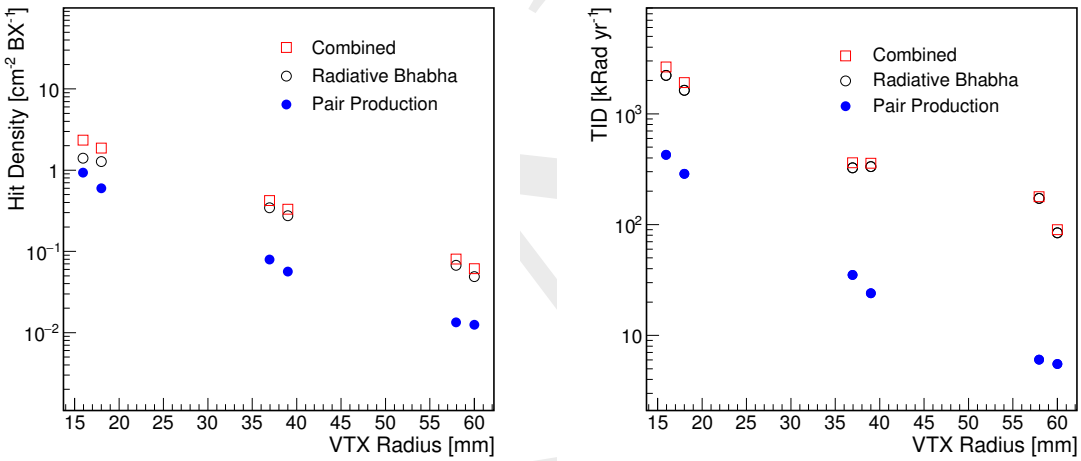

(a) (b)

Figure 10.4: Comparison of of hit density (a) and TID (b) due to pair production and radiative Bhabha scattering.

In addition, Fig 10.5 shows the distributions of non-ionizing energy loss (NIEL) due to pair production and radiative Bhabha scattering. Highest annual NIEL levels are in the range of $10^{11} \sim 10^{12}$ on the first vertex detector layer ($r = 1.6$ cm) and decrease at larger radii.

10.3.4 Beam-gas interactions

Interactions between the beam particles and the residual gas in the beam pipe can induce electromagnetic showers in the interaction region and enter the detector. Gas pressure is assumed to be 10^{-7} mbar, and results can be linearly rescaled for other pressures. Preliminary result suggests that detector backgrounds induced by beam-gas interaction is small compared to other types of backgrounds but more detailed evaluation needs to be performed.

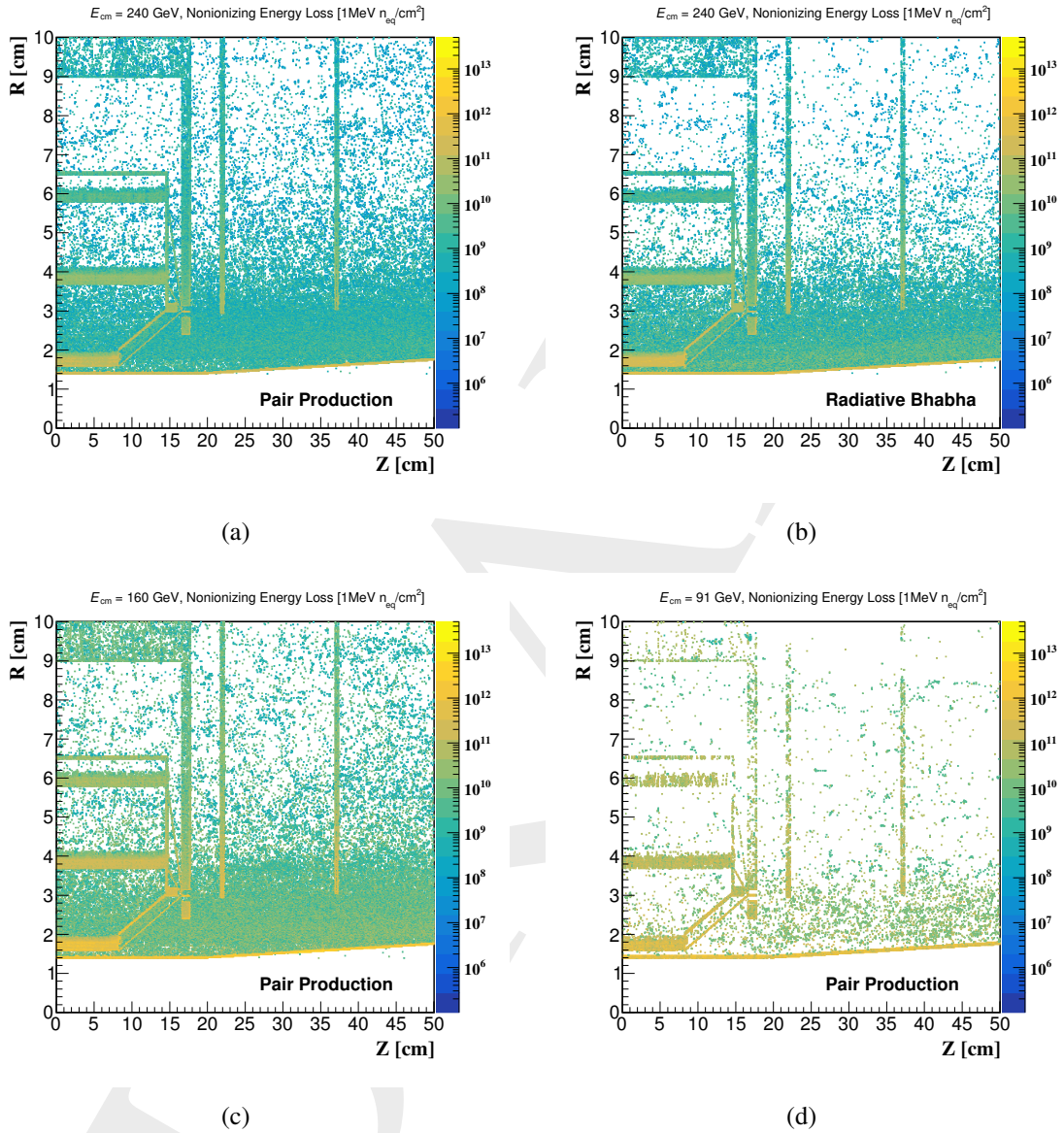

Figure 10.5: Distributions of non-ionizing energy loss (NIEL) due to pair production (a) and radiative Bhabha scattering (b) for machine operations at Higgs, as well as pair production results for machine operations at W (c) and Z (d).

10.3.5 Summary on detector backgrounds

The main detector backgrounds originate from the pair production and the beam lost particles due to radiative Bhabha scattering. For the machine operation at Higgs ($E_{\rm cm} = 120$ GeV), the maximum hit density at the first vertex detector layer is estimated to be ~ 2.5 hits/cm^2·BX. The annual TID and NIEL at the inner most detector layer are around 2.5 MRad and 10^{12} 1MeV $\rm n_{eq}/cm^2$, respectively.

10.4 Luminosity instrumentation

Very forward region at CEPC will be instrumented with a luminometer (LumiCal) aiming to measure integral luminosity with a precision of 10^{-3} and 10^{-4} in e^+e^-collisions at 240 GeV center-of-mass energy and at the Z_0 pole, respectively. The precision requirements on the integral luminosity measurement are motivated by the CEPC physics program, intended to test the validity scale of the Standard Model through precision measurements in the Higgs and the EW sectors. Many sensitive observables for such measurements critically depend on the uncertainty of the integral luminosity.

Several technological options for LumiCal design are under study, as described in Sec. 10.4.1, with emphases on the precision of polar angle and energy reconstruction of Bhabha particles scattered in the t-channel $V(V = \gamma, Z)$ exchange. Luminometer at CEPC is a precision device with challenging requirements on the mechanics and position control. Precision requirements on integral luminosity measurement set the precision of the opening aperture and positioning control of the LumiCal. Various sources of luminosity uncertainty in this respect are reviewed in Sec. 10.5.Encouraging estimations on feasibility of the luminosity precision goals are presented. Detailed studies are ongoing, to include the full simulation of physics and machine induced processes and of the detector itself, for various luminometer positioning and technology choices.

10.4.1 Technological and design options

In the current design of the very forward region at CEPC, luminometer is foreseen to cover the polar angle region between 26 mrad and 105 mrad what translates into the detector aperture of 25 mm for the inner radius and 100 mm for the outer, at 950 mm distance of the LumiCal front plane from the IP. Due to the $1/\theta^3$ dependence of the differential Bhabha cross-section, the uncertainty of the inner radius significantly affects the counting of the Bhabha events in the luminometer, as discussed in Sec. 10.5. Thus the alignment of LumiCal elements together with the precision of the inner radius have to be at the level of a few microns. Positioning of a finely segmented silicon or diamond layer in front of the first LumiCal plane (Fig. 1) will enable precision calibration, and in addition will enable e/γ separation in the detector. Simulation studies indicate that such a configuration enables polar angle measurement of the Bhabha electron with a precision equivalent to $1\ \mu$m uncertainty in radial position.

One of the possible technology options for luminometer is finely segmented radiation hard bismuth germanium oxide (BGO) crystal, to be read-out with simpler electronics than the traditional sandwich type calorimeters (Fig. 10.6).

Another option under study is a compact, sandwich type of SiW calorimeter consisting of 20 one-radiation length thick sensor-absorber planes. Studies performed on future linear collider projects [**?**] have shown that configuration of finely segmented silicon

sensors interspersed with tungsten absorber has Moliere radius small enough to provide sufficient energy and position resolution of Bhabha EM showers needed to reach a 10^{-4} uncertainty of the integral luminosity measurement. Such a configuration, assuming a 2 mm gap for the sensor placement between the absorbers, is simulated in Geant4 in order to estimate the leakage of the electron shower out of the edge of LumiCal outer radius contaminating the tracking volume.

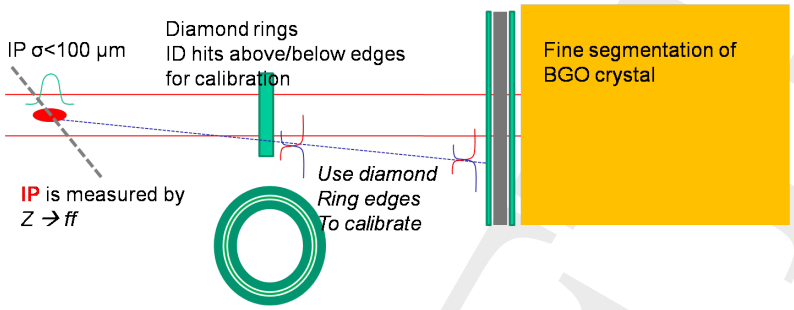

Figure 10.6: Scheme of a BGO luminometer with a diamond ring tracker.

Two detector designs are considered:

1. Cylindrical detector shape assembled of sensor-absorber disks with constant outer radii of 100 mm (TUBE configuration),
2. Conical shape with the outer radius r following a straight line projection from the IP at $\theta = \arctan 0.1$, corresponding to $r_{out} = 100\,\text{mm}$ at $z = 1\,\text{m}$.

An iron cone of 5 mm thickness, positioned at $\cos\theta = 0.992$, is used to estimate filtering of shower secondaries mostly of low momentum particles below 100 MeV. It has been shown for 50 GeV and 125 GeV electron showers that:

1. There is a larger shower leakage for all electron energies for the TUBE configuration,
2. That 5 mm Fe-cone reduces the number of secondaries reaching the tracking region by as much as 75% (depending on the energy of the EM shower and the angle of the secondary particle).

The results are given in Table 10.2.

10.5 Systematic effects

The main measure of luminosity at CepC is the count of Bhabha events N_{Bh} detected in coincidence in the two halves of the luminosity calorimeter LumiCal. The luminosity figure is then obtained from the equation,

$$\mathcal{L} = \frac{N_{\text{Bh}}}{\sigma_{\text{Bh}}} \tag{10.1}$$

The cross section for the Bhabha process, σ_{Bh}, should be integrated over the same phase space as used for the counting of Bhabha events. The limited precision with which the experimental acceptance region is defined gives rise to a number of systematic effects. Further, other processes misidentified as Bhabha and the limited accuracy of the theoretical calculation of σ_{Bh} contribute to the overall systematic uncertainty.

	50 GeV electrons		125 GeV electrons	
	TUBE	CONE	TUBE	CONE
θ (mrad)	$N_{\text{enter}}/N_{\text{pass}}$	$N_{\text{enter}}/N_{\text{pass}}$	$N_{\text{enter}}/N_{\text{pass}}$	$N_{\text{enter}}/N_{\text{pass}}$
40	15.4/5.6	13.6/5.8	38.0/16.0	35.8/14.7
90	392/155	173/76	1028/399	434/19.7
95	501/290	367/152	2389/720	937/382
98	762/216	860/284	1718/473	2176/725
99	553/140	1331/367	1102/273	3306/915

Table 10.2: Number of particles leaking out of the LumiCal outer radius (N_{enter}) and number of particles passing through the Fe-cone (N_{pass}). Two different detector designs (TUBE and CONE) and two shower energies (50 GeV and 125 GeV) are simulated.

A generator-level study was performed to assess the effects related to the precision of the Bhabha acceptance region on Bhabha counting. An underlying assumption of the study is that the LumiCal is centered on the outgoing beam axis. This assumption is essential for data-driven control of the radial offset of Lumical w.r.t. the IP, as well as for Bhabha event counting based on the mirrored asymmetric polar-angle acceptance regions on the left and right side of the detector [**?**] (in further text, *OPAL-style selection*). OPAL-style counting cancels out biases due to left-right assymmetries of the experimental angular acceptance. It is further assumed that for the final state particles hitting the radial region between 50 mm and 75 mm, corresponding to the detector fiducial volume (FV), shower leakage has a negligible effect on the reconstruction of the polar angle and the energy.

Bhabha event samples are generated using the BHLUMI generator [**?**]. Center-of-mass (CM) energy of 240 GeVis assumed, roughly corresponding to the peak of the Higgs production cross section. The particles are generated in the range of polar angles including a ~ 7 mrad margin outside the FV to allow non-collinear final state radiation (FSR) to contribute to the events. After event generation, smearing is applied to the final particle vertices and momenta according to the nominal CepC parameters [**?**]. Additional smearing or bias is then applied according to one systematic effect at a time. Four momenta of close-by particles are summed up to account for cluster merging in LumiCal. The selection criteria to count an event consist of the OPAL-style angular selection and the requirement that the energy of both detected showers is above 50% of the nominal beam energy. The relative acceptance bias is determined as the relative difference between the Bhabha count $N_{\text{Bh},i}$ obtained with the inclusion of the considered effect i and N_{Bh} obtained with the nominal set of parameters.

Table 10.3 lists the requirements on beam delivery, MDI and LumiCal installation, needed to limit individual systematic effects in the luminosity measurement to 1×10^{-3}, such as required for the Higgs program at CepC. Parameters influencing the integral luminosity precision are given as follows:

- ΔE_{CM}, uncertainty of the available CM energy affecting the Bhabha cross-section,
- $E_{e^+} - E_{e^-}$, asymmetry of the incident beam energies resulting in a net longitudinal boost of the event,

Table 10.3: Requirements on beam delivery, MDI and LumiCal installation, needed to limit **individual** systematic effects to 1×10^{-3}.

Parameter	unit	limit
ΔE_{CM}	MeV	120
$E_{e^+} - E_{e^-}$	MeV	240
$\frac{\delta\sigma_{E_{beam}}}{\sigma_{E_{beam}}}$		Effect cancelled
Δx_{IP}	mm	2
Δz_{IP}	mm	10
Beam synchronisation	ps	15
$\sigma_{x_{\mathrm{IP}}}$	mm	1
$\sigma_{z_{\mathrm{IP}}}$	mm	>10
r_{in}	μm	10
$\sigma_{r_{\mathrm{shower}}}$	mm	>1
Δd_{IP}	μm	500

- $\frac{\delta\sigma_{E_{beam}}}{\sigma_{E_{beam}}}$, uncertainty of the beam energy spread,
- Δx_{IP} and Δz_{IP}, radial and axial offsets of the IP w.r.t. the LumiCal,
- Beam synchronization, resulting in axial offset of the IP w.r.t. the LumiCal,
- $\sigma_{x_{\mathrm{IP}}}$ and $\sigma_{z_{\mathrm{IP}}}$, radial and axial fluctuations of the scattering position,
- r_{in}, inner radius of the LumiCal acceptance region,
- $\sigma_{r_{\mathrm{shower}}}$, reconstruction precision of the radial shower coordinate,
- Δd_{IP}, uncertainty of the distance between the luminometer halves.

Most requirements are technically feasible with the present state of the art of accelerator and detector technology. The most important challenge identified is the precision of the inner acceptance radius r_{in} of LumiCal. In order to keep the luminosity precision of 1 permille, r_{in} must be known to within $10\,\mu\mathrm{m}$. The precision requirement of r_{in} scales linearly with the required luminosity precision, implying a correspondingly stricter requirement for the Z-pole run.

10.5.1 Summary on LumiCal

Instrumentation of the very forward region is very important for the realization of the CepC physics program. Several technology options are under consideration. Some of them have been successfully applied at LEP or are under study at other future projects. We argue that a tracker placed in front of the luminometer can improve polar angle measurement accuracy, facilitate LumiCal alignment and enable electron-photon separation. Luminometer must be centered on the outgoing beam axis to allow control of the systematic effects at the required level. Precision requirements on beam delivery, MDI and LumiCal installation have been addressed by simulation, and proven to be feasible with the present state-of-the-art of accelerator and detector technology.

10.6 Detector integration

Both QD0 and QF1 are located inside the detector, which drastically complicates the support and alignment of the detector and machine components in the interaction region. The two final focus magnets and the LumiCal will possibly be mounted on a dedicated support structure, extended from a pillar outside the detector and suspended from the solenoid cryostat. They might have to been integrated together before being pushed into the interaction region. The shaped beam pipe and surrounded silicon detectors will possibly be supported from a structure of carbon fiber reinforced plastic, which can hang at the flanges of the field cage of the Time Projection Chamber (TPC). Significant effort is required to realize a solid mechanical design and to define a reasonable procedure for detector assembly.

References

CHAPTER 11

PHYSICS PERFORMANCE

11.1 Introduction

11.1.1 The physics requirement and detector design at the CEPC

Most of the SM Higgs events could be recorded at the CEPC. Therefore, the CEPC detector should be able to distinguish not only the Higgs signal from the SM background, but also the Higgs signal in between its different generation mode and decay final states. In other word, the CEPC detector should be able to reconstruct the key physics objects, i.e, photons, leptons, taus, jets and missing energy/momentum, at high efficiency, high purity and high precision. Explicitly, the physics requirements to the CEPC detector could be schematized as:

1, Be adapted to the CEPC collision environment;

2, Have large solid angle coverage;

3, Provide excellent lepton identification;

4, The Track should have excellent track reconstruction efficiency and a resolution better than $\delta(\frac{1}{P_t}) = 2 \times 10^{-5}(\text{GeV}^{-1})$; the latter is required by $Br(H \to \mu^+\mu^-)$ measurement at the CEPC;

5, Precise reconstruction of photons, requested by both jet energy reconstruction and the $Br(H \to \gamma\gamma)$ measurement;

6, Capability to separate charged kaons from pions, which enables an excellent flavor physics program at CEPC;

7, Good Jet/MET reconstruction;

8, Capability of separate b-jets, c-jets and light jets: requested by $g(Hbb)$, $g(Hcc)$, and $g(Hgg)$ measurements.

The detector requirement for the EW measurements should be in principle similar to these at the Higgs runs. Meanwhile, the majority of EW measurements at the CEPC would be limited by the systematic, thus, the detector for the EW measurements should also has excellent alignment, calibration and stability, to control the systematic at the CEPC EW measurements. In addition, the CEPC should provide 10^{-3} luminosity monitoring at Higgs operation and 10^{-4} luminosity measurement at Z pole operation. Ideally, the beam energy is required to be calibrated to 1 MeV level for the EW measurement.

Nowadays, with the progress of micro-electronics, the particle flow oriented detector design has became a clear trend for the collider detector design[CMS, ATLAS, CALICE]. A Particle Flow oriented detector aims at reconstruct all the final state particles, with the most suited sub-detector system. The physics objects are then reconstructed from the final state particles. The Particle Flow Algorithm, at an adequate detector design, could significant enhance the reconstruction performance all the physics objects, and largely improve the accuracy of jet energy resolution, since the majority of jet energy is stored in the charged hadrons, whose momentum is usually measured with a much better accuracy than its cluster energy to be measured at the calorimeter system.

Detector-wise, the Particle Flow oriented detector design appreciates precise tracking system with limited material budget and a limited dead space among different sub-detectors. Low-material tracker is required to limit the probability of interactions before the particle reach the calorimeter, i.e, via multi-scattering, bremsstrahlung and hadron-nuclear interactions. A high granularity calorimeter system is the key component of a PFA oriented detector design, since the calorimeter would be response to separate all the final state particle showers in the calorimeter, and provide essential information for the lepton identification accordingly.

A PFA oriented detector concept has been established as the benchmark detector design for the CEPC physics studies. The detector geometry is initialized on the ALEPH, SiD and ILD detector geometry, and the geometry parameters are determined via a series of the detector optimization studies. On the other hand, a dedicated PFA reconstruction algorithm, Arbor, aiming at a precise interpretation of the general detector signals, has been developed. The combination of CEPC benchmark detector and the Arbor algorithm provides precise reconstruction of all the physics objects, with which the CEPC physics potential has been demonstrated on a series of the full simulation analyses. We would like to summarize the reconstruction performance of this combination, at both individual physics object level as well as at Higgs physics benchmark level, in this very manuscript.

This manuscript is organized as following. The detector geometry and simulation details are introduced in section 2. Section 3 is devoting to the architecture and core algorithms of the Arbor algorithm. From Section 4 to section 7, we will demonstrate the particle flow reconstruction performance at CEPC: the reconstruction of leptons, photons, taus, jets, missing energy and missing momentums will be discussed intensively, respectively. In section 8, we will summarize this manuscript.

11.2 Simulation Geometry & Samples

To evaluate the physics potential and to design the optimized detector geometry for the CEPC project, Particle flow oriented detectors have been intensively studied at full simulation level. Different geometries have been implemented into Geant 4 simulation, reconstruction algorithms are developed, and the physics performance are evaluated at physics object level and at benchmark physics channels. Through this procedure, two milestone detector geometries are developed: they CEPC v_1, the reference detector for CEPC PreCDR studies, and the CEPC v_4, the reference detector for CDR studies.

Following the ILD concept, one of the benchmark detector geometries used in linear collider studies, both CEPC v_1 and CEPC v_2 use low material tracking system, ultra-high granularity calorimeter system, and a large solenoid that can host the entire ECAL and HCAL inside. Their MDI & Forward region, and the Yoke system has been adjusted according to the CEPC collider. CEPC v_1 has the same main geometry parameters as the ILD, i.e, the B-Field strength, the tracker/calorimeter dimensions. While these parameters of CEPC v_4 are further optimized accordingly to the CEPC physics requirement.

Comparing to CEPC v_1, CEPC v_4 has weaker solenoid B-Field (reduced to 3 Tesla from 3.5 Tesla), thinner HCAL, and reduced calorimeter longitudinal layers. To ensure the particle identification performance at CEPC Z pole operation, the ECAL system is required to provide a Time of Flight measurement with 50 ps accuracy at cluster level. The basic geometry parameters for CEPC v_1 and CEPC v_4 are listed in Table 11.1.

Both concepts uses TPC as main tracker and a silicon tracking system. The typical physics event rate at CEPC is roughly 10/1000 Hz at Higgs/Z pole operation. At these collision environment, Dedicated feasibility study shows that TPC is operational at those collision environments [1].

The TPC is divided into 220 radical layers with layer thickness of 6 mm, each layer is then divided into 1 mm cells along the phi-direction. The TPC will have 10 million readout channels in each side of the endcap, each channel with an intrinsic spatial resolution of 100 μm in $R-\phi$ direction and 500 μm resolution in the Z direction. Such configuration provides providing large number of spatial point for track finding.

The silicon tracking system consists of a pixel vertex system, and the forward/external tracking system based on silicon strip technology.

More details will be given on the geometry details.

Using the CEPC v_1 geometry, a full sets of the SM Higgs samples has been generated together with the major SM backgrounds, i.e, ZZ, WW events, single Z, singe W events and ISR return events. To evaluated the performance at new physics hunting, dedicated new physics signals are generated with the CEPC v_1 and used for the PreCDR studies.

For the CEPC v_4 geometry, dedicated samples to evaluate the performance at physics objects level and a full set of the SM Higgs signal sample is produced. The idea is to compare the Higgs signal plots at CEPC v_4 and CEPC v_1, which is still a on going study.

11.3 Arbor Algorithm & Strategy to the object reconstruction

The spatial configuration of particle showers naturally follows a tree configuration. This simple fact inspires the development of advanced pattern recognition and reconstruction algorithm. Aiming at reconstructing the tree topology of particle shower, Arbor algo-

Table 11.1: Geometry parameters of PFA oriented detector concepts for CEPC

Geometry Parameters	**Unit**	**CEPC v_1**	**CEPC v_4**
B-Field	Tesla	3.5	3
TPC inner radius	mm	330	330
TPC outer radius	mm	1808	1808
TPC half length	mm	2350	2350
Si-W ECAL Layers	-	30	20
ECAL Absorber total thickness	mm	84	84
ECAL Silicon Sensor thickness	mm	0.5	1
RPC-Iron HCAL Layers	-	48	40
HCAL Absorber total thickness	mm	1200	1000

rithm [ref XX] creates local oriented connectors between the calorimeter hits, and iterate until the global configuration of the connectors and hits follows a tree topology. The tree branches represents the trajectory of charged shower particles, while the seeds are corresponding to the incident position of the particle. In the ideal case, there is a 1-1 correspondence between the seeds and the particles stem on the Calorimeter. The separation of seeds is usually much easier and much efficient than the separation of particle showers, which is highly appreciated by the core physics requirement of the particle flow principle: to reconstruct each individual final state particle.

The essence of the Arbor algorithm is to correctly interpret all the tracks and all the calorimeter hits. The calorimeter hits induced by charged particles should be identified and combined with charged tracks. After vetoing these charged calorimeter hits, the remaining hits will be reconstructed as photons and neutral hadrons with dedicated identification and energy measurements. In terms of the software architecture, the Arbor algorithm is composed of four parts,

A, Preparation: Accumulation, cleaning and sorting of the input objects

B, Calorimeter Hit Clustering algorithm

C, Matching algorithm between charged tracks and Calorimeter Clusters

D, Globally interpret the track & cluster information, reconstruct the neutral and charged particles

Pattern recognition algorithms are heavily used in the Arbor algorithm. Since different particles and different configurations need to be treated in very different ways. The Arbor algorithm is also composed of dedicated lepton identification algorithm and photon identification algorithms. A more detailed description of the Arbor algorithm could be found in [2].

In the recent design of High Granularity Calorimeters, the readout density reaches a level of 1 channel/cm^3. At such high granularity, Arbor could efficiently separate the final state particles as well as reconstruct the shower substructures, especially for the hadronic

showers. Fig. 11.1 shows a reconstructed calorimeter shower of a 20 GeV K_L particle, where the tree branches are demonstrated as clusters with different colors, which agrees with the trajectory of charged particles with sufficient length.

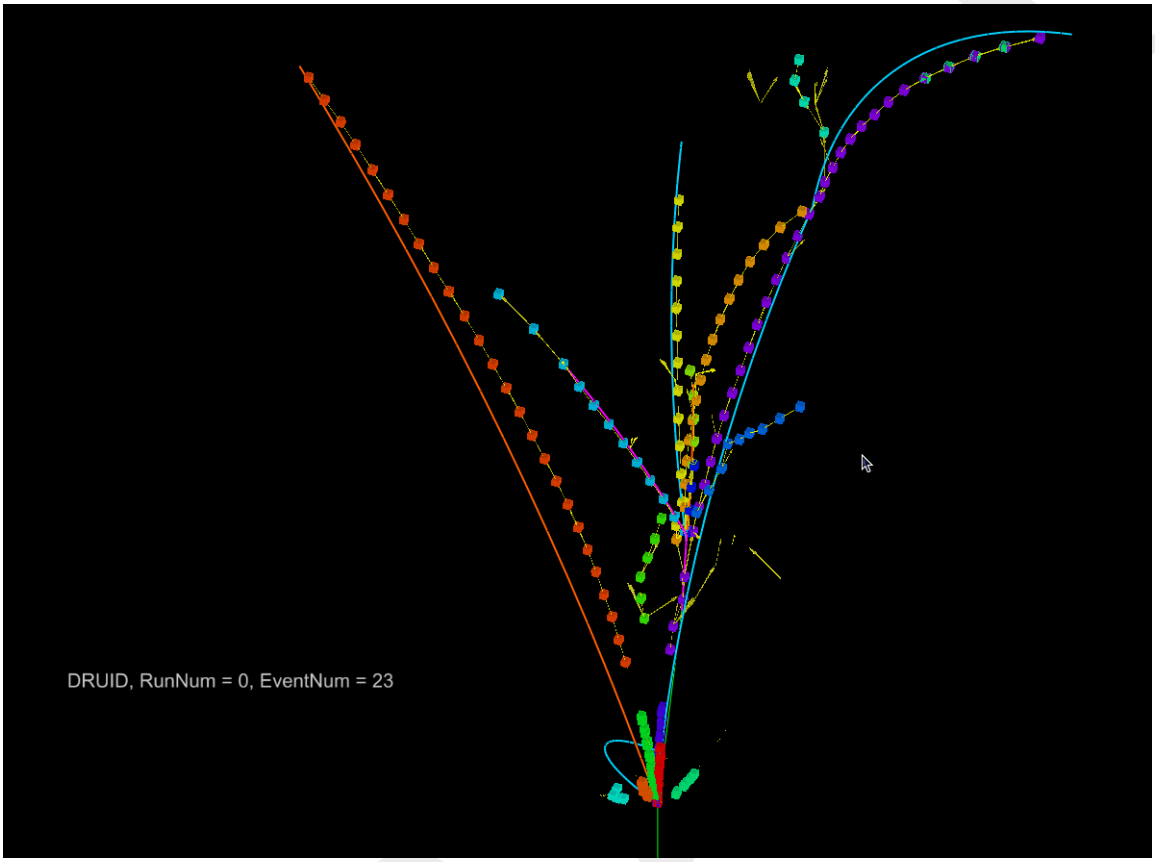

Figure 11.1: K_L shower reconstructed by the Arbor algorithm, the branches – the calorimeter hit clusters – are corresponding to the trajectories of charged particles generated in the shower cascade. The interaction points could be clearly identified.

In terms of the final state particle reconstruction, the Arbor performance can be characterized by the energy collection efficiency of single particles especially the neutral particles, and the separation performance at bi-particle samples. A particle shower is usually composed of a compact core induced by the fast and energetic component of the shower cascade, and a loose halo induced by the slow neutral particles and especially neutrons. Higher hit collection efficiency usually leads to a better energy resolution, however, it usually also increases the chance of confusions, i.e, the wrong clustering of calorimeter hits. Therefore, an optimized particle flow algorithm should balance these two effects.

The separation performance, i.e, the probability of successfully reconstruct nearby incident particle, is essential for jet energy resolution and especially for the pi0 reconstructions, which is crucial for the tau physics studies. To characterize the separation performance, dedicated di-photon sample has been generated. Fig. 11.2 shows the reconstruction efficiency of these 2 photon events (characterized as successfully reconstruct two photon with anticipated energy and positions). Defining the critical distance at which 50% of the event are successfully reconstructed, we observed that the critical distance is roughly 2 times the cell size for cell size smaller than the Moliere radius.

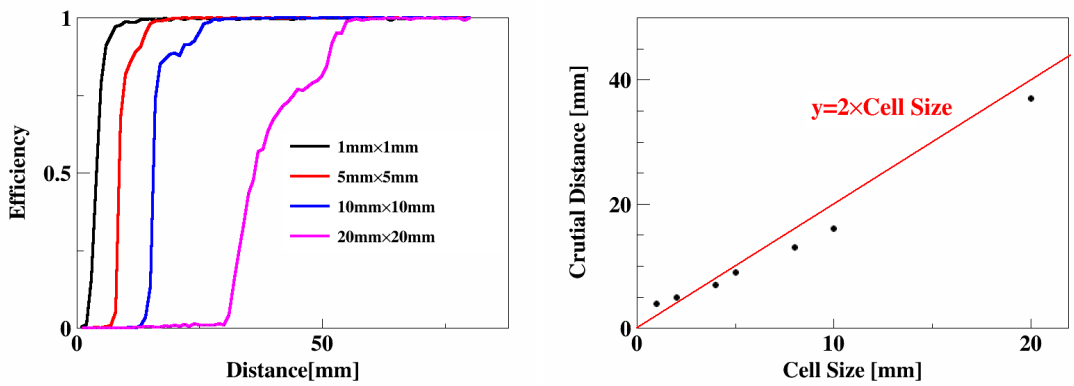

Figure 11.2: The separation performance at 2-photon events at different cell sizes.

To conclude, Arbor is a geometrical algorithm that reconstructs each shower clusters into a tree topology. At high granularity calorimeter, Arbor allows not only an efficient separation between different particles, but also leads to a reconstruction of the shower inner structure. Meanwhile, Arbor maintains a high efficiency in collecting the shower hits/energy, which is important for the shower energy estimation.

The overall performance on different physics object and physics benchmarks will be discussed in details in the following sections.

11.4 Leptons

The lepton identification is of key importance to the CEPC Higgs program. First of all, about 7% Higgs boson events at the CEPC are generated together with a pair of leptons. Those events are the golden signals for the Higgs recoil analysis, which is the anchor for the absolute Higgs measurements. A significant fraction of the Higgs boson decays, directly or via cascade, into final states with leptons. 0.02% of SM Higgs decays into muons; the leptons serve as the essentially candles of identification of $H \to WW/ZZ \to$ leptonic/semi-leptonic final states. In addition, a significant fraction of Higgs->bb/cc events generate leptons in their decay cascade.

The PFA oriented detector, especially its calorimeter system, could provide enormous information for the lepton identification. In the CEPC v_4 geometry, a high-energy electron/positron/hadrons is likely to induce thousands of hits in the calorimeter with typical spatial configurations. Using the benchmark calorimeter geometry, the shower fractal dimension could be extracted [3]. In addition, the dE/dx measured by the TPC could efficiently separate electron/positrons from muon and hadrons, at track energy less than 10 GeV.

A dedicated Lepton identification algorithm for the detectors using high granularity calorimeter, LICH [4], has been developed. LICH extract more than 20 distinguish variables from the detector and combine these information into lepton-likelihood via MVA method. The performance of LICH have been scanned over a large range of the granularity for both ECAL and HCAL, while the performance is stable for particles with energy larger than 2 GeV.

At CEPC v_4 geometry, applied on isolated charged particle candidate with energy larger than 2 GeV, lepton identification efficiency better than 99.5% could be achieved

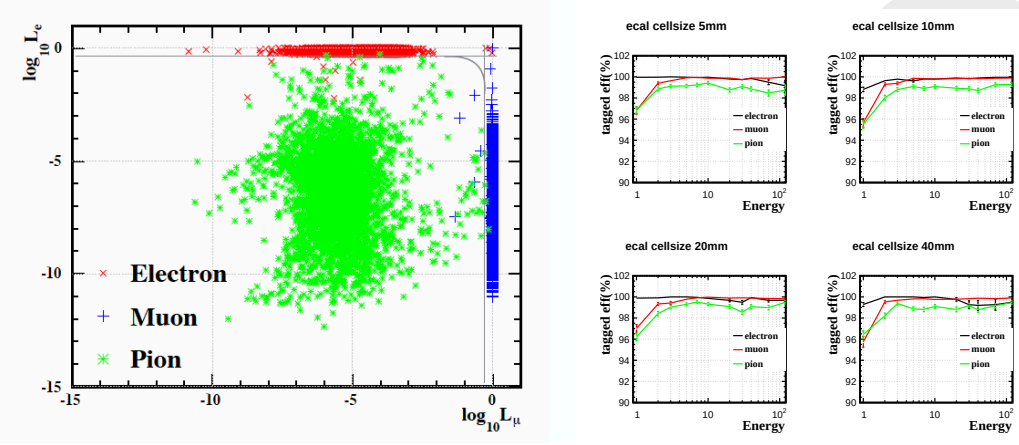

Figure 11.3: Left, calculated lepton likelihood for Electron, Muon and Pions; Right, efficiency of muon, electron and pion identifications.

with a mis-identification rate from hadrons is controlled to be smaller than 1%. This mis-identification is mainly induced by the irreducible background rate from pion decay (to muons) and highly electro-magnetic like pion clusters (via the pion0 generated from the pion-nuclear interactions). Not surprisingly, this performance is significantly better than that at LHC and LEP [Ref XX]. In the actual physics event, the lepton identification performance will be limited by the separation power of the particle detector. As a control sample, we studied the llH event reconstruction and studied the efficiency of successfully identify two leptons with opposite charge. The analysis shows that the total event reconstruction efficiency reaches 97-98%, which, taken into account the detector acceptance, is slightly degrades from the isolated particle performance, but highly consistent with Arbor separation power. In other word, less than 1% of the objective leptons in the llH events will potentially be mis-identified due to the overlapping of their cluster to the nearby showers.

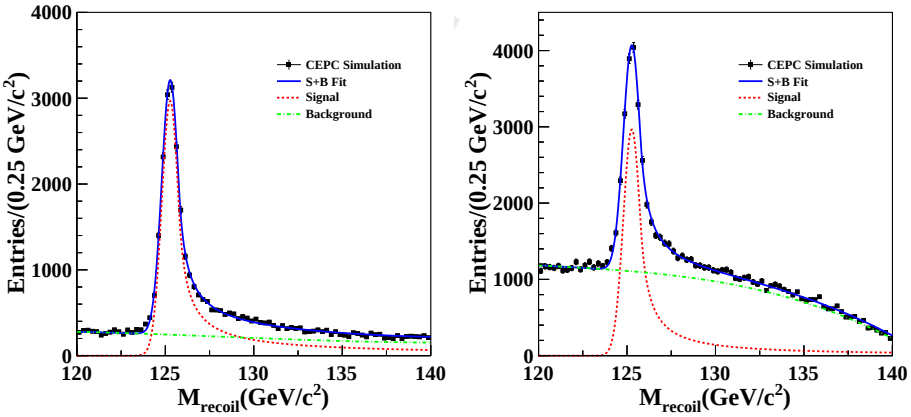

Figure 11.4: Reconstructed recoil mass distribution for the l^+l^-H events, the left is for $e^+e^- \to \mu^+\mu^-H$ and the right for $e^+e^- \to e^+e^-H$

11.5 Kaon Identification

Successful identification of the charged kaons from other hadrons, especially from charged pions, allows the tagging to the s-quark and is highly appreciated in the flavor physics. According to the Bethe-Bloch equation, in the realistic energy range (for example with energy larger than 2 GeV) and at the same track momenta, the dEdx of pions is larger than that of kaons by roughly 10%. In other word, if the dEdx resolution could be measured to a relative accuracy better than 5%, the dEdx could leads to an efficient π-K separation.

The CEPC v_4 detector geometry is equipped with a large TPC main tracker. Depending on the readout hardware performance, the dE/dx resolution leads to 2-4 σ π-K separation for 2-20 GeV charged tracks. See the left plot of Fig. 11.5. The upper boundary is the ideal separation predicted by the Geant4 simulation; while the lower boundary includes a 50which mimics a conservative estimation of readout and DAQ performance at the real experiments. (A survey of the performance at previous experiments shows the degrading varies from 15The dE/dx separation between other charged particles is also demonstrated.

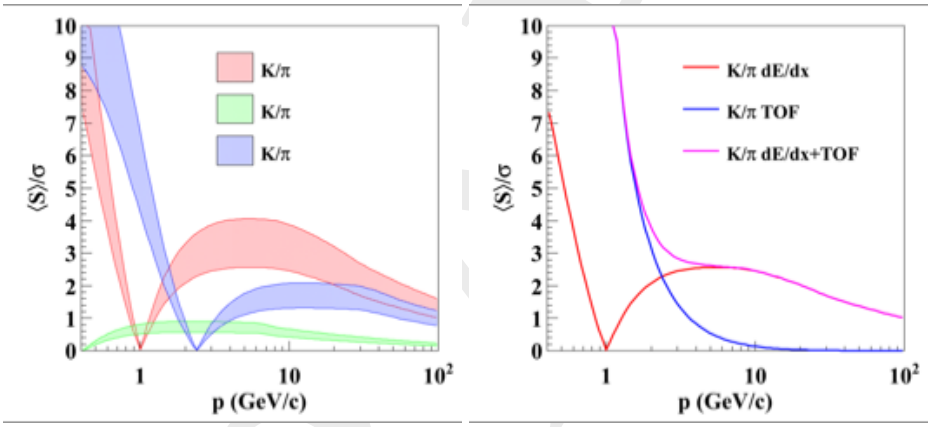

Figure 11.5: π-K separation performance at PICADOR detector. Left plot, dE/dx separation between different charged particles at $0.4 \sim 100$ GeV track momentum. Right plot, the separation power using both dE/dx and ToF information.

The difference between the dE/dx of pions and kaons vanishes at 1 GeV track momentum. On the other hand, a significant portion of charged particle is at energy lower than 2 GeV. To ensure the pi-kaon separation performance for these low energy tracks, a Time of Flight (ToF) measurement is proposed on top of the dE/dx measurement. The ToF information could be measured by the ECAL, with a few layers equipped with the Time sensitive ASICs. According to the recent progress of high granularity calorimeters, an ECAL with 50 ps time resolution is within the current technology reach. Using both ToF and dE/dx information, a separation better than 2 σ could be achieved for tracks with momenta smaller than 20 GeV.

Considering the CEPC inclusive $Z \rightarrow q\bar{q}$ sample and integrate over the full polar angle and the momenta range of $2 \sim 20$ GeV, an over all kaon identification reaches an efficiency and purity of 91%/94% at CEPC v_4 detector geometry. This performance could be significantly improved by using more homogenous and more accurate amplification/DAQ system, and to optimize the TPC geometry by using thinner radical layer and/or larger TPC out radius. It has been demonstrated that, a proper combination of the TPC ge-

ometry and a sophisticated readout system could enhance the charged kaon identification performance to an efficiency/purity of 99%/99%.

11.6 Photons

A successful reconstruction of photon is crucial for the jet energy measurement, the $Br(H \rightarrow \gamma\gamma)$ measurement and the τ physics. The reconstruction of photons could be characterized by its reconstruction efficiency, its energy resolution and the identification from other neutral objects such as neutrons.

The reconstruction efficiency of photons certainly depends on the photon energy. The PICADRO detector is sensitive to photon with energy larger than 10 MeV, and the reconstruction efficiency saturate close to 100% for photon energy larger than 1 GeV. Proportional to the material budget before the calorimeter, roughly 10% of the photons at CEPC v_1 convert into e^+e^- pairs or even start an EM showers before reaching the calorimeter. Thanks to the sophisticated lepton identification performance and the large solid angle coverage, most of these converted photons could be identified.

The PFA level photon energy reconstruction is depending on the intrinsic ECAL energy resolution and the PFA algorithm energy collection efficiency and purity. The energy collection efficiency, or say the hit collection efficiency, is certainly a function of the incident particle energy/type. Using iterative reconstruction algorithm, Arbor reaches reconstruction efficiency higher than 99.9% for photons with energy larger than 2 GeV.

The identification of photons from the neutron background is straight forward. Combined with the ToF information and the shower profile information, the identification performance could reach a level such that, at 99.9% identification efficiency, the misidentification rate of neutron to photons is smaller than 3%. Meanwhile, the overlapping between photon showers and other particle showers may degrade the identification efficiency, however, since the CEPC v_4 detector has large tracker radius and very high granular ECAL readout cells, this degrading is limited to sub-percentage level.

The overall photon reconstruction could be characterized by the $Br(H \rightarrow \gamma\gamma)$ measurement. On the other hand, the photon reconstruction is sensitive to the geometry defects, such as the cracks between ECAL modules, staves, and the dead zone between ECAL barrel and endcaps. To benchmark the impact of geometry defects, a simplified, defect-free ECAL geometry has been implemented into the Geant 4 simulation. This simplified ECAL uses cylindrical barrel layer and its endcaps is directly attached to the barrel, forming a closed cylinder. Fig. 11.6 shows the Higgs boson invariant mass reconstructed from $Br(H \rightarrow \gamma\gamma)$ signal at a simplified ECal geometry. A relative signal width of 1.7% is achieved, which agrees with the intrinsic electron energy resolution, of 16%/sqrt(E), measured from the TB data of the Si-W ECAL prototype.

The Higgs to di photon signal is also studied at the CEPC v_1 geometry, where a relative signal width of 2.2% is observed. This degrading is mainly induced by the geometry defect in between the ECAL module and ECAL staves. In addition, the impact of detector inhomogeneity and detector dead zones is also studied, where both effects causes significant degrading to the Higgs mass resolution via $H \rightarrow \gamma\gamma$ events.

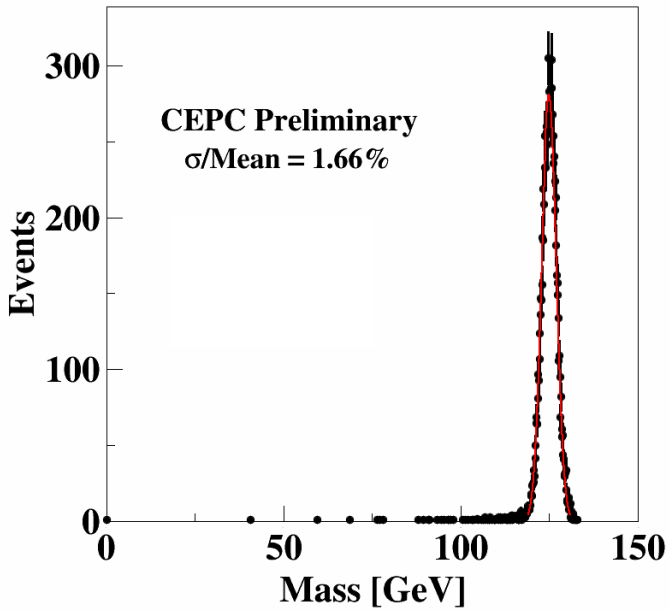

Figure 11.6: The reconstructed Higgs invariant mass of $H \to \gamma\gamma$ events

11.7 Taus

τ's are extremely intriguing physics objects. As the heaviest lepton in the SM, a significant fraction of the SM Higgs boson decays into di-tau final states. As a result, g(Htautau) is anticipated to be measured better than 1% relative accuracy at the CEPC. Measuring the polarization of Tau at the Z pole leads to a precise determination of Afb(tau) and therefore $\sin^2\theta$. The reconstructions of tau functional spectral is of key importance to the CEPC EW program.

A successful reconstruction of the tau lepton is not a trivial task, for the tau lepton has various decay final states. In the CEPC collision environment, we catalog the tau events into two catalogues according to the event topology, and the reconstruction algorithm and performances has been studied respectively.

The first catalogue is the leptonic catalogue, where no physics objects, or only lepton/photon/Missing energy momentum is generated together with the tau candidates. These events include, for example:

1, $e^+e^- \to ZH, Z \to ll$ or $\nu\bar{\nu}, H \to \tau^+\tau^-$ events;

2, $e^+e^- \to ZZ \to ll/\nu\bar{\nu} + \tau^+\tau^-$ events;

3, WW events with $l\nu\tau\nu$ final states;

3, ISR return events at Higgs runs, with Z decays into a pair of τ's;

4, $Z \to \tau^+\tau^-$ events at CEPC Z pole operation.

A successful identification of these events based highly on the reconstruction of photons and charged hadrons.

The second catalog is the hadronic catalog, where the tau pairs is generated with jets. For instance, we have:

1, $ZH, Z \to qq, H \to \tau\tau$

2, $ZZ \to qq\tau\tau$

3, $WW \to qq\tau\nu$

4, $ZH, Z- > qq, H \to WW \to l\nu\tau\nu$

To find the tau lepton in the hadronic catalog is much more challenge than that in the leptonic environments. The identification algorithm would always be a compromise between the signal efficiency and purity. A full physics analysis of the $Br(H \to \tau^+\tau^-)$ measurement at CEPC has been performaned at CEPC v_1 geometry.

The performance of the first catalogue could be represented by the $Br(H \to \tau^+\tau^-)$ measurement at $\mu^+\mu^- H$. The inclusive SM background could be efficiently subtracted by requesting the proper number of lepton and limit the number of photon and charged hadrons. The background reduction could be further enhanced by restrictions on the recoil mass against the muon system. To further suppress the remaining background, the BDT method that combines the kinematic information from tau candidates has been applied. The pull of impact parameter of the leading track in the tau candidates has been shown in the left plot of Fig. 11.7, where the signal is clearly separated from the background.

Thanks to the precise reconstruction of leptons, photons and charged hadrons, the final event selection efficiency of $\mu^+\mu^- H$ events is 93% and the entire SM background is controlled to a statistic smaller than the signal — in other word, suppressed by nearly 6 orders of magnitudes. It should be noticed that the leading remaining background is the irreducible Higgs background from Higgs to WW decays. A relative accuracy of 2.7% is achieved for the signal strength measurement in the $\mu^+\mu^- H$ channel.

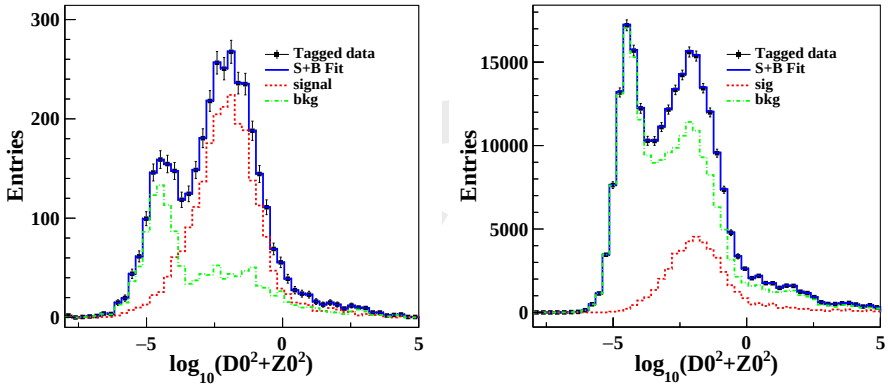

Figure 11.7: The pull of impact parameters at $Br(H \to \tau^+\tau^-)$ measurement via $\mu^+\mu^- H$ (left) and $q\bar{q}H$ channel(right).

The second catalogue includes the tau reconstruction at $q\bar{q}H$, Higgs->tautau events. A double size cone-based tau tagging algorithm has been developed. Two cones at different sizes are scanned for each individual track. The cone parameters, including the sizes, the invariant mass, and the energy ratios, are optimized toward the objective measurement. In short, by requesting two tau candidates with opposite charge, the signal efficiency is 57% and the background could be suppressed by 3 orders of magnitude. Following a similar BDT event selections as in the mumuH analysis, the pull of the impact parameters has

been extracted, see the right panel of Fig. 11.7 A relative accuracy of 1.7% is achieved in the $q\bar{q}H$ channel [ref. DanNote].

To conclude, the tau reconstruction at the CEPC is currently catalogued into leptonic and hadronic events and reconstructed using different strategy and tau finding algorithm. In the leptonic events, the tau events identification relies strongly on a successful reconstruction of the photons, charged hadrons and leptons. Since the CEPC reference detector ensures a powerful particle flow reconstruction of these final state particle, the tau candidate identification reaches almost an ideal efficiency and purity. In the hadronic events, cone-based tau-tagging algorithm has been developed, which could reach an efficiency/purity better than 70%/70%. In both cases, a precise reconstruction of the impact parameter — the pull from the IP — plays an important role in the tau events identification.

It should be emphasized that the physics requirements arisen from the tau physics is more demanding than the $Br(H \rightarrow \tau^+\tau^-)$ measurements. The former request an clear separation between the photons generated from π^0 in the τ decay cascade, while the latter only request a clear separation between signal and backgrounds.

11.8 Jet-clustering

The jet reconstruction is crucial to the CEPC physics program. Since roughly 60% of the jet energy is stored in charged hadrons, whose momentum is usually measured at a superior precision in the tracker than in the calorimeter. Therefore, Particle Flow Algorithms could improve significantly the precision of jet energy measurement, with respect to the calorimeter only reconstruction.

At CEPC reconstruction, the jet candidates are clustered from the reconstructed particles. The ambiguities from the jet clustering, i.e, wrongly grouping of the final state particle, could be a significant effect and need careful investigation. To characterize the jet reconstruction performance, a two-stage analysis has been performed on the following samples:

1, $\nu\nu qq$ events via the ZZ intermediate state;

2, $l\nu qq$ events via mostly WW intermediate state;

3, $\nu\nu H$ events with $H \rightarrow b\bar{b}, c\bar{c},$ or gg;

The first stage is the boson mass reconstruction. In these events, despite possibly one isolated lepton (in WW events) and isolated ISR photon(s), all the final state particles are decayed from one individual massive boson. Therefore, no jet clustering algorithm is needed and the boson mass could be reconstructed directly from all the visible final state particles.

A second stage analysis is applied on the jet candidates. Vetoing the isolated photon and leptons, we forced the remaining final state particle into 2 reconstructed jets via the ee-anti-kt algorithm (Reco-Jets). The same jet-clustering algorithm is also applied to the final state particles at the generator level, and forming the Gen-Jets. Therefore, the energy/angular responses could be studied via the comparison of initial quarks, the Gen-Jets and the Reco-Jets. Clearly, the difference between the initial quarks and Gen-jets is stemmed from the fragmentation and jet-clustering algorithm, while the difference between Gen-jets and Reco-jets includes the detector performances.

The result of the first stage study is shown in Fig. 11.8, which displays the reconstructed invariant mass spectra of all the final state particles except the possible isolated lepton. Clearly, each histogram exhibits a significant mass peak at the anticipated position. Meanwhile, various physics effects exhibit in these corresponding plots, lead to a wider distribution:

1, In the $\nu\nu qq$ events, most of the jets decay from a on-shell Z boson, however, the $Z-\gamma$ interferences give rises to a low energy plateau.

2, All the mass peaks exhibit a clear high mass tail, induced by the ISR photon. In the $l\nu qq$ events, the high mass tail is also induced by the physics processes where the final states jets is not decayed from a intermediate W boson.

3, Low mass tails induced by the neutrinos generated in the heavy flavor jet decay cascade (i.e, $W \to cs, Z/H \to cc$ or bb).

To disentangle these physics effects from the detector response, we restrict the samples by vetoing the heavy flavor jets (in the middle raw of Fig. 11.8) and by additionally veto events with significant ISR photons (in the lower raw). Clearly, the peaks become much narrower after applying those cuts.

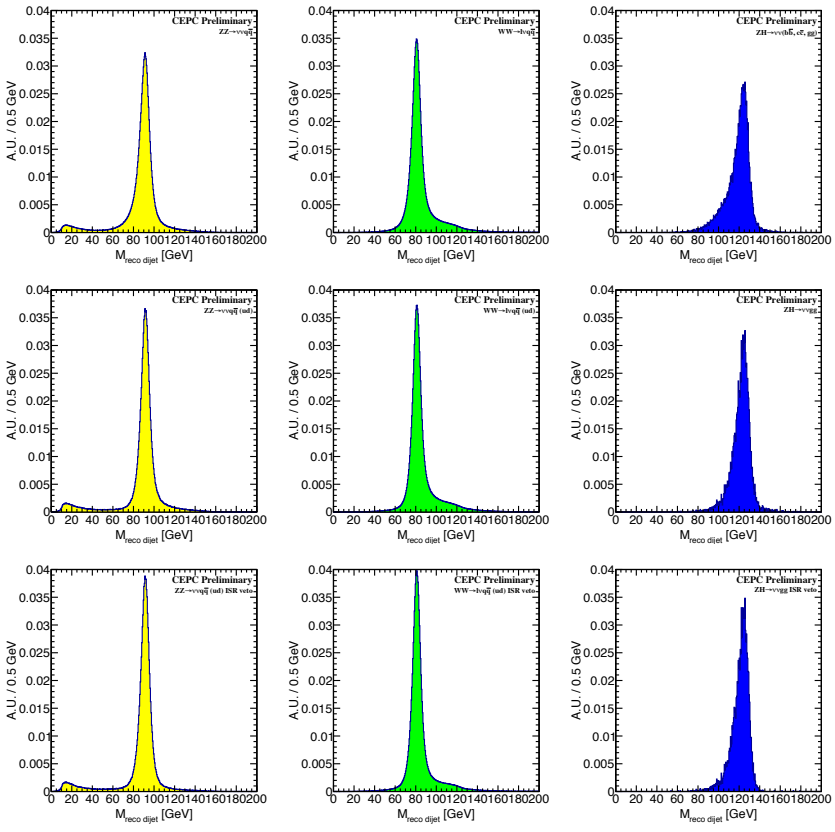

Figure 11.8: Reconstructed boson masses from physics benchmarks of $\nu\nu qq$ events (left), lvqq events(middle) and vvH, H->qq events (right). The raws are corresponding to inclusive samples, light flavor samples and light flavor + ISR cleaned samples.

After these cleaning, a relative resolution of 3.8% is reached for the Higgs invariant mass reconstruction via $\nu\nu H, H \to gg$ events. Giving the fact that the SM Higgs boson

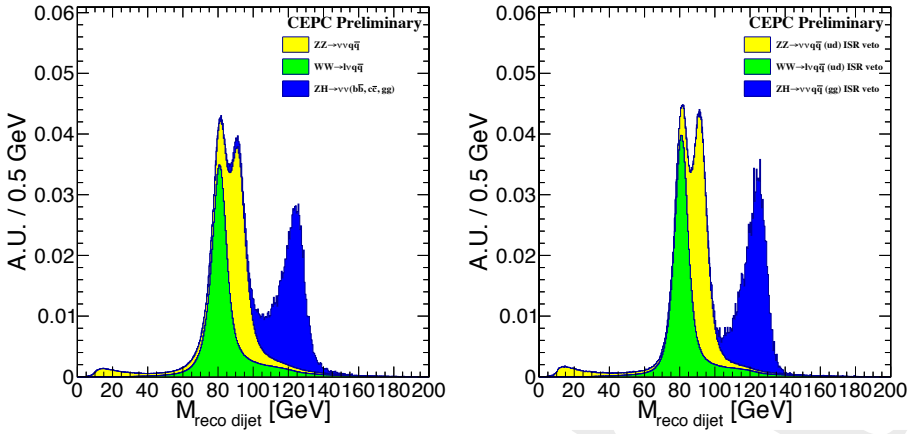

Figure 11.9: Overlapped PDFs from reconstructed 2-jets events. Left: inclusive samples; right, cleaned samples.

has a width of 4.2 MeV, this accuracy is mainly induced by the detector resolution. Similar level of Boson mass resolution is achieved for W and Z boson once the intrinsic boson mass width is deconvoluted from the overall distribution. Therefore, we conclude that the boson invariant mass could be measured to better than 4% at this CEPC reference detector.

Fig. 11.9 shows the overlapped PDFs extracted from Fig. 11.8, each normalized to a unit area. The left/right plot is corresponding to the inclusive/cleaned samples accordingly. A clear separation between the mass peak of W, Z and Higgs boson exhibits for both plots, meanwhile, cleaning the heavy flavor and ISR events significantly enhances the separation.

The second stage analysis is applied on the vvqq sample. The entire visible energy/momenta was clustered into 2 jets. These 2 jets are classified into leading/sub-leading jets according to their energy. The jet energy scale (JES) and jet energy resolution (JER), defined as the relative differences between the Genjet and the Recojet, has analyzed accordingly. The relative energy difference between the RecoJet and GenJet could be modeled by a core function (double sided crystal ball) convoluted with a Guassian. The core function is induced mainly due to the jet clustering and detector acceptance effects, while the Guassian described the detector resolution. The mean value of the Gaussian is defined as the JES while the relative width of the Guassian is defined as the jet energy resolution (JER).

Fig. 11.10 shows the JES at different jet directions for both jets. The entire amplitude of the JES is controlled to 1% level, which is roughly 1 order of magnitude better than that at LHC. The JES is completely flat along the azimuth angle. Along the polar angle, the JES increases significantly for the leading jets in the overlap part between endcap and barrel. Meanwhile, the JES is also larger in the endcap than in the barrel. One possible explanation is that the Particle Flow confusion terms, especially the artificial splitting of the charged clusters, increases in these parts.

It's interesting to see that the Leading jets has a systematically higher jet energy scale comparing to the sub-leading one, mainly due to the fact that the classification method is energy, thus jet energy scale dependent. This effect may well be jet-clustering algorithm dependent.

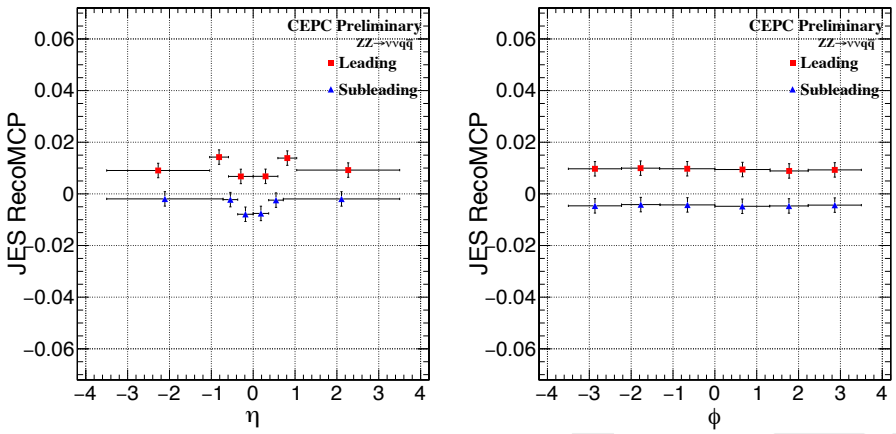

Figure 11.10: jet energy scale as a function of the jet directions.

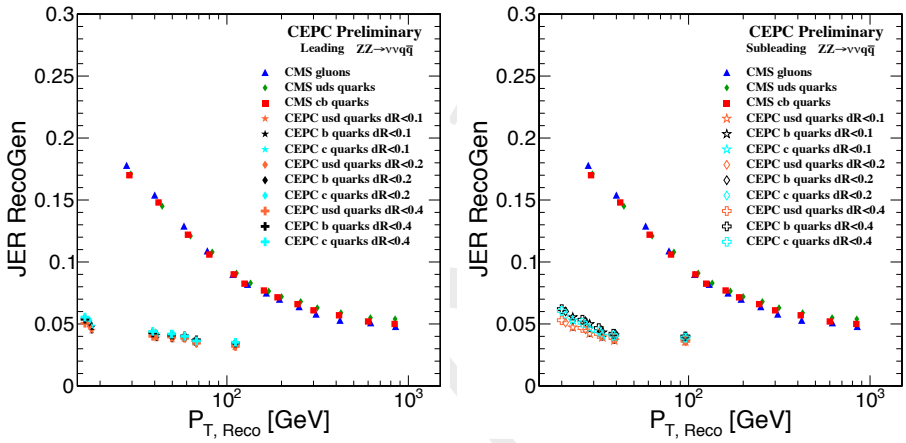

Figure 11.11: The jet energy resolution for leading (Left) and sub-leading jets (Right), as a function of the jet transverse momenta. The performance at CMS has been overlapped for a reference of comparison.

The jet energy resolution (JER) performance for jet with different transverse momenta is displayed in Fig. 11.11. The overall JER takes a value between 6% (at $P_t < 20$ GeV) to 3% (at $P_t > 100$ GeV). The leading jets usually takes a slightly better JER comparing to the sub-leading ones. Taking the performance of the CMS detector as a reference, the JER at the CEPC reference detector is 2-4 times better in the corresponding P_t range.

To conclude, the jet energy response has been analyzed at both boson mass level and at individual jets. For physics events with one massive boson decays into jet final states, the boson mass could be measured to a relative accuracy better than 4% at CEPC v_1. This resolution ensures a significant separation between the W boson, Z boson, and the Higgs boson at the inclusive physics samples; despite the separation is significantly limited by various physics effects. At individual jets, the JES is controlled to 1% level, which is one order of magnitude better than that of LHC experiments. The JER is superior by 2-4 times better than the LHC results.

This superior performance is based on the clean collision environment at the electron positron collider, and also on the development of detector design and reconstruction efforts. It not only secures the Higgs property measurements, but also is highly appreciated

in the EW measurements. For instance, this mass separation benefits the Triplet Gauge Boson Coupling (TGG) measurement in the semi-leptonic channel ($e^+e^- \to WW \to l\nu qq$ and $e^+e^- \to ZZ \to llqq, \nu\nu qq$), for the reconstructed masses provide separation power on top of the lepton reconstruction.

It should be emphasized that the jet-clustering algorithm has a strong and even dominant impact in jet reconstruction. Dedicated studies are required to search for the most suited jet clustering algorithm and the corresponding set up, especially for the 4-jets or even 6-jets events.

All the plots used in this section is based on the full simulation of CEPC v_1 geometry. Using the Higgs mass resolution at $H \to gg$ samples as benchmark, the performance of Boson mass resolution of different B-Fields, different HCAL layer thickness. It shows that changing the B-Field from 3.5 to 3 Tesla, the Boson mass resolution maintains at the same level. Reducing the HCAL layers from 48 layers to 40 layers also has negligible impact on the Boson mass resolution, since roughly only 0.1% of the energy deposited in the Calorimeter actually deposited in the last eight layers.

11.9 Jet flavor tagging

Identification of jet flavor, such as b, c, $u/d/s$, and gluon plays an important role in the event reconstruction and essentially for the measurement of the couplings of the $H \to b\bar{b}, c\bar{c}$, and gg, as well as those of $R_{b/c}$ of Z decays at the CEPC. Bottom jets can be identified by the fact that bottom quarks form hadrons which have specific masses and prolonged lifetimes compared to jets formed from lighter quarks. Charged tracks decaying from bottom hadrons tend to have sizable impact parameters measured with respect to the primary vertex. If there are two or more tracks originating from the same hadron, its decay vertex can be reconstructed directly. Bottom jets can be identified if the distance between the primary vertex and the decay vertex is sufficiently large, and that the reconstructed mass from the combination of the charged tracks is consistent with that of a hadron containing a bottom quark. The identification of bottom jets based on the impact parameter of charged tracks and information about secondary vertices has been an essential tool in the event reconstruction of recent energy-frontier collider experiments. The flavor tagging algorithm of the CEPC benefits from the excellent vertex measurement, as well as the PFA oriented design concept, which ensure a very good secondary vertex reconstruction and jet energy resolution. Recently, the identification of the charm c jet has also become a target of study with the planning of future e^+e^- colliders, such as the ILC and the CLIC. The capability of c jet identification allows us to probe the complete hadronic decays of the Higgs boson $H \to b\bar{b}, c\bar{c}, gg$ as well as flavor-changing neutral currents in the top sector such as $t \to cZ$ and $t \to cH$. Since charm hadrons have smaller masses and shorter lifetimes compared to bottom hadrons, charm hadrons are more difficult to identify. Fortunately, the excellent point resolution in the vertex detectors to be employed by future e^+e^- linear colliders makes it possible.

11.9.1 Base line

The LCFIPlus package [5] is used for secondary vertex reconstruction, jet-clustering, and flavor tagging. The LCFIPlus employs the Boosted Decision Tree (BDT) in TMVA [6] to do the flavor tagging. This is a machine learning appoach and based on dedicated training

samples, which may be from data or Monte Carlo simulation. Roughly 60 variables of each jet are used and all jets are categorzied into four according to the number of vertex reconstructed. Each category has its own independent TMVA application.

The CEPC as a Higgs factory is also planned to run at Z-pole, and a huge statistics of Z sample will be accumulated, which can be used for the detector calibration and alignment, and as the control sample for systematic uncertainty control. The data sample of Z pole also provides a set of large statistics and pure training samples for flavor tagging application.

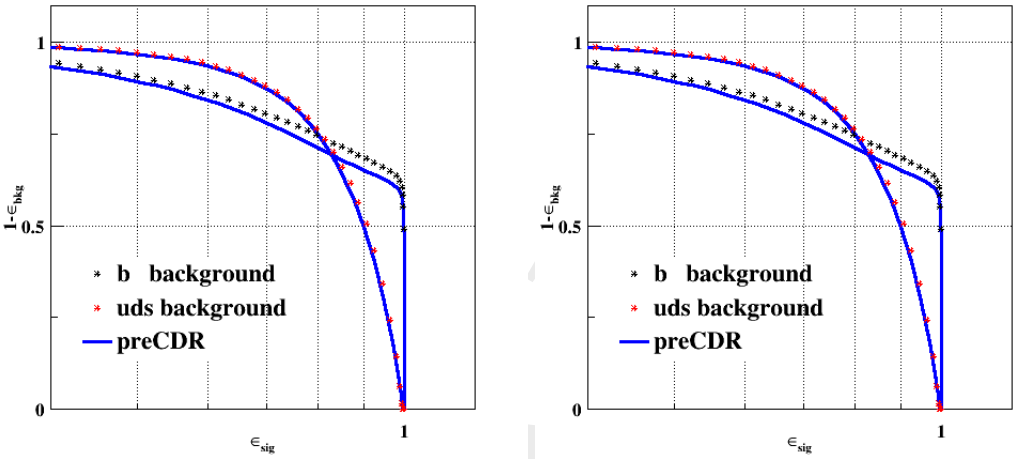

Figure 11.12: The Receiver operating characteristic (ROC) curve of b/c-tagging shows the performances of flavor tagging compared with those of preCDR.

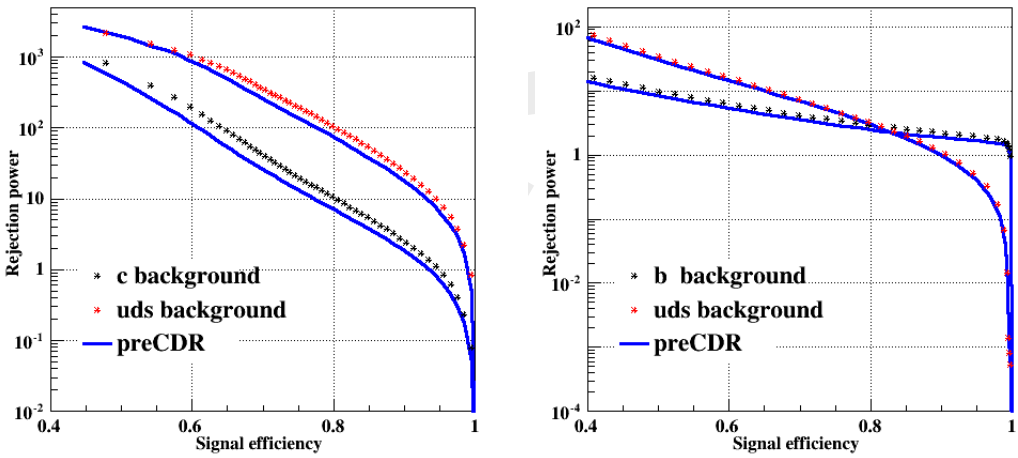

Figure 11.13: The rejection power vs signal efficiency curves of b/c-tagging compared with those of preCDR.

11.9.2 Other machine learning approaches

Besides the BDT approach in TMVA&ROOT is used as baseline for CEPC flavor tagging, ohter machine learning appoaches are also tried. A comparison of the prediction per-

formances of state-of-the-art machine learning methods, namely, deep neural networks (DNN), Gradient Boosting Decision Trees (GBDT), eXtreme Gradient Boosting (XGboost), and multi-Grained Cascade Forest (GCForest) are performed. Moreover, the effect of feature selection with Recursive Feature Elimination (RFE) in flavor tagging is investigated as well.

11.9.2.1 DNN

In the deep neural network(DNN) algorithm, we use the tensorflow package which is an open source software library for numerical computation using data flow graphs. For the implementation of DNN, the training set has been preprocessed with the min-max scaling method, which transforms features by scaling each feature to the range from 0 to 1. The neural network contains an input layer, hidden layers and an output layer. The input layer has 68 neurons which represent 68 physical variables, and there are four hidden layers with 512 neurons for each layer. The output layer has 3 neurons representing b quarks , c quarks and o quarks. Each hidden layer has the dropout values of 0.5. We use the adam optimizer to optimize the DNN model. The batch size is 100 events per step. After 500,000 steps of training, we achieve an accuracy of 78.8% on the test dataset.

11.9.2.2 Boosted Trees

In the function estimation or "predictive learning" problem, one has a system consisting of a random "output" variable y and a set of random "input" variable $x = x1, ...xn$, the goal is to obtain an estimate or approximation function $F^*(x)$ mapping x to y, that minimizes the expected value of some specified loss function $L(y, F(x))$.

$$F^* = argminL(y, F(x)) \ . \tag{11.1}$$

A common procedure is to restrict $F(x)$ to be a member of functions $f(x)$ with fixed forms, namely,

$$F(x) = \sum_{i=1}^{r} f_i(x) \ , \tag{11.2}$$

where the function $f(x)$ is called basis function or weak learner.

Boosting is a stage-wise strategy which readjust input terms when new ones are added.

$$F_t(x) = F_t(x) + f_t(x) \ , \tag{11.3}$$

where $f_t(x)$ is obtained by minimize loss function $L()$, namely,

$$f_t = \text{arg min}L(y, F_t(x)) = \text{arg min}_f L(y, F_{t-1}(x) + f(x)) \ . \tag{11.4}$$

where frequently employed loss function $L(y, F)$ includes squared-error $(y - F)^2$ and absolute error $|y - F|$ for regression or classification.

11.9.2.3 GBDT

Gradient boosting decision tree (GBDT), introduced by Friedman, is a member of the tree ensemble learning Boosting family. Different from Adaboost where the error rate of the previous weak learning is used to update the weight of the training set, in GBDT, the

weak learner was limited to the CART regression tree model, and the iterative ideas are also different from Adaboost, as follows,

1. Use training residuals instead of input cases as training data (steepest descent strategy)

2. The result of the basis learner (CART tree) is added as the final output

A new model was created on the gradient of the residual reduction so that the residuals of the previous model are reduced in the gradient direction. The iterations will be executed repeatedly until a particular are met. Finally, we can get an optimal model.

Negative gradient gives the best steepest-descent step direction

$$-g_t(x_i) = -\left[\frac{\partial L(y_i), F(x_i)}{\partial F(x_i)}\right]_{F(x)=F_{t-1}(x)} . \tag{11.5}$$

Objective function can be reformed as

$$f_t = \arg\min_f L(-g_t(x_i), f(x)) , \tag{11.6}$$

11.9.2.4 XGBOOST

XGBoost is another Gradient Boosting algorithm which performed even better than GBDT in efficiency and accuracy. Second-order approximation of loss function is used to optimize the prediction learner. XGBoost synthesizes many of the previous works on the gradient boosting algorithm and has done a lot of optimization.

1. XGBoost is a flexible boosting framework integrated with various loss functions

2. The final prediction for a given example is the sum of predictions from each basis learner (tree).

Minimized regularized objective:

$$L(y, F) = \sum_i l(y_i, F(x_i)) + \sum_k \Omega(f_k) , \tag{11.7}$$

where $\Omega(f_k) = \gamma T + \frac{1}{2}\lambda |vertw|^2$ and l is a differentiable convex loss function that measures the difference between the prediction $F(x_i)$ and the target y_i; The second term penalizes the complexity of the model. T is the number of leaves in the tree. Each f_k corresponds to an independent tree and w is leaf weights (w_i represents score on i-th leaf).

11.9.2.5 GcForrest

GcForest (multi-Grained Cascade Forest) is a novel tree ensemble method proposed by Zhihua Zhou. Compared to the framework of deep learning, gcforest is a new exploration beyond deep learning and has caused extensive concerns. It has been tested to apply to many domains and achieved some success. Here we firstly use gcforest for flavor tagging.

Gcforest consists of multi-grained scanning and a cascade forest. Multi-grained scanning, a similar structure with the CNN window sliding, can further enhance representation learning when the inputs are with high dimensionality. Cascade forest enables gcForest to perform representation learning. Each level of the cascade forest consists of two random forests and two completely-random tree forests. Each layer of the cascade forest receives the input X, which is processed and passed to the next layer.

11.9.2.6 Comparison

11.9.3 Gluon identification

The gluon jet identification is essentially important for the study of Higgs to gluon pair decays. The baseline approach uses Z-pole data as traning sample, where the $u/d/s$ jets are used instead of gluon in the training stage. In fact, gluon jets are quite different with $u/d/s$ jets in many aspects. Here we expand the baseline approach to try classify the jets from 3- to 4-classes, including gluon jet as an independent class. In order to increase the seperation power, more shape related variables are added to identify gluon jet from the others at both jet and event level, such as sphperity, thust, ...

Figure **??** shows the Receiver Operating Curve (ROC) of 4-class classification.

11.9.4 Conclusion

References

[1] M. Zhao, M. Ruan, H. Qi, and Y. Gao, *Feasibility study of TPC at electron positron colliders at Z pole operation*, JINST **12** (2017) no. 07, P07005, arXiv:1704.04401 [physics.ins-det].

[2] M. Ruan and H. Videau, *Arbor, a new approach of the Particle Flow Algorithm*, arXiv:1403.4784 [physics.ins-det]. http://inspirehep.net/record/1286443/files/arXiv:1403.4784.pdf.

[3] M. Ruan, *Shower fractal dimension analysis in a highly-granular calorimeter*, Journal of Physics: Conference Series **490** (2014) no. 1, 012227. http://stacks.iop.org/1742-6596/490/i=1/a=012227.

[4] D. Yu, M. Ruan, V. Boudry, and H. Videau, *Lepton identification at particle flow oriented detector for the future e^+e^- Higgs factories*, Eur. Phys. J. **C77** (2017) no. 9, 591, arXiv:1701.07542 [physics.ins-det].

[5] T. Suehara and T. Tanabe, *LCFIPlus: A Framework for Jet Analysis in Linear Collider Studies*, Nucl. Instrum. Meth. **A808** (2016) 109–116, arXiv:1506.08371 [physics.ins-det].

[6] J. Therhaag, *TMVA Toolkit for multivariate data analysis in ROOT*, PoS **ICHEP2010** (2010) 510.

CHAPTER 12

FUTRUE PLANS AND R&D PROSPECTS

This [1] is an example with plots, please edit ...

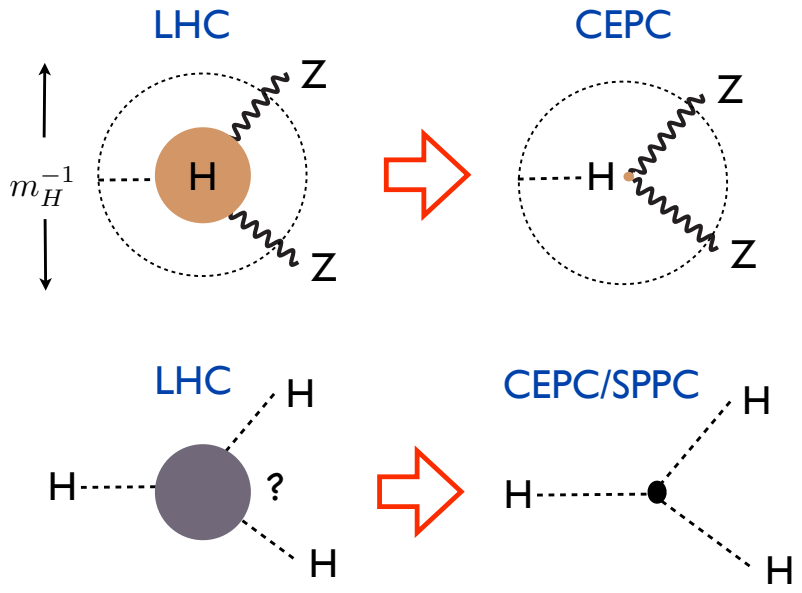

Figure 12.1: A sketch of two of the central goals of the CEPC and SPPC. The CEPC will probe whether the Higgs is truly “elementary", with a resolution up to a hundred times more powerful than the LHC. The SPPC will see, for the first time, a fundamentally new dynamical process — the self-interaction of an elementary particle — uniquely associated with the Higgs.

12.1 New Colliders for a New Frontier

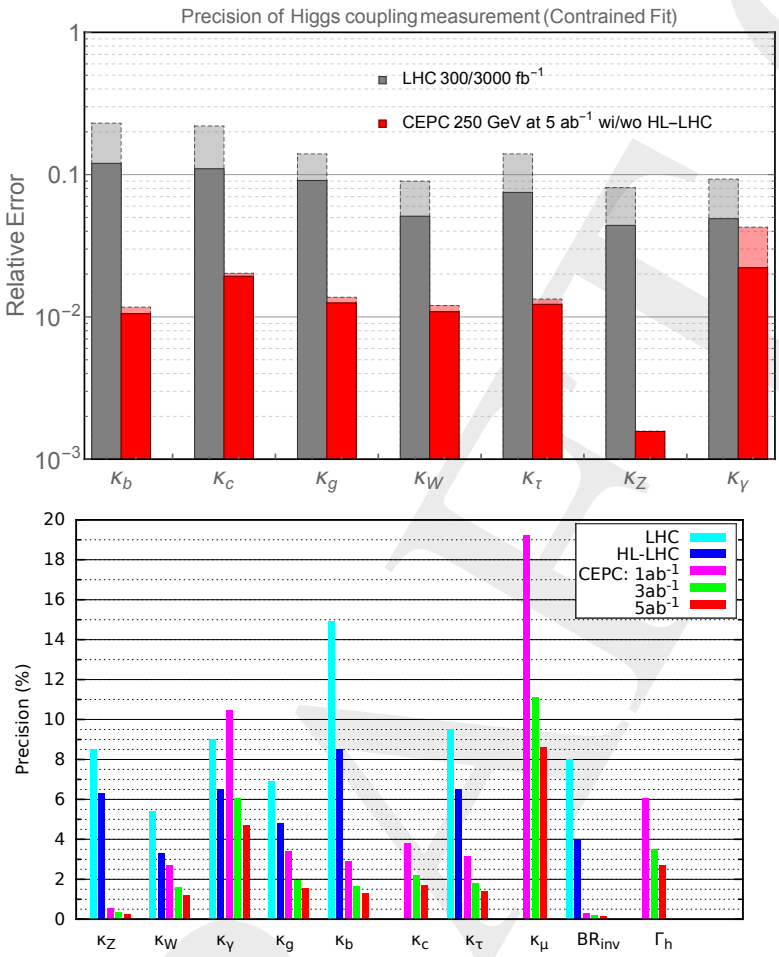

Figure 12.2: Top: The 7 parameter fit, and comparison with the HL-LHC, discussed in detail in Chapter 11. The projections for CEPC at 250 GeV with 5 ab^{-1} integrated luminosity are shown. The CEPC results without combination with HL-LHC input are shown with dashed edges. The LHC projections for an integrated luminosity of 300 fb^{-1} are shown in dashed edges. Bottom: Comparison between the LHC and several benchmark luminosities of the CEPC.

References

[1] CEPC project website. http://cepc.ihep.ac.cn.

Appendices

CHAPTER 1

μRWELL PROTOTYPE

1.1 μRWell prototypes performance

The gas gain of the detectors has been measured with a collimated flux of 5.9 keV photons generated by an X-ray gun. The measurement is performed in current mode, by monitoring the current drawn through the resistive layer as a function of the potential applied to the amplification stage.
The gas gain of each detector, measured for the Ar:i-C_4H_{10} 90:10 gas mixture, is typically $\geq$ 10000, being stopped when current instabilities are observed: the largest gain seems to be reached with the most resistive detector (fig. **??**). The dependence of the rate capability on the resistivity of the various prototypes has been measured at the gain G$\sim$4000 with the usual collimated (2.5 mm diameter) photon X-ray gun.
As shown in fig.**??**, the gain decrease is correlated with the voltage drop due to the resistive layer: the higher the DLC resistivity the lower is the rate capability, ranging from few tens of kHz/cm^2 up to a few MHz/cm^2. A more trustworthy measurement of the rate capability achievable with the single-resistive layer configuration of the detector has been obtained irradiating with a $\sim$3x3 cm^2 (FWHM) pion beam (see section **??**) two different sectors of a large area detector with a $\sim$ 70 M$\Omega/\square$ resistivity (section 8.3.1). The result, as reported in [**?**], indicates that the detector can stand a particle flux above 35 kHz/cm^2.
The tracking performance of the three prototypes and its dependence on the resistivity of the DLC film has been tested with a muon beam at the H4 line of the SPS test area at CERN.
All detectors have been operated in Ar:i-C_4H_{10} 90:10 and read-out by APV hybrid cards [**?**] handled by an SRS system. The APV chip, supplying analog output signals, allows the study of the detector tracking performance based on the charge centroid method.

The resistive anodic film is equivalent to a distributed 2-D resistive-capacitive network with respect to the readout plane. The localized charge produced in the amplification stage of the detector arriving on the resistive anode surface is dispersed with a time constant depending on the surface resistivity and the capacitance per unit area (see section 6.1).
As a consequence the spatial resolution, as shown in fig. 1.1, depends on the surface resistivity of the DLC film showing a clear minimum around 100÷200 M$\Omega/\square$. At low surface resistivity the charge dispersion increases, the distribution loses the typical Gaussian shape and consequently the σ becomes larger. At high surface resistivity the charge dispersion is so negligible (the strip cluster size being close to 1 - in strip unit) that the charge centroid method becomes no more effective and the σ approaches the limit of pitch/$\sqrt{12}$ (strip pitch = 0.4 mm).

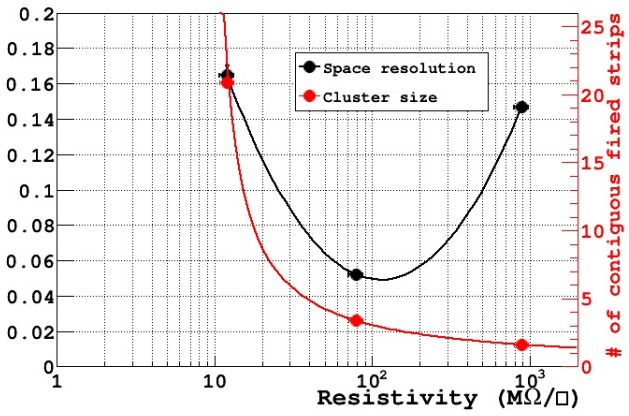

Figure 1.1: Space resolution and strip cluster size (0.4 mm strip pitch) as a function of the DLC resistivity.

1.2 The double-resistive layer detector

As discussed in [**?**], the μRWell based on the single-resistive layout characterized by a 2-D evacuation scheme (with grounding all around the edge of the detector surface) suffers at high particle fluxes of a non-uniform response over its surface. This is due to the resistance (Ω_{single}) seen by the current generated by the incident radiation that depends on the distance to ground (for the definition of Ω see the appendix B of the cited reference).
In order to get rid of such a limitation a double-resistive layout (fig. **??**) has been proposed: the first DLC film, in contact with the amplification stage of the detector, is connected to a second DLC film by means of a matrix of through-vias and then grounded with a second matrix of through-vias to the underlying readout electrodes.

In this way a sort of discrete 3D-current evacuation layout is obtained and the Ω_{double} seen by the current is minimized with respect to the single-resistive layer scheme just for geometry and Ohm's law considerations.
Comparing a 50×50 cm^2 single-resistive detector with a double-resistive detector of the same size, but with a through-vias density of 1 cm^{-2}, and assuming the same surface resistivity of the DLC films for both devices, a $\Omega_{double}/\Omega_{single}$ ratio (and correspondingly the ratio between the voltage drop $\Delta V_{double}/\Delta V_{single}$) of the order of 1/10 is obtained. As a consequence an improvement of a factor of ten of the rate capability could be achieved with the double-resistive technology.

The rate capability for different DLC-film resistivity 10×10 cm^2 double-layer proto-

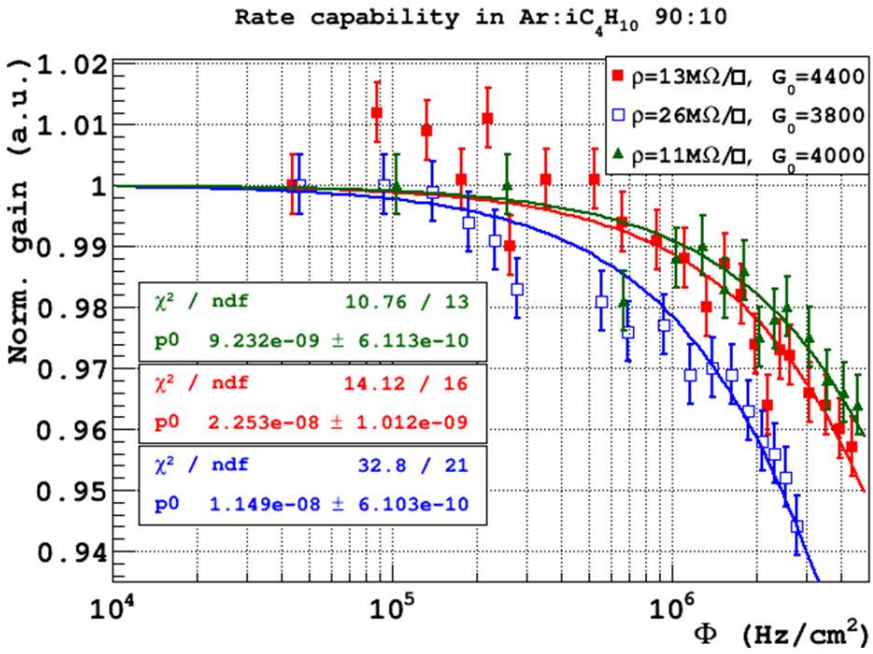

Figure 1.2: Normalized gain for double-layer prototypes: 11 MΩ/□ (green triangles), 13 MΩ/□ (red full square) and 26 MΩ/□ (blue empty sqaure)

types with 1 cm^{-2} through-vias grounding density (pitch) has been measured with 5 mm diameter collimated X-ray beam. In this case the results, shown in fig.1.2, even though performed with local irradiation are practically equivalent to those obtained with global irradiation.

1.3 μRWell ageing tests at the GIF++

In order to test the behavior of μRWell detectors under heavy irradiation, the GE11 size μRWell prototype has been exposed to the GIF++ high-intensity source, together with two smaller prototypes. The GE11 size detector is operated with an $ArCO_2$ 70-30 gas mixture. At the end of September 2017, the detector has already accumulated a dose equivalent to 32 mC/cm^2, as can be seen in figure 1.3 , that corresponds to more than 100 years of operation under HL-LHC conditions.

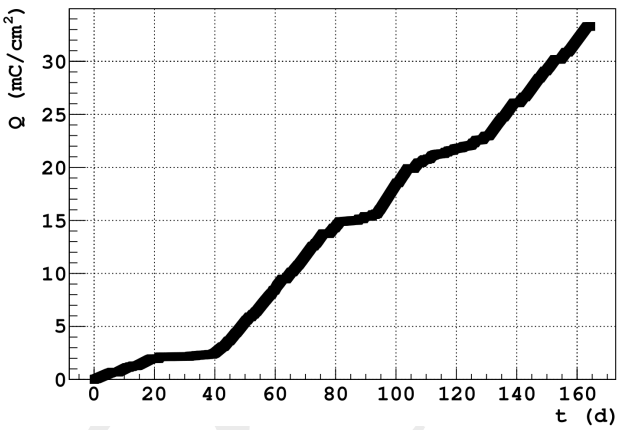

Figure 1.3: Dose accumulated at the GIF++ by the GE11 size detector. The detector has accumulated about 32 mC/cm^2, equivalent to more than 100 years of operation at HL-LHC conditions.